Investigation of strained interfaces of Fe/(Ga, Al, In)As based spintronic heterojunctions

Dissertation with the aim of achieving a doctoral degree

at the Faculty of Mathematics, Informatics and Natural sciences

Department of Applied Physics

of Universität Hamburg

submitted by

M.Sc. GSN Rajkiran Tholapi

from Srikakulam, India

2017 in Hamburg

Gutachter der Dissertation:	Prof. Dr. W. Hansen Dr. M. Sprung
Zusammensetzung der Prüfungskommission:	Prof. Dr. W. Hansen Dr. M. Sprung Prof. Dr. R. H. Blick Dr. P. Gaal Prof. Dr. S. O. Moch
Vorsitzender des Prüfungskommission:	Prof. Dr. S. O. Moch
Datum der Disputation:	26. October 2017
Vorsitzender des Promotionsausschusses:	Prof. Dr. W. Hansen
Leiter des Fachbereichs PHYSIK:	Prof. Dr. M. Potthoff
Dekan der Min-Fakultät:	Prof. Dr. H. Graener

Abstract

Spin electronics or "spintronics" is identified as one of the potential technologies to replace the currently prevailing metal-oxide-semiconductor field-effect transistor (MOSFET) technology for information processing. For realization of spintronic devices like spin-valves in which spin currents are injected and detected, a large combination of ferromagnet-semiconductor (fm-sc) interfaces are being investigated. To replace the current MOSFET technology with the spin-transistors, high spin-injection efficiency is necessary which is not yet reported. Therefore, understanding the structural state of these fm-sc interfaces is essential for fabricating highly efficient future spintronic devices.

This dissertation describes the investigation of structural properties of Fe/III-V semiconductor interfaces. This work also encompasses the correlation of the observed structural state to the measured spin-injection across the interface. These investigations are performed on three material systems, namely Fe on moderately doped GaAs (001), Fe on InGaAs/InAs quantum wells and Fe on MgO/GaAs surfaces. Spin injection across the first two material systems is successfully measured by using an all electrical non-local spin-valve setup. In this work the emphasis is on the structural studies conducted on Fe layers under the influence of intrinsic and extrinsic strain.

Structural investigations are performed on Fe/GaAs interfaces that are grown as a function of Fe layer deposition temperature and subjected to post growth annealing cycles. These investigations are performed by utilizing various X-ray scattering geometries available at both laboratory and third generation synchrotron facilities. The Fe layers in this system are found to be compressively strained and this strain state is observed to be influenced by post-growth annealing at 200°C. In addition, grazing incidence diffraction measurements reveal the existence of a Fe_3GaAs phase at the interface which is also observed to be influenced by post-growth annealing. In correspondence, the spin-injection efficiency across the interface is also affected by the post-growth annealing which was non-existent before annealing. But, after first annealing cycle, it increased to a value of 5.5%. However, after a second annealing cycle, the spin-injection efficiency is reduced to 2.6%.

The structural investigations were also performed on Fe/InGaAs/InAs quantum wells material system to study the local crystallinity of $In_xAl_{1-x}As$ buffer layers on which the active layers containing quantum well are deposited. The structural information of these buffer layers is essential, because the strain relaxation leads to local tilt of lattice planes and composition variation resulting in cross-hatches at the surface of the heterostructure. These cross-hatches in turn determine the non-planar nature of the quantum well. Therefore, the local structural integrity of these layers is probed by using scanning diffractive imaging which revealed two networks of defects that vary as function of Indium content.

The spin-injection measurements performed on InGaAs/InAs quantum wells reveal that spin-transport occurs in the semi-ballistic regime in this system. However, the obtained spin-injection results also indicate that a ballistic model proposed for calculating the spin-injection efficiency is inadequate as it does not take the crystallographic anisotropy of Spin-orbit interaction.

The last system that is investigated in this thesis is the Fe/MgO/GaAs interface. Unlike the other two material systems, the Fe/MgO/GaAs interface is characterized on an atomic scale by high resolution transmission electron microscopy (HRTEM)to reveal the influence of the MgO thickness and its deposition conditions on the morphology and magnetic characteristics of Fe layers. The structural studies including energy dispersive spectroscopy (EDS) mapping and X-ray reflectivity (XRR) analysis are also performed to study the relevance of intermixing at the interface. The magneto-optic Kerr effect (MOKE) investigations reveal that in-plane cubic and uniaxial magnetic anisotropy coexist in Fe/MgO/GaAs samples. The strength of cubic and uniaxial anisotropy contributions are found to vary with the deposition conditions of MgO and Fe.

Kurzfassung

Der Spin-Elektronik oder Spintronik wird großes Potential für die Ablösung der derzeitigen, auf Feldeffekttransistoren (MOSFETs) basierenden Datenverarbeitungstechnologie zugeschrieben. Für die Realisierung von Spintronik-Bauelementen, die Spinströme im Halbleiter generieren oder detektieren können, sogenannte Ferromagnet-Halbleiter (FH)-Spinventile, werden derzeit eine ganze Reihe von möglichen Kombinationen unterschiedlicher Materialien untersucht. Zwingend notwendig für die Ablösung der MOSFET-Technologie durch Spintransistoren ist eine hohe Spininjektionseffizienz, von der die bisher an Ferromagnet-Halbleitergrenzflächen nachgewiesenen Effizienzen noch weit entfernt sind. Essentiell für die Entwicklung neuer, hoch effizienter Spintronik-Bauelemente ist folglich ein grundlegendes Verständnis des strukturellen Aufbaus der FH-Grenzflächen.

In dieser Dissertation werden die strukturellen Eigenschaften von Grenzflächen zwischen einem Eisenfilm (Fe) und verschiedenen III-V Halbleitern untersucht. Außerdem wurden die Auswirkungen der beobachteten strukturellen Eigenschaften auf die Spininjektion betrachtet. Insgesamt wurden drei Materialsysteme studiert: Fe auf epitaktischem, moderat dotiertem (001) GaAs, Fe auf InGaAs/InAs Quantentöpfen und Fe auf (001)-GaAs mit einer Zwischenschicht aus MgO. Die Spininjektion in den beiden erstgenannten Materialsystemen wurde erfolgreich in elektrischen Transportexperimenten nachgewiesen. Hierzu wurden sogenannte nichtlokale Spinventil-Anordnungen verwendet. Den Schwerpunkt dieser Arbeit bilden aber die strukturellen Studien der Eisenschichten unter Einwirkung interner und externer Verspannung.

Im Detail erfolgte an Fe/GaAs Grenzflächen eine Variation der Fe-Film-Depositionstemperatur sowie die nachträgliche Behandlung in einem Temperprozess. Entsprechende strukturelle Untersuchungen wurden mit verschiedenen Röntgenmethoden sowohl im Labordiffraktometer als auch in Synchrotonlaboren durchgeführt. Die Resultate zeigen, dass die Fe-Schichten kompressiv verspannt sind und dass die Verspannung durch einen Temperprozess bei 200°C nach dem Wachstum beeinflusst wird. Darüber hinaus weisen Röntgenbeugungsexperimente unter streifendem Einfall auf die Existenz einer Fe_3GaAs Phase an der Grenzfläche hin, die ebenfalls durch den Temperprozess bei 200°C beeinflusst wird. Zudem ergibt sich durch den Temperprozess eine signifikante Änderung der Spininjektionseffizienz. Während zunächst an den Grenzflächen keine Spininjektion nachgewiesen werden konnte, wurde nach einem ersten Temperprozess eine Spininjektionseffizienz von 5,5% gemessen. Nach einem zweiten Temperprozess war die Effizienz mit 2,6% jedoch wieder reduziert.

Darüber hinaus wurden strukturelle Studien an einem InGaAs/InAs Quantentopf eingebettet in InAlAs durchgeführt. Ein Gesichtspunkt war dabei die lokale Kristallinität der metamorphen $In_xAl_{1-x}As$ Pufferschicht, auf der der elektronisch aktive Quantentopf deponiert wird. Informationen über die strukturellen Eigenschaften sind hier essentiell weil die Relaxation der Verspannung zu einer lokalen Verkippung der Kristallebenen und Veränderung der Komposition des Films führt, die sich global in einem sogenannten Cross-Hatch Muster auf der Kristalloberfläche niederschlagen. Dieses Muster wiederum

führt zu einer Nichtplanarität des Quantentopfes, welche sich auf die Tranporteigenschaften auswirken kann. Die lokale strukturelle Beschaffenheit dieser Filme wurde daher mit scanning diffractive imaging untersucht, wobei zwei vom Indiumgehalt abhängige Netzwerke von Defekten gefunden wurden.

Spininjektionsexperimente an entsprechenden InGaAs/InAs Quantentöpfen zeigen, dass der Spintransport in diesen Systemen semiballistisch ist. Die aus den Tranportexperimenten ermittelten Resultate für die Spininjektionseffizienz zeigen weiterhin, dass das hierfür verwendete, ballistische Modell nicht ausreicht. Eine Ursache dafür wird darin vermutet, dass die in unserem System vorliegende Anisotropie der Spinbahn-Wechselwirkung in dem Modell nicht berücksichtigt wurde.

Im dritten und letzten System, das in dieser Arbeit untersucht wurde, befindet sich ein dünner MgO Film zwischen der Fe-Elektrode und dem GaAs Substrat. Im Gegensatz zu den anderen beiden Systemen wurden hier die Fe/MgO/GaAs Grenzflächen mittels hochaufgelöster Transmissions-Elektronenmikroskopie auf atomarer Skala untersucht, um den Einfluss von Filmdicke und Depositionsbedingungen des MgO auf die Morphologie und die magnetischen Eigenschaften des Fe-Films aufzuzeigen. Die strukturellen Studien beinhalten insbesondere auch ortsaufgelöste, energiedispersive Elementuntersuchungen (EDS-mapping) und Röntgenreflektrometrie-Messungen, um die Durch mischung der Filmzusammensetzung an der Grenzfläche aufzuklären. Messungen des magnetooptischen Kerreffekts (MOKE) zeigen eine zur Schichtebene parallele Magnetisierung des Fe-Films der Fe/MgO/GaAs Strukturen sowie eine Koexistenz von uniaxialer und kubischer Anisotropie. Bei unterschiedlichen Depositionsbedingungen variiert dabei die Art der dominierenden Anisotropie.

Neben den oben aufgeführten, strukturellen Untersuchungen und Spininjektionsexperimenten wurde im Rahmen dieser Arbeit eine in-situ Technik entwickelt, um den Effekt eines externen Drucks auf den Verspannungszustand in Spintronik-Bauelementen zu untersuchen. Diese Technik umfasst die Integration eines Rasterkraftmikroskops in Diffraktometern an Synchrotronexperimenten für Röntgenmikroskopie und ermöglicht so den gleichzeitigen Zugang zum reellen und reziproken Raum unter externem Druck. Diese Entwicklung erlaubt Abbildung und Ausrichtung von Mikrostrukturen sowie deren Untersuchung bei gleichzeitiger Manipulation.

Contents

1 Introduction **1**

2 Theory and experimental techniques **5**

2.1 Lateral spin valve device and non-local spin detection 5

2.1.1 Spin polarization of ferromagnets 5

2.1.2 Electrochemical potential 7

2.1.3 Spin dependent conductivity 7

2.1.4 Spin transport across FM/SC interface 8

2.1.5 All electrical spin-injection in non-local spin-valve setup 11

2.2 Magnetism of ferromagnetic thin films 15

2.2.1 Magnetic anisotropy 15

2.3 Experimental techniques 18

2.3.1 Molecular Beam Epitaxy 18

2.3.2 Reflection High Energy Electron Diffraction 19

2.3.3 Principle of X-ray Diffraction 23

2.3.4 Out-of-plane X-ray Diffraction 23

2.3.5 Grazing Incidence X-ray Diffraction 26

2.3.6 X-ray Reflectivity 27

2.3.7 Transmission Electron Microscopy 27

2.3.8 Magneto-optic Kerr effect Microscopy 29

3 Experimental results: Fe/GaAs interface **33**

3.1 Introduction 33

3.2 Structural investigations of Fe/GaAs heterojunctions 34

3.2.1 Effect of elevated growth temperatures on Fe layer crystallinity 35

3.2.2 Effect of post-growth annealing on Fe layer crystallinity 40

3.2.3 Effect of post-growth annealing on Fe layer studied by GID 48

3.3 Spin injection through Fe/GaAs interface 54

3.3.1 Sample design and band structure of Fe/GaAs heterostructure 54

3.3.2 Non-local measurement on Fe/GaAs spin valve 55

3.3.3 Effect of post-growth annealing on spin injection 58

3.4 Chapter Summary 60

4 Experimental Results: Integration of portable AFM at Synchrotron facilities 63

4.1 Introduction 63
4.2 Integration at P10 beamline of PETRA III 64
4.2.1 AFM-X-ray scattering geometry 64
4.2.2 Sample design of microstructures 67
4.2.3 Alignment of microstructures 68
4.2.4 GID measurements on the microstructures 69
4.3 Integration at Microfocus beamline, ID13,ESRF 70
4.3.1 Specifications of beamline and samples 71
4.3.2 Alignment using photocurrents 72
4.3.3 Effect of indentation on Fe Interface 74
4.3.4 Local deposition on microstructures 80
4.4 Chapter Summary 83

5 Experimental Results: Fe/InAs interface 85

5.1 Introduction 85
5.2 Structural investigations of Fe/InAs heterojunctions 86
5.2.1 Indium composition in Inverted, Modulation doped InAlAs heterostructures . . 86
5.2.2 Morphology of Inverted, Modulation doped InAs heterostructures 89
5.2.3 Tilt analysis of buffer layers 92
5.2.4 Diffraction mapping of InAlAs buffer layers 96
5.3 Spin injection through 2D InAs quantum wells 118
5.3.1 Sample design and band structure of modulation-doped InAs heterostructure . 119
5.3.2 Magneto-transport and contact properties 119
5.3.3 Non-local measurement on spin valve 122
5.4 Chapter summary 127

6 Experimental Results: Fe/MgO/GaAs interface 129

6.1 Introduction 129
6.2 Structural investigation of Fe/MgO/GaAs heterojunctions 130
6.2.1 Effect of MgO growth conditions on the layer crystallinity 131
6.2.2 Effect of MgO layer thickness on interface intermixing 133
6.3 Magnetic Investigations on the Fe/MgO/GaAs heterojunctions 144
6.3.1 Magnetic anisotropy as function of MgO thickness in Fe/MgO/GaAs heterostructures 145

6.3.2 Magnetic anisotropy as function of MgO annealing temperature in Fe/MgO/-GaAs heterostructures 152
6.3.3 Magnetic anisotropy as function of Fe deposition temperature in Fe/MgO/GaAs heterostructures 154
6.4 Chapter Summary 157

7 Summary and Outlook **159**

8 Appendix **165**
8.1 Additional material of GID measurements during indentation 165

Literature **167**

List of publications **187**

Acknowledgments **189**

Declaration on oath **190**

1 Introduction

Conventional MOSFET (Metal-Oxide-Semicondcutor Field-effect Transistor) technology uses the charge of the electron to perform information processing. A gate voltage controls the change in a channel between the source and drain contacts to obtain the "on" and "off" states in the transistors. This technology is the backbone of our current computational power and the advancement in this technology is largely related to miniaturization of the MOSFET feature sizes to increase the total number of transistors on the chip. This strategy of increasing the density of transistors per unit area has been hugely successful up till now and this has been predicted by Intel co-founder Gordon E. Moore and famously referred as Moore's law. However, MOSFET devices will eventually reach a physical limit where further miniaturization of the device will be fundamentally impossible. Also, the power dissipation from leakage currents is observed to pose a challenging problem with decreasing feature size of these transistors. So it became apparent in semiconductor community that a new technology is required to continue the rapid progress made in the semiconductor industry.

Spin transport electronics or commonly called as spintronics is identified as one of the several technologies that has the potential to replace current MOSFET technology by simultaneously utilizing both the charge and the spin degree of freedom of electron for information processing. The proposed field not only has the potential to advance transistor technology beyond Moore's law but can also add additional functionalities like non-volatile data storage to the current technology.

The electron spin exists as two quantum states (spin up and spin down) in reference to an external magnetic field and therefore it can be used efficiently for both data processing and storage than compared to property like charge. The other advantages of using spintronics is that it offers decreased power consumption and increased processing speeds.[1–3] But there are many challenges that are yet to be solved for the proposed spintronic devices to out-perform both the current and future MOSFET technology capabilities.[4] The main focus of current research community in spintronics is understanding the spin transport phenomenon and improving the efficiency of the spintronic devices.

In principle, every spintronic device should be able to inject/detect, transport, and control/manipulate the spin polarized carriers inside a non-magnetic medium such as a semiconductor, insulator, or a metal. Based on these three processes, spintronic devices can be loosely classified into two types; passive and active spintronic devices. The former category of devices are based on magnetoresistive effects like Gaint Magneto Resistance (GMR) for sensing and storing data.[5] Passive spintronic devices are already available in the market in the form of GMR read heads for hard disk storage, non-volatile magnetic

random-access memory (MRAM) devices,[6] and programmable spintronic logic devices based on magnetic tunnel junction elements.[7] All these passive spintronic devices are based on working principle of sensing how a spin-polarized electric current behaves when it is injected across a ferromagnet-non ferromagnet (for example paramagnet) interface.[5] On the other hand, the active spintronic devices incorporate a semiconducting material at the interface of ferromagnet in order to better control the spin manipulation. These active spintronic devices with a ferromagnetic/semiconductor (FM/SC) interface offer much advanced applications like spin LED (light emitting diode),[8] spin FET (Field Effect Transistor)[9] and a potential application of achieving spin based quantum computing.[10]

In all the devices mentioned above, the injection and detection of spin polarized carriers is achieved either by adopting optical or electrical means. During the first few studies of spin injection in FM/SC interfaces, the spin polarized currents were injected by passing a electrical current through a serial FM/SC heterojunction.[11,12] In these studies, the detection of spins is measured optically by measuring the magneto-optical Kerr effects due to coupling of spin polarized carriers to the light. In the following studies, injection and detection of spin polarized currents by means of all-electrical setup is preferred as this configuration can be integrated into current device technologies. Even though there are many studies on all-electrical spin injection in FM/SC heterostructures, the mechanisms governing the transfer of spin polarized currents into a semiconductor are not well understood.[13,14] This thesis is aimed to understand and study few of these mechanisms, especially the influence of the structural characteristics of FM/SC interface on the efficiency of spin injection.

Three different FM/SC interfaces are structurally characterized with the aim of studying the intrinsic strain present at different interfaces of FM/SC heterojunctions. The extensive strain investigations are motivated by the reported influence of the interface properties on the spin injection efficiency[15–17] in few FM/SC material systems. The results obtained during this thesis regarding the strain state of interfaces could be used in evaluating both theoretical and experimental understanding of spin injection in FM/SC heterostructures. In addition, all-electrical spin injection measurements are carried out in two FM/SC material systems by using lateral non-local spin-valve structures. These spin injection measurements have been performed in collaboration with Dr. Lennart Liefeith. The three FM/SC interfaces and their structural and spin-injection results are discussed individually in three separate chapters 3, 5 and 6.

First, Fe/GaAs interface is studied due to its ease of fabrication by Molecular Beam Epitaxy (MBE) due to small lattice mismatch of Fe and GaAs unit cells. Moreover, the Fe/GaAs system with n-doped GaAs channel is reported to show large spin-diffusion lengths of about $5\,\mu\mathrm{m}$[18] rendering fabrication of spin-valve devices with rather larger dimensions than compared to other semiconductor systems like InAs. This property of large spin-diffusion lengths makes this system a attractive option for fundamental study of spin-injection phenomenon. However, the spin-injection in Fe/GaAs heterostructures is observed to be significantly affected by post-growth annealing.[19–21] So we performed both spin injection measurements and structural investigations hand in hand to expose the role of the interface on the resultant spin-injection efficiency. The crystallinity of Fe layers and strain at the interface of Fe/GaAs as a func-

tion of growth parameters like deposition temperature and post-growth annealing are investigated and are discussed in chapter 3. The structural properties in this system are probed by using different high resolution X-ray diffraction techniques available either in laboratory or various synchrotron facilities.

In framework of this thesis, the strain at Fe/GaAs interface due to external applied stress is also studied with help of an *in-situ* technique developed as a part of this doctoral work. This particular study is motivated to investigate the effect of both intrinsic (strain due to lattice mismatch) and extrinsic (due to external applied pressure) strain on the transport properties in Fe/GaAs interfaces. This study also inevitably led to additional investigation of strain at reduced dimensions of Fe/GaAs interfaces due to the adopted sample design. The technical details of developed *in-situ* technique and results of the study are discussed in chapter 4.

The second interface that is investigated is the Fe/$In_xAl_{1-x}As$ heterostructure with underlying InAs quantum well. In principle, this semiconductor system is adopted due to reported enhanced electron mobilities[22] and large Spin-orbit interaction[23] in this system which can be used to study spin injection in ballistic conduction regime.[24] Recently, spin-injection studies in ballistic transport regime has become a topic of major interest due to reported surprisingly high values of spin injection efficiency.[14] However, the spin-injection efficiency in the work of Oltscher[14] is estimated by using diffusive transport model which led to observation of non-physical spin-injection efficiency values. This led to the development of a new model proposed by Chen *et al.* for calculation of spin-injection in ballistic regime.[25] This model introduces a new parameter called spin dephasing length which in turn depends inversely on spin-orbit coupling interaction as a key parameter for spin transport in ballistic regime. So we aim to study the spin-injection in ballistic limit in presence of reported large Spin-orbit coupling interaction in InAlAs/InAs quantum well system[26–28] as compared to GaAs material used in ref 13.

This material system is also unique in regard that the metamorphic buffer used in the sample design results in a rough cross hatch pattern at the surface of semiconductor. These cross-hatches result in morphological undulation of quantum well which in turn could lead to change in energetic position of sub-bands in the quantum well as evident in few other material systems.[29,30] So we intended to structurally characterize the cross-hatch morphology in detail to identify the magnitude of these cross-hatches in buried InAs quantum well. The measured spin-injection properties and structural characterization of the cross-hatch morphology are discussed in chapter 5.

One of the key issues of FM/SC heterostructures that are used for spin-injection studies is the inevitable occurrence of so-called conductivity mismatch that manifests due to different conductivities of FM and SC.[31] However, the Schottky barriers formed at the Fe/n-GaAs interface are shown to act as tunnel barriers which can be tuned by varying the doping in GaAs.[32] An alternate way to introduce tunable tunneling barriers at the FM/SC interface is to deposit thin MgO barriers with varying thicknesses. These MgO layers are two-fold advantageous as they can also act as diffusion barriers.[33,34] So we have studied the Fe/MgO/GaAs system as the third and last interface of investigation. However the MgO layers are reported to form pin-holes[35,36] and vacancy defects[37] in thin thickness ranges. These structural

in-homogeneities will indeed affect the resultant magnetic and electrical properties. So the intermixing between the layers and the resulting magnetic properties should be characterized before realizing spin injection by using MgO tunnel barriers. We therefore performed extensive structural characterization and magnetic investigations on MgO interface by using electron microscopy and MOKE magnetometer respectively. These results are discussed in chapter 6.
Finally the conclusions are drawn in chapter 7 by summarizing the main results and giving an outlook of few selected aspects for future developments and investigations.

2 Theory and experimental techniques

This chapter introduces few essential topics related to this thesis. First, some relevant concepts regarding lateral spin-valve devices will be discussed. Secondly a selection of the relevant theory and experimental details of magnetic characterization will be given, followed by the sample preparation techniques. Finally principles of experimental techniques used here for structural characterization will be discussed.

2.1 Lateral spin valve device and non-local spin detection

The spin-injection studies performed in this thesis are entirely done on all-electrical lateral spin-valve devices in non-local geometry. The basics to understand the spin-transport phenomena are described in this section along with non-local measurement setup used to measure the spin injection efficiency. In addition, the model of spin-injection in diffusive regime is also briefly discussed.

2.1.1 Spin polarization of ferromagnets

For successful spin-injection into semiconductors, a spin reservoir is required which can supply a current of spin polarized carriers and generally a ferromagnetic metal is used for this purpose. Ferromagnetic materials are generally transition metals which exhibit spontaneous magnetization. This effect of magnetization without the influence of external magnetic field happens because of a delicate balance between the exchange interaction and the atomic hybridization. In ferromagnetic transition metals the itinerant exchange interaction between the conduction band electrons is prominent. This exchange interaction tends to aligns the spins while the hybridization tends to reduce the spin polarization and these two interactions are described by Heisenberg exchange interaction which is given by Eq 2.1.

$$E_{ex} = -2j_{ex}S_iS_j \ = -2j_{ex}S_iS_j\cos\theta \tag{2.1}$$

where j_{ex} is known as the exchange integral and θ is the angle between the spins S_i and S_j.[38] The energy gain from aligning the spins arises from the Pauli exclusion principle which keeps the electrons with the same spin orientation further apart, on average, resulting in lowering the Coulomb repulsion between electrons.[39] In metals, the electron states are described using band theory.[40] Therefore, the

band structure is determined by the competing exchange energy, which favors parallel spins, and the increased kinetic energy needed to fill electrons into one spin band.

In ferromagnets like Fe, Ni and Co the energy gain from the exchange interaction is strong enough to cause a splitting of the d-bands leading to reshuffling of spin-polarized 3d bands. This split results in an imbalance of the concentrations of spin-up and spin-down electrons which leads to ferromagnetism.[39] These favorable conditions leading to ferromagnetism are described by Stoner criterion which is given by Eq 2.2

$$UN(E_F) > 1 \tag{2.2}$$

The Eq 2.2 is also expressed as $j_{ex}(E_F)N(E_F) > 1$, where $N(E_F)$ is the density of states (DOS) at the Fermi level E_F and U is the Stoner parameter, a material dependent measure of the energy reduction in the system. From the Stoner criterion, it is evident that ferromagnetism will arise in materials which have a strong exchange integral and a large DOS at the Fermi level. The DOS of ferromagnetic metal is shown in Fig 2.1 illustrating the splitting of 3d band. By convention the larger amount of spin-polarized carriers are called majority carriers ($N_\uparrow(E_F)$) and the smaller amount as minority carriers ($N_\downarrow(E_F)$). This asymmetry in the DOS at the Fermi level can be defined as polarization of ferromagnet and is expressed in Eq 2.3.

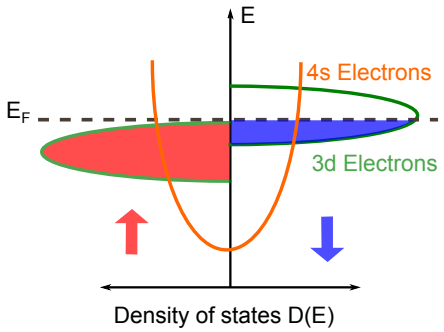

Figure 2.1: A simplified band structure of a ferromagnetic metal showing splitting of 3d band and net density of states at Fermi level between spin-up and spin-down states. The arrows indicate the spin direction of the carriers.

$$P = \frac{N_\uparrow(E_F) - N_\downarrow(E_F)}{N_\uparrow(E_F) + N_\downarrow(E_F)} \tag{2.3}$$

When current is injected from a ferromagnetic into a semiconductor, the spin polarization of conduction band electrons in ferromagnet leads to the generation of spin-polarized carriers . In this entire thesis, Fe is used as ferromagnetic electrode for spin injection experiments and Fe is experimentally observed to show a spin polarization as high as ≈45%.[41] A more detailed description of origin of ferromagnetism

and spin polarized currents are discussed in the following textbooks: (B. D. Cullity & C. D. Graham, 2008),[39] (N. W. Ashcroft and N. D. Mermin,1976).[40]

2.1.2 Electrochemical potential

To understand the concept of spin-injection across a FM/SC interface it is necessary to comprehend the subject of chemical and electrochemical potentials and the difference between them. Chemical potential (μ_{ch}) is generally defined as the energy required to add an atom to the a system. So if a system is in thermodynamic equilibrium with the surroundings, then it will have a constant chemical potential. If two systems with different chemical potentials are placed in contact, then the chemical potential difference leads to a driving force of electron/hole transport. By convention, the chemical potential of electrons at the Fermi surface is often set to zero. But any deviation from equilibrium ($\Delta\mu << E_F$), the chemical potential is related to the excess particle density (n) via the density of states at the Fermi energy $N(E_F)$ which is expressed by Eq 2.4.

$$\mu_{ch} = \frac{n}{N(E_F)} \tag{2.4}$$

In addition to the kinetic energy the electrons also have a potential energy. So if a system kept at a constant electrostatic potential difference (V), then the relevant quantity in describing the thermodynamic equilibrium will be the electrochemical potential (μ) and is expressed as;

$$\mu = \mu_{ch} - eV \pm \frac{1}{2} g\mu_B B \tag{2.5}$$

The term $\pm\frac{1}{2}g\mu_B B$ is the conventional Zeeman energy and is introduced to replace electrostatic potential by potential energy to include interactions in magnetic field. Where g is the gyromagnetic ratio, e the electronic charge, μ_B the Bohr magneton and B is the applied field. The electrochemical potential is linearly related to the electron density. Therefore, a gradient in the electrochemical potential provides the driving force that leads to electron transport induced by both applied field and diffusion of electrons due to spatially varying particle density.

2.1.3 Spin dependent conductivity

When a voltage is applied across a non-ferromagnetic material, the rate of charge flow can described by carrier drift and diffusion of non-equilibrium carriers which is expressed in Eq 2.6.

$$\vec{\boldsymbol{j}} = \sigma \boldsymbol{E} + eD\nabla\delta n \tag{2.6}$$

where $\vec{\boldsymbol{j}}$ is the current density, σ the conductivity, $\boldsymbol{E}$ the applied electric field, D the diffusion constant and ∇n is the change in carrier density from equilibrium. But, however, the model represented in

Eq 2.6 cannot be applied to spin-transport as it does not take into account the different spin population. In ferromagnets, the transport equation can be split into two spin dependent channels as represented in Eq 2.7.

$$\vec{j}_{\uparrow(\downarrow)} = \sigma_{\uparrow(\downarrow)}\boldsymbol{E} + eD_{\uparrow(\downarrow)}\nabla\delta n_{\uparrow(\downarrow)} \tag{2.7}$$

The notations of the physical quantities are same as used in Eq 2.6 but are spin dependent as represented by the subscript arrows $\uparrow$ $(\downarrow)$. This concept of spin dependent conduction channels is called as two-current model and was introduced by Sir Neville Mott to explain the decrease in resistivity of ferromagents as they are cooled through the Curie point.[42] Later this model is extended by Campbell *et al.*[43] and Fert *et al.*[44] to explain the Magnetoresistive effects like GMR (Gaint magnetoresistance). This idea can also be extended to the chemical potential separation given by Eq 2.8 which ultimately leads to the formation of two spin channels.

$$\mu_{\uparrow(\downarrow)} = \frac{n_{\uparrow(\downarrow)}}{N(E_F)_{\uparrow(\downarrow)}} \tag{2.8}$$

where $N(E_F)_{\uparrow(\downarrow)}$are the spin dependent density of states at the Fermi energy and $n_{\uparrow(\downarrow)}$ is the excess particle density. It is evident from Eq 2.8 that if the spins in a non-magnetic material like III-V semiconductors are driven out of equilibrium, it will result in a change in electrochemical potential. This shift is used to detect spin imbalance and is exploited in non-local configuration used for spin-injection measurements which will be discussed later (subsection 2.1.5).

2.1.4 Spin transport across FM/SC interface

Prior to interest of spin transport across FM/SC interfaces, the transport of spin polarized currents across FM and non-ferromagnetic metals has been a topic of interest due to discovery of GMR.[45,46] But shortly after the proposal of the Datta-Das transistor,[3] the research on spin transport across FM/SC has gained momentum. Early work on spin transport across FM/SC has been performed by Valet and Fert,[47] and they derived the one dimensional spin diffusion model from Boltzmann transport equation by using suitable approximations. But it was soon discovered that the spin-injection and spin-detection across a FM/SC interface suffered from a fundamental problem called conductivity mismatch.[48] This issue is schematically explained in Fig 2.2, which represents a simplistic ferromagnet-semiconductor heterostructure.

As depicted in Fig 2.2.(a), a significant current spin polarization is achieved at the interface of a ferromagnetic metal and a non-magnetic metal. However, when current is injected from a ferromagnet into a semiconductor, the achieved spin injection is relatively small. This stems from the large difference in the conductivities of the ferromagnetic metal and the semiconductor. When the current flows

from the ferromagnetic metal into semiconductor, a spin accumulation is created at the proximity of interface as shown in Fig 2.2.(c). This spin accumulation decays with a characteristic length called the spin-diffusion length (λ_{diff}) which represents the mean distance between two spin-flip scatterers.

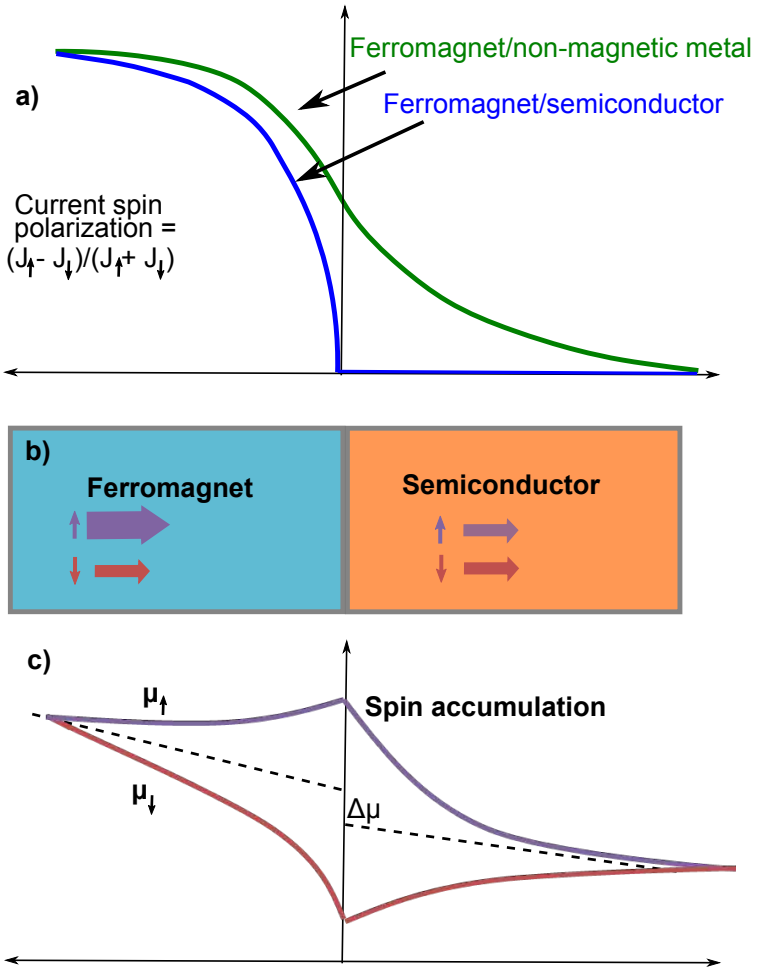

Figure 2.2: (a) Comparison of spin polarization between the ferromagnetic/non-magnetic metal and ferromagnetic/semiconductor interface indicating significant current spin polarization achieved for injection into non-magnetic metals but the spin injection is severely reduced in non-magnetic semiconductors. Where $J_\uparrow$ and $J_\downarrow$ are the current densities for majority and minority electrons respectively. (b) cartoon depicting the FM/SC interface. (c) schematic depicting spin accumulation in semiconductor where the dashed lines represent the average chemical potential. $\mu_\uparrow$ and $\mu_\downarrow$ are the are the electrochemical potentials for majority and minority electrons respectively. The shown schematics are inspired from the work of Fert *et al.*[47]

Interestingly, the transport regime depends on the scale of spin-diffusion lengths. In the limit of diffusive transport, the distance at which the spin-polarization is randomized scales with the spin-diffusion length that in-turn depends on the mean spin-flip time (τ_s) and the diffusion constant D.

Their relation is given by:

$$\lambda_{diff} = \sqrt{D\tau_s} \tag{2.9}$$

Whereas in the ballistic limit, the distance in which the spin-orientation is randomized is called spin-dephasing length (λ) which in turn depends only on the spin-orbit coupling in the structure due to the absence of scatterers. The spin-dephasing length is relatively a new parameter and is used only during discussion of spin transport in ballistic regime and it is inversely proportional to the spin-orbit coupling parameter implying that a strong spin-obit coupling necessarily leads to a short spin-dephasing.[25] The knowledge of spin-diffusion length parameter is important prior to fabrication of spin-valve devices as this sets the needed separation between the ferromagnetic electrodes in non-local configuration. The center-to-center separation (L) between the ferromagnetic contacts should be in the order of the spin diffusion length for successful spin injection.

As seen in Fig 2.2, a significant current spin polarization can be achieved at the interface of a ferromagnetic metal and a non-magnetic metal. But due to the large conductivity of the ferromagnetic metal, spin injection achieved is very small. As seen in Fig 2.2, when current flows from a ferromagnetic metal into a non-magnetic material, a spin accumulation decays with spin diffusion length and must remain unchanged across the interface. The current spin polarization must also remain unchanged across the interface. Due to the large conductivity of the ferromagnetic metal, a small spin accumulation can lead to a large current spin polarization, however, a small spin accumulation can only support a small current spin polarization in the semiconductor. A consistent solution is achieved only for a very small spin-injection and current spin polarization at the interface. This effect is discussed in detail by Schmidt *et al.*[48] Later it was shown by Rashba that by using a suitable spin dependent interface resistance the problem of conductivity mismatch can be solved.[49]

The interface resistivity decouples the ferromagnet from the semiconductor and leads to a discontinuity of the electrochemical potentials $\mu_{\uparrow(\downarrow)}$ at the interface which is shown in Fig 2.2.(c). By applying the spin diffusion model, Fert *et al.*[50] showed that the interface resistance must be well tuned to lie in an optimum range in order to observe a significant spin-injection into semiconductors which in other words is referred to as spin injection efficiency (η). In principle the spin-injection efficiency is defined as the degree of spin-polarization which is transferred from the ferromagnet into the semiconductor and is given by Eq 2.10

$$\eta = \frac{J_\uparrow - J_\downarrow}{J} \tag{2.10}$$

By applying the spin diffusion model and considering the spin dependent interface resistance proposed by Rasbha,[49] the spin injection efficiency shown in Eq 2.10 is modified and is represented in Eq 2.11.

$$\eta = \frac{\beta r_{fm} + \gamma \rho_c}{r_{fm} + r_{sc} + \rho_c} \tag{2.11}$$

where β is the spin-polarization of the injected current through the ferromagnet, r_{fm} and r_{sc} correspond to characteristic resistances of ferromagnet and semiconductor respectively which are in turn given by the product of material resistivities ($\rho_{sc,fm}$) and the corresponding spin diffusion lengths $\lambda_{diff,sc,fm}$. The indices *fm* and *sc* refer to the ferromagnet and semiconductor respectively. While γ is the material dependent spin-asymmetry coefficient[49,50] which can be increased by inserting a tunneling barrier like MgO between the ferromagnet and semiconductor. MgO layers are proposed to have spin filtering characteristics which can enhance the spin-splitting of the electrochemical potentials $\Delta\mu$.[51] ρ_c is contact resistivity between the ferromagnet and semiconductor.

2.1.5 All electrical spin-injection in non-local spin-valve setup

In this thesis, spin injection in different materials system is studied by using so-called spin-valves adopting a four-terminal configuration called the non-local spin valve setup (NLSV). This technique of spin injection/detection was first proposed by Robert Silsbee and Mark Robinson[52] and was initially applied to all-metallic spin valve devices.[52–54] Later the non-local configuration was also used as a tool for studying spin transport in ferromagnet/semiconductor systems.[55] Side and top views of the non-local setup are schematically shown in Fig 2.3 (a) & (b) respectively. This setup mainly consists of two ferromagnetic electrodes with varying widths (W_1 & W_2) in contact with doped semiconducting channel and two outer non-magnetic reference contacts. The ferromagnetic contacts are separated from each other by a length L that is in the order of spin-diffusion length. While the outer reference electrodes are present at distances several times larger compared to spin-diffusion length, in order to isolate the reference electrodes from spin-polarization induced effects. The setup is designed and run in such a way that the spin and charge currents are separated. As shown in Fig 2.3, the left ferromagnetic contact FM_1 (injector electrode) carries a current, which leads to the generation of a spin accumulation in the semiconducting channel. On the left-hand side, where the charge current flows, the spin accumulation is subject to both drift and diffusion. To the right of the spin generating contact, however, the spin transport is purely diffusive, and the spin accumulation decays exponentially with distance from the spin generating contact. The spin accumulation is detected by the open circuit on the right-hand side due to the Johnson-Silsbee spin-charge coupling[52] which induces measurable potential drops across the right ferromagnetic contact FM_2 (detector electrode).

The working principle of spin injection/detection in the non-local spin valve can be explained in terms of the simplified band structure diagram as shown in Fig 2.4. As discussed before, the density of states in the ferromagnetic metals like FM_1 and FM_2 contacts is spin-dependent. So when an electrical bias V_{inj} is applied across the FM_1/SC junction, it inevitably leads to injection of spin polarized currents. This

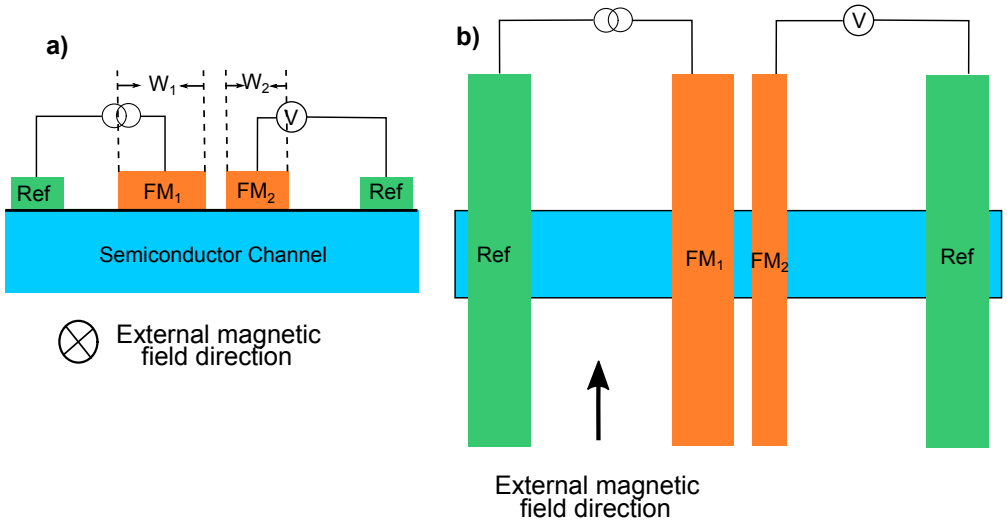

Figure 2.3: (a) side view and (b) top view schematic of non-local spin valve device. Left circuit is the current-flow loop for electrical generation of spin accumulation. The right circuit is a current-free loop for electrical detection of spin-accumulation.

in turn leads to spin splitting $\Delta\mu$ of electrochemical potentials causing spin-accumulation in the semiconducting channel which is indicated by the higher filling of the spin-up band in SC in Fig 2.4. It should be noted that the schematics shown in Fig 2.4 assumes FM as fully spin- polarized material and the spin-relaxation is neglected for the sake of the simplified explanation. But as the spin carriers diffuses towards the FM_2, the spin accumulation forces the electrochemical potential of the FM_2 to adjust in order to maintain the steady prerequisite state of no charge flow into FM_2. This mechanism results in the appearance of a spin-induced non-local voltage. In other words, the detector electrode (FM_2) is sensitive to those spins that have the same polarization orientation as the detector magnetization and this phenomenon will be referred as "sensitivity" of the detector electrode.

In principle, the operation of a non-local spin-valve device is based on measuring the voltage between the FM_2 and semiconductor channel while switching the magnetizations of FM_1 and FM_2 from parallel to the anti-parallel configuration with an external magnetic field applied along the easy-axis directions of the electrodes. In this way the differential measurement of the voltage between FM_2 and semiconductor channel provides the non-local voltage signal. In other words, the spin valve measurement makes use of a magnetic field applied along the easy axis of magnetization of the ferromagnetic contacts so that a switching between a parallel and antiparallel magnetization configuration results in the change in the non-local voltage. The magnetizations of the electrodes are forced in-plane by the magnetic shape anisotropy of the thin ferromagnetic films and their coercive fields are accordingly controlled by different widths of Fe electrodes maintained at equal length. The principles of in-plane crystallographic and shape anisotropy are discussed in detail in the next subsection 2.2.

The evolution of a non-local signal as a function of external magnetic field is schematically depicted in

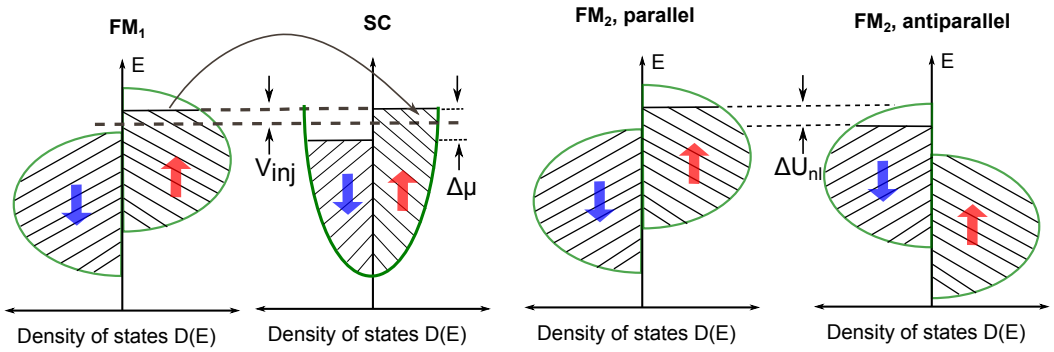

Figure 2.4: Pictorial representation of the density of states for the injector contact (FM_1), semiconducting channel (SC), and for the detector contact (FM_2) in parallel and antiparallel magnetic orientation with respect to (FM_1) contact. A voltage V_{inj} is applied to FM_1 leading to spin injection which in turn leads to a spin splitting $\Delta\mu$ of electrochemical potentials causing spin-accumulation in the semiconducting channel. This spin accumulation is detected at FM_2 due to Johnson-Silsbee spin-charge coupling[52] and results in change of a non-local voltage ΔU_{nl} upon magnetization reversal. The depicted schematics are inspired from the work of Mark Johnson.[56]

Fig 2.5, which shows orientations of electrodes in the top row. The "sensitivity" of detector electrode and evolution of non-local signal is shown in the middle and bottom row, respectively. The magnetization orientations of injector and detector electrodes are indicated by the arrows. While the "sensitivity" of the detector electrode is indicated by the green dot beneath. The magnetization orientation directions and corresponding electrochemical potentials are colored similarly.

At large negative magnetic fields, both electrode (FM_1 and FM_2) magnetizations are oriented in the same direction. The sign of injected and detected carriers is same leading to detection of non-local voltage U_{nl} that reflects the spin-up electrochemical potential. As the external field is further ramped up to opposite magnetic orientation, the electrode magnetization with the smaller contribution from the shape anisotropy switches first at lower magnetic field. This establishes an antiparallel state of both electrode magnetizations and at this present condition, the majority of injected carriers has polarization with opposite sign compared to the detection electrode. This in turn results in a change in the U_{nl} signal which reflects the difference between the spin-up and spin-down electrochemical potentials. When the magnetic field is further increased, the second electrode magnetization also switches to opposite magnetic orientation which causes the non-local voltage U_{nl} to jump back to the initial value. The jumps in non-local voltage due to change in electrode magnetization from parallel to antiparallel direction will be referred as ΔU_{nl} in the further text.

From the diffusion model (Eq 2.11), it is evident that the magnitude of ΔU_{nl} increases with the magnitude of current. Hence, a new parameter, of ΔR_{nl} is introduced that normalizes of ΔU_{nl} to the driven current I. Takahashi *et al.*[57] proposed a model to calculate the efficiency of the spin-injection (η) based on the approach developed by Valet, Fert[50] and van Son.[58] This model is developed to consider the

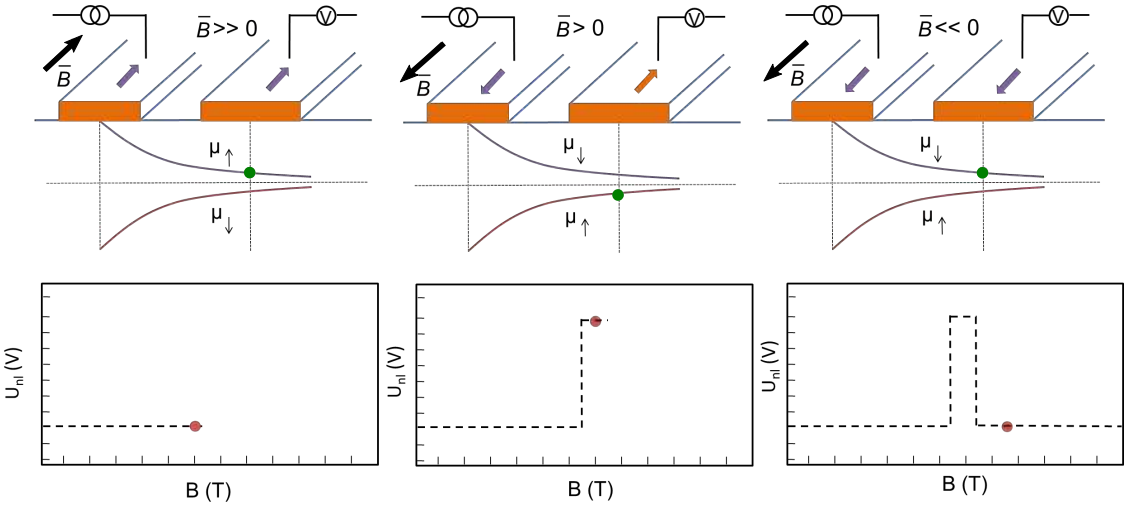

Figure 2.5: Top row: schematic depiction of magnetization orientation in FM_1, FM_2 electrodes. Middle row: "sensitivity" of the detector electrode (represented by a green dot) as a function of external magnetic field. Bottom row: corresponding evolution of non-local signal as a function of external magnetic field.

geometric factors of non-local setup and to relate the two parameters ΔR_{nl} and η and is given by:

$$\Delta R_{nl} = \frac{\Delta U_{nl}}{I} = R_{SC} e^{-\frac{L}{\lambda_{diff,sc}}} \prod_{i=1}^{2} \left(\frac{\eta \frac{R_C}{R_{SC}}}{1-\eta^2} + \frac{\beta \frac{R_{FM}}{R_{SC}}}{1-\beta^2} \right) \times \left(\prod_{i=1}^{2} \left(1 + \frac{\eta \frac{R_C}{R_{SC}}}{1-\eta^2} + \frac{\beta \frac{R_{FM}}{R_{SC}}}{1-\beta^2} \right) - e^{-\frac{2L}{\lambda_{diff,sc}}} \right)^{-1} \quad (2.12)$$

Where the index $i = 1, 2$ represents the injector and detector electrode. The R_{SC} and R_{FM} represent the resistances of FM and SC with cross-sections A_{fm} and A_{sc} and spin-diffusion lengths $diff, sc/A_{sc}$ and $diff, fm/A_{fm}$ respectively. The relation between all three parameters is given by:

$$R_{SC} = \rho_{sc} \lambda_{diff,sc} / A_{sc} \quad R_{FM} = \rho_{fm} \lambda_{diff,fm} / A_{fm} \quad (2.13)$$

R_C in Eq 2.12 is the total interface resistance. Some quantities like λ, η and L used in Eq 2.12 are already introduced in subsection 2.1.4. It is evident from Eq 2.12 that the non-local resistance ΔR_{nl} is dependent on contact resistance. For example, ΔR_{nl} increases with contact resistance and saturates when the contact resistance is much larger then the sheet resistance leading to decoupling of ferromagnet and semiconductor. In this case, the Eq 2.12 is simplified into Eq 2.14 where the both spin-injection efficiencies into injector and detector are assumed to be equal:

$$\Delta R_{nl} = \frac{\Delta U_{nl}}{I} = \frac{\eta^2 \rho_{sc} \lambda_{diff,sc}}{A_{sc}} . e^{-\frac{L}{\lambda_{diff,sc}}} \tag{2.14}$$

The equation 2.14 is widely used for evaluation of spin-injection efficiency in the diffusive limit. The parameter $\lambda_{diff,sc}$ used in the equation is experimentally measured using a three-terminal technique called Hanle measurement. The technique is based on Hanle effect which describes the precession of in-plane polarized spins in a semiconductor induced by an out-of-plane magnetic field. This technique is not described in detail here as the results from Hanle measurements are not discussed in this thesis. The details of Hanle measurements performed on Fe/GaAs interface are mentioned in the thesis of collaborator.[59] The non-local measurements are performed at liquid Helium temperatures using a 300 mK cryostat and details of this setup are explained in detail in the thesis of Lennart Liefeith.[59]

2.2 Magnetism of ferromagnetic thin films

Fe layers are exclusively used as the ferromagnetic material in the FM/SC heterojunctions that are studied in this thesis. The Fe layer thickness in all fabricated samples is fairly kept constant around the values of 4-5 nm. This section introduces few fundamental concepts and terms that are required to understand the process of magnetization reversal of Fe layers at the mentioned thicknesses. In particular, only important topics are discussed to explain the magnetic anisotropy observed in the Fe electrodes of fabricated spin-valve devices. The description of magnetic terms is kept short to keep the thesis concise. For a detailed discussion, the readers are referred to specialized literature.[60–62]

2.2.1 Magnetic anisotropy

The direction of magnetization in ferromagnetic metals is classically described by using Stoner-Wohlfarth model.[63] This model defines that the magnetization is aligned in the local minimum of energy density *E*, which is defined as:

$$E = -\vec{H}.\vec{M} + \sum_i E_i \tag{2.15}$$

Where the term $-\vec{H}.\vec{M}$ is called the Zeeman term. But the land scape of energy density is influenced by several contributions called anisotropy contributions (E_i) and the combination of all of these contributions will in-turn dictates the direction of magnetization. It should be pointed out that the Stoner-Wohlfarth model is valid for coherent rotation of magnetization which implies that the film is considered to have a mono-domain state and the magnitude of magnetization vector is constant. In principle, anisotropy can be defined as the tendency of magnetic moments to align in a preferred direction. In isotropic media, for the minimum of *E*, the magnetization $\vec{M}$ is parallel to the external magnetic field

$\vec{H}$. Meanwhile in anisotropic media, the anisotropy contributions come into play changing the energy landscape which results in the fact that different direction of $\vec{M}$ may be favored over the direction of $\vec{H}$. The main anisotropy contributions for ferromagnetic thin films are classified into following types: magneto-crystalline anisotropy, shape anisotropy, growth induced uniaxial anisotropy, interface anisotropy, and exchange bias. The two most important anisotropies required for describing the magnetic phenomenon in thin epitaxial layers are the magneto-crystalline and shape anisotropy which are briefly discussed below.

Magneto-crystalline anisotropy

Magneto-crystalline anisotropy stems from the effect of spin-orbit interaction. The periodic arrangement of atoms in crystalline material results in a periodic potential. This potential efficiently fixes the electrons orbital angular momentum to the lattice leading to negligible orbital contribution to the magnetic moment. While the spin-orbit interaction couples the spin angular momentum and orbital angular momentum of the electron leading to preferred orientation of spins. If a ferromagnetic material has no other anisotropy contributions, the magnetocrystalline anisotropy makes the magnetization align along a preferred direction with respect to the crystal structure. This inevitably leads to formation of preferred and non-preferred axis of magnetization in the crystal structure. The magneto-crystalline anisotropy is defined with various material dependent constants and coefficients. For example, the magneto-crystalline anisotropy for cubic crystal structures is given by:

$$E_{cub} = K_1(\alpha_1^2\alpha_2^2 + \alpha_2^2\alpha_3^2 + \alpha_3^2\alpha_1^2) + K_2\alpha_1^2\alpha_2^2\alpha_3^2 \tag{2.16}$$

Where, K_1 and K_2 are material and temperature dependent ansitropy coefficients while α_1, α_2, and α_3 are the direction cosines with respect to the edges of cubic structure. In crystalline bcc lattice of Fe, the magnetization $\vec{M}$ aligns along energetically favored [100] crystal direction, while in fcc lattice of Ni, the favored $\vec{M}$ direction is along [111]. It is also worth noting that the observed anisotropy can be two or four-fold depending on the thickness of the ferromagnetic layers. The preferred axis of magnetization is typically referred as the easy axis while non-preferred direction is called hard axis of magnetization. However, the magnetization lies along the direction defined by magnetocrystalline anisotropy only if other anisotropy contributions are absent. For example, thin layers of Fe deposited on GaAs show preferred magnetization along in-plane [1-10] direction and this is due to the dominant interface anisotropy contribution arising from As-dimers present on the reconstructed GaAs substrates.[64]

As mentioned earlier, 4-5 nm of Fe layer is exclusively used as ferromagnetic electrode material in the spin-valve devices fabricated and discussed in this thesis. The Fe layers at these thicknesses are reported to show uniaxial in-plane magnetic anisotropy with easy axis of magnetization varying with the underneath semiconductor material. For example, Fe layers are reported to have easy axis of magneti-

zation along [1-10] when deposited on GaAs,[64] while this easy axis is shifted to [110] direction when the underneath material is InAlAs.[65]

Shape anisotropy

It is widely observed that devices with ferromagnetic layers structured into elongated structures prefer to be magnetized along the largest spatial expansion. This phenomenon is observed due to anisotropy contribution called shape anisotropy. This anisotropy contribution arises due to long-range magnetostatic interactions. In thin ferromagnetic elongated bars, magnetic dipoles at the surface are uncompensated and result in formation of demagnetization field $\vec{B}_{demag}$ at the surface of the sample. The shape anisotropy contribution to the energy density is given as:

$$E_{demag} = -\int \vec{B}_{demag} d\vec{M} \tag{2.17}$$

Where in an ellipsoidal solid $\vec{B}_{demag}$ can be defined as

$$\vec{B}_{demag} = -\mu_0 \hat{\aleph} \vec{M} \tag{2.18}$$

μ_0 is the vacuum permeability and $\hat{\aleph}$ is the demagnetization tensor. The integral in Eq 2.17 is solved by using $E_{demag} = -\int \vec{B}_{demag} d\vec{M}_{\perp}$ as the out of plane magnetization component $\vec{M}_{\perp}$ is decisive in thin films. $\vec{M}_{\perp}$ can be expressed as saturation magnetization M_S, which gives the relation between the magnitude of the magnetization vector ($\vec{M}$) and the angle ($\vartheta_{\perp}$) between the $\vec{M}$ and the normal of sample surface. The resultant relation that denotes the shape anisotropy contribution term is given by Eq 2.19:

$$E_{demag} = \frac{1}{2}\mu_0 M_S^2 \cos^2 \vartheta_{\perp} \tag{2.19}$$

It is evident from Eq 2.19 that the shape anisotropy contribution is maximum when $\vartheta_{\perp} = 0^{\circ}$ and it is minimum when $\vartheta_{\perp} = 90^{\circ}$. Therefore the magnetization $\vec{M}$ is preferred in-plane due to shape anisotropy in absence of other anisotropy contributions.

In all the spin-valve devices studied in this thesis, the Fe electrodes are designed to have same length and thickness but with varied widths. This variation is intended to exploit the shape anisotropy for achieving different coercivity values in Fe electrodes with different dimensions. The shape of electrodes determines the magnetic dipolar energies which in turn control the coercivity of the electrode. So by using long electrodes with different width, the parallel and antiparallel states of magnetization are achieved in the spin-valve devices at different external magnetic fields. So the elongated direction of Fe electrodes in spin-valve devices is chosen such that the easy axis of the magneto crystalline anisotropy is coincides with the direction of the shape anisotropy.

2.3 Experimental techniques

This section contains description of methods used for fabrication of heterojunctions as well as the *in-situ* and *ex-situ* techniques used to study the morphology of the deposited layers. It also includes few techniques used to study the residual strain in the fabricated heterostructures.

2.3.1 Molecular Beam Epitaxy

Molecular Beam Epitaxy (MBE) is the widely accepted method of choice used for epitaxial growth of metal-semiconductor heterojunctions. In principle, MBE involves a beam of molecules or atoms impinging on a crystalline substrate held at elevated temperatures leading to formation of a crystal consisting species of the impinging beam. This deposition technique allows controlled growth of layers within the regime of monolayers with the help of mechanical shutters that open and close the effusion cells. The other advantage of this technique is the ability to control of the deposition parameters to achieve sharp composition and doping profiles with high precision.

As mentioned earlier in the introduction, three material systems are fabricated as a part of this thesis work. All these three systems are fabricated in the MBE-cluster containing different chambers as shown in Fig 2.6.(a). The chambers exclusively used for this thesis are marked in red color. The chamber marked as Riber C21 is used for deposition of all III-V semiconducting layers. This chamber is maintained at a base pressure in the range of 10^{-11} mbar with the help of a cryogenic pump. The C21 chamber is also equipped with a outer liquid cryogenic shroud to freeze out the impurity atoms and reduce the residual gas pressure. A separate metal MBE chamber is used for deposition of Fe and Au layers. This chamber is maintained at a base pressure close to the value of 5×10^{-10} mbar with combination of an a ion-getter pump and Ti sublimation pump. Both C21 and metal-MBE chamber have RHEED setups to monitor the growth speed and to observe the surface reconstructions. In both chamber, the materials are evaporated from effusion cells equipped with individual thermocouples which are controlled by power limiting PDI controllers. In both the C21 and the metal chamber, the samples are rotated during deposition to enable homogeneous growth of the layers.

A MgO chamber is exclusively used for the deposition of MgO tunnel barrier layers. This chamber differs from the other two chambers in the sense that the MgO layers are deposited by electron-beam evaporation of MgO powder which is compressed in an copper crucible as highlighted in Fig 2.6.(b). This chamber is maintained at a base pressure of 9×10^{-9} mbar with a combination of scroll and turbo pump. The growth rate in this chamber is monitored by using a water cooled oscillating crystal controlled by SQM 160 Multi-channel quartz crystal monitor.

In this thesis, all samples are grown on GaAs (001) 2-inch wafers that are $450\,\mu\mathrm{m}$ in thickness. These wafers are mounted on molybdenum wafer holders with the help of tantalum wires as shown in Fig 2.6.(c). While deposition of metal and MgO layers, the molybdenum holders are prevented from contamination with deposited material by use of a mask which is mounted few centimeters away from

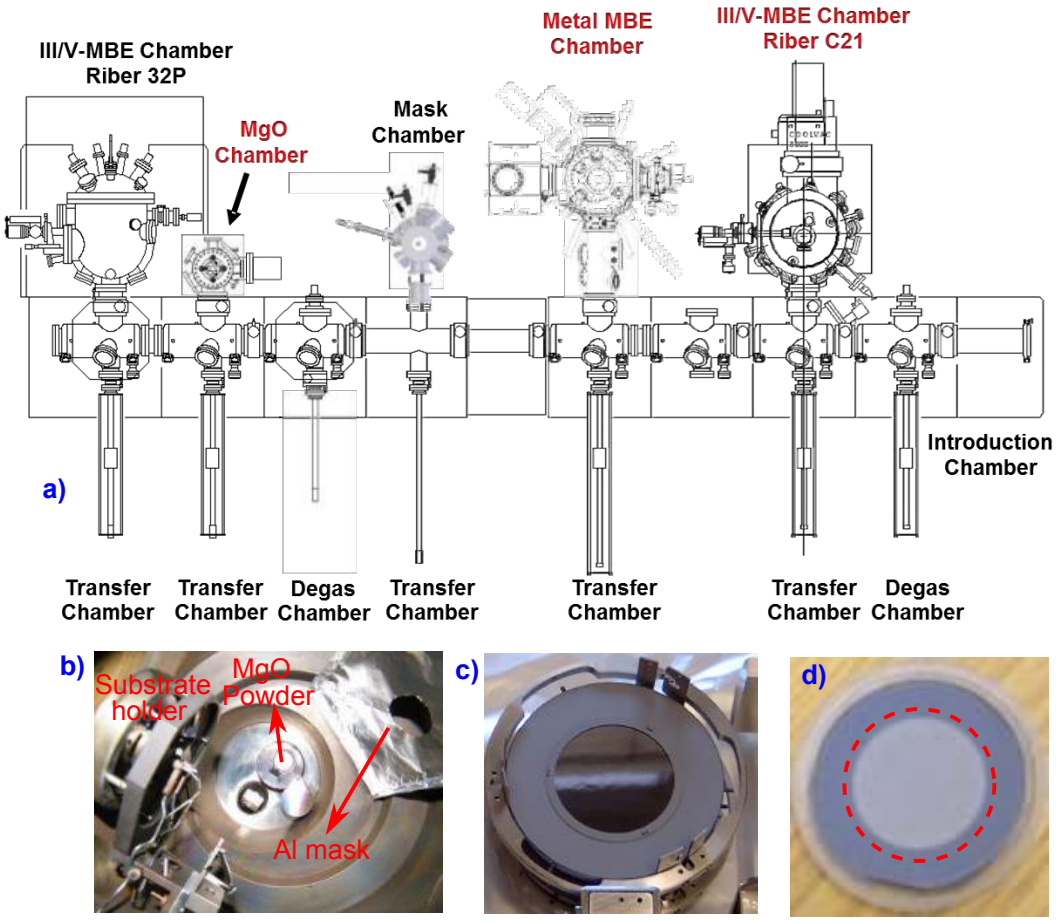

Figure 2.6: (a) Layout of MBE cluster. The chambers used during this thesis work are highlighted in red. (b) Inside of MgO chamber showing the MgO powder crucible, substrate heater and Al mask. (c) Molyblock with pristine 2 inch GaAs(001) wafer. (d) GaAs wafer after metal growth revealing localized deposition due to mask highlighted by dashed red circle.

the substrate holder as shown in Fig 2.6.(d). Deposition parameters like growth rate and deposition temperatures are varied across various sample designs and are discussed in the detail in their respective chapters.

2.3.2 Reflection High Energy Electron Diffraction

Reflection High Energy Electron Diffraction (RHEED) is widely used as an *in-situ* technique to monitor the growth processes in MBE based deposition methods. Structural parameters like smoothness of layers and surface reconstruction are obtained from the RHEED data. In a typical RHEED setup, electrons are accelerated at a high voltage of several kV (here 15 kV) and are made to impinge on the surface of the sample at a grazing angle. The diffracted electrons are detected on a florescent screen and the resultant diffraction pattern is recorded by a camera connected to the computer. A more detailed description of

working principle is discussed in the literature.[66] In a well calibrated setup, the RHEED data can also be used to access in-plane and out of plane lattice parameters.

The electron beam samples only few top layers of the sample due to the small grazing angle as a result of small penetration lengths of electrons. Therefore, the sampled two dimensional array of surface atoms transform into vertical one dimensional rods called truncation rods in reciprocal space. A typical RHEED frame consists of ordered spots of intensity maxima called reflexes. These reflexes are formed when the truncation rods intersect the Ewald sphere as shown in the Fig 2.7, where Ewald sphere is a geometrical construct based on the elastic scattering of electrons during surface diffraction and its radius is given by:

$$\mid \vec{k_0} \mid = \frac{1}{\hbar}.\left(2m_0E + \frac{E^2}{C^2}\right)^{\frac{1}{2}} \tag{2.20}$$

Where m_0 is the electron rest mass, *E* is energy of the accelerated electron beam and *C* is the speed of light. The recorded electron diffraction patterns are used to identify the surface reconstructions of the substrate and the deposited layers. The oscillation of the specular beam during the growth of layers is used to calibrate the growth speed of deposited layers. In addition, the distance between the RHEED reflexes can be used to the calculate the lattice parameters of the deposited layers. This calculation is based on prior knowledge about the lattice constant of substrate. The lattice constant of film is calculated by using the Eq 2.21

$$a_{film} = a_{substrate} \times \frac{\sin(\arctan(\frac{x_{substrate}}{L}))}{\sin(\arctan(\frac{x_{film}}{L}))} \tag{2.21}$$

Where L is given as

$$L = \frac{x_{substrate}}{\tan(\arcsin(\frac{n\lambda}{2a_{substrate}}))} \tag{2.22}$$

$x_{substrate}$ and x_{film} are the distances between the (0,0) reflex and its immediate neighbor reflex as for substrate and film, respectively, as shown in Fig 2.8.(a). The RHEED frame is integrated towards the sample horizon (indicated by red line in 2.8.(c)) to obtain a line profile. The separation distances between the reflexes are obtained from this line profile. $a_{substrate}$ is the lattice constant of the substrate, λ is the wavelength of the electron which is defined by the accelerating voltage and is given as $\lambda = \frac{2\pi}{k_0}$. By the using the Eq 2.20 and accelerating voltage of 15 kV, the λ is calculated to be 0.9×10^{-11}m. *L* is the distance between the sample and RHEED screen and *n* is the order of diffraction which is taken as $n = 1$. This technique is also extended to extract more information regarding the orientation of the deposited layers. For this purpose, RHEED frames collected as a function of sample rotation and line profiles from each frame are used to construct a polar plot that reveals an entire plane of reciprocal

space that is parallel to the sample surface. During this thesis, this technique is used to study the lattice parameter of thin layers of MgO deposited on GaAs.

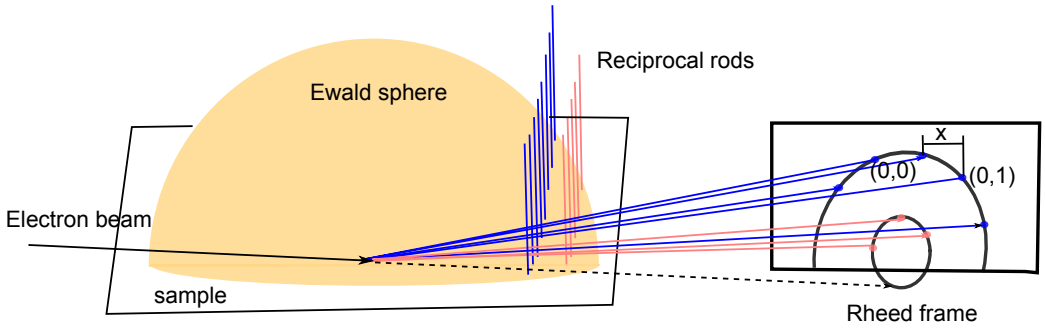

Figure 2.7: Simplified schematic showing the RHEED diffraction geometry

This technique is also referred as azimuthal RHEED scan in literature and is developed to allow the assessment of the entire accessible reciprocal space which is not possible in stationary configuration as only a small fraction of reciprocal space is accessible.[67] In this setup, RHEED frames are obtained at every possible azimuths. The basic diffraction geometry of RHEED setup in both side and top view is shown in Fig 2.8.(a) and b) respectively which point out that both k_0 and k_f should lie on the Ewald sphere for the diffraction to occur. If this condition is satisfied, the diffraction spots appear on the RHEED screen as shown in Fig 2.8.(c). The angle θ between the incident and exit beam and this value is chosen to be as small as possible to increase the sensitivity of surface diffraction.

The schematic of reciprocal space mapping by RHEED is shown in Fig 2.8.(d). As the sample is rotated, the reciprocal lattice revolves around the (00) rod, while the Ewald sphere stays fixed. RHEED frames are simultaneously recorded to observe the changes in diffraction patterns due to movement of Ewald sphere. Therefore the other reciprocal rods intersects Ewald sphere that are accessible while rotation of sample. The movement of reciprocal rods across the Ewald sphere due to rotation is shown in Fig 2.8.(b). After one complete sample rotation, the collected frames contain sufficient information to construct an entire plane of reciprocal space that is parallel to the surface. But in practice, only a plane of reciprocal space close to the specular spot is constructed into polar plot (highlighted in red box in Fig 2.8.(c)).

The RHEED frame shown in Fig 2.8.(c) is a single frame obtained on bare GaAs(001) sample terminated with 2×4 reconstruction. The reason for choosing a small part of reciprocal plane close to the specular spot is that, it is the only plane that continuously shows (00) reflex across all the frames during one rotation. The intensity from each frame is integrated in the direction towards the shadow edge of the frame to obtain line profiles. The resultant line profiles of all frames in one rotation are used to construct a complete plain of reciprocal space called the RHEED polar plot. An example of a RHEED polar plot obtained on bare GaAs 2×4 reconstructed surface is shown in Fig.2.8.(e) which reveals the underlying 1×1 mesh of surface reciprocal lattice highlighted by the red square. The shown rectangle is slightly

mismatched with the reflexes due to the wobble of the sample rotation during measurement of RHEED images. A more detailed description of this technique and clear polar plots of GaAs are presented in the works of Satapathy *et al.*[68] and Braun *et al.*[67]

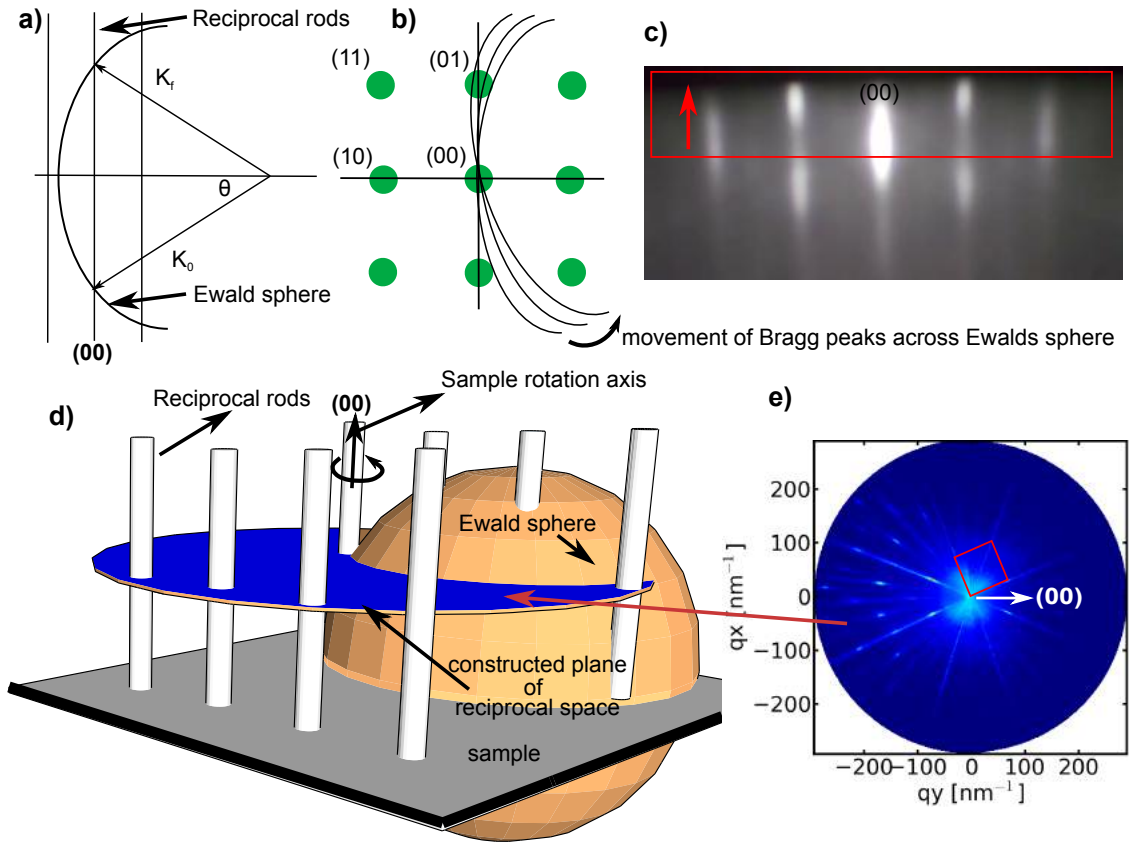

Figure 2.8: (a) Side view showing intersection of Ewald sphere with the truncation rods. (b) Top view of reciprocal space showing the movement of reciprocal lattice rods across Ewald sphere due to rotation of sample. The (0,0) reflex represents the specular spot and rotation axis is along this reflex. (c) RHEED frame obtained on bare GaAs(001) sample terminated with 2×4 reconstruction. The red rectangle highlights the chosen plane close to specular spot used for constructing the polar plot. (d) 3-dimensional schematic showing the geometry of truncation rods, axis of rotation of sample, reconstructed plane of reciprocal space and the Ewald sphere. (e) RHEED polar plot obtained on GaAs(001) sample terminated with 2×4 reconstruction.

X-ray Scattering Techniques

The morphology and the strain state of deposited epitaxial layers in all three sample designs are studied by using various X-ray scattering methods. The techniques like XRR (X-ray Reflectivity), HRXRD (High Resolution X-Ray Diffraction) and GID (Grazing Incidence Diffraction) are consistently used in this thesis to study the structural state of epitaxial layers across various sample designs.

These measurements are performed by using both lab-based X-ray sources and synchrotron radiation. But, most of the structural investigations discussed in this thesis are performed at synchrotron radiation facilities like PETRA-III, DESY (Deutsches Elektronen-Synchrotron), Germany and ESRF (European Synchrotron Radiation Facility), France.

2.3.3 Principle of X-ray Diffraction

Before discussing either the XRR, HRXRD or GID techniques, first principles of X-rays diffraction have to be understood as all the X-ray scattering techniques are based on this principle. Periodically ordered crystalline structures lead to interference of X-rays resulting in formation of characteristic diffraction patterns. These diffraction patterns are unique for different crystalline structures and depend on the atomic distance between the lattice planes of the material. This unique property of the X-rays is used to study the strain state of materials by measuring the inter-planar distances (d).
The working principle of X-ray diffraction is well explained in the terms of Bragg law which was proposed by William Lawrence Bragg and his father William Henry Bragg in 1913. This law called the Bragg condition is expressed as:

$$n\lambda = 2d\sin\theta \tag{2.23}$$

2.3.4 Out-of-plane X-ray Diffraction

It should be noted that the Bragg condition is applied to two dimensions, however Bragg condition can be extended to three dimensions by using Laue conditions which in simplified form is given by:

$$k_f - k_i = \vec{G} \tag{2.24}$$

Where k_i is the wavevector of the incoming (incident) beam, and k_f is the wavevector of the outgoing (diffracted) beam. Then the vector $\vec{q} = |k_f| - |k_i|$ is called the scattering vector and it denotes the change in momentum. $\vec{G}$ is called the reciprocal lattice vector and these terms are generally introduced while defining the reciprocal space. In diffraction measurements, the crystal lattice is often addressed in terms of reciprocal lattice as it describes the periodicity of the lattice planes. A reciprocal lattice is generated by performing Fourier transform on the real lattice. A lattice in real space with primitive vectors $\vec{a}, \vec{b}$ and $\vec{c}$ can be converted into reciprocal space with corresponding reciprocal primitive lattice vectors denoted as $\vec{a^*}, \vec{b^*}$ and $\vec{c^*}$ which are given by:

$$\vec{a^*} = \frac{2\pi}{V_{UC}}(\vec{b}\times\vec{c}),\ \ \vec{b^*} = \frac{2\pi}{V_{UC}}(\vec{c}\times\vec{a}),\ \ \vec{c^*} = \frac{2\pi}{V_{UC}}(\vec{a}\times\vec{b}) \tag{2.25}$$

Where $V_{UC} = \vec{a}.(\vec{b} \times \vec{c})$ is the volume of the unit cell in real space. Subsequently, a linear combination of all three primitive vectors are used to express any reciprocal lattice vector $\vec{G} = h\vec{a^*} + k\vec{b^*} + l\vec{c^*}$. By using both Eq 2.24 and 2.25, the Laue conditions in three dimensions are expressed as:

$$\vec{q}.\vec{a} = 2\pi h, \;\; \vec{q}.\vec{b} = 2\pi k, \text{ and } \vec{q}.\vec{c} = 2\pi l \tag{2.26}$$

The scattering vector ($\vec{q}$) must satisfy all three conditions for the constructive interference to occur and these three conditions in Eq 2.26 are famously referred as Laue conditions. The terms *h*, *k*, and *l* are integer numbers and are called miller indices. The reciprocal lattice points where Laue conditions are fulfilled are called Bragg peaks and are observed as intense spots in diffraction patterns.

The pictorial distinction between the real and reciprocal space is shown in Fig 2.9.(a), where the lattice planes of simple cubic crystal are represented by blue dots while the corresponding reciprocal lattice points are represented by green dots. While the Fig 2.9.(b) shows the diffraction geometry in reciprocal space.

The reciprocal lattice points are generally probed in two different geometries called specular and non-specular configurations. In the former case, the incidence angle with respect to the lattice plane (ω) is same as the exit angle (θ). In this configuration, the value of ω is always equal to 2θ, where 2θ is the angle between the incident and diffracted X-ray beam. This geometry is mainly used to probe the lattice planes that are parallel to the sample surface because the scattering vector is always normal to the lattice planes in this configuration. The specular geometry is also referred as symmetrical scan geometry in some parts of this thesis.

While the non-specular geometry represents a condition where the incoming and outgoing X-ray beams are at a different angle with respect to the surface normal. This configuration is used to observe diffraction from lattice planes that are tilted with respect to sample surface. In another words, all Bragg peaks on the [001] axis are called symmetrical (since $\omega = \theta$) and the other peaks are called asymmetrical. The specular and non-specular scans are schematically depicted in Fig 2.9.(a) where incident (k_i) and diffracted (k_f) wave-vectors are shown.

Throughout this thesis, the movement of X-ray source (incident angle) and detectors (diffracted beam angle) during measurements are defined with respect to the scattering geometry in reciprocal space. An example of scattering geometry is shown in Fig 2.9.(b) where the (k_i), (k_f) and $\vec{q}$ represent the incident, diffracted and scattering wave-vectors respectively. The subscripts $k_i spec$ and $k_f non - spec$ represent the wave-vectors in specular and non-specular geometry respectively.

The movement of either the source or detector or combination of both distinguishes measurement by using different scan direction through reciprocal space. For example, the diffraction signal along scattering vector is measured by varying the incoming inclination and exit angles simultaneously and this measurement will be referred as $\omega - 2\theta$ scan or radial scan in further text. The scan perpendicular to the scattering vector is referred as ω-scan and it is achieved by changing only the angle of incident beam

with respect to sample. This scan is used to identify the crystallinity of the layers as a sharp peak of a layer reflex indicates a well ordered film and vice-versa. While the scan around the Ewald sphere is achieved by changing the angle of the detector with respect to the diffracted beam. The discussed three scans are schematically shown in Fig 2.9.(b).

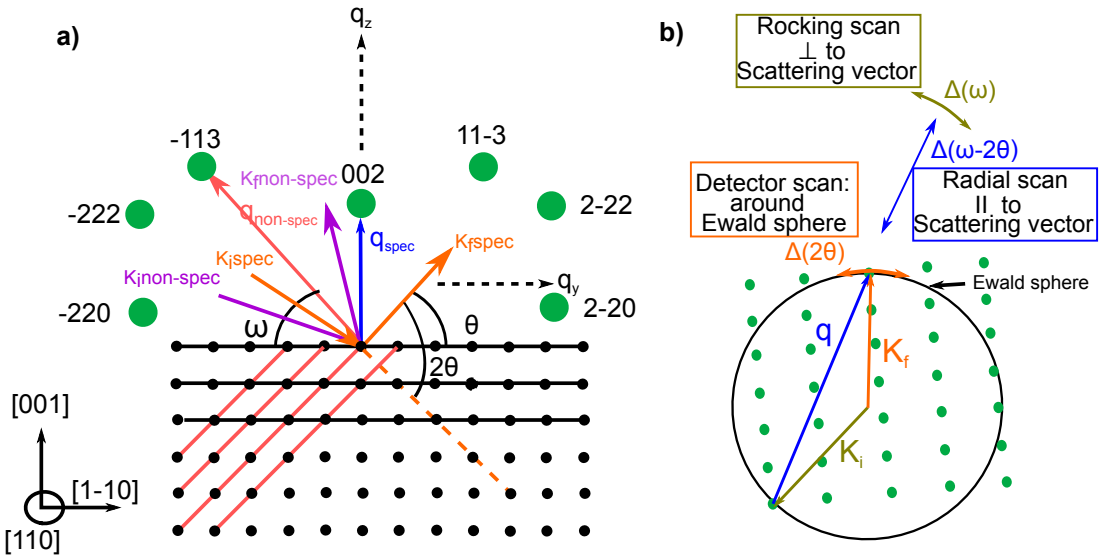

Figure 2.9: (a) Schematic showing the scattering geometry of specular and off-specular diffraction configurations. The out-of-plane and tilted lattice planes are shown as black and pink lines. Few selected Bragg peaks in reciprocal space are shown as green dots. The subscripts $k_i spec$ and $k_f non-spec$ represent the wave-vectors in specular and non-specular geometry respectively. (b) Schematic depicting the scan directions in reciprocal space. The magnitudes of wave vectors are not to scale in both sub-figures.

By using a combination of scans like $\omega - 2\theta$ and ω scans, a cross-section of Bragg peaks in reciprocal space can be mapped. This technique of probing the reciprocal space is called reciprocal space mapping. The components of the scattering vector parallel and perpendicular to the sample surface are referred as $q_{\parallel}$ and $q_{\perp}$ respectively. These two scattering components are calculated from the incident and diffracted angles used during the measurements and are given as:

$$q_{\perp} = \frac{2\pi}{\lambda}(\sin(2\theta - \omega) + \sin(\omega)) \tag{2.27}$$

$$q_{\parallel} = \frac{2\pi}{\lambda}(\cos(2\theta - \omega) - \cos(\omega)) \tag{2.28}$$

The notations used in this subsection will be used further in the chapter to describe other X-ray scattering geometries.

2.3.5 Grazing Incidence X-ray Diffraction

Grazing Incidence X-ray Diffraction or GID technique as the name suggests adopts a configuration where X-rays are incident at small angle to observe diffraction from lattice planes that are perpendicular to the sample surface. The diffraction signal observed with this technique has very little contribution from the thick substrate layers due small penetration length of X-rays at small inclination angles. The scattering geometry of the GID technique is illustrated in Fig 2.10. It has to be noted that the incidence angle (α_i) is kept constant throughout the measurement and is independent of the scattering angle (θ). The incidence angle is chosen in such a way that it is larger than the critical angle to avoid total reflection from the sample and obtain highly intense GID signal.

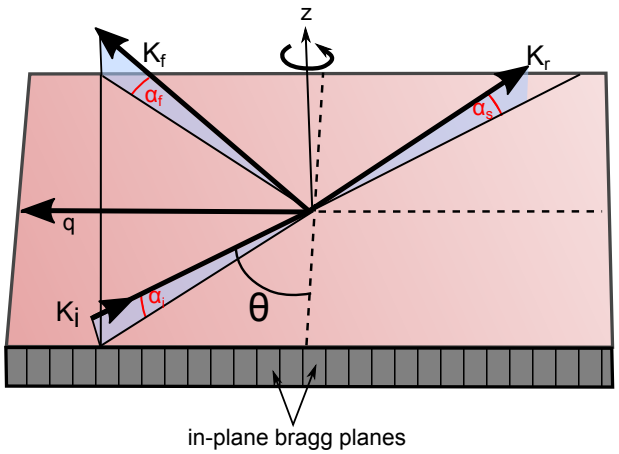

Figure 2.10: Schematic showing the side view of scattering geometry of Grazing Incidence Diffraction highlighting the incidence (α_i) and exit (α_f) angles along with the scattering angle (θ). The in-plane lattice planes are depicted as black lines in gray area.

As shown in Fig 2.10 a X-ray beam with wave vector k_i is incident on the surface with a grazing angle (α_i) and produces a specular reflected beam k_r. When the sample is rotated around the surface normal, the Bragg condition is satisfied at a particular angle θ by the planes perpendicular to the surface. At this angle, a scattered beam with wave vector k_f emerges with an angle (α_f) with respect to the sample surface. For detailed description of the GID working principle and geometry conditions, the readers are referred to literature[69,70]

The inter-planar spacing of Fe layers is half of that of GaAs unit cell so that Bragg peaks of (004) GaAs and (002) Fe are closly spaced in reciprocal space. In addition, the diffraction signal of GaAs dominates in out-of-plane diffraction condition due to very thick substrate layers in comparison to the 5 nm Fe layer. Therefore, GID technique is regularly used in this thesis to study the crystalline nature of Fe films due to enhanced signal from Fe layers at low inclination angles used in GID geometry. GID measurements are performed at both P10, PETRA III and ID13, ESRF synchrotron facilities on uniform films and on patterned samples with structures in dimensions of few micro-meters. The experimental

setups of these beamlines are discussed in the detail in chapters 3 and 4.

2.3.6 X-ray Reflectivity

X-ray Reflectivity or XRR is a specular X-ray technique widely used to characterize the density, thickness and the roughness of individual layers in single or multi-layer heterojunctions. When X-rays are incident at small angles (ω > critical angle), the difference in electron density in different layers of the heterojunction leads to reflection of X-rays at the interfaces of the layer stack. Interference of the reflections when measured as a function of incident angle results in an oscillatory pattern of reflected intensity called Kiessig fringes. The intensity and period of the oscillations are then used to model thickness (t) and interface roughness(r) of individual layers in the heterojunction. To obtain these parameters, the reflectivity profile is fitted by using X'pert reflectivity program supplied by PanAlytical company which use recursive Parratt algorithm[71] for fitting the experimental profiles.

The fitting procedure used to obtain the layer properties like thickness and density is based on analysis of reflectivity curve in terms of classical Fresnel equations similar to well-known interference in parallel plates. It has to be noted that the roughness of individual layers has a significant influence on the measured XRR profile as roughness of layers leads to diffuse scattering. This scenario is difficult to model as most of the reflectivity algorithms do not consider diffuse scattering in the model. Therefore we employed different XRR-models for analysis of reflectivity data and we also applied other techniques like electron microscopy to tackle the layer roughness issue. The XRR line scans and reflectivity reciprocal space maps presented in this thesis are exclusively measured by using X'Pert-PRO four-circle diffractometer which is also supplied by PanAlytical. The diffractometer is operated at energy of characteristic Cu Kα radiation ($E = 8048$ eV) equipped with a Ge (220) 3-bounce analyzer and a homemade incident collimator. The same instrument is used for all laboratory-source based XRR and XRD measurements mentioned in this thesis.

The schematic of geometric conditions of XRR is shown in Fig 2.11 where a X-ray beam k_i is incident on the sample surface at small angle. At these low incidence angles, the X-rays get reflected at the interface of the layers and this reflected intensity is recorded as XRR signal by the detector. In general, XRR scans are performed in $\theta-2\theta$ (incident-reflected angle) geometry as explained in subsection 2.3.4. Later, the incident angle is transformed into the out of plane reciprocal scattering vector q_z, with $q_z = 2k\sin\theta$, where k is the X-ray wave vector. However, the magnitude of the scattering vector is small due to much smaller ω angles used when compared to the ω angles used in diffraction configuration. So the resultant q_z is far away from Bragg peaks in reciprocal space.

2.3.7 Transmission Electron Microscopy

Transmission Electron Microscopy or TEM in combination with Energy Dispersive spectroscopy (EDS) is widely used to study the structural properties of thin layers on the atomic scale-limit. The working

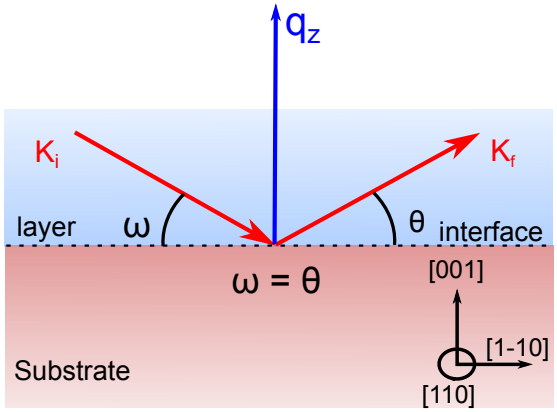

Figure 2.11: Schematic showing the side view of scattering geometry of X-ray reflectivity in single layer heterojunction highlighting the incidence (k_i) and reflected (k_f) wave-vectors along with the scattering vector q_z. The scattering vector is along the [001] direction due to the adopted specular geometry.

principle and main components in a conventional TEM are schematically shown in Fig 2.12. In principle, a TEM setup uses a filament at high voltage to produce monochromatic electron beam which is accelerated to high energies (300 kV in our case).[73] Later several electromagnetic lenses are used as condenser lens to focus the electron beam onto a thin sample. The electron beam scatters both elastically and in-elastically through the sample and the scattered beam is focused by an objective lens. At this stage, the transmitted beam also consists two components: direct beam or main beam and scattered beam. The objective lens then focuses the beam onto an intermediate lens which has the strength to magnify the image before forming a image on a CCD camera by projector lens.

Different imaging modes are achieved in TEM by selecting the part of the beam to propagate further. The imaging mode in TEM is selected before focusing the propagating beam on the intermediate lens. At this stage, an aperture is introduced near the back-focal plane that allows either the direct or scattered beam to propagate. By allowing only the main electron beam, a bright field image is obtained where the contrast is created due diffraction in sample. The contrast also depends on the mass and thickness of the sample. If the aperture at the back focal plane of objective lens is set to allow only the scattered beam, then a dark-field image is created. The dark-field image essentially is a diffraction pattern corresponding to a area of interest.

In this thesis, two TEM setups (Titan 80-300 and Osiris,FEI) are used for studying the intermixing and crystallinity of MgO layers. The second TEM equipment (Osiris, FEI, Oregon) has Scanning Transmission Electron Microscopy (STEM) capabilities and is used to observe TEM micrographs in large view-fields. In this technique, the electron beam generated by field emission guns can be used to scan the sample. This setup is used in combination with EDS detectors for microanalysis like elemental mapping of interfaces. The TEM measurements are performed at Shubnikov Institute of Crystallography, Russia in collaboration with Professor V.E. Asadchikov. The description of TEM sample preparation

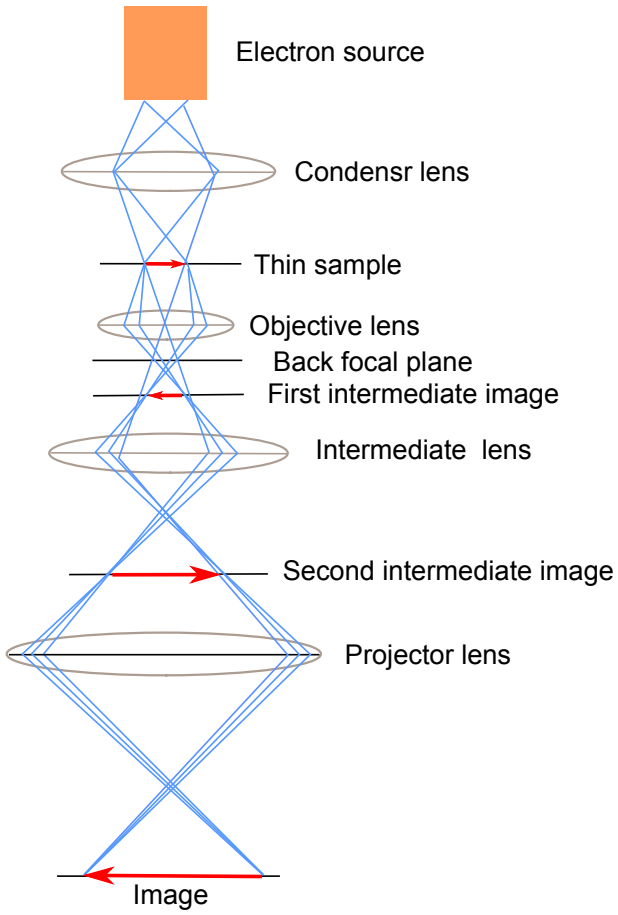

Figure 2.12: Schematic showing the optical path of electron beams and main components in a conventional TEM setup. The red arrows indicate the orientation of sample and images. The depicted schematic is inspired from the literature.[72]

and instrument specifications are discussed in detail in chapter 6.

2.3.8 Magneto-optic Kerr effect Microscopy

In this thesis, Magneto-optic Kerr effect (MOKE) measurements are performed to investigate the in-plane magnetization reversal and magnetic anisotropies of uniform Fe films in Fe/MgO/GaAs heterojunctions. These measurements are performed in collaboration with Stephan Martens from the group of professor K. Nielsch. Separate MOKE measurements are also performed on fabricated spin-valve devices to investigate the abruptness of magnetization reversal of Fe electrodes as a part of thesis work of Lennart Liefeith.[59] This subsection gives an overview about the magneto-optic Kerr effect, the experimental MOKE setup and the adopted measurement procedures.

In principle, Magneto-optic Kerr effect is described as the change of linearly polarized light to an tilted elliptical polarization due to reflection on a ferromagnetic metal.[74] So usually, the MOKE effect is

measured by shining a linearly polarized light which contains equally distributed left and right circular polarizations on the ferromagnetic layers and then studying the polarization of the reflected light. The reflected light exhibits an tilted and elliptical polarization and by studying these two parameters, the magnetic characteristics like magnetization reversal and magnetic anisotropy are investigated. The mechanism of change of polarization of linearly polarized light is only briefly explained, and for the detailed explanation, the readers are referred to well established literature.[60–62]

As the linearly polarized light is incident on the magnetic surface, it undergoes two changes. First, it couples to the magnetization resulting in a phase shift of left and right circular polarization which is similar to the widely observed phenomenon of Faraday effect.[75] Due to the resultant phase shift of both polarizations, the plane of polarization of the reflected light is tilted by the Kerr angle ϕ_k (which is also referred as Kerr rotation) with respect to the plane of incidence. Second, the amplitudes of the reflected left and right circular polarized light also changes, which results in the ellipticity (η_k) of the reflected light. The ellipticity characterizes the change in polarization and is defined as ratio of semi-major a and semi-minor b axis of the ellipse: $\eta_k = \arctan(\frac{b}{a})$ The parameters, η_k and ϕ_k are related by complex Kerr amplitude (ψ_K) and is given by:

$$\psi_K = \phi_k + i\eta_k \tag{2.29}$$

The technique of MOKE can be categorized into three geometries by the direction of the magnetization vector of the sample with respect to the reflecting surface and the plane of incidence of linearly polarized light. The three types of MOKE are named as 1) Longitudinal, 2) Transversal and 3) Polar MOKE. However, only longitudinal and transversal types are used in the setup adopted for measurements during this thesis. In the longitudinal MOKE setup, the magnetization vector is parallel to both the reflection surface and the plane of incidence as shown in Fig 2.13.a). The longitudinal setup involves light reflected at an angle (θ) from the reflection surface. In this setup, the incoming linearly polarized light becomes elliptically polarized. The resultant change in polarization is directly proportional to the component of magnetization that is parallel both to the reflection surface and the plane of incidence. In transversal MOKE setup, the magnetization vector is perpendicular to the plane of incidence and parallel to the reflection surface as shown in Fig 2.13.b). In this configuration the intensity of the reflected light changes instead of the Kerr rotation depending on the absolute value of the magnetization.

The MOKE setup used in thesis is a commercial available unit called *NanoMOKE2* supplied by *Durham magneto Optics LTD.* and has both longitudinal and transversal detection geometries. The schematic of the setup is shown in Fig 2.14 which uses a laser with wavelength 630 nm and maximal output power of 2.5 mW as a source of linear polarized light in combination with polarizer in front of the laser. An objective lens is used to focus the laser beam on to the sample surface which is mounted on a rotating sample stage. The stage is tilted by 45 $^\circ$ with respect to the optical axis and moves the sample in x and y direction while also enabling rotation around the sample normal. A quadrupole magnet is

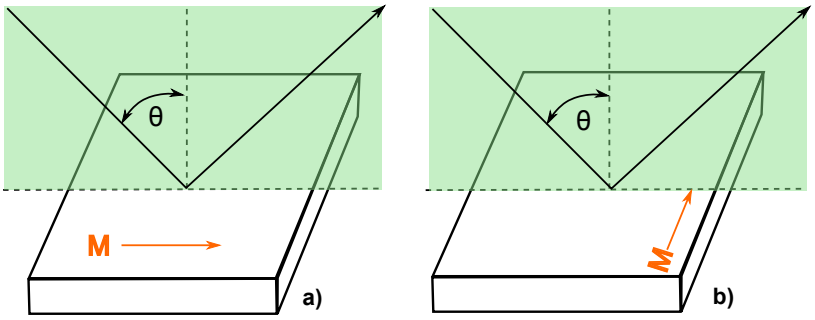

Figure 2.13: Different geometries of MOKE setup: a) Longitudinal setup, b) Transversal setup. The green hatched region indicates the plane of incidence.

placed near the sample to apply in-plane magnetic fields. The maximal magnetic fields achieved by this electromagnet is close to $\pm$90 mT with a sweeping frequency of 7.2 Hz. The reflected beam from the sample is focused by the receiving lens on to the beam splitter which sends 50% of the beam in both longitudinal and transversal detectors.

The longitudinal optical axis consists of an analyzer which is used to convert the polarization of the reflected light into an intensity signal to allow detection of Kerr signal. In addition, a quarter-wave plate has to be removed and inserted to measure Kerr-rotation and Kerr ellipticity respectively. The transversal optic axis consists of an attenuator which is used to prevent the saturation of the transversal Kerr detector. In addition to the described main components, few other optical parts are also present in the setup to image sample surface and allow proper positioning of laser spot on the sample. The components used for laser positioning and sample imaging are: a white lamp, attenuator, diffuser, beam-splitter, stopper, and a combination of microscope and CCD-camera.

Calibration procedure for MOKE measurement

Before each measurement, the following procedures are performed in order to allow comparison between the samples and to prevent saturation of the detectors during measurements. First, the easy axis of the magnetization of sample is recognized which is identified by a characteristic square hysteresis loop in longitudinal geometry and no signal in transverse geometry. In this configuration, the longitudinal detector reads a maximal signal of $\pm$20 mV (specific to the detector). This signal strength is referred as saturation signal (M_S) and all the further longitudinal signals measured are normalized with respect to this. Therefore, in all longitudinal MOKE measurements, the magnetization axis of hysteresis loops are represented by normalized longitudinal Kerr signal ($M_{L,N} = M_L/M_S$). However, the longitudinal Kerr detector detects the sum of the longitudinal and transversal Kerr signals. Therefore the transversal Kerr signal has to be subtracted from the longitudinal signal. So the normalized transversal Kerr signal (described later) is multiplied by the DC voltage ratio between the detected and saturated longitudinal and transversal Kerr signals and subtracted from the longitudinal Kerr signal.

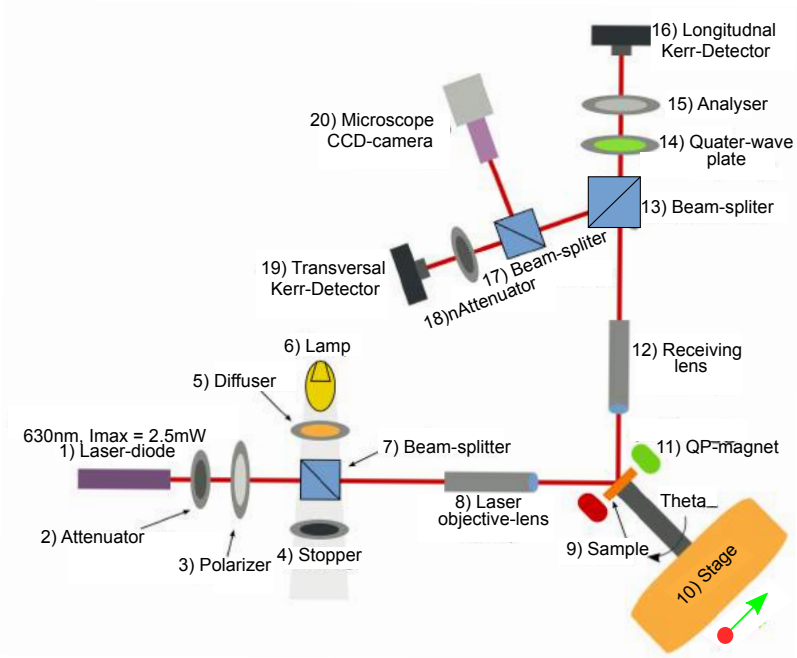

Figure 2.14: Sketch of MOKE setup and its optic components

In the second step, the magnetic field is swept in transversal MOKE geometry (plane of incidence $\perp$ to applied field). This configuration typically yields hysteresis loops with reduced intensity in both detectors when compared to longitudinal geometry. In this configuration, a maximal voltage of ± 2 mV is observed in transversal detector and is used to normalize all the further transversal detector data and is referred as normalized transversal kerr signal ($M_{T,N} = M_T/M_S$). In this configuration, the longitudinal detector also detects the transversal signal. To correct this, the normalized transversal detector signals are multiplied by the DC voltage ratio between the longitudinal and transversal detector signals and subtracted from the normalized longitudinal detector signal.

3 Experimental results: Fe/GaAs interface

3.1 Introduction

Thin Fe layers on bulk GaAs are widely used as a ferromagnet(FM)/Semiconductor(SC) model system for spin injection studies using electrical and optical techniques.[11,76,77] One advantage of this system is the ease with which Fe layers can be epitaxially deposited on GaAs[78] due to a relatively small lattice mismatch of 1.4% between the substrate and twice the bulk Fe lattice constants. The other advantage of Fe/GaAs is the high Curie temperature exhibited by the Fe films[79] which allows the study of spin injection even at room temperature.[76] The spin-injection efficiency from Fe into GaAs calculated from first-principle calculations[80] by using experimental spin-diffusion lengths of $5\,\mu m$[55,81,82]is expected to be around 99%. However, the actual spin-injection efficiency measured by using spin-light-emitting-diodes[83] and Esaki diodes[84] are 10% and 75% respectively, which is considerably less than the expected value from first-principle calculations.[80] Moreover, the spin-injection values determined from all-electrical spin-valve devices are even smaller than the values measured by using optical measurements which indicates incomplete understanding of the spin-injection processes. Also, the dominating mechanisms driving the spin-injection are not completely understood. Additionally, an unexpected bias dependent asymmetry of spin injection is observed in the all-electrical spin-valve devices.[19,85] All these factors point to need of further investigation on Fe/GaAs system to understand the fundamental properties influencing the spin-injection.

In fact, Fe/GaAs interface is widely reported to be very sensitive to post-growth annealing influencing the spin injection efficiency.[19,81,86,87] So several studies have attempted to correlate the influence of post growth annealing on spin injection by analyzing the atomic structure of the FM/SC interface.[15,86,88] Zega *et al.* proposed a model of ordered and coherently intermixed interface of Fe and As atoms.[15] Fleet *et al.* reported coexistence of intermixed and abrupt interfaces[86] and they also observed that the interface becomes more abrupt[89] due to annealing. On the other hand, Lebeau *et al.* reported an interface consisting of Fe atoms substituting the As and Ga sites.[88] The nature of interface discussed in these studies will indeed influence the strain state of the interface as reported in the already mentioned literature. There are also few reports which observed interdiffusion of Fe, Ga and As atoms at the interface.[15,90] These observations prompted us to investigate the Fe/GaAs interface structural properties to understand the interface contribution to spin-injection and also, if possible, to identify mechanisms influencing the spin transport across the interface. So we decided to study the annealing effect on

Fe/GaAs interfaces by adopting high resolution X-ray scattering methods. Also, the effect of different growth temperatures on the morphology and crystallinity of Fe layer is investigated.
In addition, spin-injection measurements by means of all-electrical non-local spin-valve configuration are performed to study the effect of structural variation on spin-injection efficiency as a function of post-growth annealing. The structural results of Fe/GaAs interface are discussed first followed by spin-injection measurements to draw structure-property correlation.

3.2 Structural investigations of Fe/GaAs heterojunctions

A single Fe/GaAs sample design was used for both structural and spin-transport measurements. The Fe/GaAs heterostructures were prepared in a multi-chamber MBE system consisting of a Riber C21 III/V semiconductor chamber and a metal deposition chamber both connected via an ultra-high vacuum channel. All the heterojunction layers were deposited on undoped GaAs (001) wafers. Before deposition of any layers, the wafers were degassed at $400°\mathrm{C}$ for 1 hour in a degas station. Afterwards, the wafers were transported to the semiconductor growth chamber where the native oxide was removed at $540°\mathrm{C}$ under background As flux. The growth rate of GaAs was calibrated for every single sample using RHEED oscillations. GaAs layers were deposited at a growth speed of 0.8 ML/sec.
Initially an undoped GaAs buffer layer of few microns thickness was deposited, followed by a 300 nm of n-doped GaAs channel with the carrier density of $5\times$ 10^{16} cm^{-3}(n^{+}). Later, a 30 nm transition layer ($n^{+} \rightarrow n^{++}$) was grown and terminated with 15 nm of highly doped GaAs layer (n^{++}, $3\times$ 10^{18} cm^{-3}). The n-doping was achieved by using silicon as dopant and the nominal doping concentration was calibrated beforehand by using magneto-transport and capacity-voltage measurements. After deposition of all semiconductor layers an As terminated (2×4) reconstructed surface was observed by Reflection High Energy Electron Diffraction (RHEED). Later the samples were transferring into the metal MBE chamber *in-vacuo*. In the metal chamber a 5 nm Fe layer was deposited at the growth rate of 0.4 nm/min. The structure was finalized by deposition of 15 nm Au layer with a growth rate of 0.2 nm/min which acts as a protective cover to prevent oxidation of Fe layers underneath. Both the Fe and Au growth rates were calibrated beforehand by deposition of Au and Fe layer separately on two different GaAs wafers and measuring their thicknesses by XRR technique. The layout of the fabricated heterostructure with nominal thicknesses is shown in Fig 3.1.
The growth of Fe layers was mostly performed at room-temperature except for one sample that was grown at 200°C. The results from this sample are discussed in the next subsection 3.2.1. For spin-injection experiments, Fe layers were solely deposited at room-temperature. The gold layers were always deposited at room-temperature irrespective of the Fe deposition temperature. Also, the samples were always rotated during the growth of both metal layers unless mentioned otherwise. The samples used for structural investigations are named as C21541 (Fe grown at room-temperature) and C21540 (Fe grown at 200°C) and will be referred in the following text as Rt and 200°C samples, respectively.

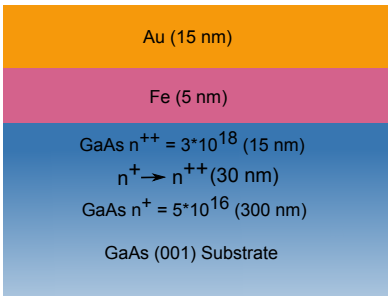

Figure 3.1: Sample layout of the Fe/GaAs heterostructure and the corresponding nominal thickness of individual layers.

3.2.1 Effect of elevated growth temperatures on Fe layer crystallinity

Theoretically, abrupt crystalline interfaces of ferromagnetic/semiconductor (FM/SC) are considered as ideal spin-filters for transmission of spin-polarized electron flux at the interface.[91] So we assume that a sharp interface is a prerequisite for successful spin-injection experiments. However, the growth temperature of Fe is reported to influence the quality of Fe film as this temperature dictates the surface migration during deposition.[92,93] Filipe *et al.* reported an out-diffusion of As and Ga elements at elevated Fe deposition temperatures, while, Freeland *et al.* reported a reduced but noticeable intermixing at room-temperature (Rt) Fe deposition.[94] To resolve the effect of growth temperature on the quality of Fe layer, we have prepared two samples in which the Fe layer was deposited at Rt and 200°C, respectively. These samples are studied by using AFM, XRR and HRXRD techniques to investigate the morphology and crystallinity of Fe the layers. The X-ray investigations of this work are performed by Michael Wachter as a part of his bachelors thesis work.

The $5\,\mu m \times 5\,\mu m$ AFM topographic scan obtained on Rt and 200°C samples are shown in Fig 3.2(a) & 3.2(b) respectively. The scans reveal a clear distinction in the surface morphology of both samples. The AFM images are shown in different height scale as both samples have largely different surface roughness. The AFM image of the Rt sample in Fig 3.2(a) reveals the presence of small island like features on the surface. The total volume of these islands corresponds to an equivalent Au layer thickness of 2.2 nm with root-mean-square (rms) roughness of 2 nm. The equivalent thickness of these islands is significantly smaller than the nominally deposited layer of 15 nm, which implies that the whole Au layer consists of small islands on a thick continuous layer.

In contrast, the 200°C sample has continuous dendrite like features with maximum height of 22 nm and rms of 2.5 nm. The roughness observed in both sample by AFM is positively correlated to the roughness calculated by XRR fitting which is discussed later in the section. Therefore we conclude that the difference in surface morphology and roughness of both samples is caused by different morphology adopted by underneath Fe layer. This conclusion is based on the fact that the deposition conditions of the heterostructure are kept constant except for the Fe layer deposition temperature. So we believe that

the Fe layer adopts an island-like morphology due to the elevated Fe growth temperature causing the subsequent gold layer to adopt a rough morphology.

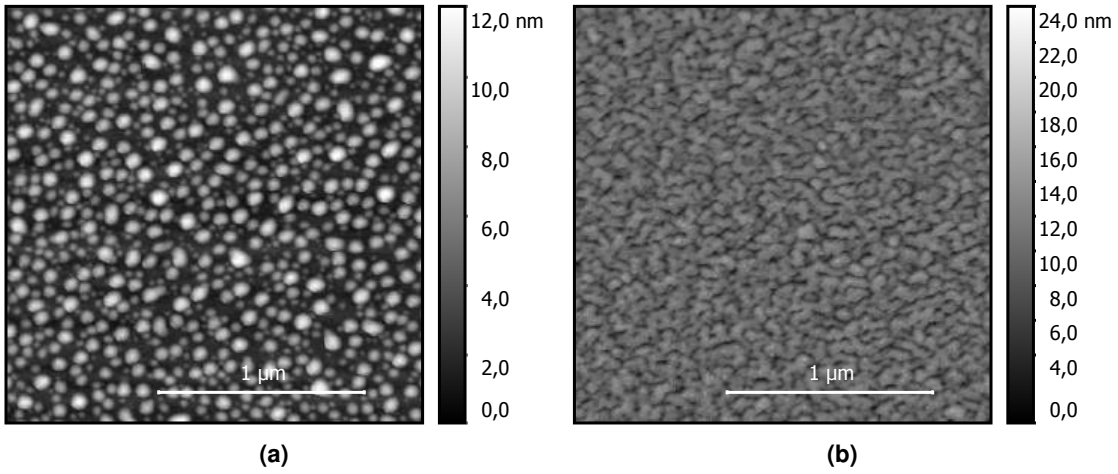

Figure 3.2: $2\,\mu\mathrm{m} \times 2\,\mu\mathrm{m}$ AFM topographic scans of(a) Rt sample, (b) 200°C sample. Both figures are shown in different height scales to improve the contrast of the observed features.

We also applied XRR mapping technique to study layer thickness and morphology of individual layers in both samples. The XRR reciprocal space maps obtained on both sample are shown in Fig 3.3(a) & 3.3(b). The intensity oscillations or Kiessig fringes are clearly visible in Rt sample but are not seen in the 200°C sample. This indicates that the Rt sample has sharp interfaces as a sharp density change at the interface causes the reflected X-rays to constructively interfere to form intensity oscillations. In contrast, if intermixing is present at the interfaces it leads to attenuation of X-rays causing faster decay of reflectivity signal as observed in XRR map of 200°C sample. Therefore we conclude that 200°C sample has significant intermixing at the interfaces.

To further analyze the XRR data, line profiles are obtained from XRR maps by projecting the map towards q_z direction and the obtained line profile represents a $\omega - 2\theta$ scan. An example of line profile obtained from Rt sample is shown in Fig 3.4. The intensity and period of the oscillations observed in line profile are then used to model thickness (t) and interface roughness(r) of individual layers in the heterojunction. The fitting is performed by using recursive Parratt algorithm[71] for converging the experimental and simulated profiles. Figure 3.4 shows a comparison between experimental and simulated reflectivity pattern of the Rt sample indicating good agreement. The inset shown in the Fig 3.4 is the model used for simulating the reflectivity profile. The best fit for Rt sample yields following thicknesses: $t_{Fe} = 4.7 \pm 0.06$ nm, $t_{Au} = 14.3 \pm 0.04$ nm for the Fe and Au layers, respectively. The roughness of Fe layer and substrate are: $r_{Fe} = 0.32 \pm 0.04$ nm, $r_{substrate} = 0.12 \pm 0.02$ nm. The results obtained on Rt sample indicate that the layers are flat without considerable roughness and measured thicknesses are close to nominal values.

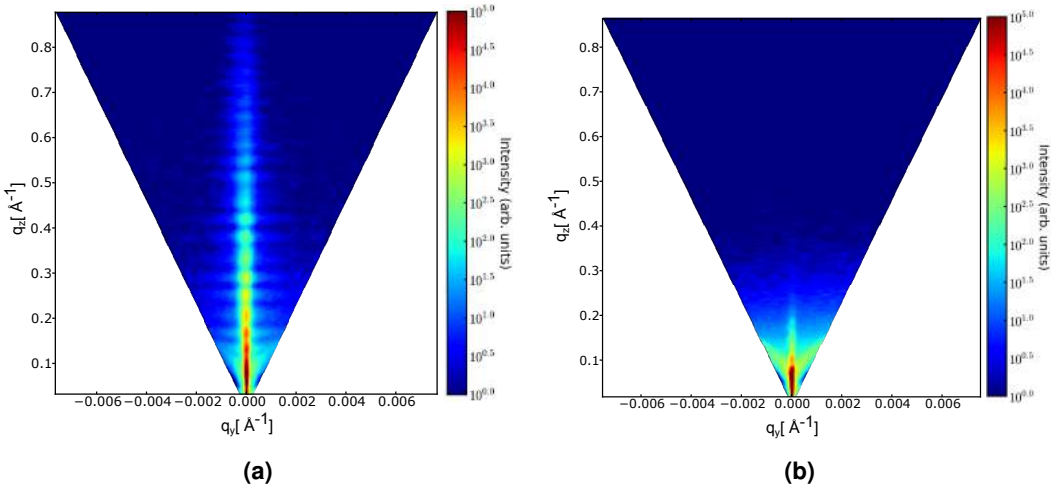

Figure 3.3: XRR reciprocal space maps obtained on (a) Rt sample, (b) 200°C sample.

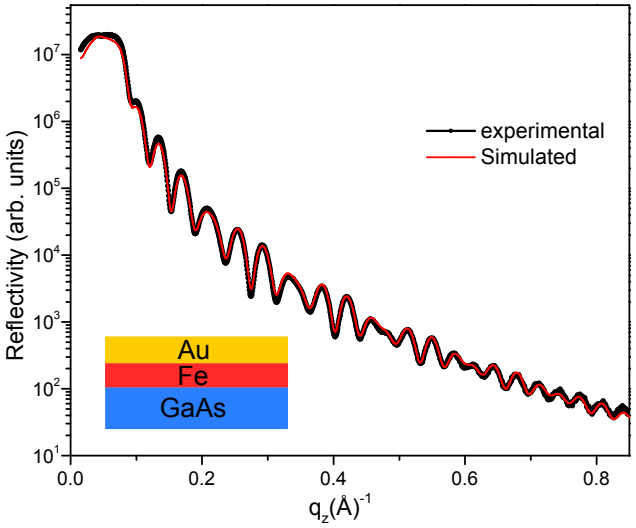

Figure 3.4: Comparison between experimental (black line) and simulated XRR line profile (red line) of Rt sample. Lower inset: Layout used for simulation of reflectivity

In contrast, the XRR line profile of the 200°C sample shows only a few intensity oscillations as evident in Fig 3.5(a) & 3.5(b) (red curve). An experimental profile is fitted at two different regions separately by using two different parameters because a single fit could not be obtained. The reflectivity profile close to critical angle contains information regarding the topmost layer. Therefore, fit_1 which has good agreement with experimental profile close to the critical angle is used to evaluate the thickness of the Au layer ($t_{Au} = 10.1 \pm 0.6$ nm). It is clearly seen that the calculated thickness is much smaller than the nominal value. The Fe layer thickness and roughness is evaluated from fit_2 which yielded values of fit_2 are $t_{Fe} = 2.62 \pm 0.47$ nm and $r_{Fe} = 0.97$ nm respectively. The measured smaller thickness of Fe might partly be due to the rough interface resulting from the island like morphology of Fe film. The

imperfect fits of XRR data also indicates the formation of different phases of Fe. To achieve perfect XRR fits all the layers must be included in the model used for simulation but the model used for shown fits in Fig 3.5(a) & 3.5(b) consists only Fe, Au and GaAs layers.

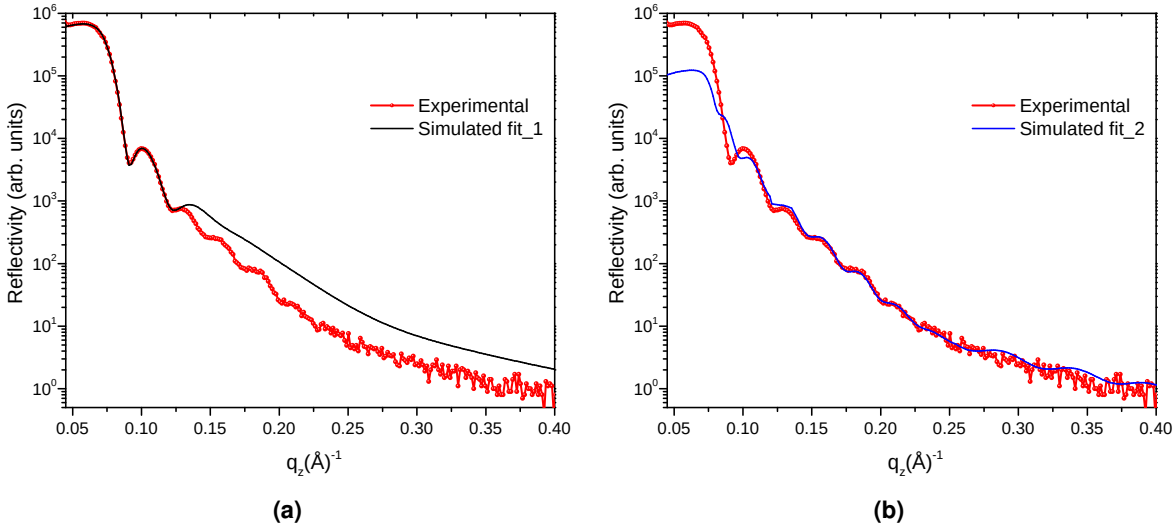

Figure 3.5: Comparison between experimental XRR line profile of 200°C sample and (a) simulated_fit_1 and (b) simulated_fit_2

To validate the crystallinity of Fe layers, reciprocal space maps (RSM) around (004) reflex of GaAs are collected on both samples. The measured RSM's are shown in Fig 3.6(a) & 3.6(b). The angular range of the RSM is big enough to observe both the (002) and (004) reflexes of Fe and GaAs, respectively. The (002) reflex of Fe in Rt and 200°C samples is marked by white rectangle and white oval, respectively in Fig 3.6(a) & 3.6(b). It is clearly evident that the Fe reflex in Rt sample is more prominent as an elongated streak. In contrast, the (002) Fe reflex in 200°C sample is only evident as a diffuse cloud which is only apparent in $\omega - 2\theta$ line scan. We conclude that the Fe layer deposited at room-temperature is more crystalline as the diffraction peak is more sharp. To further analyze the RSM's, line profiles are extracted by integrating the intensity towards q_y axis to obtain line profiles along q_z.

The q_z line profiles of both samples are plotted in Fig 3.7. Clear Laue oscillations are observed in Rt sample and the periodicity of these oscillations give information about the number of coherently scattering lattice planes. Therefore thickness calculated from Laue oscillations can be used to judge the crystalline nature of the deposited Fe layer. On the other hand the diffuse Fe diffraction peak observed in 200°C sample shifts to lower q_z values indicating a larger lattice parameter of Fe when compared to the Rt sample. Moreover the magnitude of intensity of Fe peak in 200°C sample is 20 times less than the Rt sample. The diffusive nature of the peak could be due to formation of interfacial compounds which leads to smaller thickness of Fe layer leading to lower diffraction intensity observed. It has to be noted that the different position of GaAs Bragg peak in both RSM's is due to uncorrected diffractometer

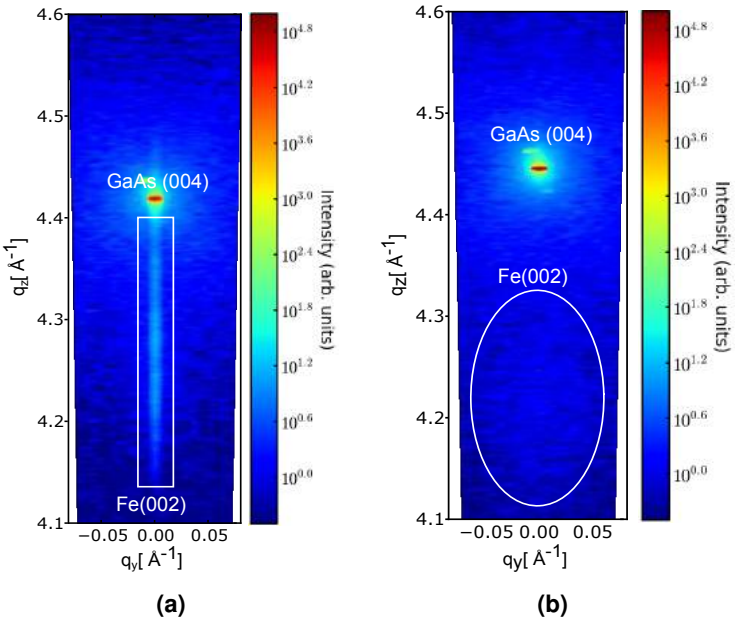

Figure 3.6: (004) Reciprocal space maps obtained on (a) the Rt sample, (b) the 200°C sample. The white rectangle and oval highlights the sharp and diffuse (002) Fe layer reflex observed in Rt and 200°C samples, respectively. The different position of GaAs Bragg peak in both RSM's is due to uncorrected diffractometer offset.

offset and is corrected during evaluation of data. In addition, the Fe peaks are further analyzed by using RCRefSimW program in which the measured diffraction profiles are fitted using a semi-kinematical algorithm[95] to obtain the lattice parameter and the thickness of the Fe layer. The simulated profiles are also plotted in Fig 3.7 as solid lines and the obtained out-of-plane lattice parameters and thicknesses of Fe layers from the simulation are tabulated in Tab 3.1.

From Table 3.1, it is evident that the thicknesses calculated from XRR are larger than the values obtained from XRD measurements. This observation is expected because layer thickness values obtained from Laue oscillations reflect the thickness of ordered crystalline volume while the Kiessig fringes in XRR measurements reflects the total film thickness. This difference in thickness obtained from two techniques indicates that both samples might have interfacial compounds at the Fe and GaAs interface. But the intermixing is much more prominent in 200°C sample. The formation of interfacial compounds is well reported in Fe/GaAs system and the observed larger lattice parameters which is close to reported Fe_3GaAs tertiary compound. So we believe that the observed diffuse Fe Bragg peaks in 200°C sample is due the existence of these compounds. But there is no clear independent evidence of occurrence of these compounds in Rt sample. The out-of-plane HRXRD and XRR techniques employed to the study the Rt sample cannot confirm the existence of these compounds but the observed structural parameters indicate the presence of these compounds.

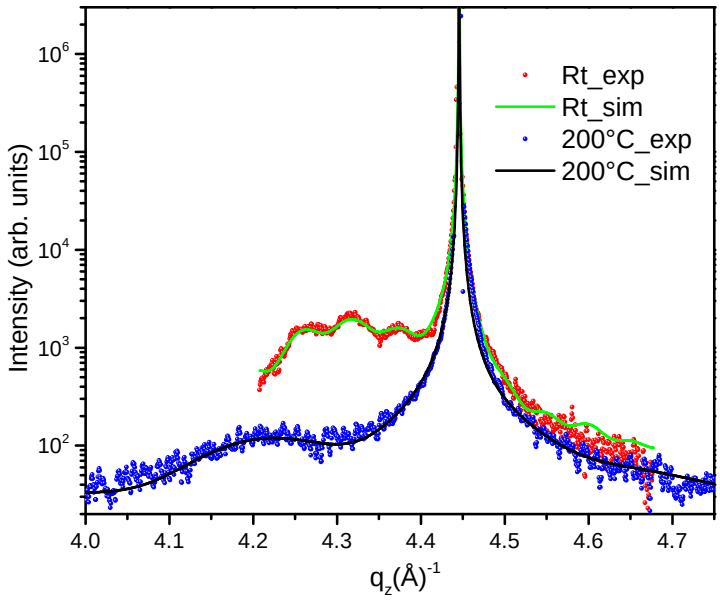

Figure 3.7: Comparison between XRD line profiles of Rt (red dots) and 200°C (blue dots) samples. The solid lines represent the simulated diffraction fit obtain from RCRefSimW program for corresponding samples.

sample	thickness from XRD(nm)	thickness from XRD(nm)	a (Å)
Rt	4.25 ± 0.56	4.7 ± 0.06	2.901
200°C	3.51 ± 1.93	2.62 ± 0.47	2.974
bulk Fe	5 (nominal thickness)	-	2.866

Table 3.1: measured out-of-plane lattice parameters and thickness of Rt and 200°C samples.

So we conclude that the samples grown at elevated temperatures (200°C) have rough interfaces due to formation of interfacial compounds at the Fe/GaAs interface. The sample grown at room-temperature shows well ordered crystalline layers of Fe with sharp interfaces. The combined analysis of XRR and HRXRD of Rt sample also suggests presence of interfacial compounds but could not be validated with the used techniques. Further investigation were performed to study the existence of interfacial compounds using different X-ray scattering geometries, and these results are discussed in following sections.

3.2.2 Effect of post-growth annealing on Fe layer crystallinity

Spin injection measurements are performed on the Fe/GaAs system as a part of this thesis in collaboration with Dr. Lennart Liefeith. The details of these measurements are discussed later in this chapter. Interestingly we observed spin-injection across the Fe/GaAs interface only after post growth-annealing

the fabricated non-local devices at 200°C under inert atmosphere.[85] Similar observations are made by other groups which reported a spin-injection enhancement due to post-growth annealing of Fe/Al-GaAs[15,32,87] and Fe/GaAs material systems.[16,19,86] In correspondence, the works of Fleet *et al*[86] and Zega *et al*[15] reported that the annealing results in more abrupt interfaces which is also reflected in an increase in contact resistance.[86]

In addition, several other studies attempted to correlate post growth annealing and spin-injection efficiency by analyzing the atomic structure of the Fe/GaAs interface.[86,88] The nature of interfaces discussed in these studies will indeed influence the strain state of the epitaxial layers. Therefore, by studying structural and strain properties of the Fe layer before and after annealing, it might be possible to reveal mechanisms controlling spin-injection efficiency. The existing reports on annealing studies in Fe/GaAs heterojunctions using diffraction techniques are conducted either on very thick or ultra-thin Fe films.[96–99] Here we consider the accumulated stress present in a Fe layer is influenced by the thickness of the film.[100,101] So we focused on studying annealing dependent structural changes in Fe film with thicknesses which are typically used for spin injection experiments in non-local geometry.

In this study a sample with an Fe layer deposited at room-temperature is structurally investigated first by using AFM and X-ray diffraction mapping. Later the same sample was soft annealed at 200°C for 10 min under nitrogen atmosphere. The sample before annealing will be referred to in the further text as “as-deposited ”and the sample after annealing as “annealed”. After annealing, we applied the same techniques as mentioned before to study the structural properties. It has to noted that we used the same room-temperature sample (C21N541) described in previous section to study the effect of post-growth annealing. But all the measurements like AFM, XRR and HRXRD are performed again to maintain consistency and allow comparison with annealed sample.

First the surface morphology of the as-deposited sample is probed to reveal the uniformity of the top Au protective layer which is critical for preventing the Fe layer from oxidation. $2 \times 2\mu m^2$ topographic images obtained in tapping mode are shown in Fig 3.8, which reveals the presence of small island-like features on the surface in both samples. The total volume of these islands in the as-deposited sample corresponds to an equivalent Au layer thickness of 2.2 nm. This equivalent thickness is significantly smaller than the nominally deposited layer of 15 nm. This implies that the Au layer is a combination of small islands on a thick continuous layer. An AFM image of the annealed sample as seen in Fig 3.8.(b) reveals that in the annealing process the islands transform into smaller features with sharper edges. The equivalent thickness of these islands decreases to 0.7 nm which indicates that these islands partially merge into the continuous Au layer during annealing.

To further analyze the surface morphology changes height distribution functions (HDF) are obtained from AFM images of both samples which are shown in Fig 3.9. A logarithmic scale is used to enhance details of the distribution. The peak at 0 nm is assigned to the surface of the continuous Au Layer. The shape of the HDFs also supports the suggestion that the surface is a combination of islands and a continuous Au layer. Sharp decrease in the counts below -1 nm indicates absence of pinholes which

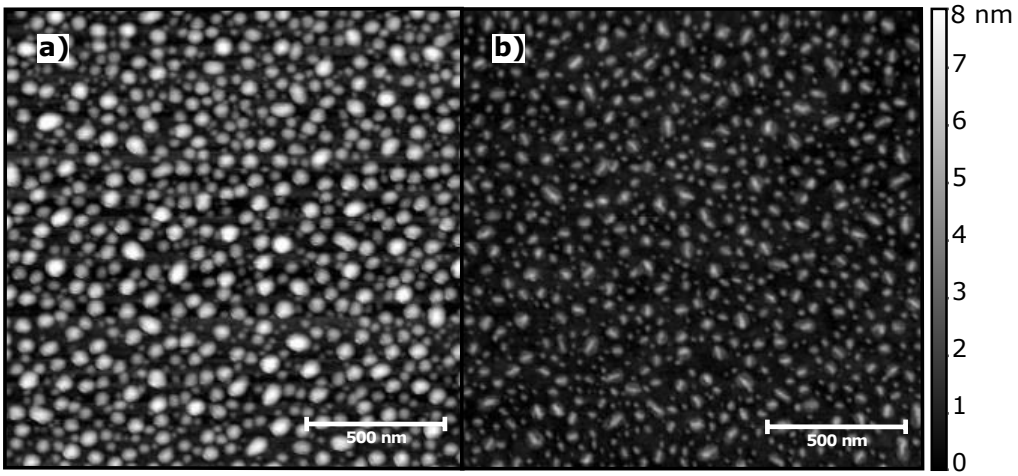

Figure 3.8: $2 \times 2\mu m^2$ AFM images of a) as-deposited and b) annealed samples.

would expose the ferromagnetic material. The broad tail on the right is attributed to the islands with a statistical height distribution on the surface of Au layer. Comparison of the HDF plots before and after annealing reveals a decrease in the height and volume of the islands after annealing. These observed changes in Au layer topography are later used to explain changes in the XRR curves discussed in the following text.

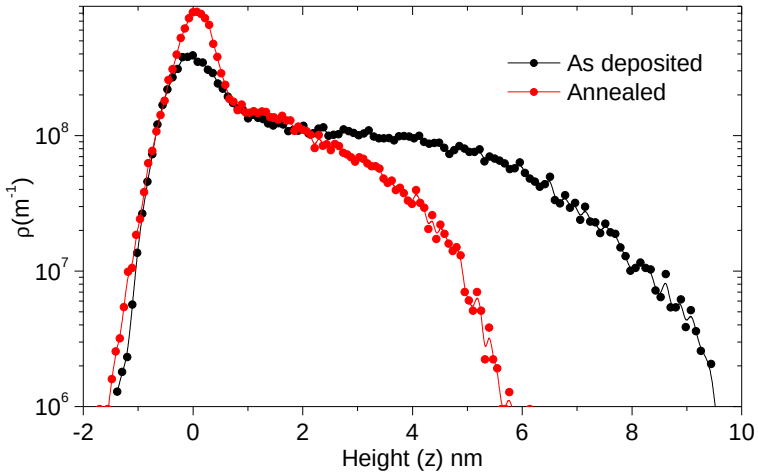

Figure 3.9: Hight distribution function of both as-deposited and annealed sample.

Information about the interfaces before and after annealing is obtained from X-ray reflectivity measurements. In this study XRR profiles are directly measured instead of measuring XRR RSM's. The X-ray reflectivity profiles of both, as-deposited and annealed samples are shown in Fig 3.10. The inset shows a comparison between an experimental pattern of the as-deposited sample and simulated reflectivity pattern indicating good agreement. The thicknesses parameters of this fit are: $t_{Fe} = 4.7 \pm 0.06$ nm and $t_{Au} = 14.3 \pm 0.04$ nm for the Fe and Au layers, respectively. The roughness parameters of Fe layer and

substrate are: $r_{Fe} = 0.32 \pm 0.04$ nm, $r_{substrate} = 0.12 \pm 0.02$ nm.

Surprisingly, the best fit for the annealed sample does not indicate a change in either thickness or roughness of the Fe layer. The layer seems to remain unaltered after annealing. Clearly, there is only little contrast between the reflectivity profiles of both samples and the difference is mainly due to the change in the surface roughness of the Au layer (as-deposited: $r_{Au} = 0.13 \pm 0.01$ nm, annealed: $r_{Au} = 0.10 \pm 0.01$ nm). This difference can be qualitatively correlated to the change in root mean square roughness (rms) of the continuous Au layer ($rms_{as-deposited}$: 0.56 nm, $rms_{annealed}$: 0.33 nm) measured with AFM. We note that one may not expect the roughness values derived from XRR and AFM to coincide. The difference arises from many factors like different ranges of lateral spatial frequencies covered by the two techniques[102] and also, due to the fact that, in the XRR simulation algorithm diffuse scattering from rough surface is not considered.

In the previous subsection 3.2.1, we concluded that interface compounds might exist by considering the fact that, different values of thickness are obtained from XRR and XRD techniques. This interpretation is also based on previous studies which reported the presence of few monolayers of binary and ternary Fe-Ga-As compounds at the interface either immediately after deposition[92,103] or, their formation after annealing.[87,96,97] Although we cannot completely exclude the existence of these compounds in our samples, we can conclude from our XRR data that there exists no continuous layer of these compounds in the studied heterojunctions. We arrive at this conclusion because incorporation of even few monolayers of such compounds into our reflectivity model resulted in significant disagreement between experimental and simulated profiles. Therefore, within the resolution of the X-ray reflectivity measurements we observe no formation of new compounds at the Fe/GaAs interface. But we note that isolated islands of new compounds may still exist at the interface.

The techniques like AFM and XRR shed light on the morphological characteristics of layers while techniques like HRXRD reveal information about the crystallinity of the layers. So we collected RSM's around different reflexes of the Fe layer and GaAs substrate which reveal information about the crystalline nature, orientation, and strain of the epitaxial layers. RSM's are collected in two different geometries called symmetric and asymmetric scans. In the former geometry, the diffraction vector is normal to the surface allowing measurement of the out-of plane lattice parameter a and layer inclination with respect to $[001]$ crystal direction of the GaAs substrate. In the latter geometry, the diffraction vector of the measured reflex is tilted by an angle with respect to the surface normal allowing evaluation of lateral distortions. We studied reflexes that reveal information on the lateral distortions along $[110]$ and $[-110]$ crystal directions.

To observe changes in lattice parameters in both out-of-plane and lateral direction, we have extensively studied reciprocal space maps around the (004)(shown in Fig 3.11(a)), (224)(shown in Fig 3.11(b)), and (-224) reflexes of the GaAs substrate. The scans are large enough so that the corresponding $(002), (112)$, and (-112) reflexes of the Fe film are also observed in the same map. By analyzing both symmetric (004) and asymmetric scans ((224),(-224)), we obtain the deformation of elementary

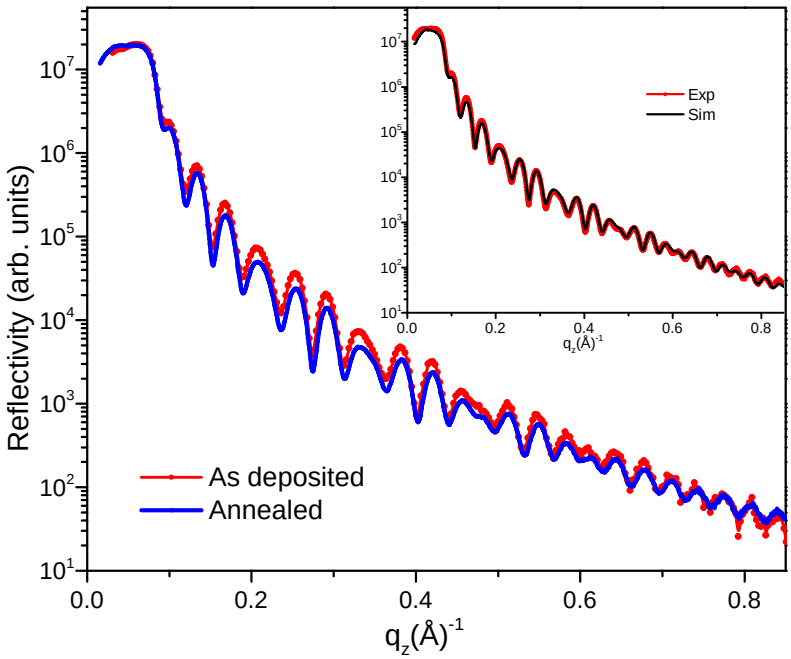

Figure 3.10: X-ray reflectivity profiles of as-deposited(red line) and annealed sample(blue line). Inset: comparison between experimental and simulated profile of the as-deposited sample. Thickness obtained from best fit is same for both samples: $t_{Fe} = 4.7 \pm 0.06$ nm $t_{Au} = 14.3 \pm 0.04$ nm. Roughness of Au: as-deposited: $r_{Au} = 0.13 \pm 0.01$ nm, annealed: $r_{Au} = 0.10 \pm 0.01$ nm.

cells in the crystalline layers. This approach complements previous studies[101,104] which use only the out-of-plane lattice constant to evaluate strain in thicker Fe films.

The obtained RSM's are shown as color maps of diffraction intensity plotted as a function of reciprocal space coordinates (q_z, q_y). In both maps the most intense and sharp peak belongs to GaAs, while the elongated streak highlighted by a black rectangle arises from the Fe layer. The reflexes of Fe are elongated because of the small layer thickness. The intensity tails highlighted by a white rectangle around the GaAs peak in the asymmetrical scan is a typical analyzer streak.

Symmetric maps are projected towards q_z axis to obtain line profiles along q_z. On the other hand, the (224) and (-224) maps are projected towards along q_y axis to obtain line profiles along $[100]$ and $[-110]$ crystal directions of GaAs respectively. These line profiles are not shown here as they resemble the already discussed lone profiles in Fig 3.7. Additionally an HRXRD measurement was performed on the annealed sample at the P08 beamline of Petra III at DESY using a photon energy of 8319 eV. Fig 3.12 shows the comparison between line profiles of the annealed sample extracted from a symmetric map and line scan obtained using synchrotron radiation. Peaks from the line profiles are fitted with pseudo-Voigt functions to obtain the exact q_z and q_y values which are later used to calculate out-of-plane lattice parameters and inter-planar spacings, respectively by using the well known relations for cubic crystal:

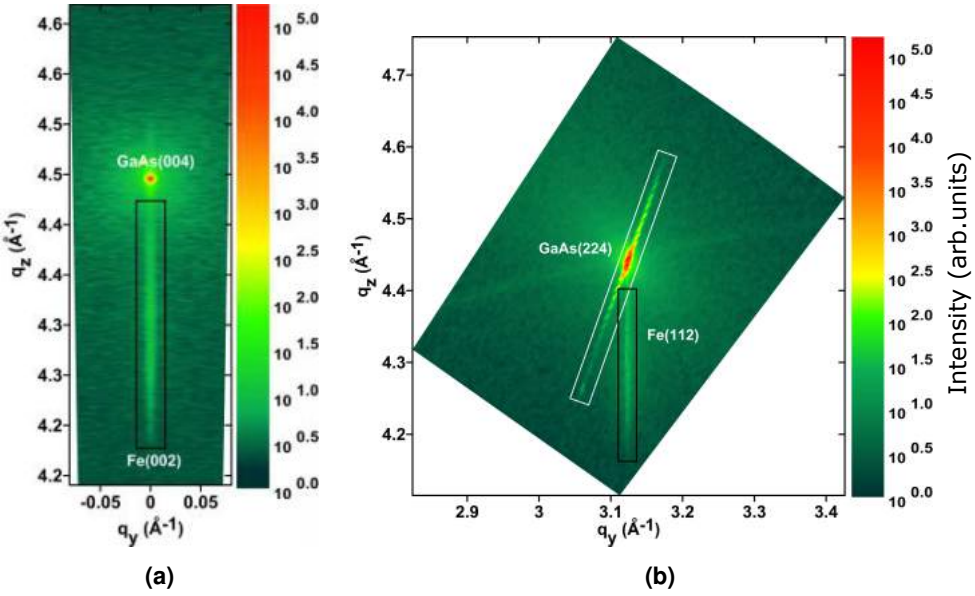

Figure 3.11: Reciprocal space maps measured on the as-deposited sample at the (a) 004 Bragg reflex of GaAs, (b) 224 Bragg reflex of GaAs. q_z and q_y are along the $[110]$ and $[-110]$ crystal directions respectively. The color scale represents diffraction intensity in arbitrary units. The regions in black rectangles highlight Fe reflexes. The white rectangle in (b) represents the analyzer streak.

$$d_{hkl} = 2\pi/|\vec{q}| = \frac{a}{\sqrt{h^2 + k^2 + l^2}} \tag{3.1}$$

The results of fitting are summarized in tables 3.2 & 3.3. From table 3.2 it can be seen that, the inter-planar spacing *d* for the as-deposited sample is less than the expected bulk value of Fe. Such an in-plane contraction is expected for the epitaxial structure[105] due to lattice mismatch. It has been observed before using polarization-dependent X-ray absorption fine-structure spectroscopy.[106] As a result of annealing *d* shrinks further towards the bulk value of GaAs (1.998Å). To allow this compression, the out-of-plane lattice should expand, and that is exactly what we observe in table 3.3 where the out-of-plane lattice constant is found to be greater than the bulk Fe value and increases further after annealing. In other words, the Fe film is inherently strained in the as-deposited sample and this compressive strain increases after annealing. The increase might be caused by improved atomic level ordering at the interface after post-growth annealing.[15,86] Compressive strain resulting from the mis-matching between in-plane lattice spacing of substrate and Fe layer also supports our inference that, there is no continuous intermediate layer of Fe-Ga-As compounds at the interface because their existence would result in tensile strain of the Fe layer as observed by Filipe *et al.*[92]

It can be further noted that the inter-planar spacing for the as-deposited sample differs in both $[110]$ and $[-110]$ directions which indicates anisotropy in the strain distribution which is also expected from first principle calculations.[105] Similar behavior was already observed in the size of Fe coherent domains on

sample	q_y (Å^{-1})	d (Å)
bulk Fe 110	3.1004	2.026
as-deposited 110	3.1276	2.008 ± 0.001
as-deposited -110	3.1398	2.001 ± 0.001
Annealed 110	3.1488	1.995 ± 0.002
Annealed -110	3.1468	1.996 ± 0.002

Table 3.2: Spacing of 110 lattice planes in the as-deposited and the annealed sample with respect to bulk Fe.

sample	q_z (Å^{-1})	a (Å)
bulk Fe 004	4.384	2.866
as-deposited 004	4.333	2.900 ± 0.001
Annealed 004	4.319	2.909 ± 0.001
Annealed (beamline) 004	4.318	2.910 ± 0.003

Table 3.3: Out-of-plane lattice parameters of as-deposited and annealed sample with respect to bulk Fe.

GaAs[99] and also in strain relaxation of Fe film on InAs[107] and was attributed to preferential bonding of Fe to As dimers present on the reconstructed surface.[64] We believe the anisotropy observed in our sample also stems from the same effect. Structural anisotropy of the interface is expected to influence the magnetic anisotropy of the Fe film.[99] Recently Tivakornsasithorn *et al.* proposed that the structural anisotropy is also responsible for a widely reported magnetic uniaxial anisotropy in thin Fe/GaAs films.[108]

Interestingly, after annealing, the in-plane components in both crystal directions have very similar inter-planar spacing leading to the disappearance of the lateral strain anisotropy. However, the compressive strain of the Fe layers is still preserved after annealing. As evident from Fig 3.12 and table 3.3, we got very consistent data from the lab diffractometer and synchrotron measurements which validates the resolution and accuracy of our measurements.

In an ideal Fe/GaAs heterojunction four Fe unit cells are epitaxially connected to one GaAs unit cell. A fully relaxed iron layer would show lattice mismatch of 1.4%, i.e the side lenght of 2 fe unit cells is 1.4% larger than the conventional GaAs unit-cell. In our as-deposited sample the difference between the lateral components of the Fe and GaAs unit cells calculated from the inter-planar spacing d_{110} was found to be 0.5% and becomes more isotropic after annealing decreasing to the value of 0.12%. This in-

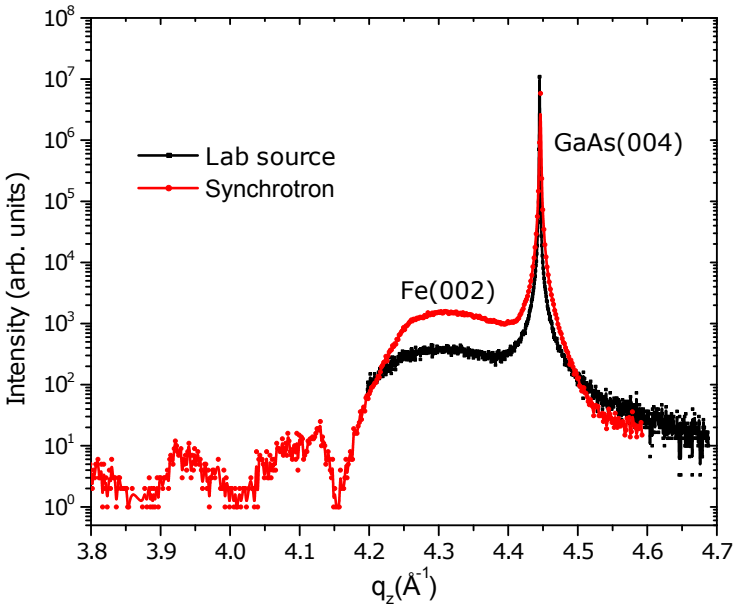

Figure 3.12: Comparison between diffraction profiles of annealed sample obtained using lab source and synchrotron source.

plane compression is pictorially depicted in Fig 3.13 where brown dashed lines and pink box represents the bulk and measured Fe unit cells respectively. The Fe unit cells lateral lengths are shown with respect to half of GaAs unit cell and the black line is drawn as guide to the eye.

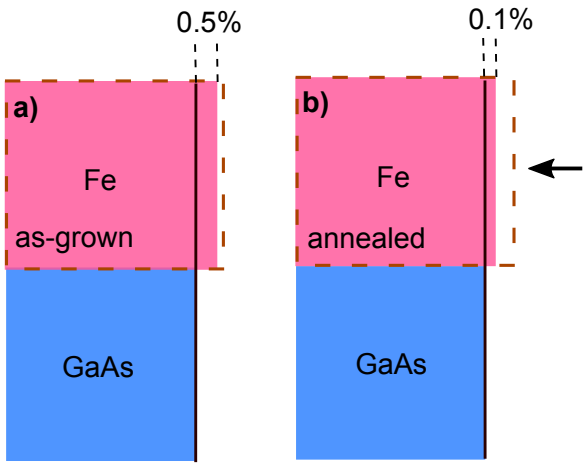

Figure 3.13: Schematic showing in-plane compression of Fe unit-cell due to annealing with respect to half of GaAs unit-cell. (a): as-grown sample. (b): annealed sample. brown dashed lines: bulk unit-cell of Fe. black-line: guide to the eye. arrow indicating the compression. The extent of compression is not to scale.

In summary, we studied the effect of post growth annealing on epitaxial Fe layers deposited on GaAs (001). We did not observe any significant change in morphology of the Fe layer. From our XRR results

we exclude the formation of a continuous interface layer. On the other hand, post growth annealing is found to result in a significant variation in the strain of the Fe layer. The as-deposited sample was found to be compressively strained. This strain was observed to increase further after annealing and to become isotropic. So we speculate that the observed reduction in the structural anisotropy will also cause a reduction of the uniaxial magnetic anisotropy of Fe film. Similar behavior was reported in previous studies where the interplay between uniaxial and cubic magnetic anisotropy of Fe layer is found to be affected by structural anisotropy resulting from Ge[109] and ZnSe[108] buffer layers deposited between the GaAs substrate and Fe layer.

The observed strain variation also makes us believe that the inter-planar spacing of Fe unit cell shrinks to match that of the GaAs unit cell. So the perfectly coordinated interfaces assumed in some simulations[105,110–112] may be extended to include the annealing induced change in the inter-planar spacing of Fe unit cell. We speculate that enhancement in the matching of inter-planar spacing of Fe and GaAs at the interface after annealing might contribute to enhanced spin injection efficiency. This might be due to a change in the Fe-As local hybridization configuration resulting from the strain variation.[86,111]

3.2.3 Effect of post-growth annealing on Fe layer studied by GID

In addition to the symmetrical and asymmetrical diffraction experiments, Grazing Incidence Diffraction (GID) measurements are also performed on Fe/GaAs samples to further understand the changes at the interface due to influence of annealing. GID technique is adopted because it is a surface sensitive method which allows probing of thin layers close to the sample surface. GID measurements are also performed to confirm the observed in-plane compressive stain and also to validate the existence of inter-facial compounds at the interface if any. For this purpose, a new sample (C21N587) is prepared as the C21N541 sample was completely used for other measurements. Both the XRR and HRXRD measurements are performed on this sample to verify thickness and crystallinity of the Fe films. The XRR experimental and simulated profile obtained on the sample named C21N587 is shown in Fig 3.14. The obtained thickness of the Fe layer is close to the previously mentioned Fe/GaAs samples. But the thickness of the Au layer is intentionally reduced to 5 nm for the purpose of indentation experiments which will be discussed in the Sec 4.3. The HRXRD measurements are performed to obtain RSM around (002) reflex of Fe which revealed a streak-like Fe Bragg peak similar to the one discussed in Sec 3.2.2. The obtained RSM is not shown here, but the lattice parameters evaluated form this RSM are close to the values represented in Sec 3.2.2. From the combined analysis of both XRR and HRXRD we conclude that the sample C21N587 is structurally similar to the C21N541 sample discussed in the previous section. After completing HRXRD measurements, the C21N587 wafer is cleaved into two 3×3 mm^2 pieces. One of these pieces is soft annealed at 200°C for 10 minutes under nitrogen atmosphere and will be referred to as annealed sample in further text while the other un-annealed piece will be referred to as as-deposited sample.

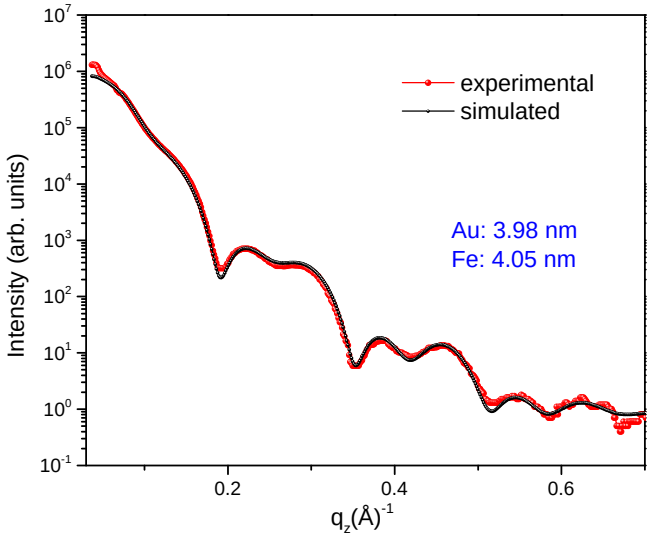

Figure 3.14: Comparison between experimental (red line) and simulated XRR line profile (black line) of C21N587 sample. Thicknesses obtained from best fit: $t_{Fe} = 4.05 \pm 0.15$ nm $t_{Au} = 3.98 \pm 0.24$ nm. Roughness: $r_{Fe} = 0.12 \pm 0.06$ nm, $r_{Au} = 0.16 \pm 0.05$ nm.

GID measurements were performed on the same sample at two synchrotron facilities, P10, Petra III and ID13, ESRF. The principle of GID geometry is mentioned in subsection 2.3.5. Initial GID measurements were performed on the as-deposited sample at P10,Petra III facility using a six-circle diffractometer with a unfocused beam at an energy of 9 keV. The diffractometer is aligned to the (220) in-plane reflex of GaAs at corresponding Bragg angle of $\theta = 20.1585°$. The diffraction signal is measured by using an 2-dimensional PILATUS 300k detector (486×619 pixcel area, 172 μm pixel size) mounted on the 2θ arm. To enhance resolution, the sample and detector have large separation distance of 2454 mm. A vacuum flight tube is used between the sample and detector to avoid background from air-scattering.

An GID RSM is obtained by rotating the sample around the surface normal in the range of 2° with 100 steps. Individual detector frames at each step is integrated along angular direction and stored as series of one dimensional arrays using an in-house developed python code. Later, a two dimensional map is created from obtained one-dimensional arrays and plotted as 2D reciprocal space map which is shown in Fig 3.15.(b).

Surprisingly, three distinct peaks are observed in the obtained RSM which are associated to GaAs (220), Fe (110) and Fe_3GaAs (110) Bragg peaks. The intense, sharp feature of GaAs and a lower intensity feature of Fe next to GaAs are expected but, the presence of broad intense feature of Fe_3GaAs is a unexpected finding. This broad feature is assigned to Fe_3GaAs after calculating the inter-planar spacing from the line profile of RSM, which will be discussed later in this section. Fe_3GaAs is reported to be a thermodynamically stable compound existing as pseudo-cubic unit cell on GaAs substrates.[92,113] However, the presence of Fe_3GaAs contradicts our previous results from the combined study of asymmetric

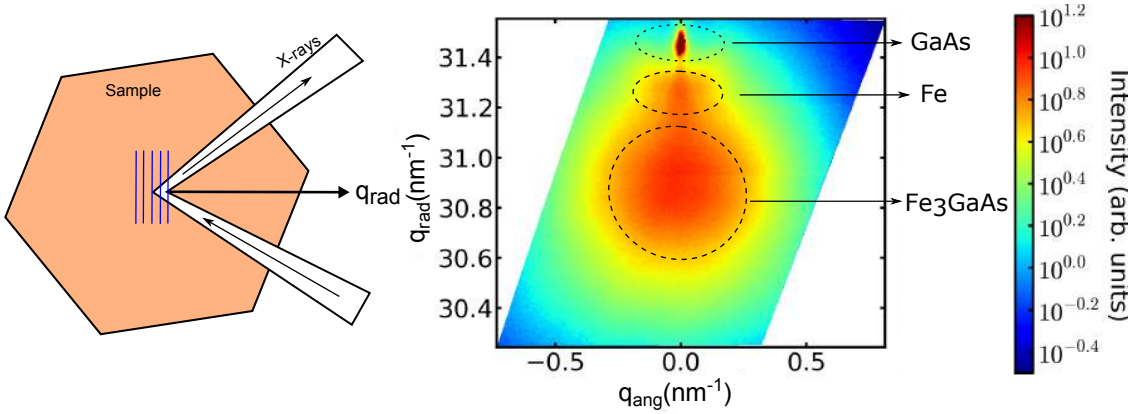

Figure 3.15: a)Schematic showing GID geometry and the corresponding diffraction vector q_{rad} which is perpendicular to the diffraction planes. b) RSM obtained around (220) in-plane reflex of GaAs. The Bragg peaks are marked correspondingly.

and symmetric reflexes in Sec 3.2.2, which concluded the absence of continuous layer of interface compounds. We believe that this conclusion is still valid because we infer that the broad intensity feature arises from isolated islands of Fe_3GaAs at the Fe/GaAs interface. We conclude that Fe_3GaAs exists as isolated islands because incorporation of even few monolayers of Fe_3GaAs into our reflectivity model led to significant disagreement between experimental and simulated profiles. The disagreement observed in XRR simulation with Fe_3GaAs as third layer is because the adopted Parratt model[71] only considers continuous layer during fitting. Therefore, we believe that Fe_3GaAs is present as isolated islands.

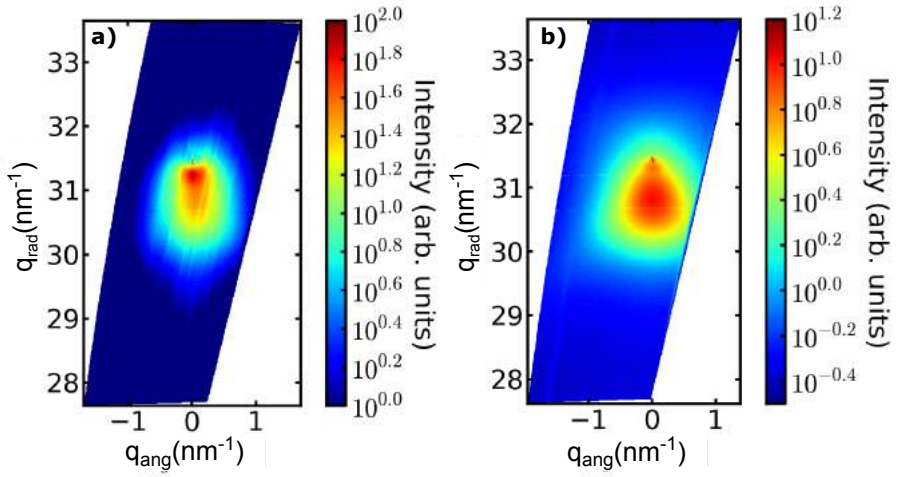

Figure 3.16: Reciprocal space maps obtained close to the (220) in-plane GaAs reflex on (a) the as-deposited and (b) the annealed sample

Unfortunately, the annealed sample could not be studied at P10,PETRA III because of the limited

beam-time. So, we have performed the GID measurements on both as-deposited and annealed samples at ID13, ESRF. A micron sized X-ray beam of 14.33 keV was used with an EIGER 4M detector at 1850 mm distance from the sample. A RSM around (220) reflex GaAs was obtained by rotating the sample around the surface normal in the range of 4° with 400 steps around Bragg angle of θ=12.49° for both as-deposited and annealed samples. The RSM's are constructed using the same procedure as described before and both maps are shown in Fig 3.16. The RSM's obtained at ESRF resemble the map measured at PETRA III, but to aid appropriate comparison, line profiles of all three RSM's are obtained. Line profiles along q_{radial} direction corresponding to [110] crystal direction are obtained from RSM's. The obtained line profiles from all three RSM's (as-deposited$_{petra,\ ESRF}$, annealed$_{ESRF}$) are shown in Fig 3.17.

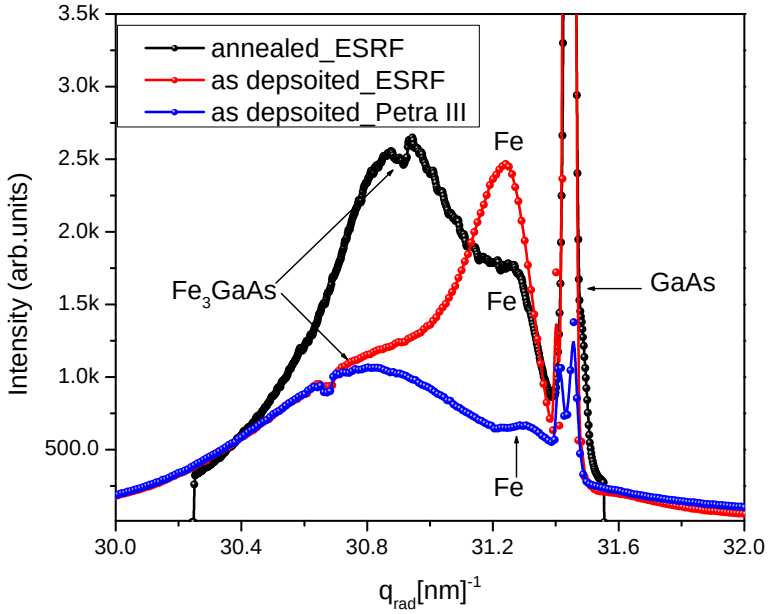

Figure 3.17: Comparison of lines profiles obtained from as-deposited and annealed samples at both PETRA III and ESRF facilities. The difference between the PETRA III and ESRF line intensity is due to different X-ray optics and incidence angles.

The most striking difference between the RSM's of as-deposited sample obtained at PETRA-III and ESRF is the change in intensity of the Bragg peaks. This intensity difference is due to different flux and beam size of the beam used at the two separate beamlines. On the other hand, the peak positions of the Bragg peaks almost remains same. The most interesting difference is observed in measurements performed at ESRF where the change in intensity of both Fe and Fe_3GaAs peaks is noticed due to post-growth annealing. The change in intensity of Fe and Fe_3GaAs peaks in as-deposited (red line) and annealed (black line) sample is clearly evident in Fig 3.17 where the Fe peak intensity decrease while the intensity of Fe_3GaAs increases after annealing. This change in intensity is much more clearly illustrated in Fig 3.18 (a) & (b) which shows the individual peak fits obtained on the as-deposited and

annealed sample, respectively. The line profiles are fitted with pseudo-Voigt functions to obtain the exact peak positions. The individual fit of GaAs peaks are not shown to emphasize the fits from Fe and Fe_3GaAs peaks. Later, the inter-planar spacings d_{110} of the Fe and Fe_3GaAs layers are calculated from the obtained peak positions using the Eq 3.1 and are tabulated in Table 3.4.

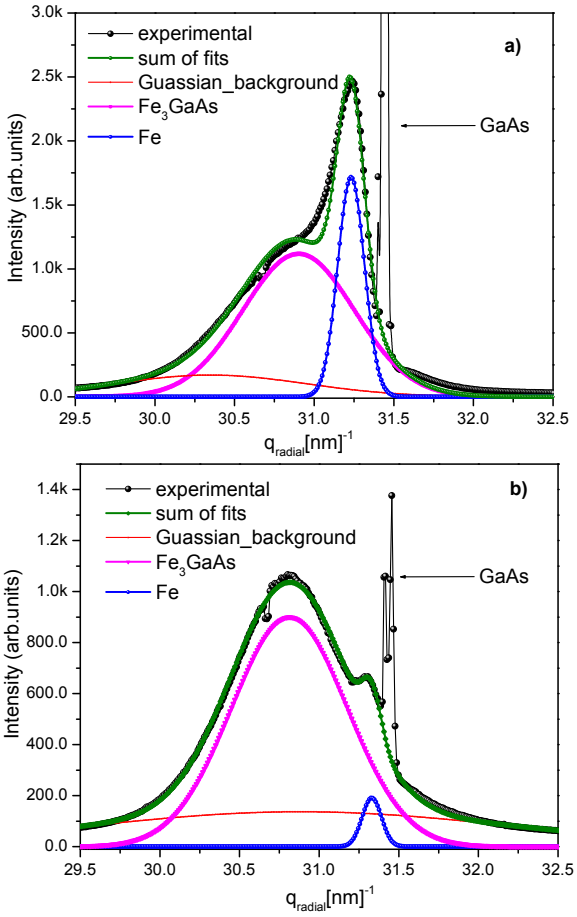

Figure 3.18: Gaussian fitting of line profiles a) as-deposited and b) annealed sample. The individual fit of GaAs is not shown to highlight the Fe and Fe_3GaAs fits.

From the calculated in-plane lattice spacings, it is evident that the Fe layer is compressively strained and the strain further increases after annealing which coincides with our previous findings. Also, the values of the in-plane d-spacings of the Fe layer calculated from GID and asymmetric reflexes measurements are found to be consistent, which validates the precision and repeatability of both our sample preparation and measurements. In correspondence, the in-plane d-spacing of Fe_3GaAs is observed to increase after post-growth annealing. Additionally, the FWHM of Fe_3GaAs peak is observed to become sharp after annealing. The sharpness of the peak indicates that Fe_3GaAs islands become more ordered and crystalline after annealing. The overall strain state of Fe layers and Fe_3GaAs islands before and after annealing are schematically represented in Fig 3.19.

The obvious assumption in any epitaxial multilayer system is that the expansion of any intermediate

sample	q_{rad} (Å^{-1})	a (Å)
bulk GaAs220	3.1442	1.9983
bulk Fe 110	3.0999	2.0268
bulk Fe_3GaAs 110	3.0789	2.0407
as-deposited Fe 110 PETRA III	3.1281	2.0086
as-deposited Fe 110 ESRF	3.1221	2.0124
annealed Fe 110 ESRF	3.1340	2.0048
as-deposited Fe_3GaAs 110 PETRA III	3.0902	2.0332
as-deposited Fe_3GaAs 110 ESRF	3.0909	2.0327
annealed Fe_3GaAs 110 ESRF	3.0785	2.0409

Table 3.4: Calculated in-plane lattice spacing's (d) of Fe and Fe_3GaAs and the corresponding q_{rad} obtained from the fitting of line profiles. The bulk d-spacing values of GaAs, Fe and Fe_3GaAs are also shown to enable comparison.

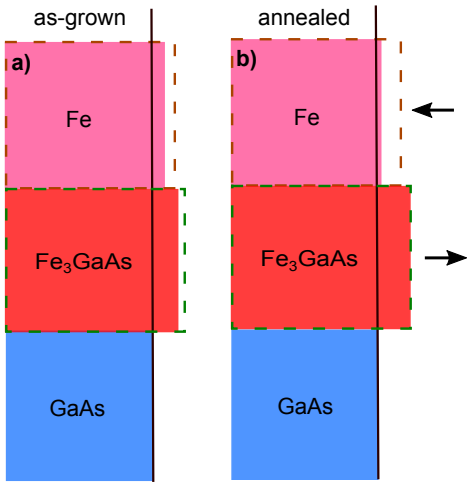

Figure 3.19: Schematic showing in-plane compression of Fe unit-cell due to annealing with respect to half of GaAs unit-cell. brown dashed lines: bulk unit-cell of Fe. black-line: guide to eye. arrow indicating the compression. The extent of compression is not to scale.

layer (like Fe_3GaAs) will definitely lead to tensile strain on the top layers. Therefore, the increase of inter-planar spacing of Fe_3GaAs should lead to tensile strain in Fe layers after annealing. But our results contradict that assumption as Fe layers become more compressively strained even though the Fe_3GaAs d-spacing expands. This behavior could be understood by considering that the Fe_3GaAs phase is present as islands but not as continuous layer. Therefore, the tensile strain due to expansion of Fe_3GaAs islands d-spacing does not influence the Fe layer. Our results agree with the TEM studies performed by Fleet *et al* which report the presence of about 20% of intermixed interface[86] in the presumed sharp interfaces.

In summary, the GID measurements enabled direct measurement of in-plane lattice spacings of Fe layers and the obtained values agree with the values calculated from asymmetric reflexes. GID investigations establish the existence of Fe_3GaAs tertiary phase at the Fe/GaAs interface. We believe that our results contribute to understanding the role of the interface in spin-injection mechanisms as the density of electron states at the interface are suggested to be responsible for the bias dependence of spin injection observed at Fe/GaAs interfaces.[12,20,87,114,115] We assume that by considering the presence of another phase at the Fe/GaAs interface in the First-principle calculations of spin currents, new mechanisms responsible for asymmetry of spin-injection as a function of applied bias voltage could be uncovered.
In the latest round of beamtime at ESRF, the mentioned samples are studied again in GID geometry. However, during this beamtime, the GID measurements are performed at different inclination angles of the incident beam to probe different parts of the Fe film and interface. Also, the samples are subjected to an additional cycle of annealing to identify the structural changes during the second cycle which incidentally also led to the decrease in spin-injection efficiency (discussed in next section). The analysis of this beamtime data is still in process and the corresponding results are not mentioned in this thesis.

3.3 Spin injection through Fe/GaAs interface

The main aim of studying Fe/GaAs material system is to achieve spin injection from ferromagnetic Fe layer into moderately doped GaAs. Fe/GaAs is widely studied as a test system for spin injection studies using electrical and optical techniques[11,76,77] and a large pool of data is available on this system. Therefore, this material system is studied first in this PhD project to establish and standardize the protocols and techniques required for spin injection studies. The spin injection measurements on the Fe/GaAs material system have been performed hand in hand with the previously described structural measurements (3.2.2 and 3.2.3) to complement and correlate the measured structural and transport properties. The spin injection is measured using non-local spin valve measurements, which were performed in collaboration with Dr. Lennart Liefeith. The details regarding fabrication of spin-valves devices and non local measurements are discussed briefly in the following subsections.

3.3.1 Sample design and band structure of Fe/GaAs heterostructure

The design and growth conditions of the samples used for spin injection measurement are same as the ones used for post-growth annealing studies described in subsection 3.2.2. The same sample design is used to maintain consistency and allow correlation between observed structural properties and spin-transport properties. The sample used for spin-injection measurements is named C21N516 and its layout with nominal thicknesses is shown in Fig 3.20.a).
Our sample design is a modified version of the layout proposed by Lou et al[13] for all-electrical lateral spin-valve measurements. The selected channel doping concentration (n^+) is above metal-insulation

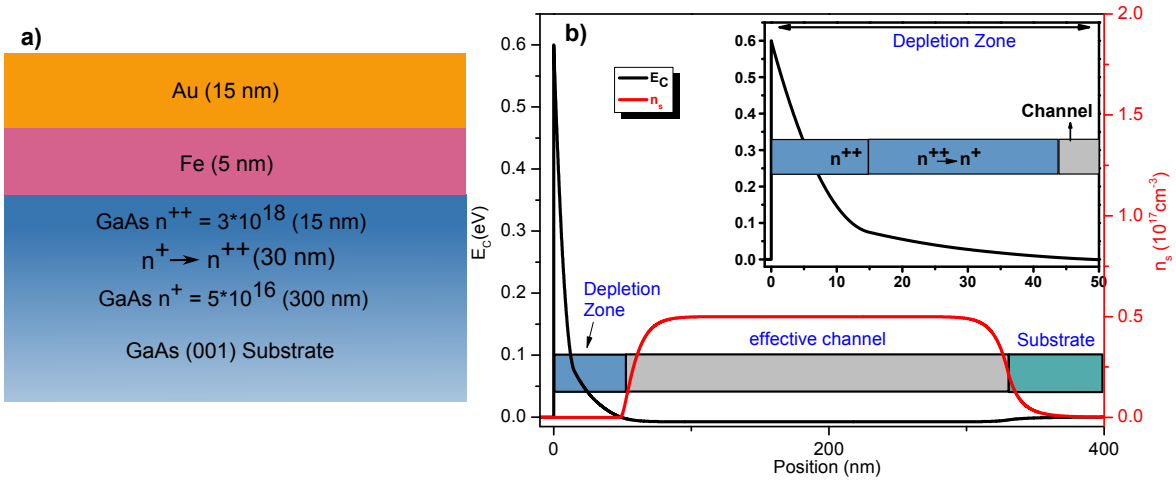

Figure 3.20: a) Sample layout of the Fe/GaAs heterostructure. b) Corresponding conduction band profile of the sample

transition of GaAs which enables electrical conduction in GaAs at liquid helium temperatures. The chosen n^+ values also enables longer spin-lifetime, which is negatively affected by the Dyakonov-Perel scattering.[116] The highly doped layer n^{++} is used to obtain narrow schottky barrier and smaller depletion zone.

The conduction band profile corresponding to the sample design is calculated using a self-consistent Schrödinger and Poisson equation solver developed by Gregory Snider.[117] For these calculations, nominal doping concentration and Schottky barrier height of Fe/GaAs interface are used as input parameters. The doping concentrations are calibrated beforehand by using magento-transport and capacity -voltage measurements. A Schottky barrier height value of 0.6 eV is used, which is taken from literature.[118] The obtained conduction band-structure and carrier concentration as a function of distance from the Fe/-GaAs interface is shown in Fig 3.20.b). A close-up of band-diagram close to the highly doped layer at the Fe/GaAs interface is shown in the inset to highlight the depletion zone. It can be seen in Fig 3.20.b) that the free carriers are located inside n^+ layer forming effective channel.

3.3.2 Non-local measurement on Fe/GaAs spin valve

The spin valves device are designed by considering a number of material properties like the magnetic easy axis orientation of the Fe layer and typical spin diffusion lengths of GaAs. These properties and boundary conditions which are essential for all electrical spin-injection experiments are discussed in detail in sec 2.2 & 2.1. The entire fabrication processes are performed with cleanroom facilities by using photo-lithography and wet etching techniques and are briefly described here. The protocols of wet chemical etching and parameters of photo-lithography are discussed in detail in the thesis work of Dr. Lennart Liefeith.[59]

One of the fabricated spin-valve device is shown in Fig 3.21, which shows two Au/Fe electrodes and two outer Au reference electrodes which are marked as 2&3 and 1&4 respectively. The metal electrodes are etched first so that the Fe layer is present only in the Au/Fe electrode parts of the device. Later, the highly doped (n^{++}) layers are etched away to define the channel and reference electrodes parts of the device which is devoid of n^{++} layers. Finally, a channel with $50\,\mu m$ width is defined by etching the GaAs layer down to 400 nm to electrically isolate n^{+} doped layers from the substrate and subsequent metal contacts. After these steps, Au supply lines of 390 nm in thickness are deposited in a evaporation chamber by using thermal evaporation technique. A SiO_2 based isolator is deposited to prevent supply lines of the electrodes from getting in contact with edges of channel.

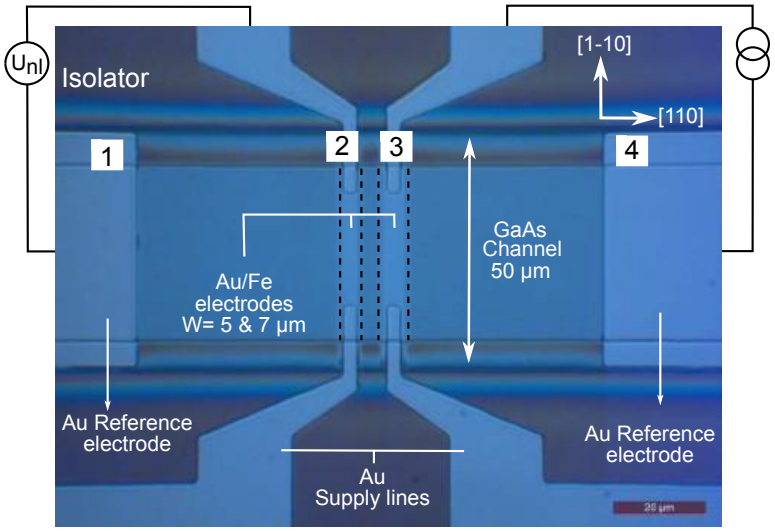

Figure 3.21: a) Microscopic image obtained on the fabricated spin valve device. Current-source and voltmeter are indicated inside the image to depict the non-local measurement configuration.

During the fabrication process, precautions are taken to ensure that the channel is oriented in [110] direction. On the other hand, the elongated axis of the Fe electrodes (2&3) are oriented in [1-10] crystal direction of GaAs. This orientation of the channel and Fe electrodes was chosen to ensure that the easy axis of magnetization is oriented along the long side of the electrode. The easy axis of magnetization at the adopted Fe film thicknesses is along [1-10] crystal direction of GaAs and is well established by many reports in literature and was also studied in our group.[64,119,120] The separation between the Au/Fe electrodes and outer reference electrodes is maintained at $50\,\mu m$. The center to center separation between the electrodes 2&3 is varied between $1\&7\,\mu m$ in different devices to study the effect of electrodes separation on the measured spin-injection efficiency. Also, careful measures are taken to keep the widths of electrodes at different dimensions (electrode 2= $5\,\mu m$ & electrode 3= $7\,\mu m$) to ensure that the electrodes switch magnetic orientations at different magnetic fields due to the underlying magnetic shape anisotropy.

Spin injection is measured on the fabricated device by using the four-terminal non-local setup as de-

scribed in Sec 2.1. The measurement are performed at liquid helium temperatures using a 300mK cryostat. The electrodes 1&2 are used to the measure the non-local voltage while the contact 3&4 are used to drive the current. The measurement configuration is shown as a schematic in inset of Fig 3.22. In our setup convention, the reverse bias direction corresponds to electron injection from FM into SC while the forward bias corresponds to electron extraction. The magnetic field ($\bar{B}$) is applied along the long axis and swept in-plane in [1-10] direction from -100 to 100 mT with a step size of 0.1 mT at a rate of 2.4 mT/min. Non-local voltage jumps, which are characteristic of spin injection and extraction,[52,121,122] have not been observed when the non-local measurements were performed on as-prepared sample. The nonlocal voltage jumps as seen in Fig 3.22 are observed only, when the device is soft annealed at 200° under nitrogen atmosphere for 10 minutes.

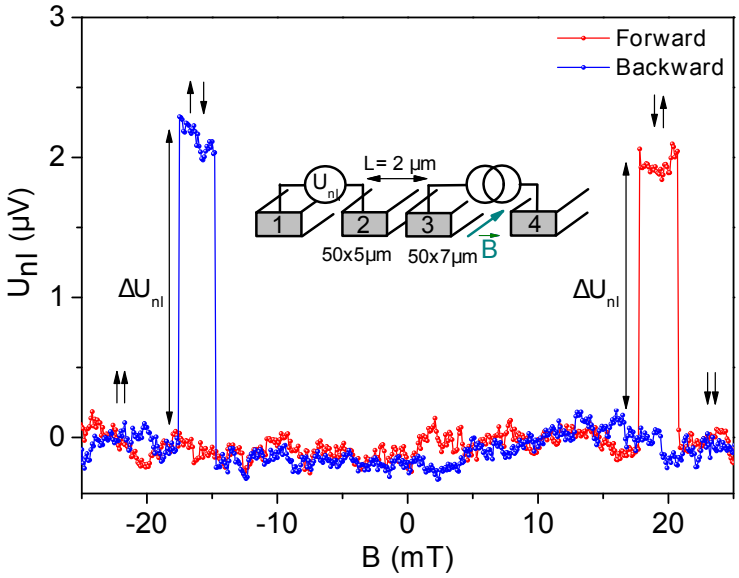

Figure 3.22: Non-local voltage measured as function of magnetic field ($\bar{B}$) which is swept in both forward and backward direction after first annealing cycle. The data were taken at liquid helium temperature. Data taken in forward (backward) sweep direction is marked with red (blue) dots. The lines are just a guide to the eye. The data were obtained with a current of 500 µA driven in reverse bias. The inset shows the configuration of the non-local setup where the numbering of electrodes is consistent with the one depicted in Fig 3.21

The non-local jumps shown in Fig 3.22 are obtained, when a current of 500μA is driven in reverse bias direction in a spin valve device with Fe electrodes separation distance (2&3) of 2 µm. The double arrows on the jumps indicate the relative magnetic orientation of electrodes 2&3 with respect to each other. When the magnetic field is below -20 mT, both electrodes are oriented in the same direction as indicated by the parallel double arrow. But as the field is ramped up, the magnetic orientation of the 7 µm electrode changes at +18 mT causing a anti-parallel magnetic orientation state with respect to the other electrode. This anti-parallel state causes an imbalance of spin-carriers below the detector electrode

(electrode 2) leading to a jump in the non-local voltage. As the field is further ramped up, the magnetic orientation of the 5 µm electrode changes at 20 mT establishing a parallel magnetic configuration with respect to the other electrode. This magnetization switching of the 5 µm electrode also leads to a jump in the non-local voltage but with an opposite sign. So one magnetic sweep in direction from -100 to +100 mT (forward direction) leads to a two jump of non-local voltage with opposite directions. The magnetic sweep is also performed in the opposite direction (backward) which results in two more jumps in non-local voltage as shown in Fig 3.22.

In addition, a Hanle measurement was also performed on the same device to corroborate the above assignment and to measure the spin diffusion length. In Hanle experiments, an out-of-plane magnetic field is swept across the electrodes that are already magnetized in-plane while simultaneously measuring the non-local voltage. A peak in non local voltage is observed when the out-of-plane magnetic field is at zero. This peak is characteristic of spin dephasing which is effected by the out-of-plane magnetic field due to rotation of spin. The shape of this peak is fitted with equation relating non-local voltage and out of plane magnetic field as discussed in thesis of Dr. Lennart Liefeith.[59] The resultant fit yields three parameters, the spin-relaxation time (τ_s), the spin-diffusion constant (D) and importantly the spin-diffusion length (λ_{diff}) which are used for the calculation of spin-injection efficiency η. For more details on the Hanle measurements the reader is referred to the thesis work of Dr. Lennart Liefeith.[59]

The measured spin-diffusion length (λ_{diff} =3.9 µm) and the non-local jumps (ΔU_{nl}) are used to calculate the spin-injection efficiency (η) by using the equation 2.14. Additionally, the spin-injection efficiencies are also measured as a function of applied bias by measuring non-local signals at different applied bias. The behavior of the calculated spin injection efficiencies after annealing processes is discussed in next section.

3.3.3 Effect of post-growth annealing on spin injection

The fabricated non-local device is subjected to two cycles of post-growth annealing to study the effect of interface on the spin-injection efficiency. As mentioned earlier, the non-local jumps are observed only after annealing the as-prepared spin-valve devices and the reason behind this observation could be due to change in the contact resistance of the Fe/GaAs interface. So we studied the contact resistance of the device separately before and after each step of annealing by using a three-terminal setup. So we obtained three sets of data on the same device as a function of annealing steps (as-prepared, fist annealing and second annealing).

The calculated differential contact resistivity ($R_{c,diff} = \frac{\partial U_{3T}}{\partial I}$) at each step of annealing is shown in Fig 3.23. The inset in Fig 3.23 shows the experimental configuration used for the contact resistance measurement as a function of applied bias. The observed resistivity curves are non-linear which is an expected characteristic of the Schottky barrier formed at the Fe/GaAs interface. The shape of the resistivity curves of all three annealing steps looks almost symmetric with respect to the zero-bias

resistance (ZBR). The change in the symmetry of the resistivity curves corresponds to the change in Schottky barrier depletion width. The obtained ZBR values of all three steps are highlighted in Fig 3.23, and these values are observed to increase at every annealing step. The first annealing step leads to increase in ZBR value by a factor two and the second annealing step leads to a slight but definite increase in the ZBR value. This rise of ZBR was correlated to an improvement of abruptness of the Fe/GaAs interface in previous reports[15,16,21,88] which in turn results in an increase of the Schottky barrier.[21]

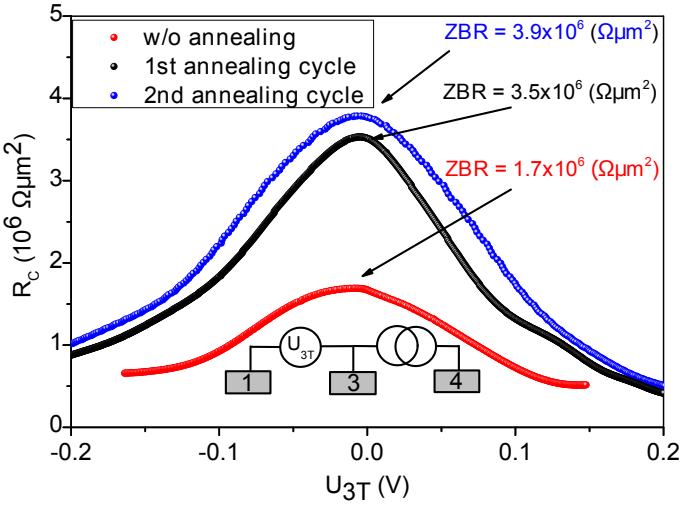

Figure 3.23: The figures bias dependence of differential contact resistivity at three subsequent annealing steps. The inset shows the three-terminal configuration used for measuring the contact resistance.

While a different trend is observed in the behavior of the spin-injection efficiency due to annealing steps. As described before, spin-injection has been not observed at all in the as-prepared device. In addition, the magnitude of non-local jumps (ΔR_{nl}) observed after first cycle of annealing are found to be strongly asymmetric with respect to zero-bias. From the measured jumps, we obtained a maximum value of η=5.5% spin injection efficiency at low reverse bias while a maximal value of 0.9% is observed in forward bias. After the second annealing cycle, the magnitude of the non-local jumps(ΔR_{nl}) decreased reflecting a reduction of spin-injection efficiency. After the second annealing cycle, η is decreased to value of 2.6% in reverse bias direction while, no non-local jumps are observed in forward bias direction. In addition to the observed spin-injection efficiencies, our experimental results revealed two distinct anomalies which cannot be explained from the conventional model of spin-injection mentioned in Sec 2.1. First, the orientation of the non-local voltage jumps ΔU_{nl} is observed to remain always positive irrespective of the applied bias direction. However, this positive orientation of non-local jumps was already observed in few reports regarding spin-injection across Fe/GaAs interface.[55,123] Second, the non-local resistance (ΔR_{nl}) is observed to be asymmetric with respect to zero bias. For more details concerning this behavior, the readers are referred to thesis of Dr.Lennart Liefeith.[59] The change in ΔR_{nl} does not correlate to the change in contact resistance due to annealing cycles. These two anomalies in-

dicate that spin-injection mechanisms are not entirely driven by the 3D bulk electronic states of Fe and GaAs and we propose the existence of spin-polarized interface states (IS) at Fe/GaAs interface. These IS's were first proposed by Demchenko *et.al*[111] to explain the bias dependence of the spin-injection efficiency observed by optical techniques.[124] Interface states were also used in previous studies to explain the observed always positive sign of ΔU_{nl} as calculated by Honda *et.al*.[112]

A lot of information regarding the density of state near the Fe/GaAs interface can be obtained from studying the magnitude of ΔR_{nl} as a function of applied bias. For example, from the values of ΔR_{nl} obtained after first annealing cycle, we observe that the maximum density of interface states are located closely below the Fermi level. Thereby, the position of these states close to Fermi level is crucial as the spin-polarized carriers are detected by the unbiased electrode in the adopted non-local configuration. So even a slight modification of the energetic position of these states could lead to a profound change in the measured spin-injection efficiencies. We believe this change in interface states positions is caused by the structural changes happening at the interface due to annealing which might be driven ba a change in local Fe-GaAs hybridization. For example, the increase of compressive strain and tensile strain in Fe layers and Fe_3GaAs islands, respectively as function of annealing might indirectly influence the position of spin-polarized interface states. However the exact mechanisms leading to this change could not be established during this thesis. But we believe that the structural variations observed at the beginning of this chapter definitely play a important role in behavior of spin-injection as a function of annealing.

3.4 Chapter Summary

Comprehensive structural and spin-transport measurements are performed on MBE deposited Fe/GaAs heterojunctions to study the spin-injection across the interface and to identify the structural state of the Fe layer at the Fe/GaAs interface. First, the crystalline state of the deposited Fe layers as a function of growth temperature is investigated to establish the ideal deposition temperature for obtaining single crystalline Fe layers and sharp Fe/GaAs interfaces. Later, Fe/GaAs spin-valve devices are fabricated to measure spin-injection efficiencies by using an all-electrical non-local configuration. The spin-injection efficiencies and the corresponding structural changes due to post-growth annealing cycles are studied.

The Fe/GaAs samples where Fe grown at 200°C resulted in formation of amorphous Fe layer. Also, the combined analysis of both XRR data and HRXRD reciprocal mapping indicated the formation of tertiary Fe-GaAs interfacial compounds at the interface of these samples. In contrast, the Fe layer deposited at room-temperature resulted in a crystalline Fe layer with sharp interfaces. Therefore, we studied spin-injection exclusively in Fe/GaAs samples where Fe layers were deposited at room temperature.

The spin-injection efficiency measured in non-local configuration showed a strong dependence on the post-growth annealing cycles. The first annealing cycle led to an increase of the spin-injection efficiency (η) from 0% to a maximum value of 5.5% and a second annealing cycle lead to decrease of η to 2%. In addition, we also found that the non-local jumps ΔU_{nl} are always positive irrespective of applied

bias direction between the reference and injector electrode. In addition, the spin-injection efficiency is found to be asymmetric with respect to zero bias. Also, the spin-injection measurements as a function of annealing cycles indicate that the interfaces resistances are not responsible for the observed behavior of η. These observations indicate the presence of spin-polarized interface states (IS) at the interface proposed by Demchenko.[111] These IS's were first introduced to explain the bias dependence of spin-injection and their presence can also explain our observation of an asymmetric behavior of η with respect to zero bias. The presence of these IS's is also used to explain the positive sign of ΔU_{nl} irrespective of the bias direction as indicated by the work of Honda *et al.*[112] So the assumption that IS's are present in our sample system leads to a consistent evaluation of our non-local results. In addition, the assumed position of the IS's derived from the ΔR_{nl} values as function of applied bias are observed to be very close to the Fermi level. Therefore, any small change in the energetic position of these states can hugely influence the spin detection since the detector electrode is unbiased in our non-local configuration. This change could probably result from structural variation due to annealing.

This post-annealing effect is structurally addressed by measuring both the out-of-plane and in-plane Bragg reflexes of the Fe layer by utilizing both lab and synchrotron sources. The diffraction data analysis is also complemented by high resolution XRR data to evaluate the changes in the interface. We obtained consistent data from both synchrotron and laboratory source based measurements which revealed that the Fe films are inherently in-plane compressed and the first cycle of annealing leads to increase in the compressive strain. We noticed that the in-plane d-spacing mismatch between the GaAs unit-cell and corresponding two Fe unit cell is reduced from 0.5% to 0.12% during first cycle of annealing. The observed trend in lattice mismatch implies that the Fe layers at this particular thickness tend to epitaxially almost match with the underlaying GaAs with annealing.

GID measurements performed on the same system also showed the same trend in strain evolution as function of annealing. However, GID measurements also revealed the presence of the Fe_3GaAs phase at the interface in form of islands. The occurrence of these islands is agreeable with the work of Fleet *et al.* which reported presence of intermixed regions[86] in a presumably sharp Fe/GaAs interface. The work of Fleet *et al.* also suggests a decrease in the amount of intermixing region as a function of annealing. In contrast, we observed that Fe_3GaAs islands become more crystalline after annealing but we cannot evaluate the change in amount of intermixing region with the applied technique. We believe that the structural changes observed at the interface might directly or indirectly influences the behavior of spin-injection efficiency. However, we could not establish the direct mechanisms that are responsible for the observed spin-injection behavior as a function of annealing.

4 Experimental Results: Integration of portable AFM at Synchrotron facilities

4.1 Introduction

In the previous section, the intrinsic strain developed in the Fe layers due to various growth and post-growth conditions are studied. But the aim of this thesis also encompasses structural investigation of Metal-Semiconductor epitaxial layers under both intrinsic and extrinsic strain. The spin-valve devices fabricated in the previous section have Fe electrodes of size of a few microns. The strain at these reduced dimensions has to be addressed to establish the effect of fabrication induced external strain on the spin-transport. This aspect of strain behavior at reduced dimensions is one of the neglected aspect of investigation in Fe/GaAs system. Therefore, an *in-situ* technique is developed during this thesis to study the strain at reduced dimensions and also to study the structural changes in Fe layer due to external stress.

As mentioned earlier, the Fe/GaAs heterostructures are fabricated into non-local spin-valve devices which are few microns in dimensions. But generally, as the dimensions of any device is reduced, process-induced strain increases due to accumulation of deformations and defects as a result of extra steps needed to achieve precise alignment of masks.[125] In some scenarios, strain can be used to enhance device properties as evident in widely established strained silicon technology[126,127] where, engineered strain in the active layers is used to enhance carrier mobility. Similarly, understanding the strain state of ferromagnetic layers at reduced dimensions is necessary to establish any strain dependent changes to the transport properties. For this purpose microstructures are fabricated from the Fe/GaAs samples and we intend to study strain of the microstructures by using grazing incidence diffraction. We also aim to resolve the external stress-induced changes in strain state of Fe layers.

For the intended studies, we need a measurement technique which can simultaneously image nanostructures and measure structural changes under the induced stress. This is usually achieved by combining real-space imaging techniques like surface probe microscopy and reciprocal space mapping methods like X-ray diffraction techniques.[128–130] Since the strain revealed by X-ray diffraction methods represents an average value over the illuminated surface area, the strain in sub-micron structures is generally probed by a micron sized beam. These type of investigations involving combination of scanning probe and micro-beam X-ray scattering have previously been performed by few research groups.[131–134] How-

ever, as the dimensions of sample and probing beam approach the micron range, complexity of the surface scanning probe increases demanding a dedicated and custom designed setup on the beamline. We propose and demonstrate integration of a commercially available Atomic Force Microscope (AFM) which involves minimal modification of the AFM setup reducing the need of dedicated setups and allowing easier installation at beamline facilities. In addition the integrated AFM also offers additional features like Scanning Spreading Resistance microscopy (SSRM) allowing to obtain information about the local conductivity of the microstructures under investigation.

4.2 Integration at P10 beamline of PETRA III

A portable and off the selves available AFM supplied by Anfatec Instruments, Germany, is integrated onto two separate micro-beam synchrotron end-stations (P10, PETRA III and ID13, ESRF) to achieve the simultaneous imaging and probing the strain state of microstructures. Our setup design offers a AFM scanning probe operating at ambient conditions in combination with a micro-focused X-ray beam. The AFM installation at beam-lines is similar to any table-top installation procedure which enables quick and easy integration within allocated beam-time at a synchrotron. The initial integration of the setup including standardization and testing is done at P10 coherence beamline of PETRA III synchrotron facility at DESY in collaboration with beamline scientists Dr Michael Sprung and Dr Alexey Zozulya. The measurements at P10 are performed on Fe/MgO/GaAs microstructures ($\approx$4 μm in diameter) and these results are discussed first in this section. Later, nano-indentation measurements are performed on smaller Fe/GaAs microstructures ($\approx$2 μm in diameter) atthe Microfocus Beamline ID13 of ESRF synchrotron facility and the corresponding results are discussed in the section 4.3.

4.2.1 AFM-X-ray scattering geometry

The Anfatec Level AFM is a room-temperature setup operating in all standard AFM techniques like, contact, non-contact and dynamic modes. In addition to the standard AFM scanning modes, our AFM setup is also designed to perform SSRM mode of scanning which is commonly referred as Conductive Atomic Force Microscopy (CAFM). Some features of CAFM mode is also used to assist alignment of the microstructures in the X-ray beam which is discussed in detail in Sec 4.3.2.

Our AFM setup consists of two main parts namely a body and a head as shown in Fig 4.1.(a). The head consists of a small camera used for initial sample alignment and a red laser which is used to observe the deflection of the cantilever during the scan. A standard 4-segment photo-diode is used to observe top-minus-bottom (T-B) and left-minus-right (L-R) signals, which are produced due to horizontal and lateral movements of the tip respectively. The head part is customized by the manufacturer to suit our experimental need where two conical grooves with opening angle of 40° are added as highlighted in the Fig 4.1.(b). These grooves are needed for X-ray experiments as discussed later in the section.

While the entire head rests on three motor driven shafts present on the body part of AFM. These shafts are used for initial approach of the tip to the sample and also for easier removal of the head during sample change. The experimental setup and modifications to the AFM setup are designed by as a part of PIER DIMAP (PIF-2013-14) project.

In our setup, the sample is mounted on a piezo-driven stage in the body part of AFM. These piezo crystals are used to move the sample in all three translation directions (x,y and z) during the topographic scans. In laboratory conditions, the external vibrations are suppressed by hanging the body of AFM on three rubber strips. But this arrangement is not possible on a diffractometer as precise alignment of AFM tip and X-ray beam is essential for the experiment. Therefore the entire AFM is mounted on three adjustable pivots (highlighted in Fig 4.1.(a)) that are fixed to a horizontal diffractometer present in the second hutch of P10 beamline. In addition, thick porous rubber pads are place between the pivots and the AFM body to reduce external vibrations. In recent reports, where AFM's were used in combination with X-rays, the movement of the beam was synchronized with the movement of the tip leading to an complicated setup conditions. Whereas in our setup, the position of tip and beam are kept constant while the sample and the entire AFM are moved independently.

By considering the above setup of the AFM, we have identified two major design requirements that are essential for the task of simultaneous X-ray and AFM measurements of individual microstructures. First, the X-ray beam should be perpendicular to the cantilever to allow free propagation of beam. Second, the beam should probe the microstructure that is directly under the AFM tip. By considering these two requirements, a basic working design of the setup is devised which is shown in Fig 4.2. By examining the design, few geometrical constrains of the setup are identified. It is clearly evident that, at low inclination angles of X-rays, the experiment can be carried out efficiently as the cantilever of the AFM does not impede the X-ray beam. Therefore our AFM setup is perfectly suited for applying grazing incidence geometry such as Grazing Incidence Small angle Scattering (GISAXS) and Grazing Incidence Diffraction (GID) to study the strain of microstructures, while the sample is being probed by the AFM tip.

However, at higher inclination angles the beam will be hindered by both cantilever and the equipment holding the tip-cantilever system. These higher inclination angles are needed to perform the X-ray diffraction measurements in symmetrical geometry ($\omega = 2\theta$) that give information about the out-of-plane Bragg peaks. Therefore to access the symmetrical geometry measurements, conical grooves are machined on the head part of the head (highlighted in Fig 4.1.(b)). However, only about 70° out of sample plain could be used X-ray scattering as the opening angle of the conical groove is 40°. However, the width of cantilever and height of AFM tip must be considered to calculate the accessible incident and exit angles in the direction perpendicular to the cantilever. By assuming a typical cantilever width (w) of $30\,\mu\mathrm{m}$ and tip height (h) of $15\,\mu\mathrm{m}$, the accessible angles are calculated by $Q = \arctan\frac{2h}{w}$. The resulting maximal opening angle available for diffraction experiments is therefore 45°.

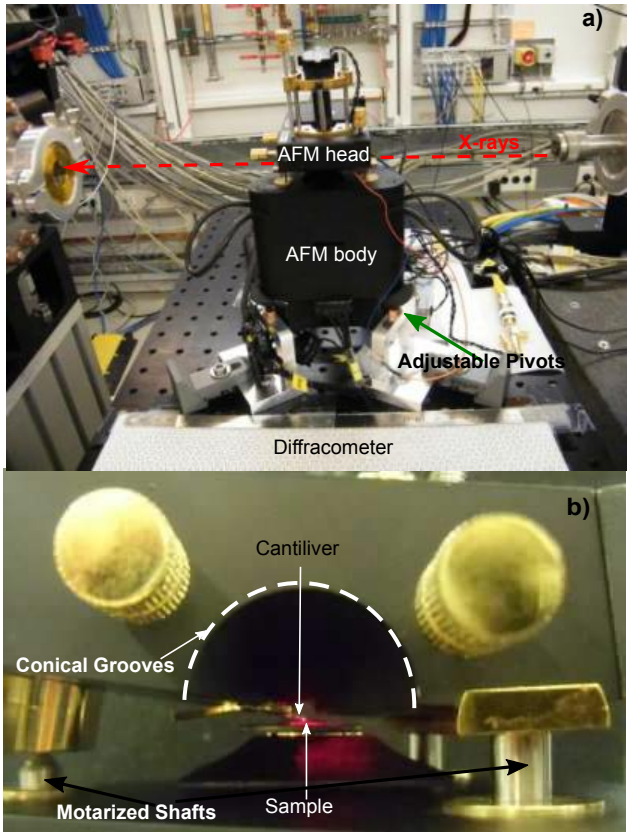

Figure 4.1: (a) Image showing the portable AFM fixed on the diffractometer table P10, PETRA. The red and green arrows highlight the direction of X-rays and adjustable pivots respectively. (b) Side view of the modified head of the Anfatec AFM showing the conical grooves and also highlighting the sample and cantilever. Black arrows indicate the motorized shafts on which the head rests.

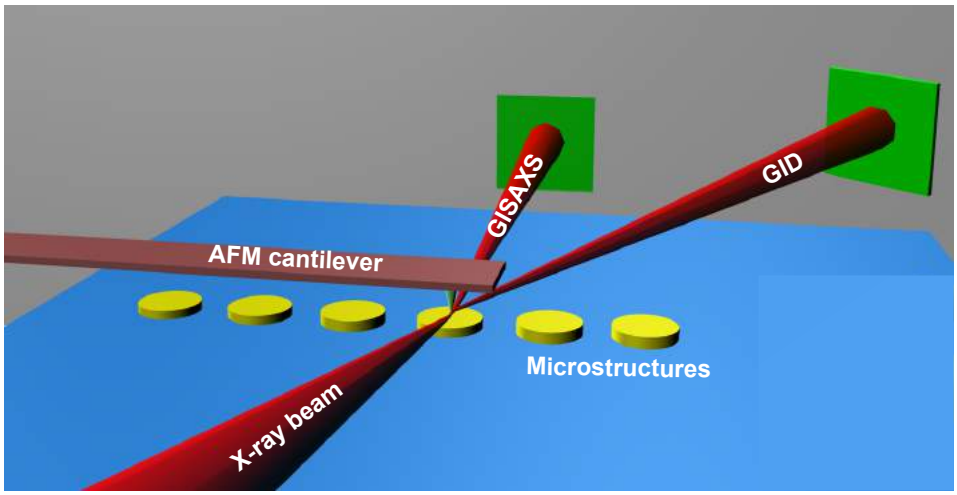

Figure 4.2: Schematic showing the combination of AFM cantilever and X-ray scattering geometries.

4.2.2 Sample design of microstructures

The microstructures that were used for integration testing experiments are fabricated from Fe/MgO/-GaAs heterostructures. The sample layout with nominal layer thicknesses is shown in the upper inset of Fig 4.3.(a). These samples were fabricated by Dr.Boris Landgraf as a part of his doctoral project.[119] The sample layout is same as the design described in Chapter 6 except that the MgO layers are deposited in the presence of an additional oxygen background pressure and are annealed at 250° before deposition of the metal layers. Later the samples are fabricated into microstructures shaped as rings by using standard lithographic techniques and wet-chemical etching. The rings are systematically distributed as rhombus shaped clusters connected by a single line of rings as shown Fig 4.3.(a). The schematic of the mask design used for fabricating rings is shown as lower inset in Fig 4.3.(a). The rhombus shaped clusters are used as visual markers for alignment as they are visible to the naked eye.

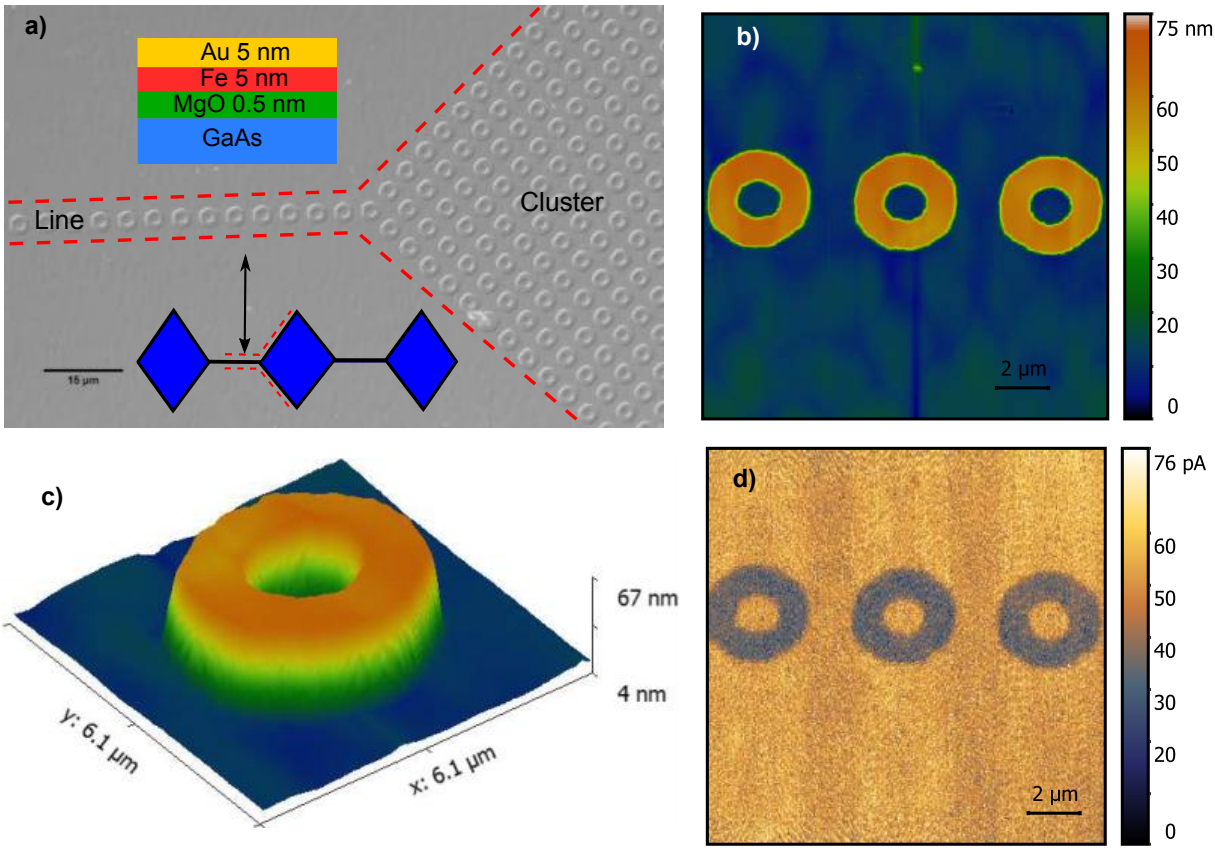

Figure 4.3: (a) Microscopic image showing the Fe/MgO/GaAs ring patterned into a single line and rhombus shaped clusters. The lower inset in blue color is the larger view schematic of the mask used for obtaining the microstructures while the upper inset shows the sample design. (b) AFM topographic image obtained on the microstructures. (c) 3D AFM image showing the height of the ring pattern . (d) SSRM image obtained showing the local conductivity of the microstructures

The individual rings have an inner and an outer radius of 700 nm and 1900 nm respectively. The height of the rings is observed to be around 52 nm and this height and diameter are estimated from the topography images measured after the AFM is installed in the diffractometer. At this height, the surface of ring is the Au layer while the bare surface of the sample is the doped region of GaAs. The obtained $16 \times 16 \mu m^2$ topography scan and 3-dimensional image of individual ring are shown in Fig 4.3.(a)& (b) respectively.

The AFM scans are performed by using a conductive AFM tip in contact mode to enable simultaneous measurement of topography and SSRM images. For this purpose, an electrical contact is established between the bare surface and the AFM tip and the obtained SSRM image is shown in Fig 4.3.(d). The data shown in Fig 4.3.(d) represents a processed image, where a parasitic frequency of 50 Hz is subtracted from data to remove the noise. The obtained SSRM image is a representation of resistance measured by AFM tip at every point of contact with the sample. In another words, it is an image showing lateral distribution of sample conductivity. We observed a homogeneous conductivity on the bare surface which is expected as it a highly doped semiconductor. This homogeneous distribution of conductivity is due to constant current flowing between the tip and sample. In contrast, the rings shows lower conductivity when compared to the bare GaAs surface due to higher resistivity of MgO barrier leading to domination of total resistance by the tunneling barrier. The tunnel barrier reduces the current flowing in the tip-sample system leading to the observed contrast in the SSRM image.

Both topography and SSRM images obtained when the AFM was mounted in the diffractometer resemble the images when the AFM is suspended on the vibration stabilizing elastic bands. This similarity of the AFM images validates the vibrational stability of the integrated AFM setup. Moreover, we did not observe any significant jumps in the T-B signal when the entire AFM is translated during reciprocal space map measurements which are discussed later. In essence, the vibrational stability of the AFM is not compromised by integrating it in the diffractometer.

4.2.3 Alignment of microstructures

A major bottleneck in studying microstructures simultaneously with micro X-ray beam and scanning probe microscopy is the alignment of both components with respect to each other. In addition, these two probing components should be aligned on the microstructure of interest. Previous works have used various strategies like scanning mirrors[135] and moving AFM tip[136] to align all three components of tip-beam-microstructures system. Whereas our alignment strategy is based on translating the entire AFM setup with respect to the fixed X-ray beam. The alignment of the micro-beam and the microstructures in our setup is achieved by following a series of carefully executed steps described below.

For the purpose of alignment, the AFM head is dismounted and the sample is placed on the AFM body. Later, the sample is aligned to a specific GID Bragg angle that is chosen for further investigations and this step is schematically depicted in Fig 4.4.a). After this step, the sample surface is brought parallel to

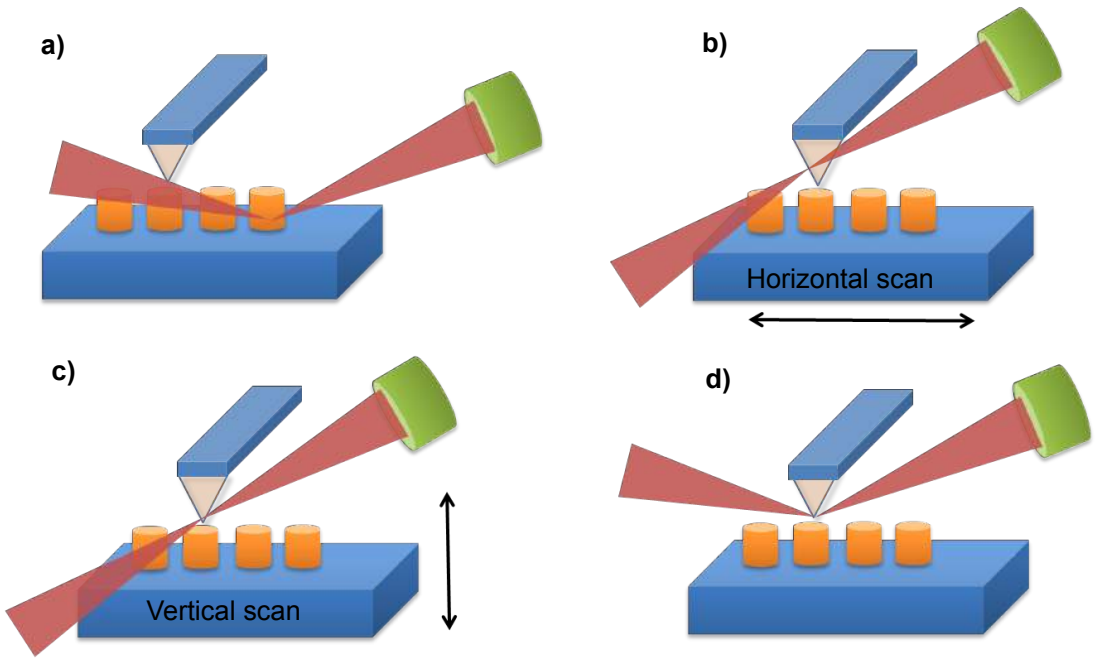

Figure 4.4: (a-d) Sequential alignment steps adopted in P10 coherent beamline for aligning microstructures, tip and beam with respect to each other.

the beam propagation direction and the AFM head is mounted back on the AFM body. In the next step, the tip is approached to the sample and the entire AFM setup is scanned in horizontal direction with respect to stationary X-ray beam. This step is performed to ensure that the X-ray beam illuminates the AFM tip. When the beam hits the AFM tip, an increase in small angle scattering signal is observed due to interaction of the beam with the tip. This step is shown in Fig 4.4.b). In the next step, the beam must be aligned to the tip apex so that the beam probes the microstructure which is directly under the tip. The apex of the tip is found by vertically translating the AFM and fixing its position where the horizon of the sample is observed in the 2D-detector. The steps b & c involving horizontal and vertical translations of AFM ensures that the beam is at apex of the tip so that the beam probes the structures under the tip. After steps b & c, the diffractometer position are noted down to ensure the constant relative position between the beam and AFM tip. Later, the tip is moved to the microstructure of interest and this movement is compensated by moving the entire AFM in opposite direction to maintain the alignment between the AFM tip and X-ray beam. Finally, the AFM is moved to the previously aligned diffractions conditions to obtain high resolution GID data of individual microstructures.

4.2.4 GID measurements on the microstructures

After the alignment procedure, individual microstructures are studied using Grazing Incidence Diffraction geometry at a photon energy of 13 KeV. The X-ray beam is focused by using a set of parabolic refractive lenses consisting of a total of 8 lenses with curvature of radius of $50\,\mu\mathrm{m}$. The size of the

beam at the center of the diffractometer is measured to be 1.5 $\times$ 3 μm^2 (vertical $\times$ horizontal). The 2-theta arm in the horizontal diffractometer hutch of P10 can be rotated up to 30° in horizontal plane. A 2D Pilatus detector is mounted on the 2-theta arm at a distance of 5 m from the rotation center of the horizontal diffractometer. The GID reciprocal space maps (RSM's) are obtained around (220) reflex of GaAs at a Bragg angle of 13.8° .

It is worth noting that, in our experimental configuration, the X-ray beam propagation is perpendicular to the line of rings as shown in Fig 4.3.(a). So by considering the size of the rings and beam and also the orientation of the X-ray beam, we can address individual rings. A GID reciprocal space map obtained on an individual ring is shown in Fig 4.5.(b). The shown GID map is obtained on the left most ring of AFM image shown in Fig 4.3.(b).

We obtained another RSM (shown in Fig 4.5.(a) when the tip and center of the beam is moved to the bare surface between the rings. A clear contrast is observed between the two RSM obtained at different positions of the sample. A circular cloud of diffuse intensity is observed in the RSM obtained on the ring microstructure and this circular cloud is highlighted by black dashed circle. However this cloud of diffuse intensity is observed to depend on the exit angle. Similar dependence of the diffusive scattering as a function of exit angle is observed in InAs quantum dots on GaAs system[137] and it is reported to be caused by the stress fields of InAs dots. So we associate the diffuse cloud in our system to the strain field induced by both MgO and metal layers present in the ring structure. On contrary, the diffusive cloud intensity is not observed around (220) reflex of GaAs when the beam is used to probe the bare surface where the MgO and metal layers are etched away. This observation validates our inference that the MgO and metals layers are responsible for the presence of the diffuse cloud in RSM recorded on micro rings.

We did not observe a characteristic Fe peak close to the GaAs (220) peak, which is clearly seen in Fe/GaAs samples as discussed in Sec 3.2.3. This non-existence of Fe diffraction peak indicates the Fe layer deposited on MgO is not crystalline. This feature of non-existence of Fe Bragg peak is observed in MgO containing samples and is discussed in detail in chapter 6.

4.3 Integration at Microfocus beamline, ID13,ESRF

As mentioned earlier in this section, The aim of integrating an AFM onto a beamline facility is to serve two purposes. First, to study the effect of accumulated strain at reduced dimensions of the heterojunction. Second, to study the effect of externally induced stress on the strain state of Fe layers. Unfortunately, the study of strain evolution under external pressure could not be performed in the limited time of beamtime at P10, PETRA III facility. Moreover, for these measurements, the size of the fabricated rings would have been too big to induce any detectable changes in the strain. Therefore new microstructures with reduced dimensions are prepared for the beamtime at ID13, ESRF facility.

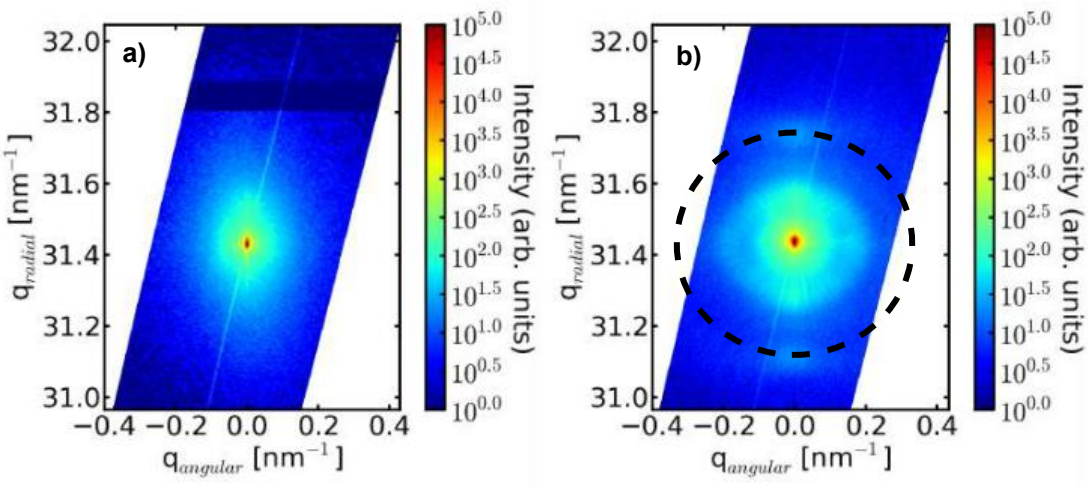

Figure 4.5: GID RSM around (220) GaAs Bragg peak (a) obtained on bare surface in between two ring structures (b) Obtained on a individual ring showing diffuse intensity highlighted by the black dashed circle.

4.3.1 Specifications of beamline and samples

The same portable Anfatec AFM setup used at P10, PETRA III facility is integrated at the Microfocus Beamline (ID13, ESRF). The optics of the ID13 beamline is specifically designed to achieve X-ray beam in sub-micron dimensions. A simplistic layout of the AFM and beamline optics of ID13 is schematically shown in Fig 4.6. We used a micron sized X-ray beam of 14.33 keV for these investigations. The beam is pre-focused by Compound Refractive Lenses (CRL) which are positioned upstream to the channel-cut monochromator(CCM). The beam is then focused on the sample using a gold Fresnel zone plate (FZP) with the diameter of 200 μm and the outer zone width of 70 nm in combination with a order sorting aperture (OSA). The FZP focal distance is 160 mm, which provided source demagnification factor of 612. The entrance aperture of the FZP optics is set to 200×200 μm^2. The undulator (U) to sample distance is 98 m and the beam size at the sample position is 1(horizontal)$\times$0.7(vertical) μm^2 with beam flux of 3.5×10^{10} photons/second.

We used a Frelon detector at 780 mm distance from the sample for alignment of the direct beam, and a EIGER 4M detector at 1850 mm distance for GID measurements. The exposure during the measurements is controlled by using a fast shutter. The AFM is integrated on a high precision hexapod and the detectors are mounted on a separate arm that moves horizontally. The major modification of the setup at ID13 as compared to the PETRA III integration experiments is the application of a photocurrent signal for the alignment and the use of the AFM tip as an indenter for applying stress to the microstructures. These aspects are discussed in detail in the next few sections.

As mentioned earlier we require smaller microstructures to induce considerable pressure by the AFM tip, therefore, new masks are designed to fabricate microstructures that are smaller than the size of the X-

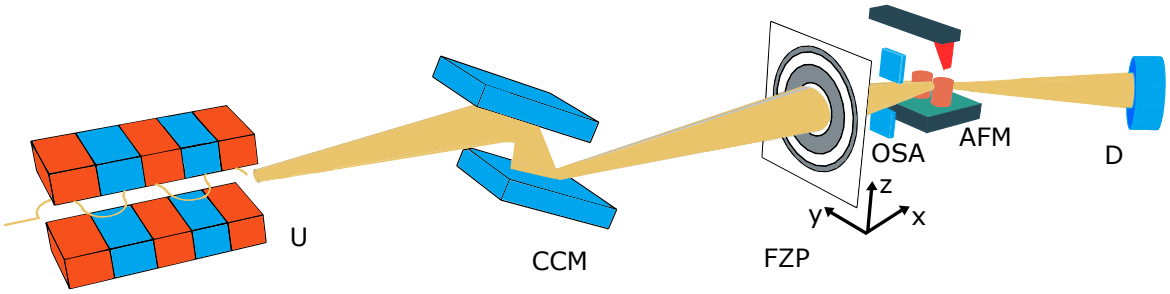

Figure 4.6: Schematic presentation of main components of ID13, ESRF beamline and experimental setup. U: undulator, CCM: channel cut monochromator, FZP: Fresnel zone plate, OSA: order sorting aperture, D: detector.

ray beam. For these studies, a Fe/GaAs sample named C21N587 is used to fabricate the microstructures. The sample is also used for GID measurements on uniform films and is described in detail in Sec 3.2.3. The sample contains 4 nm of Fe layer capped with 3.5 nm of Au layer. The Fe/GaAs films are patterned into cylindrically shaped microstructures with step height of 40 nm by standard e-beam lithography and wet chemical etching. The diameter of the microstructures is 2 μm and the edge-to-edge separation is 3 μm as shown in Fig 4.7.(a). The figure represents only a part of the fabricated structure. The entire structures is shown in the inset of Fig 4.7.(a). A line of 10 single dots is enclosed between large structures serving as markers for optical alignment of the AFM tip as shown in in Fig 4.7.(a). This patterned sample containing the microstructures will be referred in further text as the structured sample.

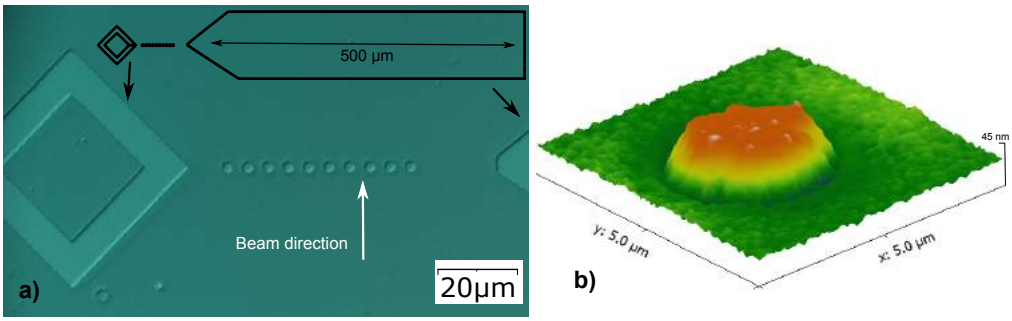

Figure 4.7: (a) Optical microscopy image showing part of structured sample. Inset: Schematic of the full mask used for developing structured sample. The long pointed structure is a marker used for optical positioning. (b) 3D AFM topographic image of an individual microstructure

4.3.2 Alignment using photocurrents

The process of alignment of microstructures and tip adopted at P10 beamline and described in Sec 4.2.3 is a time consuming process as it involves several iterative steps of AFM translations. This problem of alignment is solved in several ways by other research group by implementing various strategies. One

solution that is widely used is to increase the probability of finding any microstructures in the beam by studying self organized and homogeneously dispersed structures.[128] Another possibility demonstrated in some studies is to use a variety of techniques like X-ray-fluorescence[129] and photo-current imaging[136] as alignment tools for finding the nanostructures on the sample. Alignment in such a way requires dedicated setups, in addition to the scanning probe apparatus already used for imaging which in turns leads to complexity of the setup. Here we demonstrate that the Conductive Force Atomic Microscopy (CAFM) mode available in our AFM setup can be employed as a alignment tool.

In the CAFM mode, a small DC bias is applied between the conductive tip and the sample as shown in Fig 4.8. Photoelectrons are generated when the high-energy X-ray beam interacts with the sample. These electrons are driven towards the conductive tip by electric field present due to the applied bias. The resultant photocurrent signal is maximal when the illuminated spot is closest to the tip, and this signal is used as a tool for alignment.

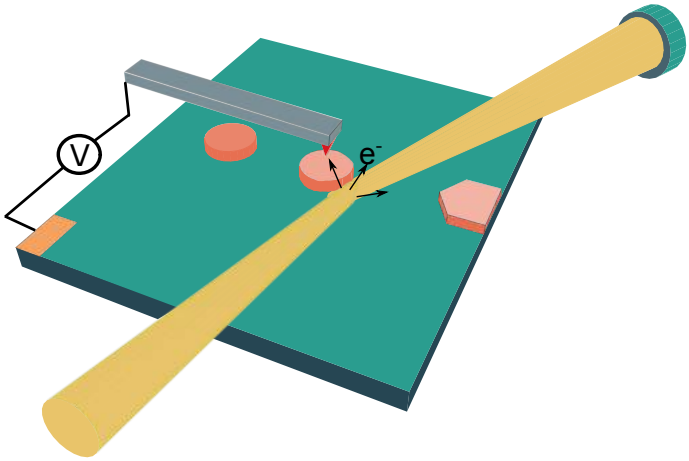

Figure 4.8: Schematic showing CAFM components of the AFM setup on the X-ray diffractometer along with an illustration of the microstructures on the sample and the X-ray beam geometry.

Some of the previous reports have adapted a similar approach where the tip is moved across the beam and a lock-in technique is utilized to find the precise position of tip with respect to sample and beam. The photocurrent signal is detected at the operating frequency of a dedicated beam chopper installed upstream to the sample.[138] In contrast, in our setup the entire AFM is moved across the beam and the fast shutter present upstream provides a modulation of the photocurrent signal. This opening and closing of fast shutter is coincidentally advantageous as it prevent the saturation of pre-amplifier in the CAFM setup. We did not apply a dedicated pre-amplifier as it would require a additional integration with the beamline operational software.

For the sake of alignment, a GID reciprocal space map around the 220 reflex of GaAs is measured on an uniform (un-structured) sample beforehand as shown in Fig 4.9. This measurement is performed to

adjust the grazing incidence angle and align the AFM in Bragg position for further GID measurements on structured samples. The GID RSM obtained is similar to one shown and described in Fig 3.15 of section 3.2.3, because the same sample was used for both experiments. After the entire setup is aligned to the desired Bragg position, the unstructured sample is replaced with the structured sample and the following iterative steps are performed to align tip, sample and X-ray beam with respect to each other.

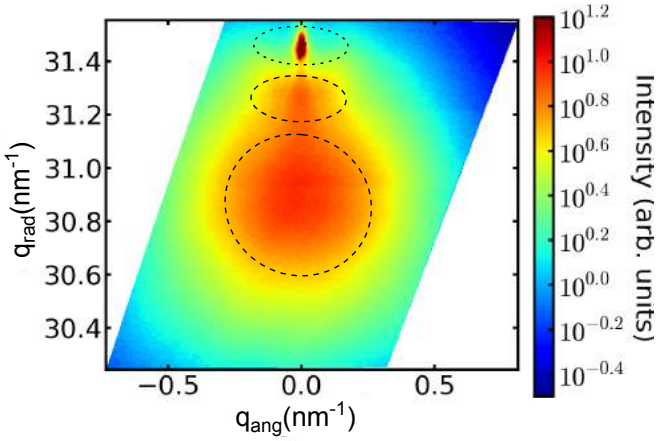

Figure 4.9: GID reciprocal space map obtained on unstructured Fe/GaAs sample. The indexed peaks are highlighted by black circles and intensity values are represented in logarithmic scale.

First, the AFM tip is roughly positioned close to the structures by using optical markers and an AFM topography scan is performed later to find the microstructures precisely. Then the AFM tip is moved to the center of an individual microstructure and the position with respect to the tip and the sample is fixed. In the next step, the entire AFM is scanned transversely to the beam in y and z-directions. The alignment of the beam to the tip is controlled by the photocurrent yield as shown in Fig 4.10. In vertical direction the AFM is placed at a position marked in Fig 4.10.(a). Above or below this position, the beam does not hit the horizon of the sample. Afterwards, a horizontal translation scan perpendicular to the beam propagation direction is performed to align the tip in the beam. A photocurrent scan along y-direction is shown in Fig 4.10.(b). The AFM is positioned at the maximum yield of photocurrent signal. The steps shown in the inset of Fig 4.10.(b) are due to the fast shutter which acts to prevent over exposure of 2D detector. After the photo-current scans, the microstructures should be aligned to the Bragg condition. Therefore, a GID scan is performed and presence of diffraction signal from Fe layer validates alignment of the beam, tip and structures at the same position. These steps are repeated iteratively to fine align all three components of the experiment.

4.3.3 Effect of indentation on Fe Interface

In our AFM setup, the sample is mounted on a piezo stage controlled by a feedback mechanism. This stage is moved in x, y and z-direction to perform topography scans. Once the tip is placed on microstruc-

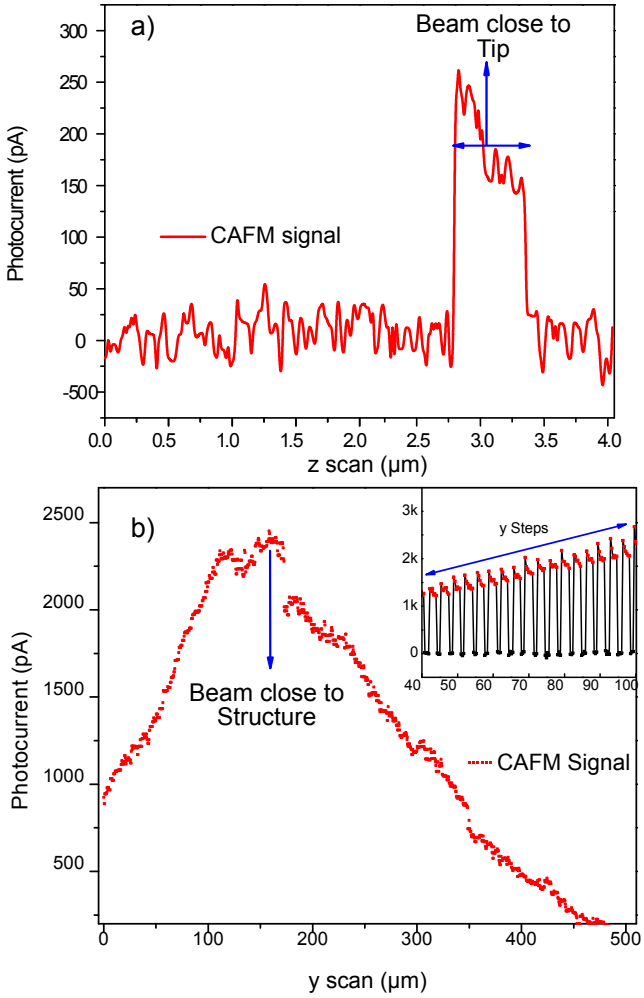

Figure 4.10: (a) CAFM signal in z-direction and (b) CAFM signal in y- direction (The dots represent maximum of CAFM signal at each step of translation). Inset: Continuous CAFM signal in y direction.

ture of interest, this stage is exclusively moved in z-direction to apply pressure on the microstructure. After alignment procedure, a so called normal force versus distance curve is obtained to calculate the force applied with respect to the cantilever deflection (T-B). The T-B signal is the movement of laser spot in the detector due to a certain translation of piezo in z-direction. The force applied on the microstructure is calculated using the equation 4.1, where, k is spring constant of the tip (2.7 N/m) as specified by the tip manufacturer (BRUKER), while the sensitivity is the slope obtained from force versus distance curve and reference value is the T-B value used for applying pressure. The equation 4.1 is used for force calculation because the entire displacement of piezo stage is not converted to applied force due to the bending of cantilever. Later external stress is applied in intervals by increasing the set-point of top-bottom (T-B) signal to a total cantilever displacement of 400 nm from initial contact of tip and sample. At every step, the entire AFM is translated by same magnitude of displacement in opposite direction (-z) to keep the beam at the same part of the AFM tip.

$$Force = \frac{k}{Sensitivity} \times reference\_value(T - B) \tag{4.1}$$

An initial displacement of 100 nm equivalent to the force of $\approx 269\ nN$ is applied first and increased in steps to 1.08 μN for the final displacement. Henceforth, we refer to the steps of displacement as loading steps. Simultaneously, GID reciprocal space maps are collected after every loading step. The GID technique is specifically suited in our investigation since it is sensitive to the layers close to the surface of the sample. The GID maps recorded with AFM tip in equilibrium (no load), the first displacement (first load) and final displacement (final load) are compared in detail to understand the changes in the Fe layer. The T-B signal of AFM is regularly monitored during the rocking scans to ensure the stability of the AFM.[139]

Indentation induced effects are investigated by studying the change in the Bragg peak features in the RSM at every displacement step. Typically two additional diffraction peaks are observed in reciprocal space maps measured in the vicinity of GaAs (220) reflection. They are indexed to Fe(110) and Fe_3GaAs (110) peaks was highlighted in Fig 4.9. Fe_3GaAs is reported to be a thermodynamically stable compound existing as pseudocubic unit cell on GaAs substrates.[92,113] The detailed analysis of these peak positions and features are discussed in Sec 3.2.3; nevertheless, the most relevant results are summarized here. The diffraction peak of Fe_3GaAs is broad since the Fe_3GaAs is distributed as isolated islands at the interface. The existence of the islands is inferred by a combination of XRR and GID analysis.

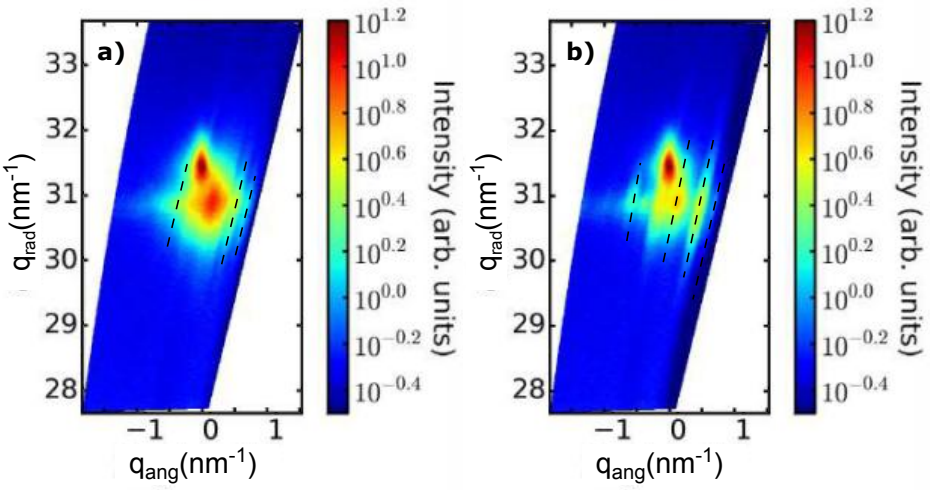

Figure 4.11: a) GID maps of structured Fe/GaAs sample with no load and b) with maximum load.

To illustrate the change in diffraction peak features due to indentation, GID maps obtained on the structured sample under no load and final load conditions are shown in Fig 4.11.a) and 4.11.b) respectively. The intensity of Bragg peaks appears as separate streaks as highlighted by dashed lines in

both Fig 4.11.(a) & (b). These intensity streaks named as intensity fringes might occur be due to the attenuation of the incident or exit beams with surface bound dust particles on the sample. Another noticeable difference that was observed is the intensity distribution around Bragg peaks between the RSMs obtained on the unstructured (Fig 4.9) and structured sample(Fig 4.11.(a). This is due to the lower scattering volume of Fe layer available in the latter. The rest of the signal seems to be identical. GID maps corresponding to all loads are shown in Appendix 8.

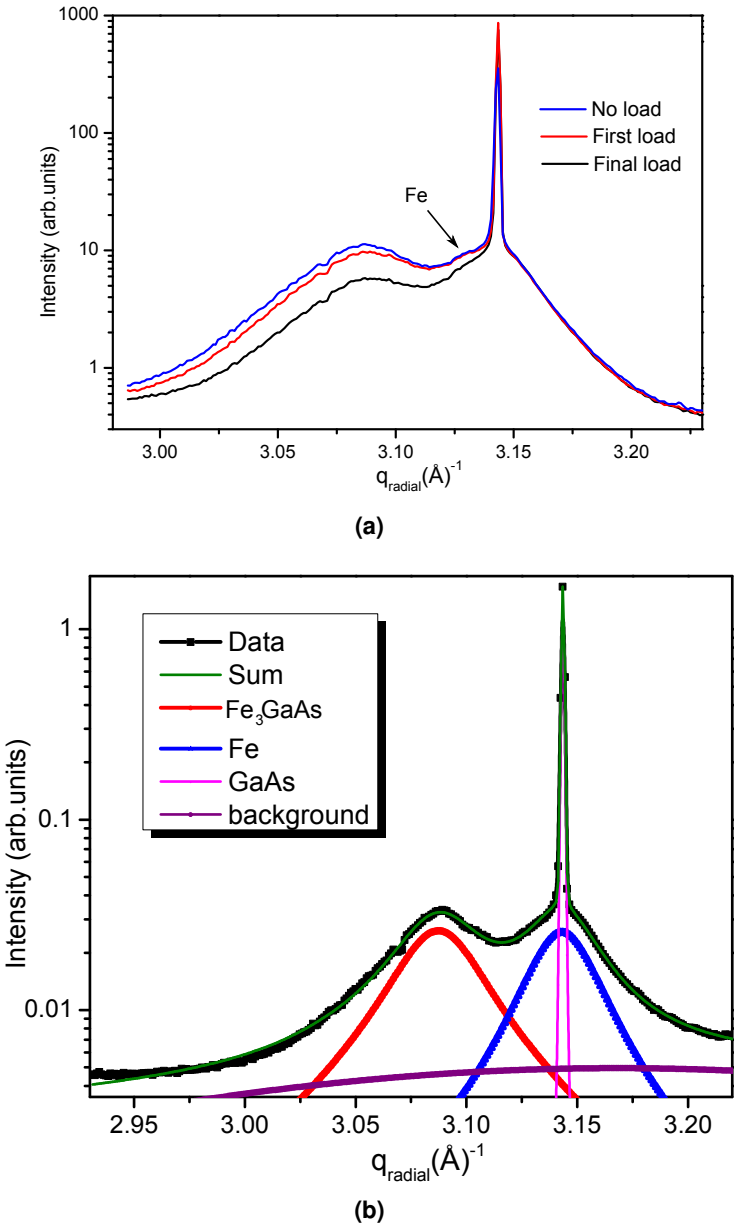

Figure 4.12: a) Comparison of lines profiles obtained from RSM measured at different loading steps. Fitting showing individual fits performed on line profile obtained from RSM measured at no loading step

However, to draw comparisons between all loading steps, line profiles are obtained from GID RSMs. The GID maps are integrated in q_{ang} direction to obtain line profiles along q_{rad} direction which are then used to reveal the inter-plane lattice spacing (d). The line profiles are obtained by choosing a small region (range) in RSM to integrate intensity along q_{ang}. This range is chosen so that the fringe features do not affect the obtained line profiles. Fig 4.12(a) shows three line profiles which correspond to GID maps measured with no load, first and final load. The obtained line profiles are fitted with pseudo-Voight functions, and an example of fitting is shown in Fig 4.12(b). The resultant magnitudes of $\vec{q}$ vectors are used to calculate the inter-planar lattice spacing (d) using the Eq 3.1.

The calculated d-values along with uncertainties for Fe_3GaAs, Fe and GaAs at different loads are plotted in Fig 4.13. The inter-planar lattice constant of the Fe layer with no applied load indicates that the Fe layer is compressively strained and this observation agrees with our previous report[140] and the observations discussed in Sec 3.2.3. As the load is systematically increased the Fe inter-planar spacing decreases further with a total change of 0.1%. The in-plane lattice constant of Fe_3GaAs also decreases with increasing load. The bulk d-spacing values of GaAs (220) and Fe (110) reflexes are 1.9975 Å and 2.026 57 Å respectively. As evident from Fig 4.13, the d-spacings values of Fe and GaAs are very close to each other and Fe d-spacing is observed to reach towards the value of GaAs at maximum load. The bulk GaAs d-spacing is shown in Fig 4.13 as green dashed line for comparison with respect to the measured value which remains constant as expected.

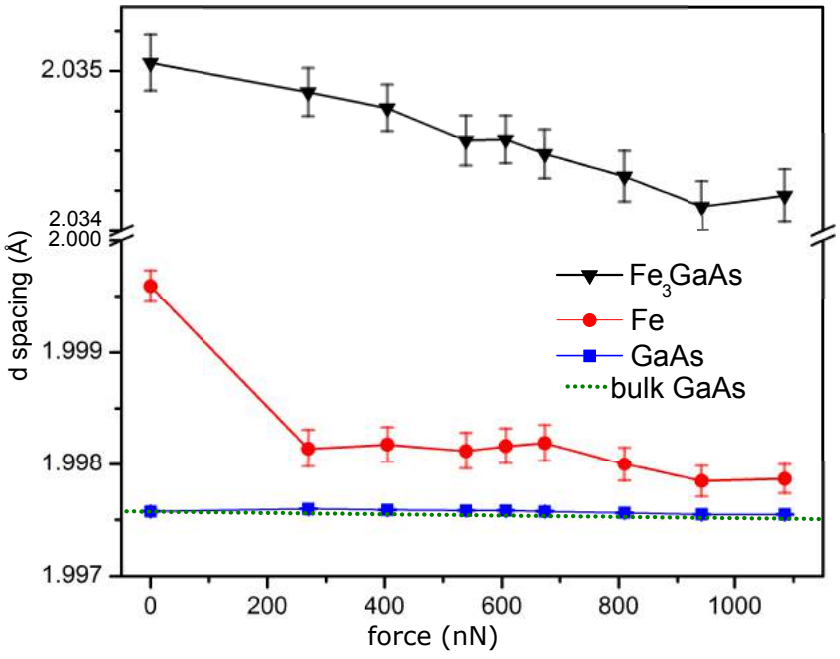

Figure 4.13: Measured in-plane lattice spacing as a function of force applied by AFM tip. lines connecting data points are only guide to eye and the green dashed line represents the bulk inter-planar spacing of GaAs (220) lattice planes.

From Fig 4.13 it is evident that the initial load induces a major change in the in-plane lattice constant of Fe when compared to subsequent loading steps. This behavior could be explained by considering both the dimension of our tip and contact mechanics of the tip and interacting surface. We have used a sharp diamond coated tip with the radius of 40-150 nm which is far smaller than the dimensions of the investigated structures. Therefore a sharp indentation is created on the surface in contact which in our case is the Au layer. So we speculate that the larger initial change of lattice constant of Fe layer is caused by this sharp indentation resulting in a small local deformation in the Fe film during the first loading. In this case, the contact mechanism can be generally described by Sneddon model[141] where the contact is assumed as infinitely hard cone on a elastic flat surface.

Similar reports on indentation in combination with X-ray scattering are performed using a micron sized blunt tip where the radius of the tip is close to the dimension of indented structures.[128,136] These blunt tips are also used to facilitate homogeneous strain distribution on indented structures. Blunt tips also lead to smaller indentation depths which results in a gradual change of inter-planar lattice spacing of the layer under investigation. Contact mechanics of these type of systems involving blunt tips are generally modeled by the Hertz model.[142]

Unfortunately, the resultant indentation depth in our system could not be measured due to beam induced depositions observed on the investigated structures which will be discussed later in the text. However, an indentation depth of 8 nm is measured separately by performing similar loading process on a different microstructure in the absence of an X-ray beam. The observed 8 nm deep indention implies that the tip has displaced the entire Fe layer at the position of the tip. However, the lateral size of indentation is far less than the dimensions of investigated micro-structures. Therefore most of Fe layer in microstructure remains intact.

We applied a Finite Element method (FEM) to describe the effect of indentation depth on the resultant applied pressure and the subsequent impact on the diffraction signal. To mimic the action of the AFM tip on the metal, a lateral strain of 0.01 was applied locally at the center to an indent depth of 8 nm. The value of the lateral strain is chosen arbitrarily and reflects the magnitude of the indent. The resultant strain profile from assumed lateral strain extends symmetrically from the AFM tip as shown in Fig 4.14. In the limit of plastic deformation, any additional applied force will modify the magnitude of the signal but the shape of the strain profile will remain the same. Fig 4.14 shows a distribution of the simulated lateral strain at two regions of interest in the indented microstructure. The AFM tip is localized at the center. The blue dashed line shows the strain distribution on the top of the Fe layer (4 nm below the surface) and the green continuous line corresponds to the interface between the Fe layer and GaAs substrate (8 nm below the surface). From the Fig 4.14 it is clear that the strain decays exponentially from the center at both interfaces.

Since the dimensions of the X-ray beam is close to 1 μm, the measured diffraction signal is an average of cumulative changes in the entire microstructure. Therefore, most of the signal originates from areas with small displacement of the Fe layer. To simulate the shape of the diffraction signal we have

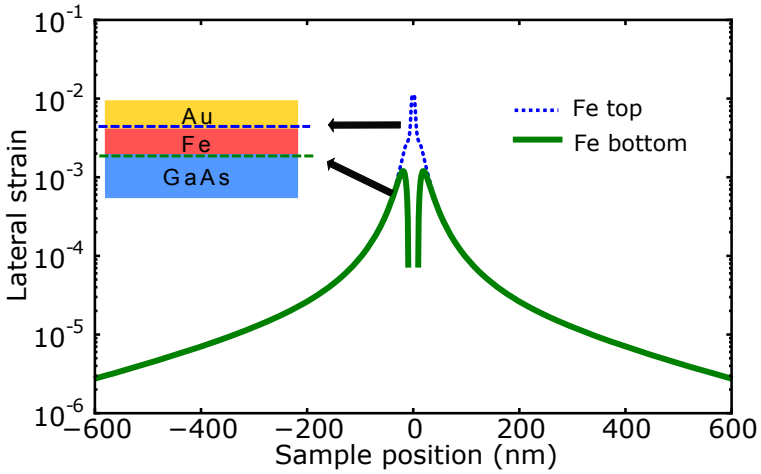

Figure 4.14: Distribution of lateral strain at two Fe depths indicated by dashed lines in the inset. Exponential decrease of strain profile corresponds to the straight lines in the figure. Inset: The sample layout showing both Fe interfaces.

integrated strain contributions along the microstructure. While the nontrivial contributions from regions underneath and in close proximity of the AFM tip are not taken into account. The integrated signal is then fitted with Gaussian function and the shifts in the position of the fit are compared to the shifts observed in the experiment. We observe that the broadening of the simulated signal is important to properly describe the shift. Therefore, we have used experimental FWHM of the Fe layer diffraction obtained at no loading condition for the Gaussian fit used for calculating the shift.

Afterwards, we compared the shift of the diffraction signal for maximum load with the results of our simulations. We found that the strain at the tip is 7300 times bigger than the simulated value obtained using FEM. This implies that the width of the indent at maximum load is about 37 nm which is compatible to specifications of our diamond tips and also to the indent width measured in the experiment without beam. These FEM simulations are performed in collaboration with Dr. Taras Slobodskyy.

4.3.4 Local deposition on microstructures

After the indentation study, we performed another topographic scan on the investigated microstructures to measure the depth of the indent. Surprisingly, deposits of unknown origin are observed on those microstructures which were used for the indentation experiments with simultaneous X-ray exposure(as seen in Fig 4.15.(a). These deposits are not observed before indentation as evident from Fig 4.7.(b). This indicates that the deposits are formed due to prolonged exposure of structures to an intense X-ray beam during the indentation. The CAFM scan performed on the microstructure revealed that the observed deposits are made of an insulating material Fig 4.15.(b). The uniform conductivity observed prior to indentation vanishes in regions of deposition. Another noticeable feature is that the deposits are

located at regions where the AFM tip has interacted with sample. This localized feature indicates that the AFM tip might be involved in assisting the formation of deposits.

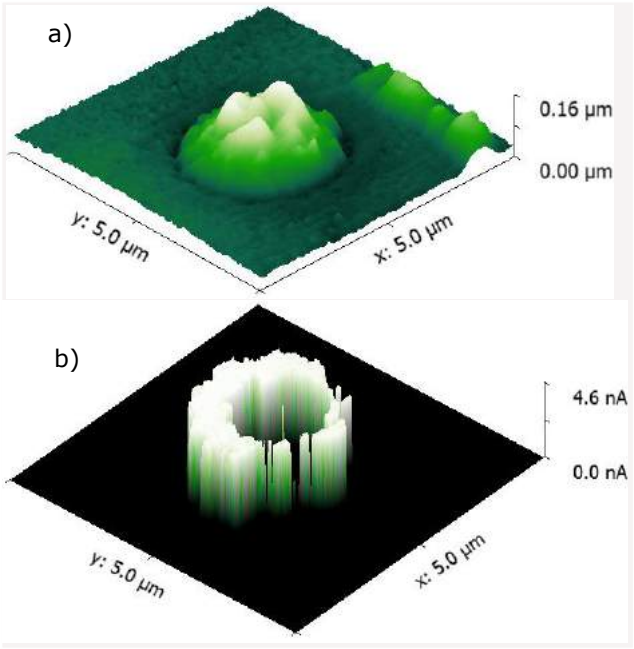

Figure 4.15: (a) AFM topographic image after indentation. (b) Simultaneous CAFM obtained on the indented structure.

A scanning electron microscopic image is obtained after the beamtime experiments to characterize the deposited structures and the state of the tip used for indentation. The SEM image reveals dark features at the same region where deposits were observed by AFM as seen in Fig 4.16.a). The SEM image of the tip revealed that the most of the tip is intact, but the apex has amorphous features as seen in Fig 4.16.b). These features might have also formed due to interaction of an ionizing beam with the tip.

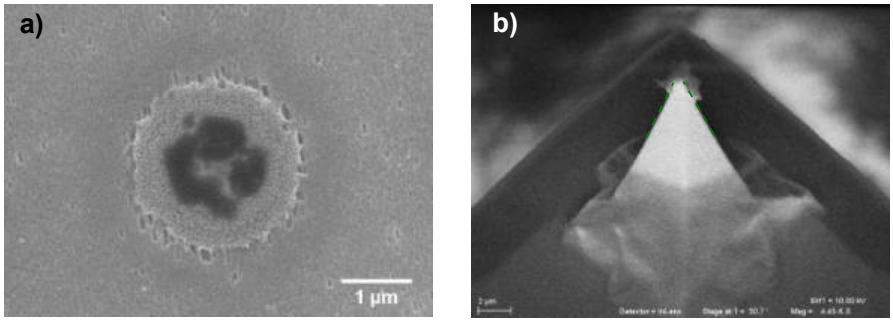

Figure 4.16: a) SEM image obtained on the indented microstructure showing local deposits. b) SEM image obtained on tip after indentation.

To understand the chemical nature of these deposits, we have performed energy dispersive X-ray spectroscopy (EDX) on the microstructures. A line scan along the white dashed line shown on the structures

in Fig 4.17.(b) is performed. During the line scan, the k-shells of carbon and oxygen, the M shell of Au and the L shell of Fe elements are monitored. The line scan is performed at a step size of 2.5 μm. As expected, we were able to observe clear Fe and Au signals from the microstructures. moreover, the EDX signal of C and O elements has distinctly increased on the indented structures as shown in Fig 4.17.a. We also observe a dark streak in between microstructures which might have formed during the alignment of the structures. We tentatively conclude that these deposits are a result of beam interaction with ambient air and the sample. Similar depositions are observed when photo-electrons are generated from metal surfaces by highly ionizing beam.[143] Recently, Vitorino *et al*[144] have reported formation about micrometric holes in the organic samples during a similar experiment involving scanning probe and simultaneous X-ray exposure. Holes might have formed because they have used higher energy beam (19 KeV) and also because organic samples are more susceptible to thermal absorption of X-ray beams. This deposition could also result from a cumulative effect of ionizing beam and photo-current emission.

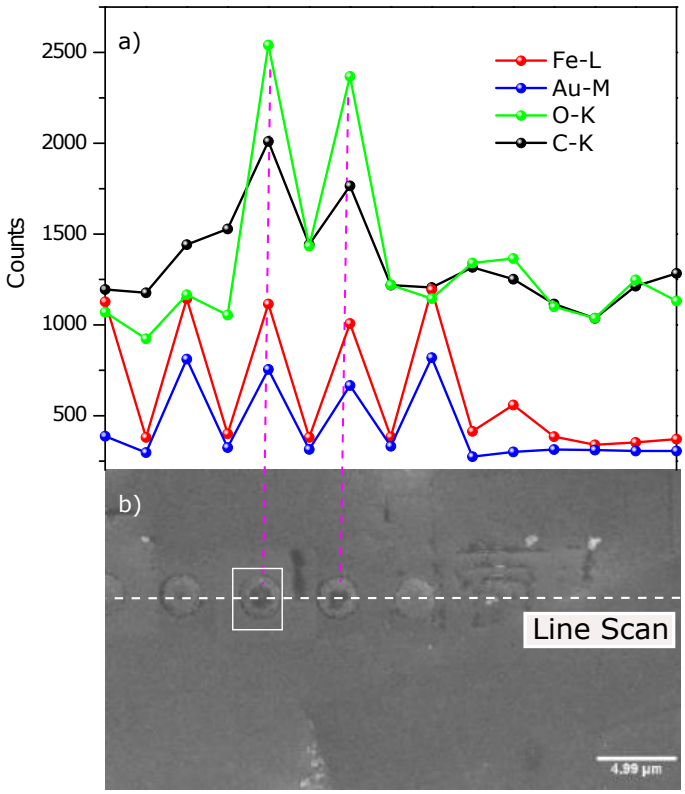

Figure 4.17: (a) EDS elemental line scans along the structures obtained after beam time. (b) SEM image. The dashed white line in the SEM figure shows the line along which the line scan is performed. The white rectangle box highlights the indented structure shown in Fig 4.16.

4.4 Chapter Summary

An *in-situ* technique is developed to study the effect of external stress on the strain state of Fe layers in Fe/GaAs system. The purpose of this technique is to integrate a scanning probe method like AFM on micro-beamline facilities to enable simultaneous access to the real and reciprocal space information of Fe/GaAs microstructures. This *in-situ* technique is developed in two stages. First, the portable AFM setup is integrated at the P10 beamline of PETRA III facility for the purpose of testing stability and accessibility of the adopted setup. The testing confirmed that the developed technique can be simultaneously used to image, address and manipulate the microstructures under investigation. In the second phase of the development, the same setup is installed at ID13, ESRF facility and a nano-indentation experiment has been performed.

At P10 facility, GID measurements in vicinity of GaAs (220) Bragg peak are performed on Fe/MgO/-GaAs microstructures which are ring shaped. The GID measurements revealed that strain in individual microstructures induced by MgO and Fe layers can be probed separately. This strain is observed in the form of circular diffusive cloud of intensity around the Bragg peak of GaAs in GID RSM maps obtained on Fe/MgO/GaAs microstructures. The measurements performed at P10 established that our setup can be easily integrated at any micro-beamline facility allowing a combination of imaging and strain mapping of microstructures.

By using the same setup at ID13, ESRF, we have studied the stress induced changes in $2\,\mu\mathrm{m}$Fe/GaAs microstructures. By applying the GID geometry and a micro-focused X-ray beam, the evolution in-plane lattice planes of epitaxial Fe layer due to nano-indentation is investigated. The Fe layer in patterned Fe/GaAs microstructures is found to be compressively strained in the direction normal to the surface and this strain is further increased due to indentation. The variation of lateral strain of Fe layer along the microstructure is also modeled using Finite Element method (FEM) which revealed that lateral strain decays exponentially from the center of the tip contact. The calculated width obtained from FEM results is found to be in agreement with measured width of indentation produced by an AFM tip. However, the model adopted is only a simplistic representation of the experiment. Therefore, further modeling is required to simulate the changes in the RSM in correspondence to applied pressure to validate the obtained results.

We also observed local depositions on microstructures due to cumulative effect of intense ionizing beam and photo-current emission. These deposits were found to be insulating carbon-oxygen based compounds. We adapted the CAFM mode of AFM as an alignment tool for addressing the sub-micron structures. This tool is also proposed as a reliable method for systematic alignment of nanostructures of interest with respect to a synchrotron beam.

5 Experimental Results: Fe/InAs interface

5.1 Introduction

The InAs/InGaAs quantum well system is desirable for spintronic applications due to enhanced transport properties of quantum wells. For example, InAs based material system offers an high spin orbit coupling interaction and high mobilities and recent reports has provoked interest in this system.[145,146] The high mobilities observed in the system can be used to realize the ballistic transport limit which was proposed to be highly efficient for spin injection due to inter-band coupling.[24,80] Therefore, the insertion of tunneling barriers to avoid the conductivity mismatch between ferromagnet and semiconductor becomes redundant. Previous spin-injection experiments on the InAs systems have been performed in lattice-matched InGaAs heterostructures on InP substrates.[23,147,148] However, there are no reports on all electrical spin injection into InGaAs/InAs quantum wells that are grown on InAlAs metamorphic buffers. These step-graded buffer layers are designed to form a virtual substrate that is lattice matched to the active layers of heterostructure. The structural properties of metamorphic buffers are studied separately using various techniques including X-ray diffraction[149–151] and electron microscopy.[152–154] But the combined study of both structural properties of the Fe/InAlAs heterostructure and spin-injection measurements are not performed together on the same sample. This information about the structural state of the sample and the corresponding spin-injection efficiency is essential as the morphology of the quantum well (QW) interfaces is observed to affect the energetic positions of sub-bands of the QW.[29,30] The local change in the quantum well morphology could also effect the effective magnetic field (B_{eff}) experienced due to Spin-orbit interaction by the charge carriers in the quantum well because this property relies on the direction of the carriers.[155,156] The local structural changes are addressed by scanning X-ray diffraction, while the spin-injection measurements are performed by spin-valves as described in the chapter. Initially the deposition and structural properties of the metamorphic buffers the spin-injection from an ferromagnetic Fe electrode into the quantum wells is discussed later in this chapter.

5.2 Structural investigations of Fe/InAs heterojunctions

A detailed structural investigation is performed on Fe/InAlAs heterojunctions to understand the crystalline quality and morphology of the deposited layers. The structural studies such as indium composition calibration and local crystallinity of buffer layers are discussed in this chapter. The structural results are mentioned first as it enables drawing structure-property correlation during analysis of magneto-transport data and spin-injection discussions.

5.2.1 Indium composition in Inverted, Modulation doped InAlAs heterostructures

The sample design of the heterojunctions used for this thesis work is shown in Fig 5.1. In Fig 5.1 the sample is divided into the buffer layers shown in Fig 5.1(a) and the electronic active layers with quantum well in Fig 5.1(b). A GaAs/AlAs superlattice (SL) is deposited prior to the growth of graded buffer to prevent the propagation of impurities and threading dislocations from the substrate into active layers.[157] Compositionally graded metamorphic buffer is inserted between the substrate and active layers to gradually relieve the strain due to lattice mismatch between GaAs and the $In_xAl_{1-x}As$ layers, where the indium concentration is increased from x = 0.05 to 0.75 in 8 steps as shown in Fig 5.1(a). The strain relaxation due to lattice mismatch of graded layers is observed relieved by the formation of Misfit dislocations.[158,159]

The adopted design of the active layers with metamorphic buffers has already been studied in our group but were fabricated by using a Riber 32p MBE semiconductor chamber. But all the samples used for this thesis are prepared in another chamber called Riber C21 to achieve repeatability and to compare results from various sample designs and material systems. This required an comprehensive calibration of In growth speed in the C21 chamber to control the content of Indium in $In_xAl_{1-x}As$ layers. The exact composition of Indium in the active layers is important as it is reported to influence the mobilities of the heterostructure.[22] A composition of x = 0.75 is selected for top most layer as it was reported to yield higher mobilities.[119] For this specific sample design, RHEED oscillations cannot be used to monitor the InAs growth speed. This is because during the growth of pure InAs on GaAs (001), RHEED intensity oscillations are not observed due to island-like growth of InAs on GaAs substrates. Therefore, the growth speed of InAs is calibrated by measuring the time required for the formation of InAs quantum dots on a GaAs (001) substrate.[160] The formation of InAs quantum dot is detected by the evolution of intensity tails on RHEED spots called *chevrons*[161] and further details of the calibration by RHEED is reported by Heyn *et al*.[160]

This calibration procedure with RHEED cannot be used for achieving precise composition of the Indium in the heterostructure. Therefore, the final composition is of indium is independently derived from HRXRD reciprocal space maps. An RSM around GaAs (004) Bragg peak is measured and the details of the observed peaks are discussed in the following sections 5.2.3. A line scan along q_z direction

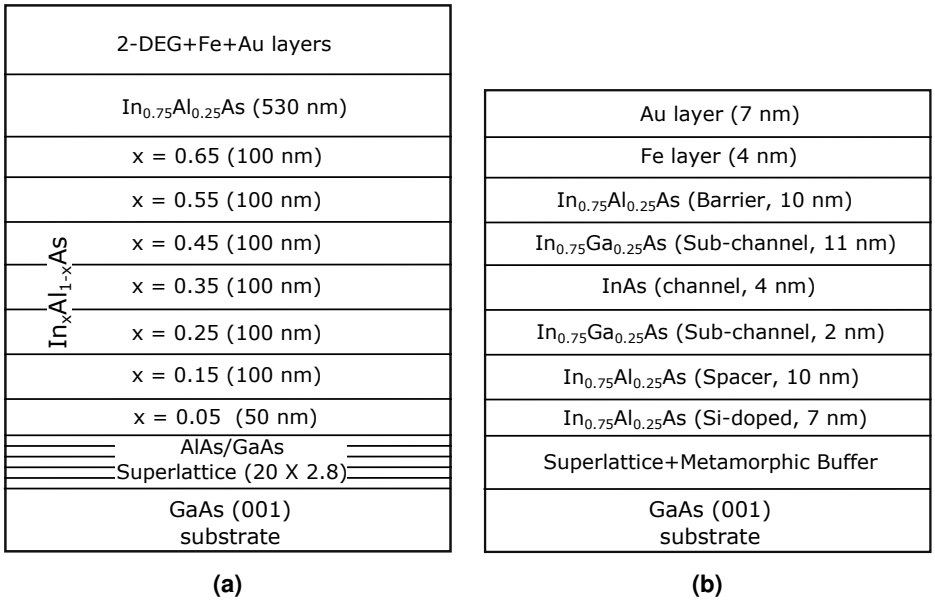

Figure 5.1: Sample layout of Fe/InAlAs heterojunction in (a) Layout illustrating the In compositions in the layers of metamorphic buffer, (b) The layer design of the topmost layer in (a) is shown in detail in (b) containing InAs channel and metal layers.

is obtained from the RSM in a similar way as described in chapter 3. The obtained line scan is then fitted with pseudo-Voight functions and the individual peak fits are shown in Fig 5.2(a)). Previous investigations on our sample design reported that the individual buffer layers are completely relaxed due to the large thicknesses of each layer.[119] Therefore, the lattice parameter calculated from fit reflects the composition of the layer. The indium composition in individual buffer layers is obtained by comparing the calculated lattice parameters against the ones obtained from Vegard's law. The comparison between the expected and calculated lattice parameters from Vegard law is shown in Fig 5.2(b). The composition marked in red labels in Fig 5.2(b) is the desired nominal composition, whereas the black labels are the real indium composition values obtained by comparison. In the next iteration of sample growth, the temperature of the Indium cell is corrected to yield the nominal composition.

In addition, the obtained q_z line profile is also fitted using the RCRefSimW program which uses an semi-kinematical algorithm[95] for simulating the diffraction profile. The simulated diffraction profile is shown in Fig 5.3(a)) where the layers are assumed as completely relaxed. The peak positions of the simulated profile matches precisely with the obtained line scan which confirms that the individual buffer layers are completely relaxed. Moreover, an additional RSM is obtained around GaAs (224) reflex which is shown in Fig 5.3(b). This figure reveals that the Bragg peaks of layers are present along the line joining the origin of reciprocal space which confirms that layers are completely relaxed in our sample. The composition of indium obtained from simulation differs by 2% from the desired nominal indium content.

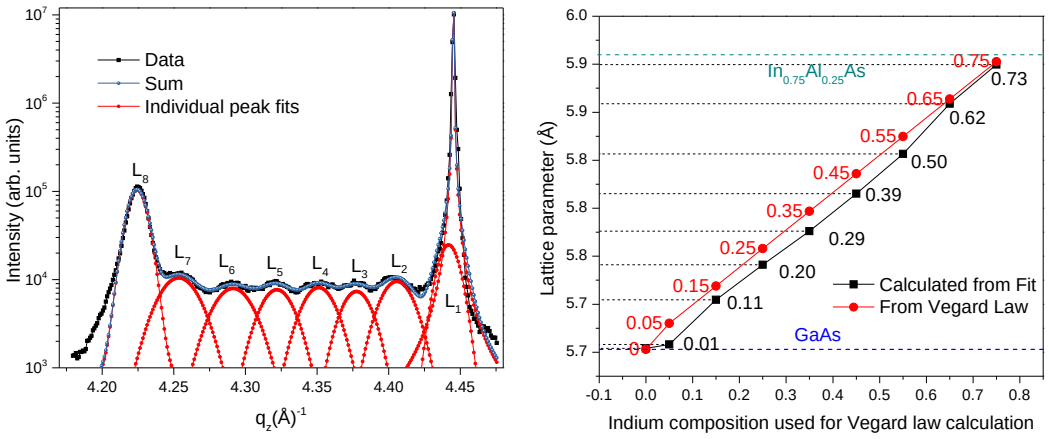

Figure 5.2: (a) Individual fits and sum of fits obtained on the q_z line scan. (b) Comparison of lattice parameter obtained from Vegard's law and calculated from fitting the q_z line profile. The composition marked in red labels is the desired nominal composition, whereas the black labels are the real indium composition values obtained by comparison. Blue and green dashed lines represent the bulk lattice constants of GaAs and $In_{0.75}Al_{0.25}As$.

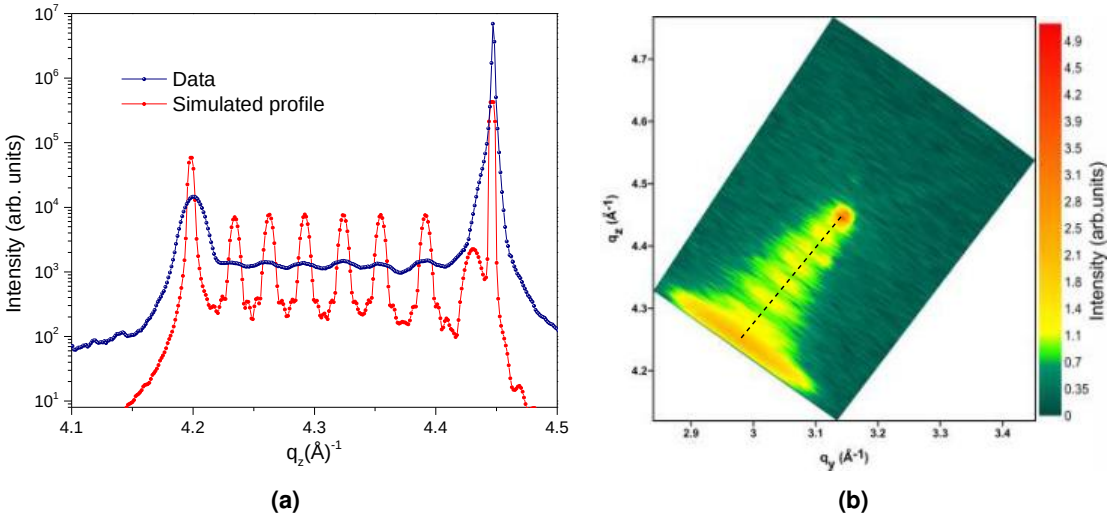

Figure 5.3: (a) Comparison between q_z experimental line scan obtained crystal truncation rod of GaAs (004) reflex and a simulated profile obtained using the RCRefSimW program. (b) 224 RSM obtained on InAs HEMT showing buffer Bragg peaks lying on a line connecting to origin of reciprocal space (dashed black line).

5.2.2 Morphology of Inverted, Modulation doped InAs heterostructures

After the exact Indium content in each layer of the metamorphic buffer has been adjusted to the desired value, new samples are fabricated. One of the samples is structurally investigated and labeled as C21N600 and the same sample is also used for spin-injection experiments described later in Sec 5.3.
In the following morphological features of the sample surface are discussed. Strain relaxation mechanisms during the growth of metamorphic buffer results in a undulating surface morphology commonly called cross-hatches. The resultant surface morphology of the heterostructure is studied by using Nomarski microscopy. This technique is used to study larger view fields of the surface morphology which is not possible to achieve by the time consuming scanning probe techniques. This technique is also used as a quality control approach as it enables quick observation of cross hatches on the entire wafer. Cross hatches are generally identified as stripes running in either $[1-10]$ or $[110]$ direction as seen in Fig 5.4. Same morphology is observed on both bare semiconductor surface and on parts covered with metal deposited subsequently.

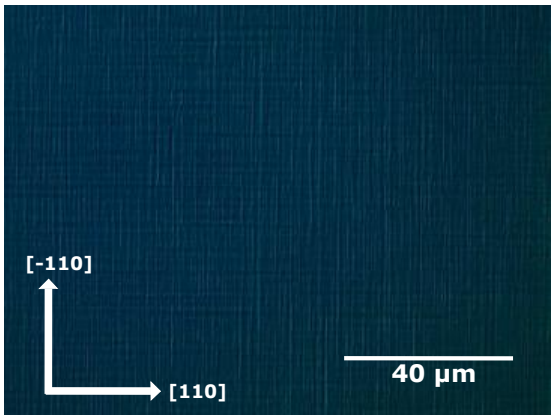

Figure 5.4: Nomarskii microscopic image showing a large-view field of cross-hatches on sample C21N600.

The surface profile is also studied by using AFM topography scans as displayed in Fig 5.5.a which clearly displays a cross-hatch pattern with periodic undulations running along both $[110]$ and $[1-10]$ crystal directions. The height variation is observed to be anisotropic with pronounced grooves along $[110]$ with maximum height of 22 nm and with a average distance of separation of about 200-300 nm. The less pronounced grooves along [1-10] direction have varying heights between $5-10$ nm with periodicity varying around $1.5\,\mu\mathrm{m}$. This anisotropy is correlated to different densities of α -misfit dislocations (running along [1-10]) and β -dislocations (along [110]) at the buffer layer interfaces.[162] In other words, the surface morphology observed on metamorphic InAlAs heterostructure can be described as superposition of two sets of lateral patterns running perpendicular to each other. These two lateral patterns can be clearly distinguished by using 2-dimensional Fast Fourier Transformation (2D FFT). This is done by using surface analysis free-source software called Gwddion. The 2D FFT of the topographic

image reveal periodicities in both horizontal and vertical direction. Frequency in both directions are filtered separately and the reconstructed image obtained after filtering are shown in Fig 5.5(c) & (d). These images clearly show vertical and horizontal patterns with varying heights which combine to form the final cross-hatch pattern. The line profiles obtained from FFT filtered images reveal that the grooves observed along [110] have larger height variations as compared to the other crystal direction which correlates to the height profiles as shown in Fig 5.5.(b).

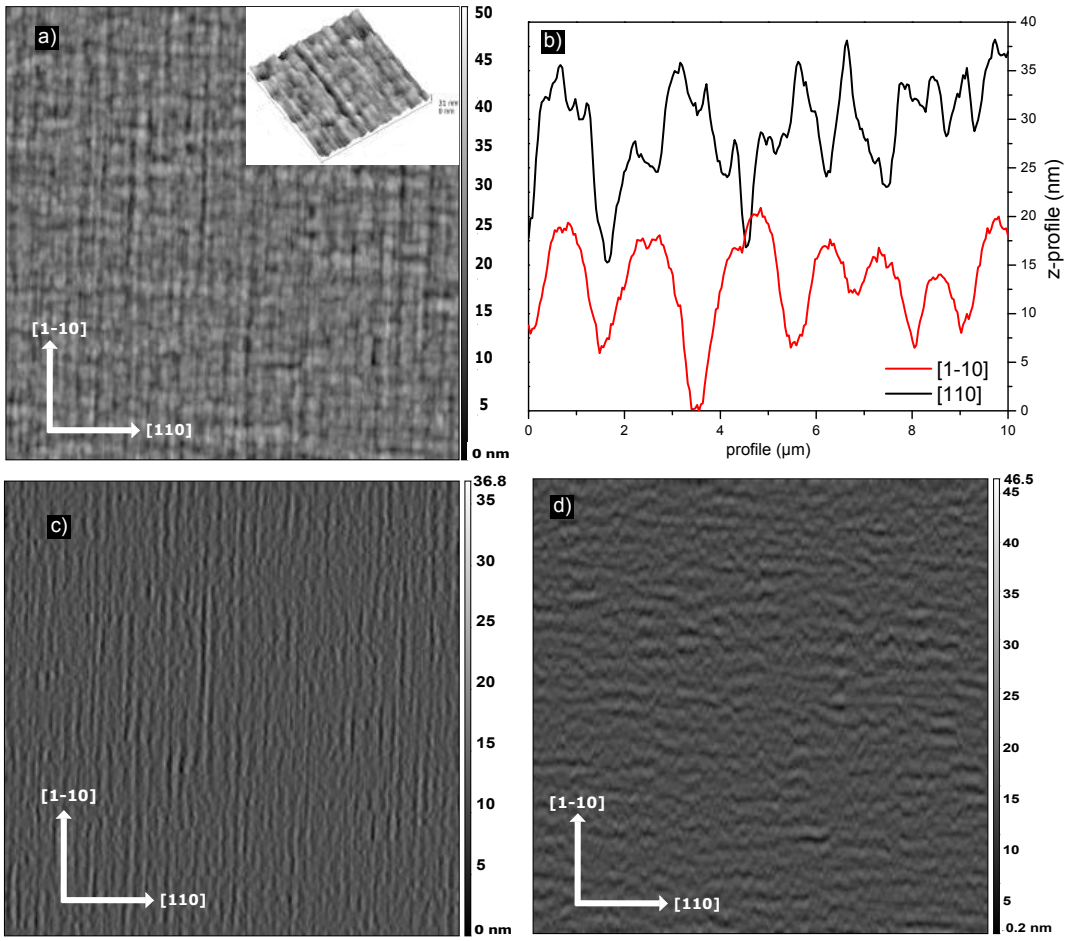

Figure 5.5: (a) $40\,\mu m \times 40\,\mu m$ topographic scan, Inset: $10\,\mu m \times 10\,\mu m$ 3d image of the same image illustrating the valleys and ridges. (b) AFM line scans along [1-10] and [110] crystal directions. The line scans are shifted by an offset to prevent overlap. (c) 2D FFT filtered images showing vertical lines along [1-10] crystal direction. (d) 2D FFT filtered image showing horizontal periodic pattern along $[110]$ crystal direction.

We also applied XRR mapping technique to study layer thickness and layer properties of the fabricated InAlAs samples. The XRR reciprocal space map obtained on the sample is shown in Fig 5.6(a) where a cloud of diffuse scattering is predominantly evident. This XRR map is obtained where the plane of incidence is along the [110] crystal direction of GaAs. The map is integrated towards q_z direction and

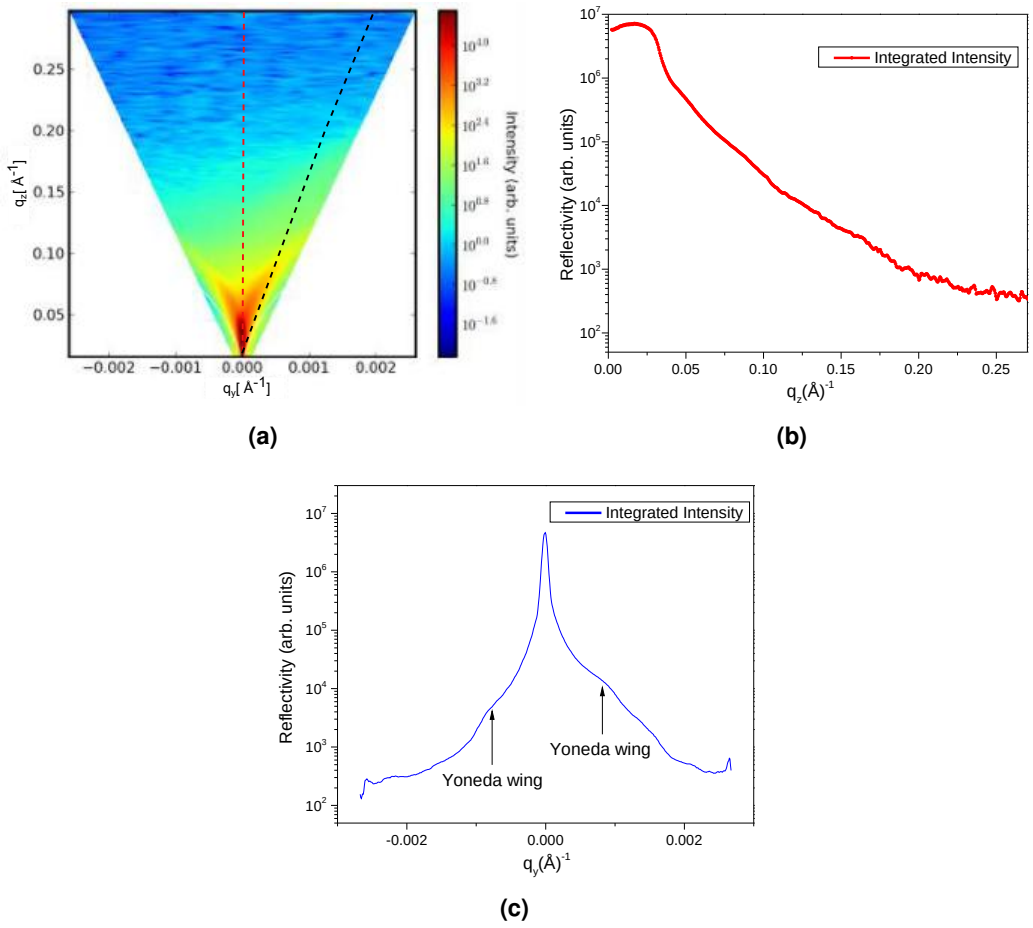

Figure 5.6: a) Reflectivity map obtained on sample C21N600; the red dashed line marks specular direction while the black dashed line represents off-specular direction. b) integrated profile obtained by projecting map towards q_z direction. c) integrated profile obtained by projecting map towards q_y direction.

the obtained $\omega - 2\theta$ scan is shown in Fig 5.6(b). The reflected intensity is observed to drop rapidly in the specular direction (indicated as red dashed line) in Fig 5.6(b).The Kiessig fringes arising from flat and sharp epitaxial layers are not observed. This is assigned to the considerable roughness at the surface caused by the cross-hatch pattern. The surface roughness redistributes the intensity away from the specular reflection into diffuse scattering, therefore, preventing constructive interference of reflected X-rays to form Kiessig fringes. In addition, the RSM also shows flare like diffusive features in off-specular direction (indicated as black dashed line) Fig 5.6(b). To analyze these diffuse features, the map is projected to the q_y axis to obtain a line profile along q_y, which is basically equivalent to the ω scan and is shown in Fig 5.6(c). On the shoulder of the sharp specular peak at q_y = 0, two broad peak like features are observed in Fig 5.6(c) and are highlighted as Yoneda wings.[163] Typically, these Yoneda wings appear when the incident (ω) or exit X-ray beam (2θ) forms an angle with the sample's

surface equal to the critical angle i_c. In principle, Yoneda peaks are a result of diffuse scattering. The intensity enhancement in the diffuse scattering at critical angle is observed due to increase of transmission coefficient at this angle. Therefore Yoneda peaks are observed to become broad if the sample surface has large roughness due to modification of transmitted field amplitude. These broad features of Yoneda wings also corroborate the fact that final sample surface has considerable roughness due to cross-hatch morphology.

5.2.3 Tilt analysis of buffer layers

The cross-hatch morphology is a result of considerable lattice mismatch between the layers resulting in textured films and layers mis-oriented with respect to the substrate, which is generally characterized as tilt. Where tilt is defined as the misorientation of the [001] direction of the individual buffer layers as compared to the [001] direction in the substrate. In other words tilt is a slight misorientation from parallelism of the crystallographic planes of neighboring layers.

The tilt in In(Al,Ga)As metamorphic buffers deposited on GaAs (001) substrates has already been extensively studied and the characteristics of this tilt is also widely reported.[158, 164, 165] But the Indium composition and the number of buffer layer steps used in the previous studies is less when compared to our sample. Also, the reported investigations are performed on samples without superlattice (SL). Structural studies on our sample design were previously conducted by Boris Landgraf, where the texture of metamorphic buffers is investigated by measuring pole figures.[119] The texture is also defined as crystallographic orientation distribution and is measured to investigate the effect of the SL on the strain relaxation and twist in metamorphic buffers. The texture of the substrate, SL, $In_{0.05}Al_{0.95}As$ and $In_{0.75}Al_{0.25}As$ layers have been individually studied by measuring pole figures at the corresponding Bragg peaks.[166] In this thesis, the tilt of each layer is analyzed by using two reciprocal space maps obtained at different sample azimuths (ϕ).

The tilt is pictorially depicted in Fig.5.7(a) where K_i and K_s represent the incident and exit wave vectors, respectively. The schematic representations of tilt in both sub-figures is inspired from the pictorial description used in the works of Lee *et al*[165] and Zhylik *et al*.[164] The vectors h and m represent the substrate and layer scattering vectors in (001) direction, respectively. η is the angle between substrate and layer Bragg peaks. The lattice tilt causes the diffraction peaks to shift away from vector h and this shift can be used to determine the value of tilt. The tilt is defined with two parameters: ϕ_o, which represents the inclination of the tilt with respect to [110] direction and the maximum tilt angle η_{max} with respect to the surface plane. By using these two parameters, the projection of lattice tilt onto an arbitrary diffraction plane at azimuthal angle ϕ can be calculated by using equation 5.1.

$$\eta(\phi) = \eta_{max} \cos(\phi - \phi_o) \tag{5.1}$$

Where ϕ_o is given by Eq 5.2

$$\phi_o = \arctan\left(\frac{\eta_2\cos(\phi_1) - \eta_1\cos(\phi_2)}{\eta_1\sin(\phi_2) - \eta_2\sin(\phi_1)}\right) \tag{5.2}$$

Where, η_1, η_2 are tilt values calculated using equation 5.3 from RSM obtained at two sample azimuths $\phi_1 = 0$ and $\phi_2 = 90$ respectively. In our analysis the inclination of the tilt is defined against the [110] diffraction plane, therefore $\phi = 0$.

$$\eta = \arctan\left(\frac{q_y}{q_z}\right) \tag{5.3}$$

Where, q_y and q_z are obtained peak positions along the both reciprocal space coordinates.

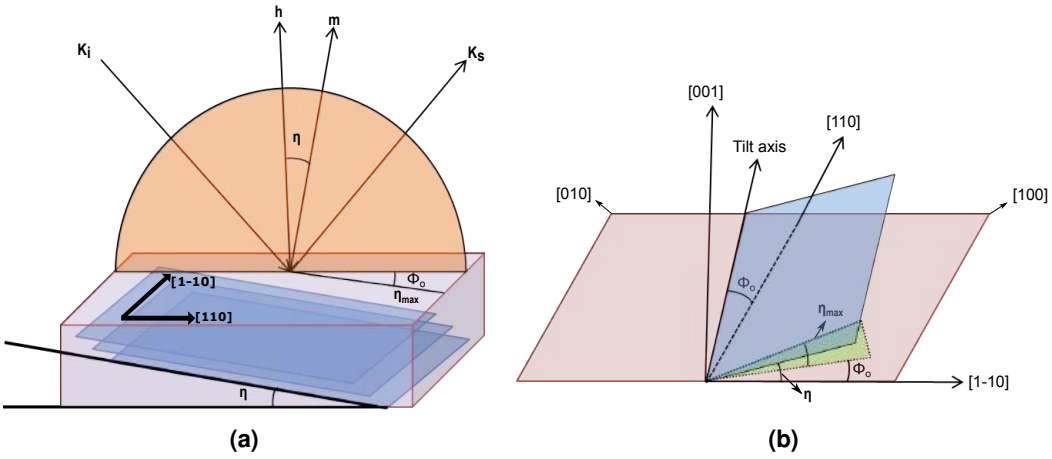

Figure 5.7: a) Schematic depiction of tilt. The orange highlighted region represents the scattering plane with incident, exit and X-ray scattering vectors of substrate and layers. The rectangular box indicating the orientation of the substrate planes while the blue planes represent the tilted layers. b) Schematic highlighting the components of tilt. The red and blue quadrangles represent the substrate and tilted planes.

The tilt is characterized in the same sample (C21N600) on which spin injection is demonstrated (discussed in Sec 5.3). To access the tilt, RSM around (004) reflex are obtained at two different sample azimuths (ϕ) and the measured maps are shown in Fig.5.8.a) & b). The measured maps show well separated isointensity Bragg peaks which correspond to individual layers of different Indium composition. The RSM obtained at sample azimuth $\phi_1 = 0$ ($\phi_2 = 90$) means that the scattering plane is along [110] ([1-10]). The white dashed line represents the GaAs (004) crystal truncation rod while black dots point out the peak position of individual buffer layers. The tilt in epilayers can be visually recognized by the misalignment of peak positions of different composition layers with the crystal truncation axis (q_y=0) of GaAs (004) as evident in Fig.5.8.a). The magnitude of the q_y deviation from the crystal

truncation rod of the GaAs substrate is smaller in the RSM measured at $\Phi = 90$ orientation. This observation is consistent with other studies[165] where the displacement of peak with respect to truncation axis is found to vary as a function of sample azimuth (ϕ).

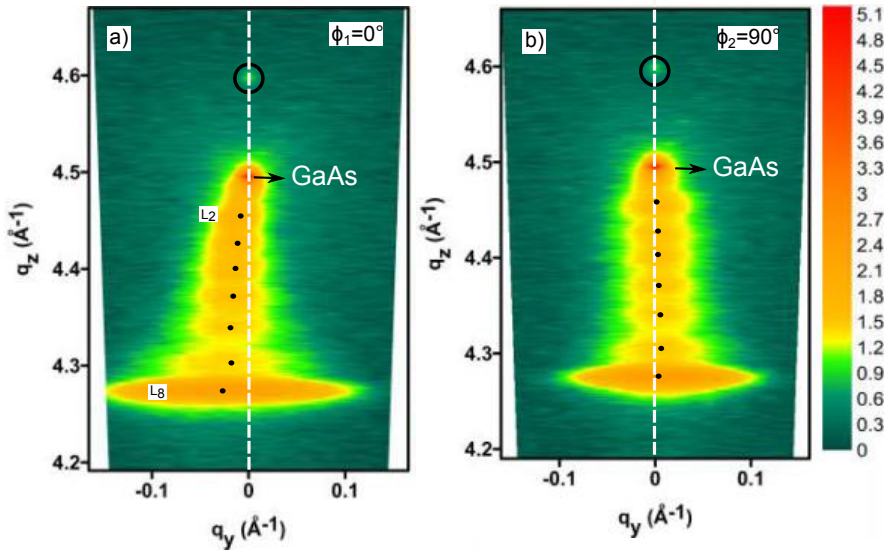

Figure 5.8: a) RSM obtained around (004) reflex of GaAs at sample azimuth ϕ_1 where the plane of incidence is along [110]. b) RSM obtained around (004) reflex of GaAs at sample azimuth $\phi = 90$ where the plane of incidence is along [1-10]. The black dots show the peak positions of the layers obtained from fitting. The white dashed line is a guide to the eye indicating peak shifts of individual layer peaks from the $q_y = 0$ position, corresponding to the GaAs substrate peak. The less intense peak marked in black circle arises from superlattice.

To calculate the tilt, the peak positions (q_y) in [110] direction is measured q_y for each layer. This is done by using a *python* program developed to plot individual peak profile along q_y direction. The intensity in small region corresponding to each buffer layer is integrated along q_z direction to obtain the peak profiles shown in Fig 5.9. The dashed line in Fig 5.9 represents the position of the GaAs (004) peak. These profiles are fitted with pseudo-voight functions to obtain the exact peak positions. The metamorphic buffer in our sample design contain eight different composition layers but only seven peak positions are clearly visible. This is due to close proximity of first composition layer ($In_{0.05}Al_{0.95}As$) to the GaAs peak, therefore, its position in q_y direction could not be resolved. Hence the peaks are labeled from L_2 to L_8 in Fig 5.2(a)).

The tilt (η) of each composition layer is separately calculated by using the equation 5.3 for both sample azimuths($\phi = 0(\phi_1)$ and $\phi = 90$ (ϕ_2)). Later, η_1 and η_2 are used to obtain the inclination of the tilt(ϕ_o) with respect to [110] crystal direction. The parameter η_{max} for each metamorphic buffer layer is calculated from equation 5.1 and shown in Fig 5.9. Other studies on similar sample structures reported higher values of tilt. For example, Lee *et al* reported a tilt of 1.06 ° in $In_xAl_{1-x}As$ buffer layer with

maximum indium content of x=0.52.[165] Our measurement with x=0.75 have shown much lower tilt value of $\eta_{max} = 0.352$ °. Also, the tilt of layers in our sample seems to decrease after first few buffer layers before increasing again for the final thickest layer. But this decrease might be also be due to error of fitting. In addition, the in-plane inclination of tilted planes is also observed to be smaller than the literature values. It changes from 1.07° in the first composition layer to 12.76° in the final layer (x=0.75). The lower values of η_{max} and ϕ_o observed in our sample might be due to the use of superlattice in our sample design which was not used by previous similar investigations. The comparison of the tilt components between our data and the reported literature is tabulated in the table 5.1

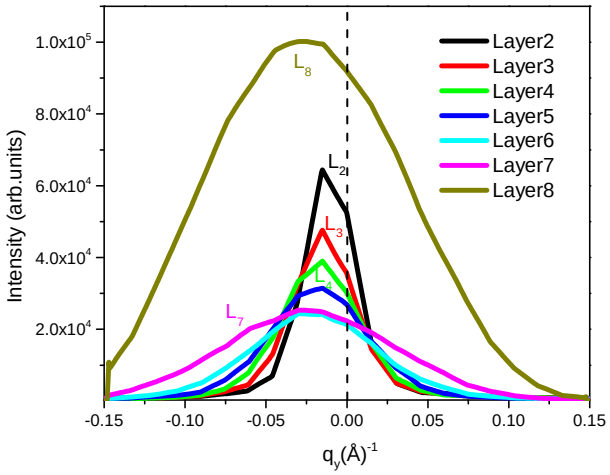

Figure 5.9: Peak profiles obtained from individual composition peaks along q_z^{004}. The black dashed is a guide to eye indicating peak shifts of individual layer peaks from $q_y = 0$ (GaAs peak)

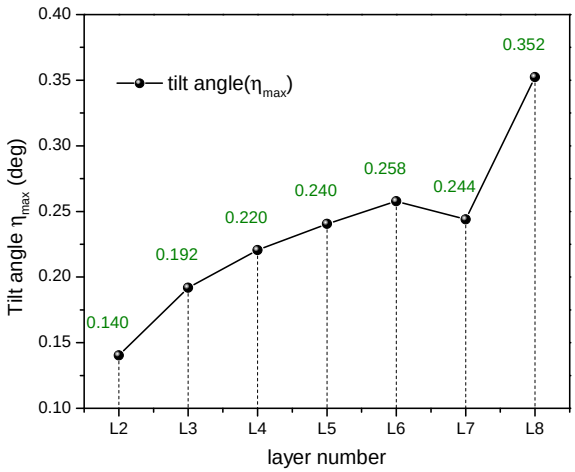

Figure 5.10: Tilt angle (η_{max}) obtained for individual buffer layers labeled as L2-L8 (indium composition x=0.15-0.75).

sample	$In_xAl_{1-x}As$	η_{max}	ϕ_o
Lee *et al*[165]	x=0.52	1.06°	-25.86°
our data	x=0.55	0.258 °	12.31°
our data	x=0.75	0.352°	12.763°

Table 5.1: Comparison of tilt parameters reported on different composition layers and our data.

5.2.4 Diffraction mapping of InAlAs buffer layers

Scanning diffraction mapping or also called as K-mapping is performed on metamorphic buffers of sample C21N600 to study the local variation of crystallinity in individual metamorphic buffers. The experiment is performed on part of the sample where the Au and Fe metal layers are not deposited. The tilt and lattice parameters measured using the lab diffractometer represents an averaged value over a large area due to the large size of X-ray beam. Whereas, the K-mapping technique provides local information in micron dimensions. As discussed in the previous section, the cross-hatch morphology arising from different densities of misfit dislocations formed along the mismatched interfaces will imperatively lead to local variation of structural properties like crystallinity, composition and tilt of the grown layers. The local variation of these properties in metamorphic SiGe buffers deposited on Si substrates are widely studied.[167–169] These studies are performed with the aid of the K-mapping technique developed at ID01, and we have used the same method to study our InAlAs buffer layers. In short, K-mapping enables measurement of diffraction mapping on a sample in micron dimension by scanning the sample in lateral direction while simultaneously measuring diffraction. The basic experimental details of K-mapping setup and beam line specifications are described in detail in the literature.[167,168] A simple schematic of the experimental setup is shown in Fig 5.11 and a few basic details of the experiment are briefly mentioned here.

The X-ray beam used for this particular experiment is focused to a size of 200 × 600 nm (Vertical × horizontal) at an energy of 8 keV. The flux of the incident beam is measured to be around 10^{11} photons/second. A 2D photon counting Maxipix detector[170] (4 chips, 516×516 pixels) with a pixel size of $55\,\mu m^2$ is used to monitor the diffraction signal. The diffractometer is initially aligned to the GaAs (004) Bragg angle (ω = 33.25, θ = 66.5). The foot print of the beam at this incidence angle is calculated to be 365 nm. After roughly aligning the diffractometer to the substrate and buffer layers, a reciprocal space map is obtained and the diffractometer is precisely aligned so that the maximum of ($In_{0.75}Al_{0.25}As$) Bragg peak is on the detector plane. After alignment, the Bragg peak of $In_{0.75}Al_{0.25}As$ layer is observed as the most intense peak (as seen in Fig 5.12) on the detector frame due to the large thickness of this layer (530 nm) and also because this maxima of this peak is aligned in the detector plane. Later the detector is shifted away to prevent the over exposure of the detector from the substrate peak. Later, the sample is scanned in real space in (110) and (1-10) directions corresponding to a scanning area of $40 \times 60\ \mu m^2$. The step size in (110) and (1-10) direction is set to $0.33\,\mu m$ and $0.5\,\mu m$

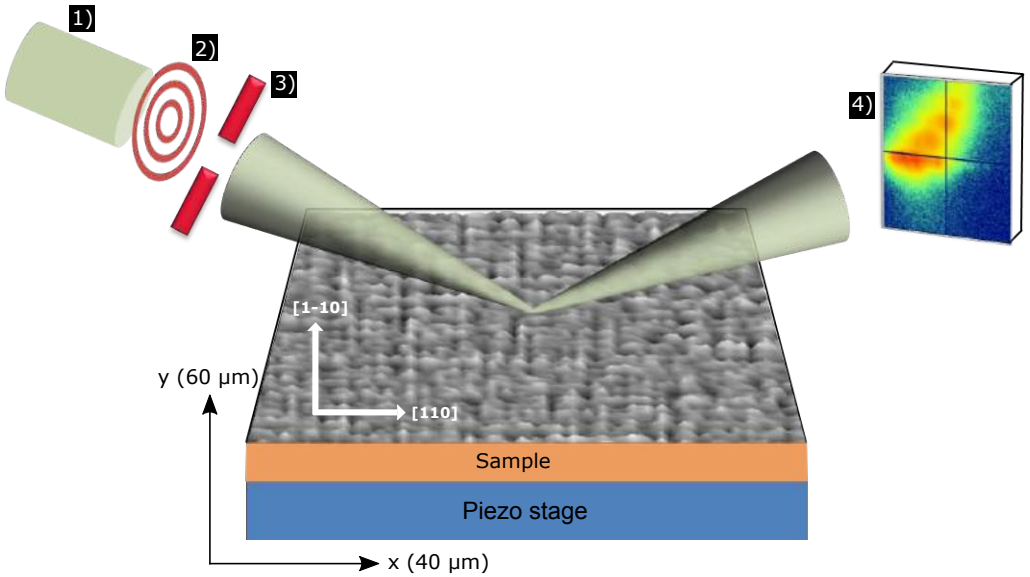

Figure 5.11: Experimental setup of K mapping: 1) 8 keV monochromatic beam, 2) Fresnal zone plate (FZP), 3) order sorting aperture and 4) Maxipix detector. The setup is aligned close to the out-of-plane (004) GaAs reflex.

respectively with acquisition time of 250 ms/frame. A total of 14000 frames were obtained which correspond to 120×120 points in the real space image. Henceforth, the K-mapping will be referred as diffractive imaging in further text.

In a typical diffractive imaging experiment, the sample is rocked (ω-scan) in small angular range at every spatial point of the scanning area which leads to measurement of 5-dimensional data (q_x, q_y, q_z, x and y).[168,169] The obtained 5-dimensional data correspond to three directions in reciprocal space q_z, q_x, q_y and two real space scanning directions x and y. The obtained 3-dimensional reciprocal space information at every point of scanning area is used to analyze the Bragg peak movement due to local variation of crystalline properties. This analysis is generally done by using the XSOCS (X-ray strain orientation calculation software) program[167] developed at the ID01 beamline, ESRF. The program performs a Gaussian peak fitting to find the Bragg peak movement and corresponding peak positions (q_x, q_y, q_z) in the reciprocal space. These peak positions are later used to obtain 2-dimensional maps containing quantitative information about the local crystallinity, tilt and composition variation as a function of x and y directions in real space.

It is worth pointing out that our sample is not rocked during the scan leading to acquisition of 4-dimensional data. Instead the x-y scan is repeated three times at different inclination angles ω of the sample. The obtained 4D data corresponds to two directions in reciprocal space (q_z, q_y) and 2 scanning directions (x,y). We did not perform ω-scans at every spatial point because of the limited beam-time. Nonetheless we repeated the scan at three different inclination angles (ω) with respect to angle of the $In_{0.75}Al_{0.25}As$ Bragg peak.

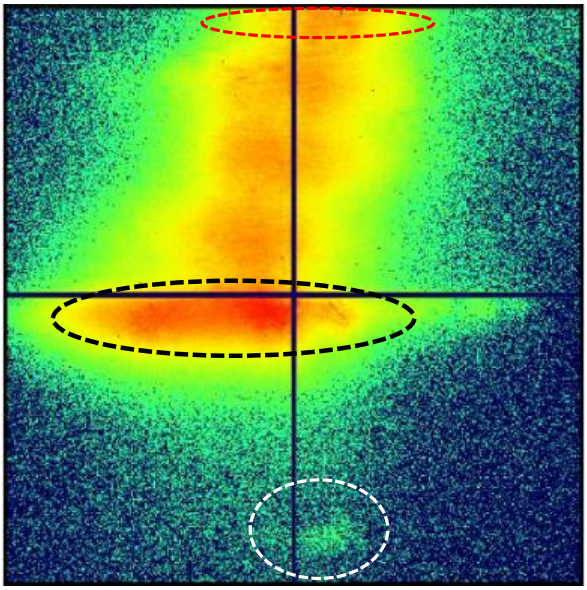

Figure 5.12: The diffraction signal observed on one of the frames of the scan. The intensity in the region marked by red and black dashed ellipses belongs to $In_{0.15}Al_{0.85}As$ and $In_{0.75}Al_{0.25}As$ Bragg peaks, respectively. The faint signal in the white dashed region arises from the 4 nm thick InAs quantum well.

The three scans at different inclination angles ($\delta\omega = -0.15°, \delta\omega = 0°$ and $\delta\omega = 0.15°$) with respect to the $In_{0.75}Al_{0.25}As$ Bragg peak correspond to three data sets. These three datasets will be referred in further text as: dataset-1 (obtained at higher inclination w.r.t to $In_{0.75}Al_{0.25}As$ Bragg peak, $\delta\omega = 0.15°$), dataset-2 (obtained at $In_{0.75}Al_{0.25}As$ peak, $\delta\omega = 0°$) and dataset-3 (obtained at lower inclination w.r.t to $In_{0.75}Al_{0.25}As$ Bragg peak, $\delta\omega = -0.15°$). The inclination step size and number of steps used are not discrete enough to construct a continuous 3-dimensional reciprocal space map. So these three scans at different inclination angles are treated as three datasets of 2-dimensional space maps at every spatial point of scanning area.

For a complete quantitative analysis of the local crystallinity, composition and tilt with the XSOCS package, a complete 3-dimensional reciprocal space information at every scanned location is necessary. As our data is devoid of this essential feature, we have adopted an qualitative approach to analyze our data. We have used our own developed python code to analyze all three datasets. In the following discussions, the treatment of the data is discussed first followed by results and conclusions obtained from data.

Our entire analysis of diffractive imaging is based on tracking the displacement of Bragg peaks in reciprocal space. In principle, the displacement of peak in a certain direction in reciprocal space corresponds variation of a different crystalline property of the layer. This displacement-property relation of Bragg peaks is pictorially depicted in Fig 5.13. The blue shaded region in Fig 5.13 represents plane of detector cutting through the reciprocal space containing the Bragg peaks of the $In_xAl_{1-x}As$ buffer layers. The

GaAs substrate peak is outside the detector plane as shown in Fig 5.13 to prevent overexposure. The detector is positioned such that the signal from the first metamorphic layer is still in the frame of detector. The peaks from first and last buffer layer are shown as orange shaded regions. The black dots represent the other Bragg peaks from the metamorphic buffer.

The local variation of the composition leads to a change in the lattice parameter of the layer which results in displacement of peak along q_z direction. The displacement in q_z could also result from local change in the strain. But as mentioned in subsection5.2.1, buffer layers in our sample design are completely relaxed. Therefore we assume that the movement of peaks along q_z direction mainly occurs due to change in composition. A slight deviation from parallelism of the crystallographic planes called lattice tilt often happens locally in metamorphic buffers which leads to displacement of Bragg peaks along q_y direction. Hence the local composition and lattice tilt variation can be tracked by monitoring the displacement of Bragg peaks along q_z and q_y directions respectively.

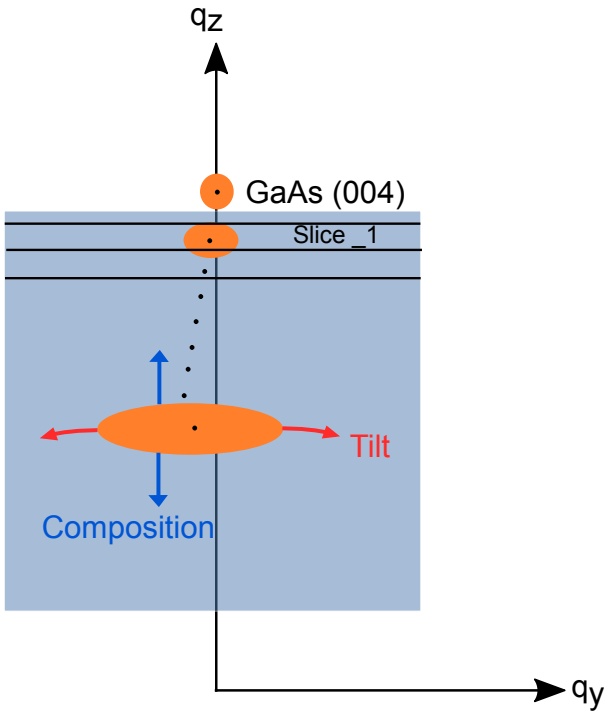

Figure 5.13: Schematic representation of single detector frame and the Bragg peaks (orange shaded and black dots) of metamorphic buffers. The slices in the frame are separated by black lines. The blue and red arrows indicate the shift of Bragg peaks due to local variation of composition and tilt respectively.

The peaks from individual layers of the metamorphic buffer are closely spaced to each other at the employed X-ray beam energy (8 KeV). To individually analyze the Bragg peaks of different buffer layers, each detector frame obtained at scanned spatial points is vertically divided into 25 (0-24) equally separated parts called “slices”. The Fig 5.14 shows the vertically divided 25 slices. In addition, the

intensity in each detector frame is averaged into 25× 25 pixels as shown in Fig 5.14.The reduction of data enables faster handling of large set of data and also allows individual analysis of different Bragg peaks. The qualitative analysis adopted enabled us to measure local change of intensity, tilt and composition in the scanned area for any particular Bragg peak of interest.

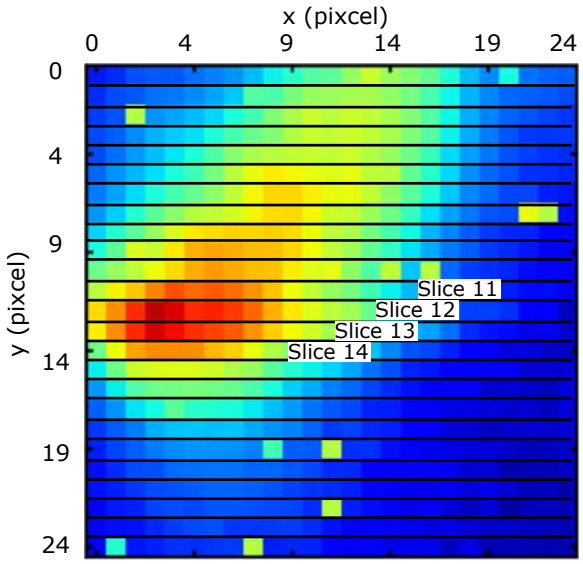

Figure 5.14: The averaged diffraction signal observed on one of the frames of the scan. The slices are separated by black lines and some of the slice numbers are indicated.

Monitoring local change in intensity

The local change of intensity is monitored separately in slices of interest. The intensity is integrated in both q_z, q_y directions from a particular slice of interest and the obtained integral intensities from every frame in the dataset are plotted as a map. The obtained map corresponds to intensity variation in the particular slice which is equivalent to a particular layer. This process is repeated for all 25 slices in each frame resulting in 25 spatial maps of intensity variation across the 60×40 μm^2 region. The method to extract the local intensity change of the diffracted beam is pictorially shown in Fig 5.15. First, the frame recorded at certain (x,y) position is divided into slices. The intensity integrated within one slice is color coded and mapped at the corresponding xy position where the corresponding frame is recorded. For example, the red and blue shaded regions in 2D map in Fig 5.15 represent the integrated intensity belonging to same slice number of two detector frames obtained subsequently. The obtained 2-dimensional maps correspond to local crystallinity of the respective layers and will be referred as "intensity maps" in further text.

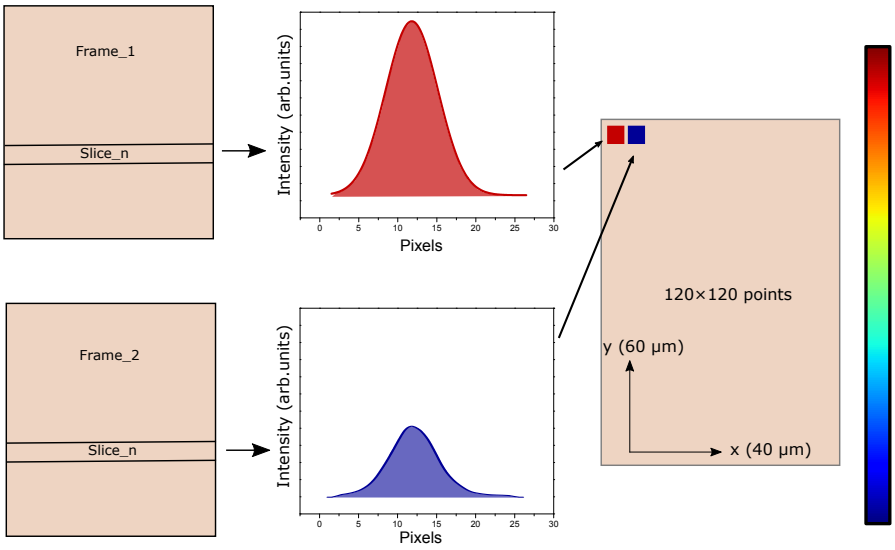

Figure 5.15: Schematic representation of data extraction for intensity variation. The blue rectangle on left represent frame recorded at adjacent positions. The shaded regions under the peak represent the integrated intensity of a particular slice of interest. The 60×40 μm^2 grid is the 2-dimensional intensity map.

Monitoring local change in composition

The local change of composition is analyzed by monitoring the displacement of Bragg peaks in q_z direction. The displacement is measured by tracking the change in intensity of two adjacent slices as the Bragg peak moves along q_z direction due to composition variation. The way the local change of composition is extracted is pictorially shown in Fig 5.16. The intensity in the slice of interest and the slice above it are integrated in both directions and the ratio between them is plotted for every frame in the scan in a map. The pink shaded region in Fig 5.16 is shown as an example to illustrate the difference between the two slices. The color encoded in the data of the map is ratio of integrated intensity calculated by using the following equation.

$$composition\_variation = \frac{[slice_{(n+1)} - slice_{(n)}]}{[slice_{(n+1)} + slice_{(n)}]} \tag{5.4}$$

This procedure is repeated for all 25 slices in the frame for the entire dataset to obtain 25 spatial maps of composition variation and will be referred as “composition maps” in further text.

It is worth mentioning that the composition variation is monitored by tracking the displacement of Bragg peak in q_z direction, but the displacement in q_z could also result from change in the strain of layers. But as mentioned earlier, the metamorphic buffer layers in our sample are completely relaxed. However, there still could exist a local strain variation in layers. In principle, to quantitatively separate the strain and composition variation, a K-mapping scan around asymmetrical Bragg peak is necessary.

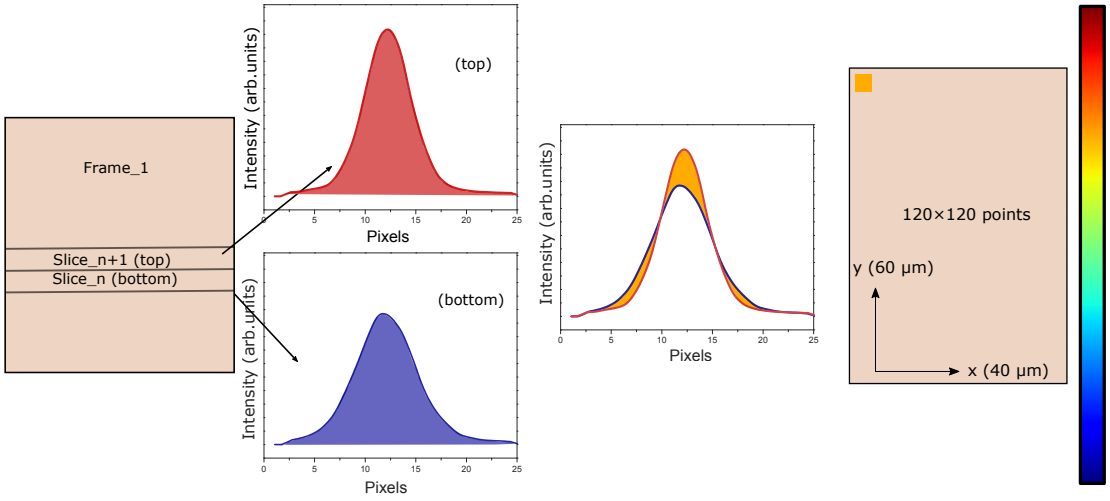

Figure 5.16: Schematic representation of data extraction for composition variation. The blue rectangle on left represents a single frame with two neighboring slices. The areas of the red and blue shaded regions corresponding to the integrated intensity of corresponding slices. The yellow shaded regions shows the intensity difference between two adjacent slices. The ratio of difference (pink square) is plotted as a point in map. The graph on extreme right end shows the 60×40 μm^2 grid of 2-dimensional composition map.

The asymmetrical K-mapping scan can be used to obtain information about the in-plane lattice constant of individual layers which can later used to calculate strain. But this scan in asymmetric geometry is not measured in our experiment. Therefore, the obtained composition analysis results represent superposition of strain and composition variation. Therefore the obtained results represent only a qualitative picture of composition variation.

Monitoring local change in tilt

In typical epitaxial structures with surface cross hatches, the lattice tilt locally changes due to stress relaxation mechanisms leading to a shift of Bragg peaks along q_y direction. The local change of tilt is analyzed by monitoring the displacement of the Bragg peaks in q_y direction. For this purpose, the intensity in each slice is divided into two parts. As each slice has 25 (0-24) pixels; the intensity observed in 0-12 pixels is treated as one part (left) and the intensity in 12-24 pixels (right) as another part. The Bragg peak shifts along the q_y direction due to local tilt causing the intensity in both parts of the slice to differ. The intensity is integrated separately in both parts and the difference in both parts is measured as a ratio of integrated intensity using:

$$tilt\_variation = \frac{[(right) - (left)]}{[(right) + (left)]} \tag{5.5}$$

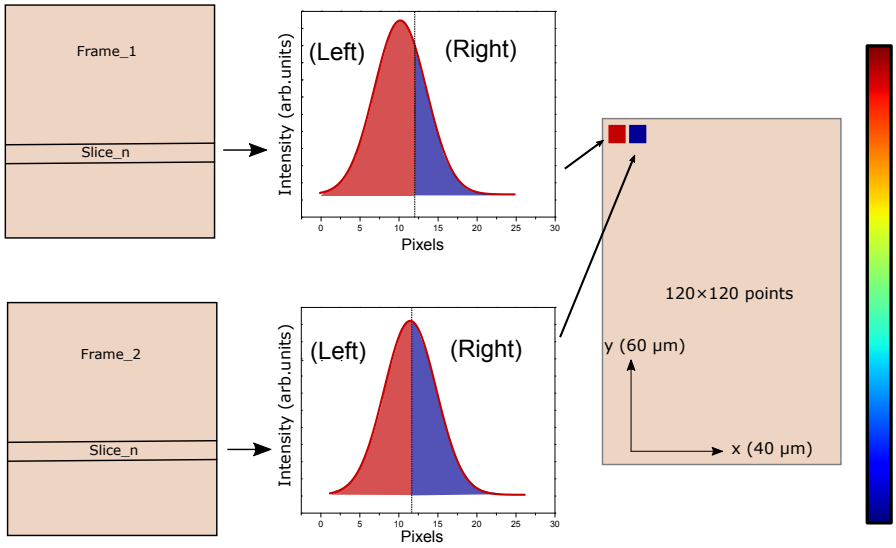

Figure 5.17: Schematic representation of data extraction for tilt variation. The blue rectangles on left represents two frames obtained consequently. The blue and red shaded region shows the integrated intensities of right and left parts of same slice. The ratio of difference is plotted as a point in a map.

The color encoded in tilt map displays the difference of the left-side and ride-side integrals of the intensity in one of the slices. If the Bragg peak is fully located in the left side of the crystal truncation road, the tilt is large. If it is symmetrical to the crystal truncation rod, no tilt exists.

The data extraction for local change of tilt for two different points in spatial map is pictorially shown in Fig 5.17. The ratio obtained from integrated intensities using Eq 5.5 is plotted as a point in spatial map. This process is repeated for all 25 slices in the frame for the entire dataset to obtain 25 spatial maps of tilt variation. They will be referred as "tilt maps" in the further text. The color scale obtained from tilt maps does not represent the magnitude of tilt but rather the qualitative local tilt. Therefore, any region in the tilt map with high value in color scale(red color) is analogous to a region with higher or lower magnitude of tilt with respect to the surrounding area.

One of the of the main advantages of diffractive imaging is that it enables correlation of the surface morphology to the underlying strain pattern and defects. Our interest also lies in the studying the network of defects that are formed due to different strain relaxation mechanisms. The information particularly regarding the periodicity of defect is essential for fabrication of spin injection devices where separation between the electrical contact plays an important role in efficiency of the working devices. Ideally, the typical separation of defects must be larger than the separation of electrical contacts for efficient working of devices. More details regarding transport properties are discussed in Sec 5.3.

Simultaneously to the scan in the diffractive imaging experiment (spanning across a area of $40 \times 60\ \mu m^2$), an AFM topography scan of the same dimensions is measured to enable correlation of surface cross-hatches to structural features like local tilt, composition variations. The topography scan is shown

in Fig 5.18, where, the surface morphology is presented in two color scales (a: gray scale, b: green scale) for better visualization of cross-hatches.

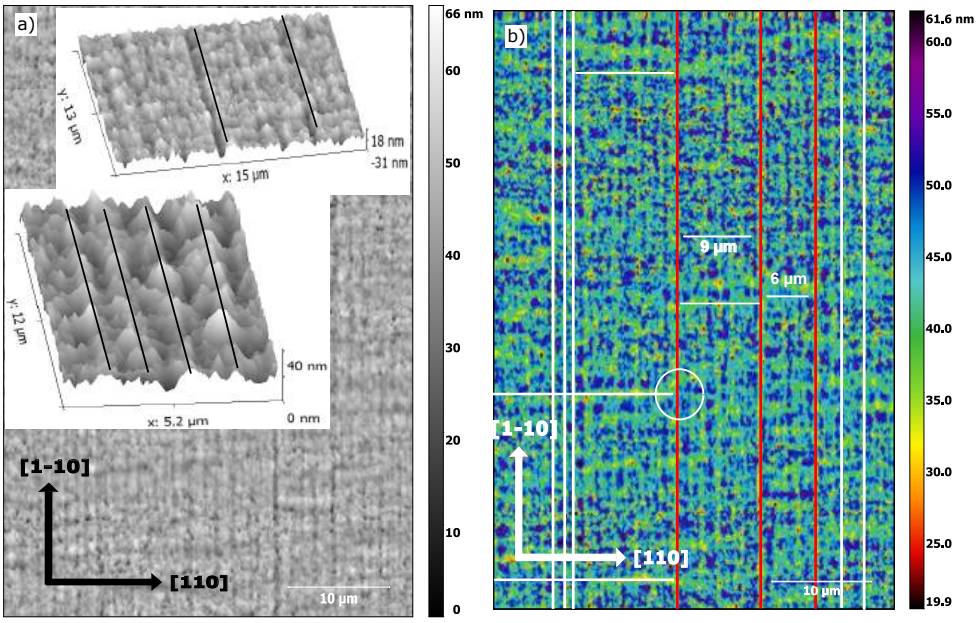

Figure 5.18: $60\times40\ \mu m^2$ AFM scan shown in (a) gray scale and (b) color scale. The white vertical lines highlight the cross-hatch lines with small magnitude of height. The red lines indicate the lines with higher magnitude of height. The horizontal white lines highlight the horizontal cross hatch lines.

The surface features observed in AFM micrographs and the dislocation mechanisms responsible for cross-hatches are discussed first as this information is necessary for understanding the results of the diffractive imaging. AFM micrographs reveal surface features that occur along different crystal directions as shown in Fig 5.18. The insets in Fig 5.18.(a) are 3-dimensional surface topography scans showing two types of features separated by $1\,\mu m$ and $6\,\mu m$.The lines running along [1-10] crystallographic direction have different heights and they are seen at different periodicities. For example, the lines with small height are observed more frequently at periodicity of $1\,\mu m$ and are highlighted as white vertical line in Fig. 5.18.(b). The lines with larger height are observed less frequently with separation of either $\approx 6\,\mu m$ or $9\,\mu m$. These lines with larger height are highlighted as red vertical lines in Fig 5.18.(b). In addition, surface features in form of lines are also observed to be running in [110] direction. The horizontal lines along [110] do not extend from end to end like the vertical lines which can also be seen in FFT Filtered image Fig 5.5.(d) as discussed in previous sections 5.2.2. Interestingly, the horizontal lines tend to disappear when they meet vertical lines of larger height. Such an instant is highlighted by a white circle in Fig 5.18.(b).

The origin and behavior of the dislocations in semiconductors heterostructures with graded layers are widely studied[171] and strategies to reduce the density of dislocations are proposed.[172,173] The strain relaxation in zinc-blend material systems occurs mainly through the formation $60°a/2$ <110>{111}

misfit dislocations (MDs). They glide to the interface on inclined {111} planes with their Burger vector (**b**= $a/2$ <110>, a is the lattice parameter) making a 60°angle with the <110> crystal directions.[174,175] The prevailing assumption is that these dislocations nucleate at the interfaces and expand in the form of half loops consisting of two arms of treading segments and a misfit segment as depicted in Fig 5.19.(a), where the isolated blue dot represents a nucleation of a dislocation and the blue loops represents the expansion of half loops to form outward segments. These two outward segments are called threading dislocations (TDs) which largely have screw character and anti parallel Burger's vector. A transmission electron image taken from work of Bolkhovityanov *et.al*[176] is shown in Fig 5.19.b to show the expansion mechanism in real layers. The dark spot highlighted by a white circle (1) is associated to the surface nucleation of a dislocation, while the dark feature marked as (2) shows a dislocation half loop moving inwards. Treading dislocations originating from different misfit-nucleation centers are highlighted as (4.a) and (4.b).

The TEM image shown in Fig 5.19.(b) is obtained on a sample with single buffer layer, whereas our structure consists of 8 buffer layers. This leads to assumption that accumulation of large density of threading and misfit dislocations gliding on all four ({111}) slip planes in multi-buffer layer system will lead to structural degradation of the heterostructure. But this expected deterioration is not observed as the treading and misfit dislocations are observed to be blocked by stress fields of orthogonal misfit dislocations leading to annihilation of perpendicularly running misfit dislocations.[175,177] This blocking mechanism also creates pile up of dislocations which in turn leads to local multiplication of dislocations by means of the modified Frank Reed mechanism (MFR).[174] The complete MFR mechanism is not discussed here as this is beyond the scope of this thesis.

Briefly, MFR mechanism explains the interaction of two perpendicular dislocations having same Burgers vector with each one having a misfit segment running in two perpendicular <110> directions and lying in two different {111} glide planes. The half loop formed at the intersection glides to relieve the excess stress in the layer. This process happens repeatedly forming pile-up of corner dislocations of the same Burgers vector. The repulsion between the dislocations of same Burgers vector pushes the misfit segments into the substrate which some times extend over few microns.[178] This multiplication occurs until sufficient strain is relaxed. The scheme depicted in Fig 5.19.(c) is the final stage of MFR mechanism showing a dislocation pile-up. Fig 5.19.(d) shows the top view of annihilation of misfit segments. The pattern observed from the top-view of annihilation resemble the cross hatch features observed on the surface. The subsequent pileups of misfit and threading dislocations results in formation of dislocation networks as shown in Fig 5.19.(d). Not all misfit dislocations end up in an annihilation process but few lead to threading segments that reach the surface or a particular interface resulting in trenches and valleys which is shown in the Fig 5.19.(e).

The occurrence of different type of dislocations leads to a rough surface forming cross-hatch pattern at every interface. The final surface features observed on the heterostructure is influenced by the roughness present at all the interfaces. We believe that the mechanisms like FMR also occur in our sample as

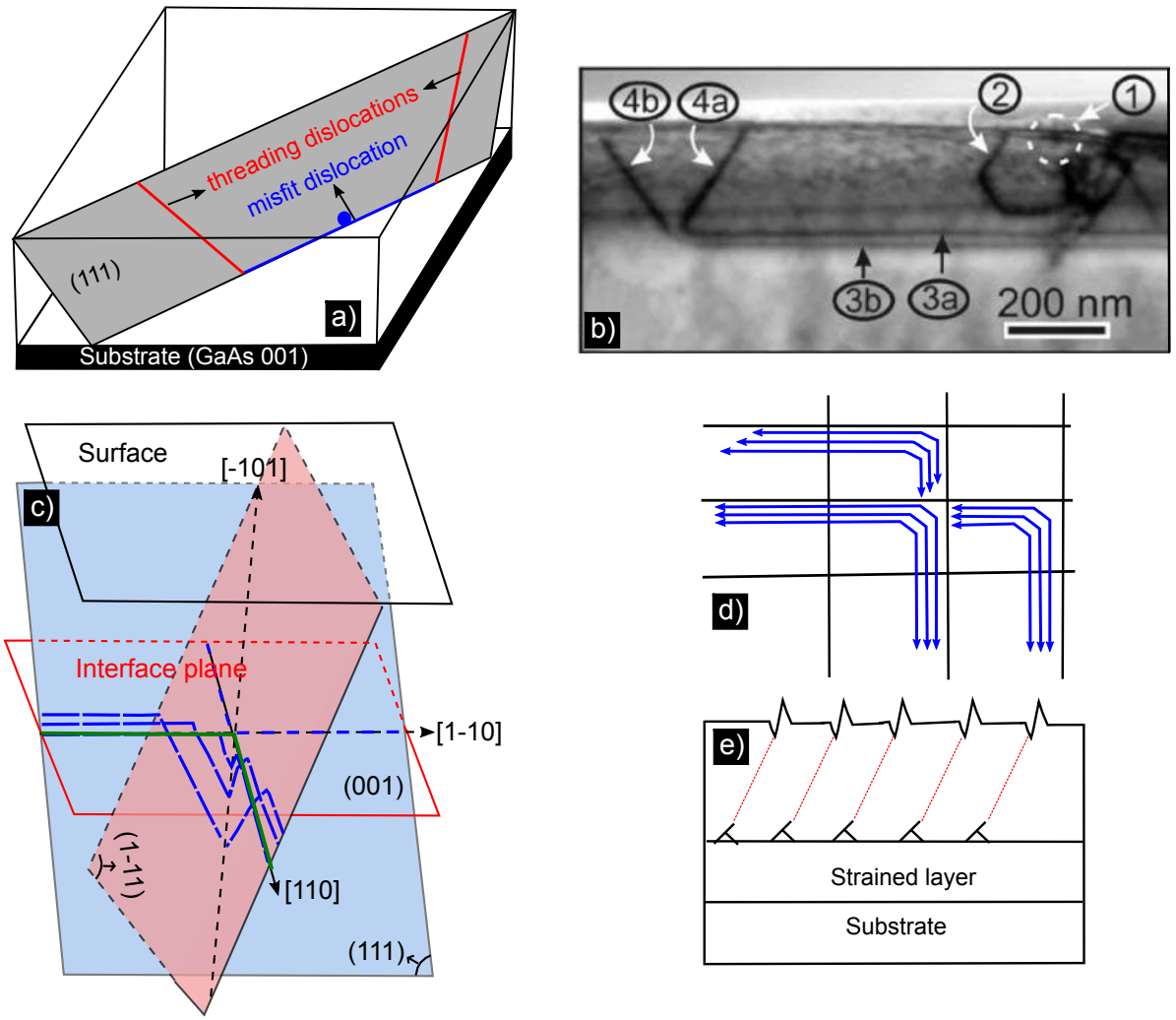

Figure 5.19: (a) Schematic representation of threading and misfit dislocations gliding on the (111) plane. Blue dot represents defect nucleation while blue line shows the half-loops of misfit dislocations. Red lines are threading dislocations. (b) TEM image taken from work of Bolkhovityanov *et.al*[176] showing dislocation half loops with threading and misfit dislocations. (c) Scheme depicting the local multiplication of dislocations arising by the MFR mechanism. Green line: two original dislocations in [1-10] and [110] directions gliding on two different glide planes, the (111) and the (1-11) plane. Blue dashed lines: multiplied dislocations through formation of half-loops. (d) top-view of dislocation running perpendicular to each other and annihilating at the meeting point. (e) side-view of misfit segments and the corresponding 60° threading dislocations leading to the surface roughness.

they are repeatedly observed and validated in similar metamorphic buffer samples.[158,171,174,175,177–180] Previous works of diffractive imaging on metamorphic buffer layers have reported subsequent high tilt and low tilt regions in form of lines running along certain crystal directions. The occurrence of high tilt lines were correlated to the pile up of the dislocations.[169] These reports also noted that the cross-hatches

pattern coincides with regions of large tilt change.

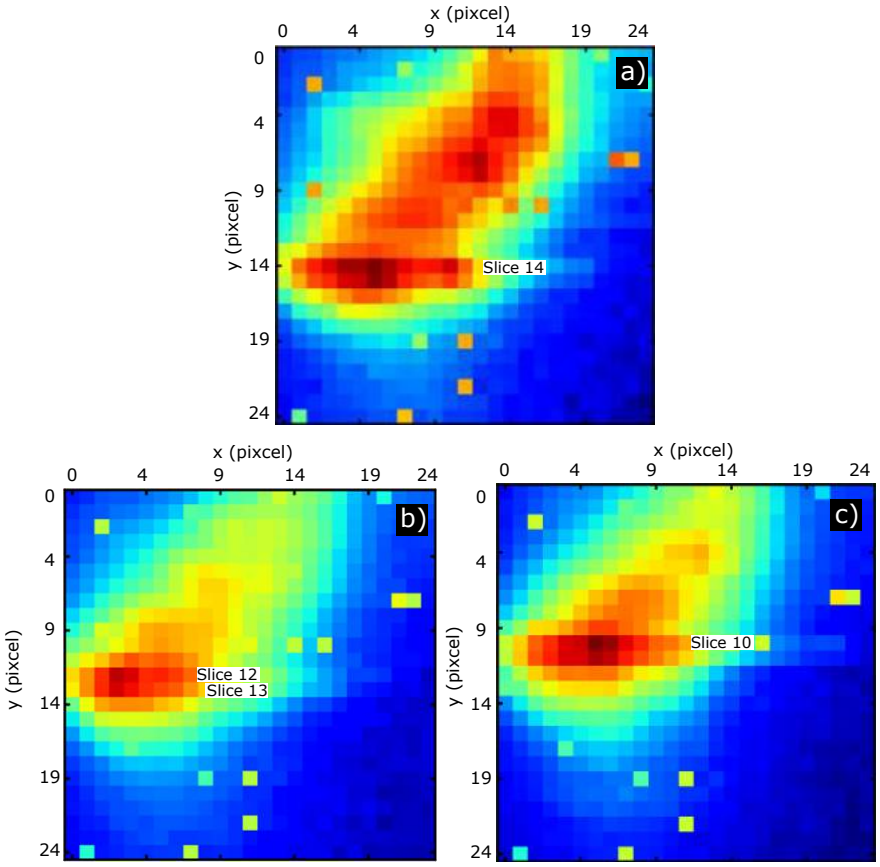

Figure 5.20: Detector frames with averaged intensity belonging to all three datasets. (a) frame from dataset-1 ($\delta\omega = 0.15°$), (b) frame from dataset-2 ($\delta\omega = 0°$) and (c) dataset-3 ($\delta\omega = -0.15°$). The mentioned slices sub-figures are the slices of interest where the maximum intensity from $In_{0.75}Al_{0.25}As$ peak is present.

As mentioned before, the inclination angle is changed for obtaining three different datasets. As a result, the position of the top layer Bragg peak ($In_{0.75}Al_{0.25}As$) on the detector frame is different in three datasets. The shift of the peak results in change in slice number of interest in different datasets which are marked in Fig 5.20. The figures shown in Fig 5.20 are the detector frames where the intensity is averaged into 25×25 pixels.

In our work, the emphasis of the analysis is concentrated on the dataset-2 where the detector is aligned to Bragg peak of the top layer of the metamorphic buffer ($In_{0.75}Al_{0.25}As$). This layer is most interesting since the electronically active layers are deposited on top of it. We expect that the structural quality of this layer strongly influences the functional aspects of the active layers. The information of other Bragg peaks corresponding to other layers in the metamorphic buffer is also extracted and analyzed from dataset-2. Whereas the datasets of 1 and 3 are only partially analyzed because the information of

the $In_{0.75}Al_{0.25}As$ layer is considered to be more important.

The slices 12 and 13 in dataset-2 are examined in detail as the maxima of the $In_{0.75}Al_{0.25}As$ Bragg peak is present in these two slices. Due to composition and strain variation the maxima of the Bragg peak shifts in these two slices but the movement is contained in only these two slices. The other slices of interest that are studied in detail are slice number 0 and and 24, where the Bragg peak from first metamorphic layer and the InAs layer are present respectively. In the following results are discussed in the order of slices starting from the first layer in metamorphic buffer which corresponds to slice #0.

The Figure 5.21) shows the maps obtained from slice #0. The AFM topography scan is shown in Fig 5.21.(a) to assist comparison between features observed from diffractive imaging technique and surface morphology. The features observed in this slice are discussed in detail so that the other slices of interest can be explained easily. The intensity map shown in Fig 5.21.(b) reveals that intensity varies in the form of lines. These lines are either parallel or inclined with respect to the x and y axis of the maps and they are observed to have different range of intensity values. Some of the observed lines where intensity value are high (low) are highlighted by black dashed lines (solid lines). The lines with low intensity are separated by $\approx 5 - 6$ µm, while the two higher intensity lines are separated by ≈ 25 µm. These lines are inclined by about $\approx 12^{\circ}$ with respect to the [1-10] crystal direction. They will be referred as inclined intensity lines or "inclined network" in the further text.

In addition to these pronounced high intensity inclined lines, faint features running perfectly parallel to [1-10] are also observed. These faint lines are separated by $\approx 1 - 1.2$ µm and are indicated by black arrow marks. They will be referred as parallel intensity lines or "parallel network" in the further text. We also observe very faint horizontal lines which are inclined with respect [110] direction. The horizontal lines are observed to be terminated when they meet with vertical inclined lines which results in local increase in intensity highlighted by black circles. As a result of termination of horizontal lines at certain points they do not extend from one end to the other end of the scan.

The intensity in the map changes due to local variation of the crystallinity of the layer which is in turn influenced by several factors like defects and local strain. To understand the origin of the observed intensity lines and the corresponding crystalline property of the layer, the magnitude of tilt change at the same area should be considered. To compare the tilt and intensity maps, the solid and dashed black lines of Fig 5.21.(b) are overlaid on the tilt map. Surprisingly, the position of lines representing high tilt change are observed to coincide with the positions of the high intensity lines. This behavior can be explained by considering the alignment of the diffraction setup. Because the detector is not aligned to the Bragg peak present in slice#0, the maxima of this peak is outside the plane of detector. So we assume that at the regions of higher tilt change (blue lines), the maxima of the Bragg peak present in slice#0 moves towards the plane of the detector resulting in an increase of the total intensity observed. This is due to displacement of Bragg peaks in q_y and q_x directions due to the tilt of sample. Similar to the intensity map, faint lines parallel to [1-10] are also observed in tilt map which are indicated by blue arrow marks.

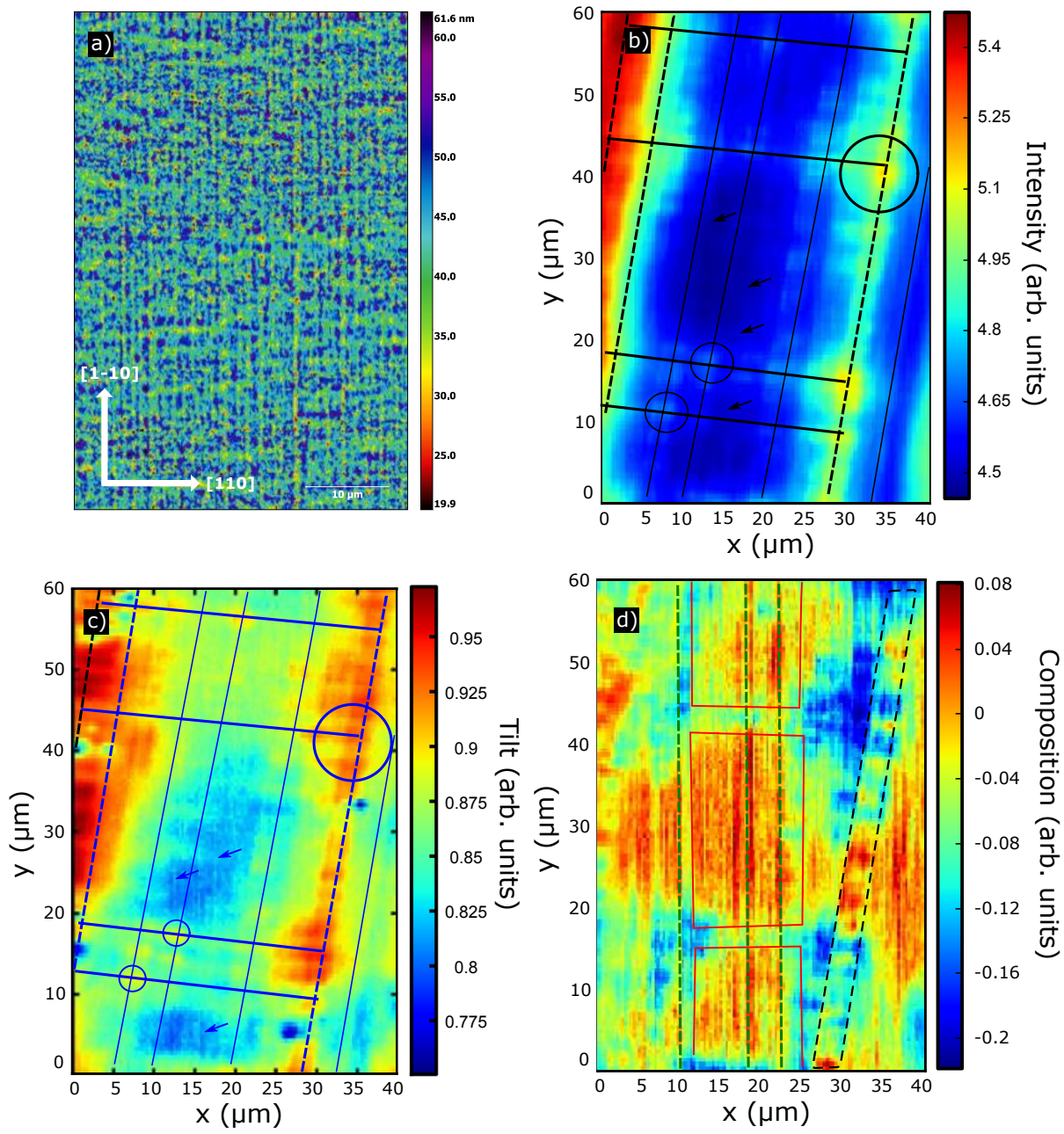

Figure 5.21: (a) 60×60 μm^2 AFM topography scan. b-d) 2D maps obtained from slice#0 using dataset-2. (b) Intensity map: solid and dashed black lines indicate low and high intensity inclined intensity lines respectively. (c) tilt map: solid and dashed blue lines indicate low and high intensity inclined tilt lines respectively. (d) composition map: green dashed lines represent composition variation lines, while the dashed trapezoidal shape highlights the inclined composition lines. Arrow in both intensity and tilt maps point to the faint network of intensity and tilt lines. The areas highlighted by circles represent the intersecting point of inclined horizontal and vertical lines resulting in higher intensity.

Because the areas with higher tilt change coincides with prominent intensity lines and considering the fact that the detector is not aligned to Bragg peak present in slice#0, we conclude that these tilt and intensity lines represent regions of high dislocation density and plastic relaxation. In other words, the red regions in both intensity and tilt maps represents areas with less structural integrity and high tilt. While the blue areas in both maps represents regions where the film is more crystalline with very little or no local variation of tilt. This observation is consistent with available literature on other material systems where regions of high tilt in heterostructure are correlated to pile-up of misfit dislocations formed during the growth.[175,181] It is worth mentioning that the highlighted lines of intensity and tilt lines do not represent an individual dislocation but may belong to pile up of many dislocations resulting in local decrease in crystalline nature of films. As both intensity and tilt lines overlap and result in less crystalline areas in the form of inclined lines and as they occur frequently in most of the slices, they will be referred as "dislocation lines" in further text.

The composition map shown in Fig 5.21.(d) provides a strikingly different picture. Here the inclined dislocation lines observed in tilt maps are not prominent any more. We observe vertical lines with alternating magnitude of composition variation that are parallel to the y axis. A few of them are highlighted with green dashed lines. These compositions lines with larger magnitude of intensity denote regions with stronger change in composition. These features are observed at a periodicity of $\approx 5-6$ µm, similar to the periodicity of the cross-hatches in the morphology of surface. As mentioned earlier, cross-hatch patterns are present at the surface of every graded layer. We observe that the composition varies along these trenches and valleys of the cross-hatch pattern because a local decrease of growth rate is expected at the cross-hatches due to pile up of dislocations.[175] Similar composition modulations are also reported by Chauveau *et.al*,[149] who analyzed TEM data on metamorphic buffers. The majority of observed lines are parallel to [1-10] axis with few minor inclined lines, which coincide with the high tilt and lower crystalline areas observed in tilt and intensity maps. Even though the composition change is seen in the form of linear lines, separated regions of fairly similar composition (highlighted by red boxes) seem to exist.

After discussing the individual features observed in intensity, tilt and composition maps of slice#0, the structural state of the corresponding metamorphic layer can be obtained. The layer is observed to contain dislocation networks in the form of periodic lines of dislocations. A network of dislocation lines which are inclined with respect to both <110> crystal directions are observed to be more dominant than the network of faint features which are parallel to <110> crystal direction in both intensity and tilt maps. The periodicity of lines in less pronounced parallel network observed in tilt and composition maps resemble the periodicities observed in surface cross-hatch pattern. This makes us believe that the local strain pattern that has developed during the early stages of buffer growth has a influence on the final morphology observed in the cross-hatch pattern. The highly tilted areas represented by dashed lines in both tilt and intensity maps indicate that the layer is a homogeneous distribution of tilted crystallites surrounded and separated by defects. The existence of this type of crystallite separation has also been

suggested from studies of X-ray pole figures of metamorphic buffers.[166]

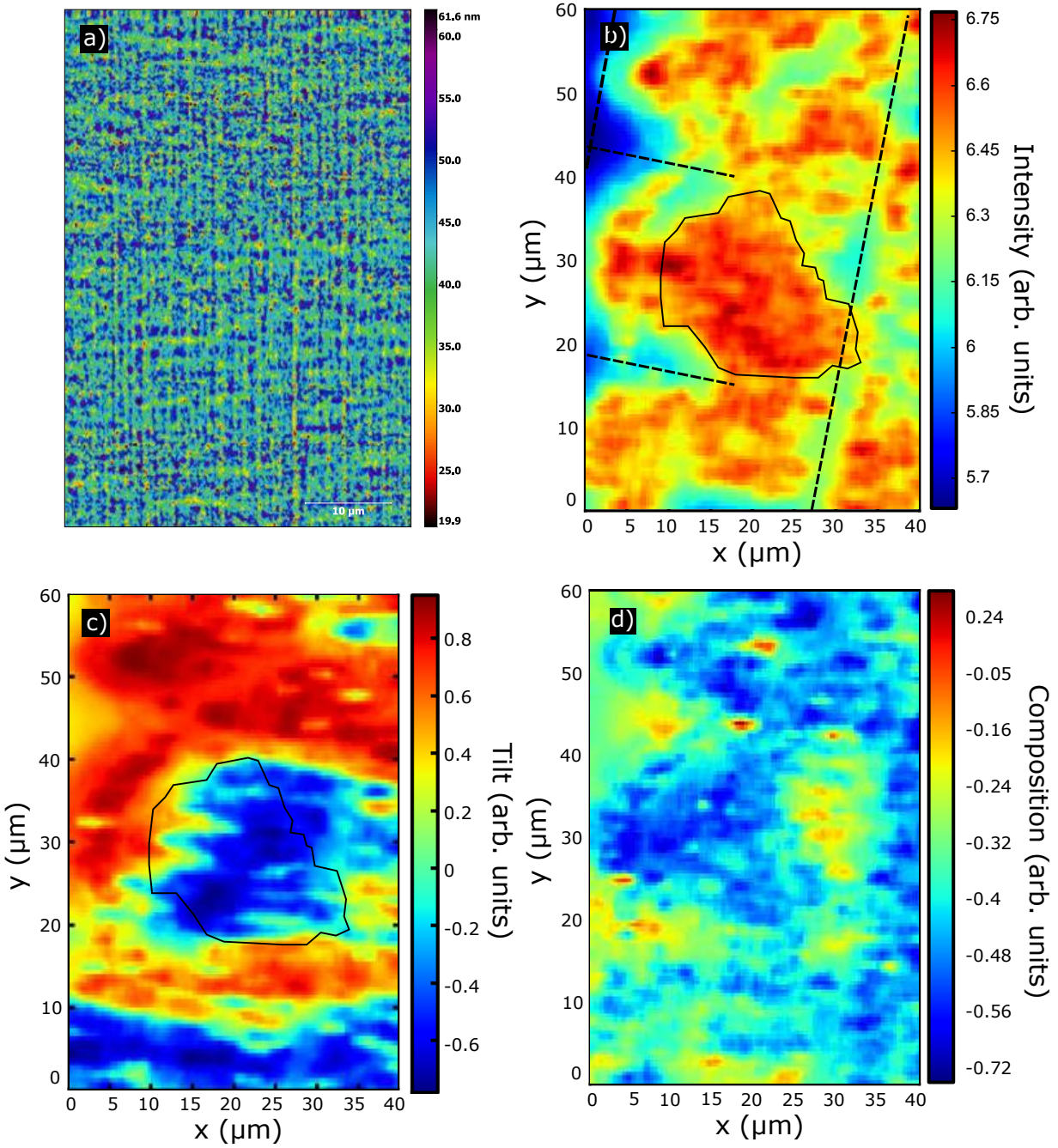

Figure 5.22: (a) $60 \times 60\ \mu m^2$ AFM topography scan. b-d) 2D maps obtained from slice#12 using dataset-2. (b) Intensity map: black dashed line highlighting the area with less intensity similar to features seen in slice#0 . (c) Tilt map. The black contour line drawn at the same position in intensity and tilt maps highlight the area with homogeneous structural quality. (d) composition map showing no periodic features in composition variation.

Fig 5.22 shows the maps obtained from the slice#12 which contains maximum of the Bragg peak of the top most layer in the metamorphic buffer ($In_{0.75}Al_{0.25}As$). The crystalline state of this layer is of utmost interest as it has a major influence on the morphology of the active layers deposited subsequently. As in Fig 5.21, the same AFM topography scan is shown in Fig 5.22.(a) to assist comparison of morphology features of surface cross-hatches to the diffraction features. Since the detector is aligned to the 004 Bragg peak of ($In_{0.75}Al_{0.25}As$), the red colored high intensity region in the intensity map shown in Fig 5.22.(b) represents a homogeneous area of layer with constant lattice parameter. The green-blue color represents an area with loss of intensity and are assumed as dislocation lines because the position of these lines coincides with ones observed in slice#0 intensity maps. The tilt map (Fig 5.22.(c) also shows a similar structural picture, where red color regions represent areas with high tilt change and blue regions with minimum tilt change.

The combined analysis of both tilt and intensity map reveals that the high tilt regions lead to low crystallinity of the layer. A rough contour line is shown in Fig 5.22.(b) to highlight the area with homogeneous intensity. This highlighted area represents crystalline part of the layer with low dislocation density. The same contour line is overlaid in the tilt map demonstrating that it matches with low tilt variation region. We also did not observe the parallel network of highly frequent dislocations lines that are observed in the slice #0. But we observed only few prominent regions of reduced intensity which are represented by black dashed lines. These lines of reduced crystallinity are noticed in every slice at the same location and may correspond to areas with plastic deformation and henceforth will be referred as major defect lines. The position of these lines are at exact same point as observed in slice#0. Unlike slice#0, the composition map shown in Fig 5.22 does not indicate a periodic variation of composition. The layer seems to have a fairly homogeneous composition distribution.

Combined analysis of intensity, tilt and composition maps reveals that the top layer of the metamorphic buffer is structurally more homogeneous when compared to the bottom graded layers. The layer seems to be made up of crystallites of dimensions $\approx 20\,\mu m$ separated from each another by a network of dislocation lines. However, only fewer dislocation lines are observed when compared to the slices from the bottom layers. Similar kind of behavior is observed in InGaAs layers studied by TEM, where the upper graded layers are found to contain a smaller density of dislocations.[182]

More information regarding the strain state and dislocation lines can be obtained by analyzing the slices recorded with different inclination angles of the sample. The intensity maps obtained on the $In_{0.75}Al_{0.25}As$ layer at three inclination angles ($\delta\omega = -0.15°, \delta\omega = 0°$ and $\delta\omega = 0.15°$) is shown in Fig 5.23.(a),(b) and (c), respectively. The maps represent the total intensity change as the incidence angle is moved away from the Bragg condition. Intensity at lower inclination angles $\delta\omega = -0.15°$ corresponds to increase in degree of relaxation with less strain and vice versa. So by studying the intensity variation in maps obtained at different inclination angles, a qualitative picture of the strain can be built up.

Similar approach has been adopted by Mondiali *et al.* for qualitative analysis of the strain state in

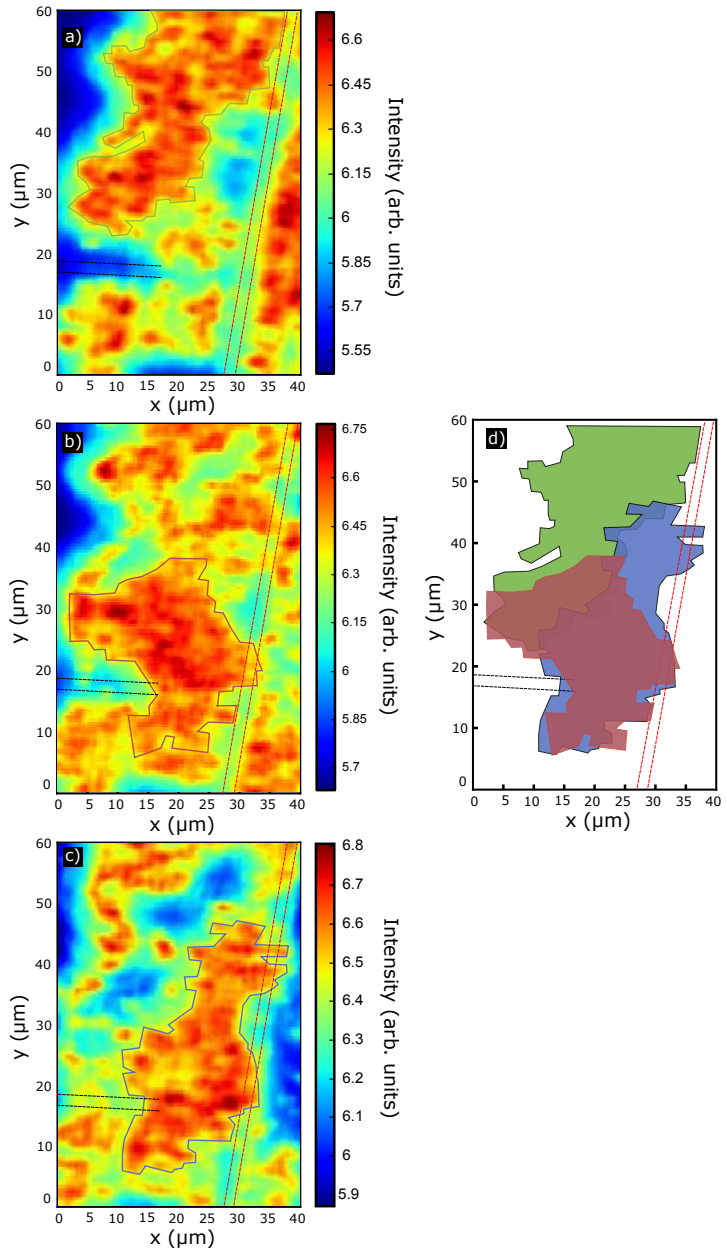

Figure 5.23: Intensity maps of $In_{0.75}Al_{0.25}As$ peak belonging to datasets 1-3. (a) from dataset-1 ($\delta\omega = 0.15°$) and slice #14, (b) from dataset-2 ($\delta\omega = 0°$) and slice #12 (c) dataset-3 ($\delta\omega = -0.15°$) and slice #10. The change in slice number between different datasets is due to shift of bragg peak due to different inclination. The slightly inclined vertical (red) and horizontal lines were placed at the same position in all four maps as guide to the eye and also to highlight the regions with less intensity. A rough contour line is drawn around regions of same intensity in all three maps. (d) The overlapped map of areas in the contour lines from $\delta\omega = 0.15°$ (green area), $\delta\omega = 0°$ (red area) and $\delta\omega = -0.15°$ (blue area). The shown maps are obtained at the same region where maps represented in Fig 5.21 and 5.22

patterned SiGe layers using diffractive imaging.[183] Rough contour lines are drawn from all three maps covering high intensity regions indicating the probable crystallites of the layer surrounded by defect lines. It is clearly seen that the intensity loss is observed at places where the major defect lines are present. The areas covered by the contour lines are merged in the Fig 5.23.(d), which reveals the areas of different strain state. The area of constant intensity obtained for $\delta\omega = 0^\circ$ (red area) is a combination of areas obtained at low and high inclination angles. This observation is consistent with the assumption that areas of different strain are mapped at different inclination angles. We also consistently noticed that there is lower intensity at the presumed locations of defect lines which validates our assumption that these regions are less crystalline areas of the layer and act as a separation between crystallites. We conclude that these regions of the layer are highly tilted with high density of dislocation pile-ups.

The Figure 5.24 shows the maps obtained from slice #24 which contains the Bragg peak from the InAs quantum well. Again, the AFM topography is shown in Fig 5.24.(a) to assist comparison between diffractive imaging technique and surface morphology. The intensity map shown in Fig 5.24.(b) reveals that the intensity variation is observed in the form of vertical lines parallel to [1-10] direction of GaAs. Few of these lines are highlighted by black dashed lines separated by $\approx 1\,\mu\mathrm{m}$. Similar lines are also observed in the tilt maps, where the regions with higher intensity corresponds to higher tilt. Considering the fact that the setup is not aligned to the Bragg peak observed in this slice and following the same analysis approach used for slice#0, we can assume that the large tilt change leads to local increase of total intensity. The periodicity of both tilt and intensity modulation is observed to be around $\approx 1 - 1.2$ $\mu\mathrm{m}$ which is close to the frequency of the lines observed on surface cross-hatches. Surprisingly, we did not observe any tilted defect lines which are prevalent in other slices. Instead, we observed isolated locations of high tilt change and total higher intensity regions which do not have a periodic distribution. These isolated areas might have resulted due to high density of dislocations in the layers underneath leading to non homogeneous growth locally. Similar to the slice#12, no major composition variation in the form of inclined lines are observed. We observed faint modulation in composition similar to tilt and intensity maps. The isolated features of composition variation were observed in the same location as seen in tilt and intensity maps and are highlighted with blue circles.

The combined analysis of all three maps obtained from slice#24 leads to the conclusion that the inclined network of defect lines are absent in the InAs layer. The network of tilt and intensity lines modulation seen in slice#24 corresponds to the faint parallel network observed in bottom graded layers. The periodicity of modulation is very important information as it leads to a non-planar 2-dimensional electron gas (2-DEG). The electric field built up in [001] direction due to asymmetric profile of layers in combination with the electron momentum transforms into an effective magnetic field due to spin-orbit (SO) interaction. This phenomenon is called Rasbha spin-orbit coupling[184] and is affected by non-planar 2-DEG.[27] Lohr *et al.*[27] reported direct observation of non-planar 2DEG in the similar sample structure that were used for our measurements. This report also noted that curvature induced SO interaction may arise and in metamorphic buffer based heterostructures and must be considered while discussing the Rasbha

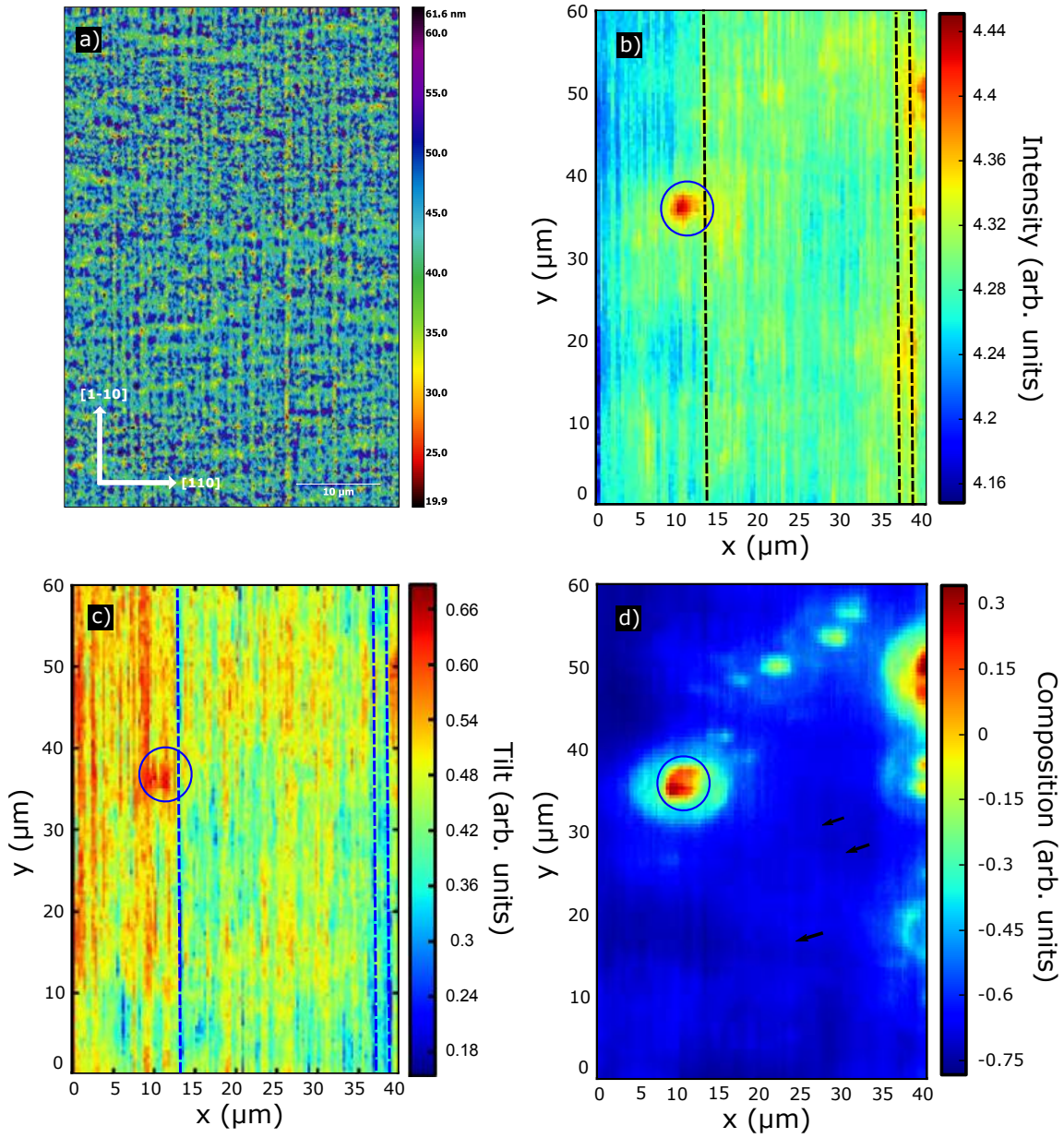

Figure 5.24: (a) 60×60 μm^2 AFM topography scan. b-d) 2D maps obtained from slice #0 using dataset-2. (b) Intensity map: black dashed line highlighting the area with increase of total intensity. (c) tilt map: blue dashed line showing lower intensity line of tilt drawn at the same position as intensity lines. (d) composition map showing very little composition variation with faint parallel network (highlighted by black arrows) similar to the one seen in tilt and intensity maps.

SO coupling. Thus, the magnitude of the periodicity of modulation is also important influencing factor when the working principle of fabricated devices heavily relies on the property of spin-orbit coupling. As mentioned earlier, results from each slice gives additional information regarding the metamorphic buffers. After analysis of slices of interest, we obtain an overall picture about the structural quality

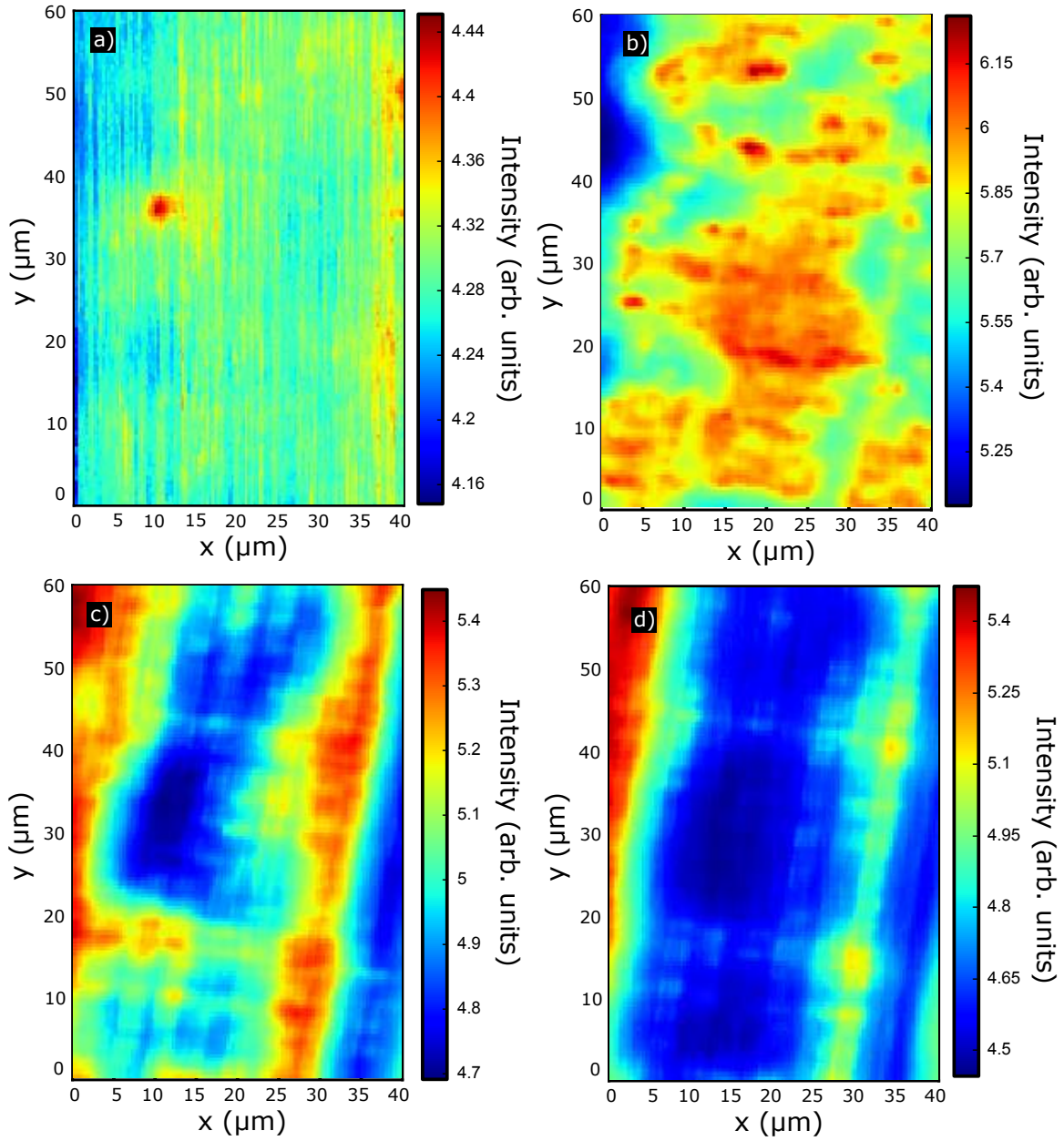

Figure 5.25: a-d) Intensity maps obtained from slice slice#24 (InAs peak), #12 ($In_{0.75}Al_{0.25}As$ peak), #4 ($In_{0.25}Al_{0.75}As$ peak) and #0 ($In_{0.05}Al_{0.95}As$ peak) respectively.

of metamorphic buffer layers and how it influences the morphology of surface cross-hatches and the properties of the active layers. To better explain the evolution of varying defect density and strain state in graded layers from substrate to top layer, maps of different slices belonging to dataset-2 are presented together. For example, the intensity maps obtained from slice#24 (InAs peak), #12 ($In_{0.75}Al_{0.25}As$ peak), #4 ($In_{0.25}Al_{0.75}As$ peak) and #0 ($In_{0.05}Al_{0.95}As$ peak) are shown in Fig 5.25.a-d respectively.

We first analyze the slice belonging to bottom most layer (Fig 5.25.(d)). The inclined network of defect

lines are clearly visible in this slice which makes us believe that this network is formed at early stages of the metamorphic buffer. In addition, a faint parallel network is also observed in this slice. The defect lines are not highlighted in this figure so that the lines can be clearly resolved. Next, we consider the slice#4 which belongs to Bragg peak of the $In_{0.25}Al_{0.75}As$ layer and its intensity map is depicted in Fig 5.25.(d). Here we can still see the network of inclined lines and they appear to be much more sharp and clear. Also, bright red spots are clearly visible at regions where horizontal and vertical inclined lines intersect. We tentatively conclude that the sharpness of the features is due to an increase in the dislocation density. Surprisingly, the sharp defect lines are not clearly visible in the top-most buffer layer (slice#12) showin Fig 5.25.(b). Instead the layer seems to contain large crystallites separated by defects. The horizontal slightly inclined lines, which are clearly visible in previously discussed two slices are hardly visible in slice#12. Also, the parallel network of defects is not observed because it might be obscured by the dominant high-intensity crystallites. The most notable feature of the slice#24 (InAs layer) is shown in Fig 5.25.(a), where the observed parallel network in this layer resembles the cross-hatch morphology, but the inclined network of defects is barely present. This analysis shows that the behavior and evolution of different dislocation network with respect to increasing indium content. We obtain the same picture of defect evolution when the tilt maps are analyzed.

The analysis of composition maps sheds a slightly different picture on the properties of different layers, where the change in composition across various layers does not follow the same trend as observed in intensity maps. Composition maps obtained from slice#24 (InAs peak), #12 ($In_{0.75}Al_{0.25}As$ peak), #4 ($In_{0.25}Al_{0.75}As$ peak) and #0 ($In_{0.05}Al_{0.95}As$ peak) are shown in Fig 5.25.a-d, respectively. The composition modulation in the bottom layer seems to occur hand in hand with respect to the parallel network where the modulation is observed to be more prominent along the parallel network. While, the composition modulation in slice#4 is observed to be more prominent along the inclined network of defect lines. However, there are no prominent periodic features of composition modulation in slice#12 indicating presence of large crystallites. The composition map of slice #24 resembles the intensity and tilt maps obtained from the same slice. The combined analysis of composition maps suggests that the variation of composition is dependent on the presence of defects and modulates along the prominent network of defect lines observed in that particular slice of interest.

In summary, we observed two dislocation networks in our heterostructure. The first network consists of dislocations that are running in perpendicular crystal directions (<110>) resembling the surface cross-hatch pattern. This network is referred as parallel network. The second dislocation network is one consisting of features in form of inclined vertical lines $\approx 12^{\circ}$ w.r.t to [1-10] direction. This network might have formed due to predominant screw nature of both the threading dislocations in two <110> directions and 60°MDs.[173,179] However the screw nature of 60°dislocations are known to deteriorate the structural quality of film not only near the interface, but also in the film volume. The presence of screw component from the already existing dislocation network might have lead to formation of lines of reduced crystallinity and high tilt variation that are tilted with respect to <110> crystal directions.

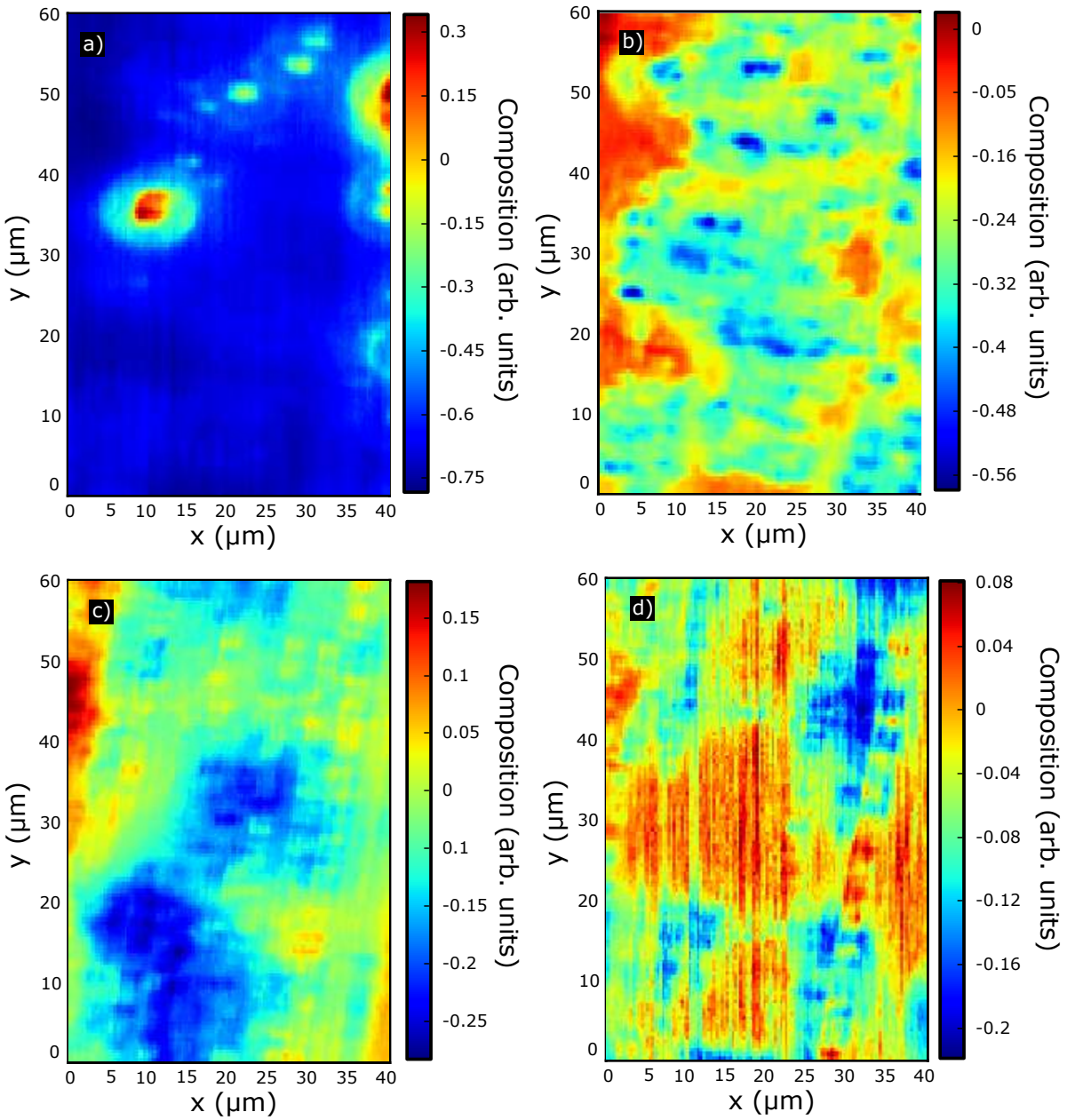

Figure 5.26: a-d) Composition maps obtained from slice slice#24 (InAs peak), #12 ($In_{0.75}Al_{0.25}As$ peak), #4 ($In_{0.25}Al_{0.75}As$ peak) and #0 ($In_{0.05}Al_{0.95}As$ peak) respectively.

5.3 Spin injection through 2D InAs quantum wells

Spin injection experiments are carried out on the same sample (C21N600) that is studied by diffraction imaging. These experiments are conducted in collaboration with Dr. Lennart Liefeith and a more detailed account of these experiments and fabrication protocols are reported in his thesis.[59] The main aim of these experiments is to achieve spin injection from a ferromagnetic metal layer into InGaAs/InAs

quantum wells. The devices operating in the ballistic transport regime have received large interest due to reported large spin injection efficiencies.[14,23,145] The design of our heterostructure is designed to obtain high mobility of the active carriers[22,27,185] which allows the device to work in ballistic limit.

5.3.1 Sample design and band structure of modulation-doped InAs heterostructure

The heterojunction is designed in a such a way that the active layers form a quantum well containing 2-Dimensional Electron Gas (2-DEG) as shown in Fig 5.27.(a). The quantum well consisting of 4 nm InAs is buried under a 10 nm $In_{0.75}Al_{0.25}As$ layer which acts a tunneling barrier. The channel is asymmetrically sandwiched by two $In_{0.75}Ga_{0.25}As$ layers which reduce the amount of strain in channel and also enhance the Rasbha SOI in the InAs channel. The quantum is separated from the doping region by 10 nm $In_{0.75}Al_{0.25}As$ layer acting as a spacer to enhance the electron mobility in the 2DEG. We used silicon doping concentration of 1.6×10^{18} cm^{-3}. The doping concentration is calibrated in advance by magneto-transport measurements using the AlGaAs HEMT structures.

After deposition of all active layers the sample is transferred into a metal MBE chamber in vacuo. A 4 nm Fe layer is deposited at a rate of 0.4 nm/min followed by a 7 nm Au capping layer at the rate of 0.2 nm/min. Both the metal layers are deposited at room temperature. The sample layout highlighting the active layers with nominal thicknesses and the corresponding conduction band diagram is shown in Fig 5.27.a&b respectively. The gray color is used to represent the quantum well in both sub-figures. The conduction band profile shown in Fig. 5.27.(b) is calculated by using the 1D self-consistent Poisson and Schrödinger equation solver nextnanomat.[186] The conduction band (E_c) and electron density n_s profiles in the growth direction are plotted against the left and right axes, respectively. The Schottky barrier height ϕ_o of Fe/InAlAs used in the calculations is adjusted so that the resultant calculated carrier densities match the experimentally determined values. The measurement and the obtained value of the carrier density is discussed in the next subsection. It is clearly seen that the conduction band is pulled below the Fermi level (E_f) at the InAs channel forming a 2DEG. The calculation is also used to obtain the band edges of ground state subband (-25 meV), as well as the first subband (66 meV) and second subband (163 meV) which are highlighted in Fig. 5.27.(b). It is also observed that there exists only one maximum of carrier density which is located inside the InAs channel indicating absence of other parallel conducting channels.

5.3.2 Magneto-transport and contact properties

Hall bars are fabricated prior to the fabrication of the non-local devices to obtain electron mobility (μ) and 2D carrier concentration (N_s) in the InGaAs/InAs quantum wells from magneto-transport measurements. Both of these parameters are obtained from the quantum Hall effect[187,188] and Schubnikov-de oscillations.[189] Details of the corresponding analysis are explained elsewhere.[190] The geometry and

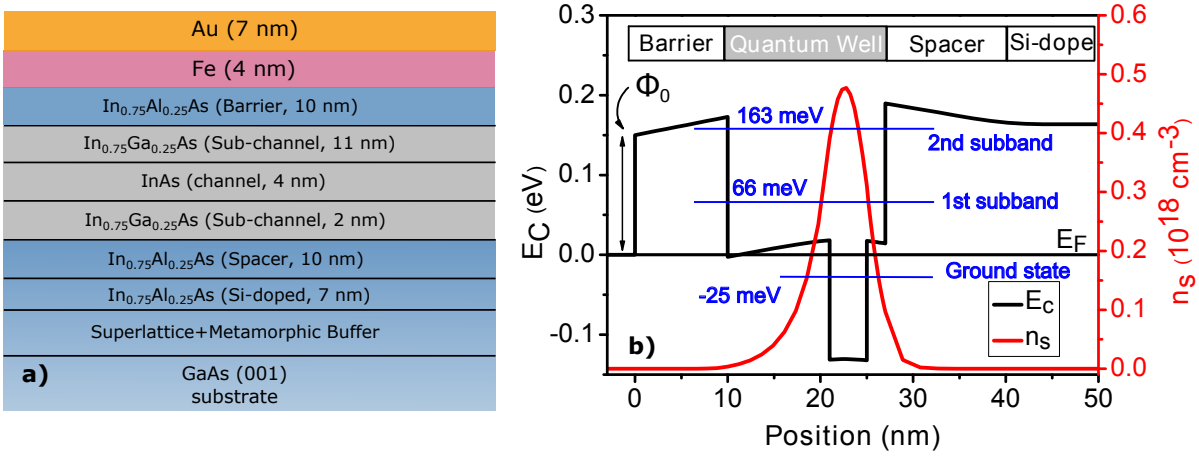

Figure 5.27: (a) The sample layout highlighting the active layers deposited on top of the metamorphic buffer. (b) The calculated conduction band and electron density profiles obtained from the sample layout.

the dimensions of the fabricated Hall bars are depicted in the Fig. 5.28.(a). The long axis of the hall bars are oriented in [1-10] direction which is the orientation of the channel used in non local devices. The measurements are performed with out-of-plane magnetic field at liquid helium temperatures using a 300 mK setup. Two different voltages called longitudinal (U_{xx}) and Hall voltage (U_{xy}) are measured as a function of magnetic field with a driving current of 100 nA. The measurements are performed with a lock-in technique at a working frequency of 76 Hz. The carrier concentration is evaluated using two separate methods.

First, the obtained longitudinal $\rho_{xx} = \frac{w}{l}\frac{U_{xx}}{I}$ and hall $\rho_{xy} = \frac{U_{xy}}{I}$ resistivity are plotted as function of applied magnetic field as shown in Fig 5.28.(b). Where, $w\&l$ are the width and longitudinal contact distance of hall bars. Due to Lorentz force, a hall voltage (U_{xy}) is built up perpendicular to the direction of current and magnetic field. In the limit of 2D quantization, the Hall voltage shows plateaus in dependence on perpendicular magnetic field. These plateaus in the hall resistivity ρ_{xy} (black line) is shown in Fig 5.28.(b). The carrier concentration ($N_{s,Hall}$) is then calculated from the hall voltage is given by:

$$N_{s,Hall} = \frac{1}{e.\frac{d\rho_{xy}}{dB}} = 4.81 \times 10^{11} \frac{1}{cm^2} \tag{5.6}$$

The resistance oscillations which are called Shubnikov-de oscillations (SdH), arise from Landau quantization of the 2DEG in presence of a perpendicular magnetic field. These oscillations are periodic in $\frac{1}{B}$The carrier concentration ($N_{s,SdH}$) can be calculated from the periodicity of the oscillations as a function of $\frac{1}{B}$ by using:

$$N_{s,SdH} = \frac{g_s g_v . e}{h\Delta(\frac{1}{B_{min}})} = 4.98 \times 10^{11} \frac{1}{cm^2} \tag{5.7}$$

Here, g_s and g_v represent spin degeneracy and valley degeneracy $g_r = 2$ and $g_r = 1$ in InAs, respectively. Where e is the elementary charge and h is the planks constant. Usually the period in Eq 5.7 is determined from magnetic fields B_{min} at the minima of the longitudinal resistance. The calculated values of ($N_{s,Hall}$) and ($N_{s,SdH}$) are both in agreement within the experimental precision indicating that the entire carrier concentration is located in the quantum well and no parallel conductance channel exist in correspondence with the simulation. From the obtained carrier concentrations, both mobilities and the resultant electron mean-free-path λ_{mfp} of the carriers in the quantum well are calculated by using the following equations.

$$\mu = \frac{1}{e.n_s.\rho_{xx}(B=0)} = 107\,000\ \frac{\mathrm{cm}^2}{\mathrm{Vs}} \tag{5.8}$$

$$\lambda_{mfp} = \frac{\mu}{e}\hbar.\sqrt{2\pi N_s} = 1.2\ \mu\ m \tag{5.9}$$

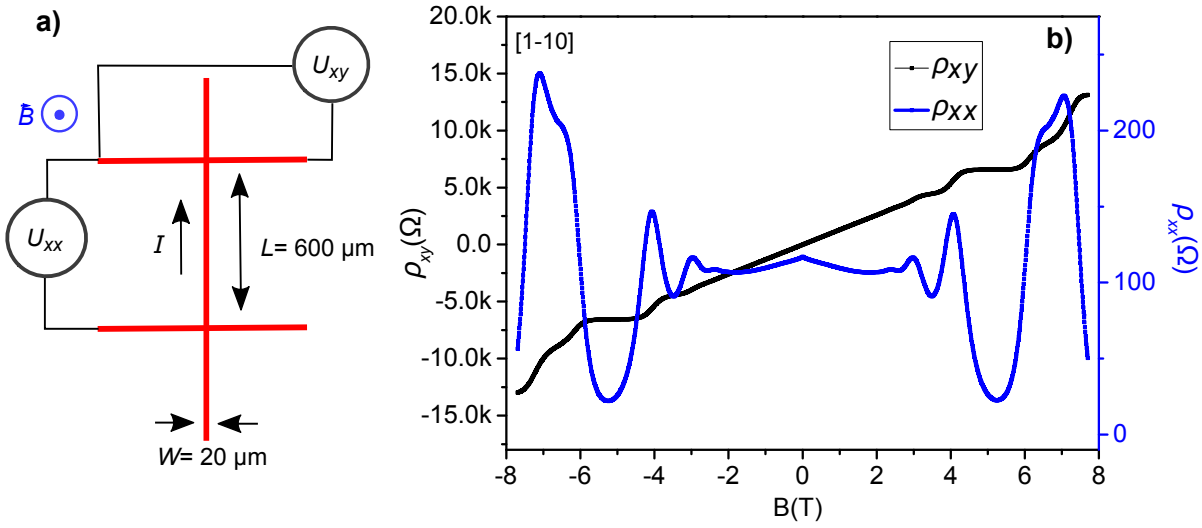

Figure 5.28: (a) measurement setup of Hall resistance and SdH oscillations. B is the applied perpendicular magnetic field while w and l are the width and length of the hall bar. (b)The measured longitudinal (ρ_{xy}) and transverse (ρ_{xx}) resistivity plotted as function of magnetic field.

The mobility μ is four times larger in magnitude when compared to reported values on InAs containing structures used for previous spin injection experiments.[147,148] The obtained electron mean-free-path (λ_{mfp}) parameter describes the average distance a carrier travels between two in-elastic scattering

events. The fabricated devices work in ballistic regime if the contact separation $L < \lambda_{mfp}$. The obtained above parameters are used for evaluation of the non-local signal. The measurement performed on Hall bars with long axis parallel to [110] resulted in lower mobilities which is consistent with previous works.[27,185] This mobility anisotropy is believed to be correlated to the observed anisotropy of the cross-hatch modulation observed from the AFM analysis and diffractive mapping.

As mentioned before, the top layer of 10 nm $In_{0.75}Al_{0.25}As$ acts as a tunneling barrier between the metal and the quantum well. The contact properties of the resultant tunnel junction between one of the iron electrodes and the active layers of the semiconductor are measured using a 3-terminal setup. The 3-terminal measurement were performed on fabricated spin-valve devices. The measured current-voltage characteristics are plotted as both conductance ($G = \frac{j}{U_{3T}}$) and differential conductance ($G_{diff} = \frac{\partial j}{\partial U_{3T}}$) as a function of U_{3T} (Fig 5.29). As the measurement are performed on the spin-valve device, both conductance and differential conductance are normalized to electrode contact area of 50 μm^2. The negative and positive bias are indicated as injection and extraction respectively. Where, injection (extraction) means tunneling of carriers from Fe electrode into the 2DEG (vice-versa).

It can be seen from Fig 5.29 that, in injection polarity, the conductance (G) increases in step-wise fashion. The derivative of conductance (G_{diff}) clearly depicts these steps as maxima which correspond to values of 80 meV and 200 meV. These peaks corresponds to the energetic positions of first and second subbands when the negative bias pulls them below Fermi level and the carriers from Fe electrode tunnel into these 2d sub-bands. The energetic positions of the sub-bands are about 1.2 times larger than the values of the simulation in Fig 5.27.(b). The conductance in extraction polarity increases exponentially which is attributed to the carriers tunneling from an rectangular shaped barrier tunneling into metal which in our case is the carriers tunneling from 2DEG into Fe electrode. The current-voltage characteristics reveal that the conductance is non-linearly dependent on the applied bias which includes observation of steps in negative polarity. The two observations strongly suggests that the transport occurs by tunneling mechanism as carrier tunnel into subbands indicating existence of 2DEG in the active layers of our structure.

5.3.3 Non-local measurement on spin valve

Unlike spin-valve devices fabricated on Fe/GaAs heterostructures as discussed in chapter 3, the fabrication of spin-valve devices on Fe/InAlAs heterostructures requires a careful design. The strategy of spin-valve design is based on four different properties of the Fe/InAlAs system. The first property is the observed anisotropy of mobilities in two crystal direction as mentioned earlier in Sec 5.3.2. The second important material property of Fe/InAlAs system is the magnetic anisotropy of Fe films on InAlAs. Fe films on InP were reported to have an in-plane magneto-crystalline uniaxial anisotropy with easy axis along [110] direction.[191] Same easy axis orientation of magnetic anisotropy is observed on our samples grown on InAlAs buffer layers by Boris Landgraf during his Ph.D[119] using MOKE technique. So the

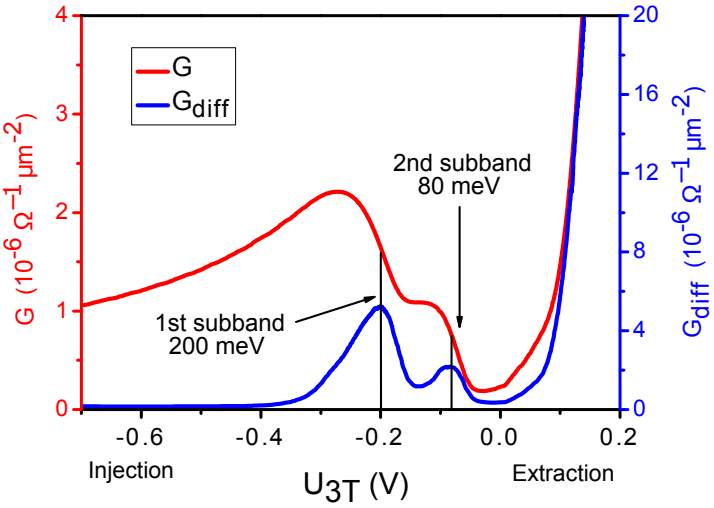

Figure 5.29: The red and blue lines represent the conductance and differential conductance as a function of U_{3T}. The energetic position of the first and second subbands are marked by arrows.

electrodes are oriented along [110] direction to match the easy axis orientation of magnetic anisotropy.

The third property that has been taken into consideration while designing the spin valve is the crystallographic anisotropy of the SOI. In the adapted configuration of spin valve with carriers propagating in [1-10] direction, an effective magnetic field (B_{eff}) is experienced by the carriers in [110] direction due to SOI. In this case the injected carrier spins are parallel to the B_{eff} which leads to longer spin-dephasing lengths and increased spin-halftimes.[146,147,155,156] To enable longer spin-dephasing lenghts the orientation of the Fe electrodes is kept perpendicular to the [1-10] direction. The effect of spin-dephasing lenghts and spin-lifetimes on spin injection efficiency are discussed later in the same subsection.

The second and third material properties and their experimental methods for their determination are not discussed as they are out of scope of this thesis. But the main results from the measurements are briefly presented and readers are referred to the thesis work of Dr.Lennart Liefeith[59] for more details. The last parameter that is considered while fabricating spin valves is the spacing between the injector and detector electrode with respect to the measured mean-free-path. To investigate the spin injection and spin transport phenomenon within the ballistic limit, the electrode edge to edge separation should be smaller than the measured mean-free-path. By combining all four properties discussed above, a spin valve is fabricated which is shown in Fig 5.30.

The Fe/InAlAs spin-valves are fabricated using electro-beam lithography and photo-lithography steps. The use of electron-beam lithography step is essential to define the smaller dimension electrodes (widths of 2& 3 µm) and the supply lines to these electrodes. The etching of the layers is performed by standard wet-chemical etching and the parts of the device without Au layer protection were covered by a insulator to prevent supply lines from shortcutting the quantum well. The width of the channel is 30 µm. For every device four Fe electrodes were defined with different dimensions marked as 2,3,4,&5 in Fig 5.31.

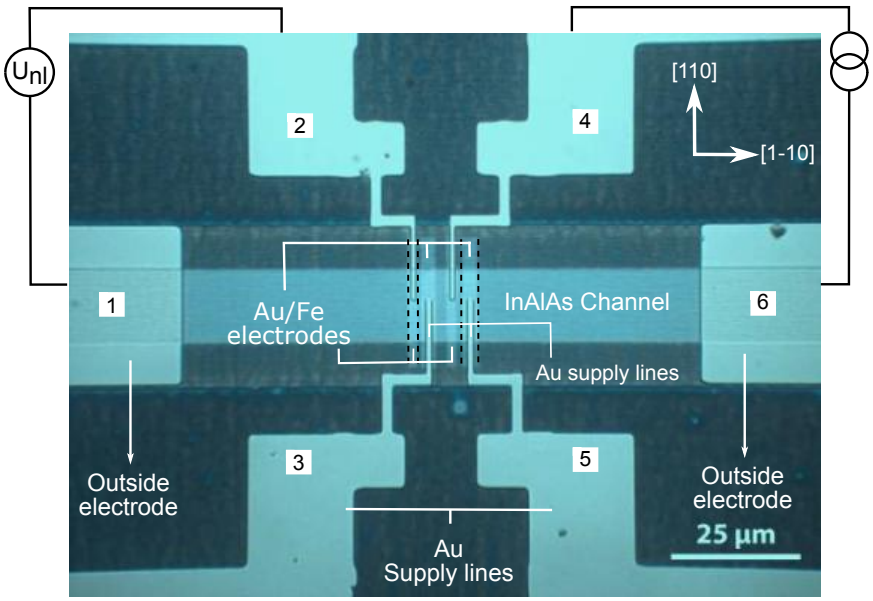

Figure 5.30: Microscopic image of the fabricated spin-valve device highlighting the important components. The channel is oriented along [1-10] while the electrodes are aligned along [110] crystal directions. The non-local voltage (U_{nl}) circuit and current source used in the experiment are also indicated.

The width of the electrodes of 2&4 is $2\,\mu m$ while for 1&3 it is $3\,\mu m$. The separation between the electrodes 2&3 is $0.5\,\mu m$, 4&5 is $1\,\mu m$, and for 3&4 it is $2\,\mu m$. The larger reference electrodes are marked as 1&6, while the Au/Fe electrodes are highlighted by dashed lines.The calculated mean-free-path in our sample is $1.2\,\mu m$ but, considering both the width of the Fe electrodes and the shortest separation distance (500 nm between 2&3), we arrive at a situation where the entire electrodes are not under ballistic conduction. This leads to the different regions between injector and detector where conduction occurs through ballistic regime while some areas with diffusive regime. The devices that work completely in ballistic regime could not be prepared due to small λ_{mfp} observed in the samples which makes the device fabrication at these dimensions challenging.

The measurement configuration resembles the already discussed non-local setup in the Sec 2.1. The non-local voltage jumps (ΔU_{nl}) measured with 1.4 μA driving current are shown in Fig 5.31. The 1&2 Fe electrodes are used to measure the non-local voltage while the contact 3&6 are used to drive the current. The measurement configuration is depicted schematically in the inset in Fig 5.31. The magnetic field (B) is swept in-plane from -60 to 60 mT with step size of 0.1 mT at a rate of 2.4 mT/min. The sweeping is done both in forward and in backward direction. At the used current polarity the observed jumps correspond to spin injection from the iron electrode into quantum well which is characteristic to spin injection experiments on different systems.[52,121,122] The baseline in the measurement corresponds to the parallel magnetic orientation of the electrodes. The jumps in the non-local voltage reflect the state of the electrodes when they have opposite magnetic orientation. The orientations of the electrodes

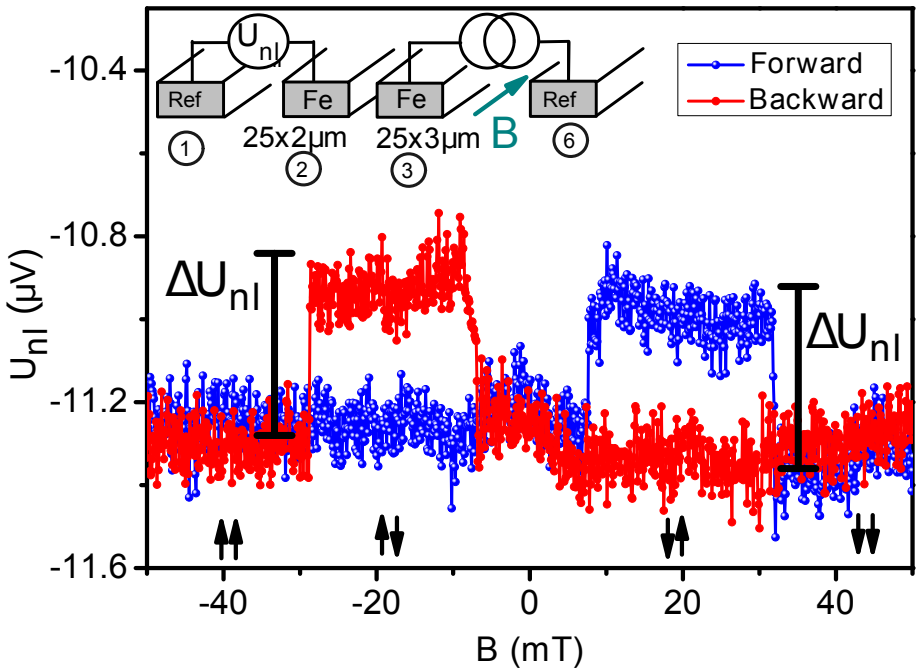

Figure 5.31: non-local signal observed in both forward and backward sweep of in-plane magnetic field. The inset shows the electrodes used for the measurements and the numbering is consistent with Fig 5.30. The black arrows represent the magnetic orientation of the two electrodes corresponding to the signal on top of them. The electrode separation between 2 and 3 is 500 nm.

are marked as arrows beneath the corresponding signal in Fig 5.31. The experiment is also performed using 1 and 2 μm electrode separation distances, but non-local jumps are not observed at these electrode separations.

The non-local signal is also measured at different applied biases and discussed in Dr.Lennart Liefeith thesis.[59] The bias dependence is not clearly understood but the data is important as non-local voltage behavior data as a function of applied bias so far is scarcely available on Fe/InAlAs system. The observed behavior of non-local jumps (ΔU_{nl}) and the corresponding non-local resistance ($\Delta R_{nl} = \frac{\Delta U_{nl}}{I}$) as a function of bias are briefly described here. In the forward bias direction the heights of jumps (ΔU_{nl}) decreases with increasing bias while it is observed to increase in negative bias regions. A maximum value of ΔU_{nl} is observed in reverse bias which corresponds to electrons tunneling into the first sub-band of the quantum well. In correspondence, an increase in ΔR_{nl} is not observed for electrons tunneling into the first sub-band. The behavior of both ΔU_{nl} and ΔR_{nl} is asymmetric with respect to the applied bias and current. The maximum non-local resistance is observed in reverse bias region with a value $\Delta R_{nl} = 0.47\ \Omega$ close to zero bias. This value is used to calculate a spin-injection efficiency η from either a diffusive or a ballistic transport model.

Initially the spin-injection efficiency (η) is calculated by using the diffusive model also used for the Fe/GaAs system discussed in chapter 3. The equation is modified to include the sheet resistance of the

2DEG. By using the calculated value of $\Delta R_{nl} = 0.47\Omega$, we obtain $\eta = 77\%$ which is very large when compared to the previously reported values, which barely exceed $\eta = 8\%$.[23,147,148] Unrealistic values of spin-injection efficiency ($\eta = 650\%$) have also been observed by Oltscher *et.al*[14] when the diffusive model has been used for their ballistic 2D AlGaAs/GaAs system. This system used by Oltscher *et.al*[14] has longer λ_{mfp} and larger contact separation than compared to our Fe/AlGaAs system and are easier to fabricate. We assume that high value of η observed in our system is attributed to the partly ballistic character of our system as it was previously reported by Oltscher *et.al*[14] in ballistic 2D AlGaAs/GaAs system.

Recently Chen *et.al* proposed a new model to calculate spin-injection efficiency to account for the ballistic contributions[25] and the spin-orbit interactions of the system. They have introduced a new parameter called spin-dephasing length which is a measure for the distance in which the spin-orientation is randomized in the ballistic limit. In their model the spin-dephasing length has inverse relation to the spin-orbit coupling parameter(α) which is calculated separately on our sample by using a SDH beating pattern measured at 250 mK. By combining the spin orbit parameter and the literature value of reduced mass ($m^* = 0.036m_e$), we obtained spin-dephasing length of $0.35\,\mu m$. By using the mentioned parameters the spin-injection efficiency for electrode separation of $0.5\,\mu m$ is calculated to by around 30%. However, unphysical values beyond 100% were obtained if larger electrode separations of L=1 and $3\,\mu m$) are used to model the spin-injection efficiencies. These unphysical values are observed to return below 100% if larger values of spin-dephasing length are used ($\lambda = 0.5\,\mu m$for L=1 μm & $\lambda = 1.5\,\mu m$for L=3 μm). This could be explained by taking into fact that in our configuration, the SOI leads to longer spin-dephasing lengths due to crystallographic orientation and of electron momentum and spin polarization direction.[146,147,155,156] Hence, we assume that the spin-orbit interaction is not appropriately modeled in the ballistic limit by model proposed by Chen *et.al*[25] and the crystallographic orientation of electron momentum and spin-polarization must be taken into account in the ballistic limit.

5.4 Chapter summary

The Fe/InAlAs heterostructures containing InGaAs/InAs quantum well deposited on metamorphic buffer has been designed. The indium content has been carefully calibrated using *ex-situ* High Resolution X-ray diffraction. The growth conditions and growth speed are modified after calibration to achieve high quality heterostructures that precisely resemble the nominal designed structure in both composition and thickness. The surface morphology of the fabricated heterostructure is studied with AFM and Nomarski microscopy which revealed the presence of a rough surface in the form of cross-hatches. Further analysis of the surface features revealed the anisotropy in both periodicity and magnitude of roughness in [110] and [1-10] directions. This anisotropy is tentatively correlated to at different density of misfit dislocations in both [110] and [1-10] directions.

The strain relaxation due to lattice mismatch is studied by reciprocal space mapping measured at different sample azimuths which revealed presence of crystallographic tilt in the metamorphic buffers. The tilt in individual layers of metamorphic buffer is studied which revealed that the magnitude of tilt (η_{max}) with respect to (001) increases with increase of Indium content. It is observed to increase from 0.14° in the first composition layer to 0.352° in the final layer (x=0.75). The inclination of tilted layers ϕ_o with respect to [110] also follows the same trend where it increases from 1.07° to 12.76°. Interestingly, the measured two parameters of tilt are considerably less when compared to the values reported on previously studied InAlAs metamorphic buffers. We believe that this is due to deposition of AlAs/GaAs super-lattice prior to growth of metamorphic layers. Tilt results in lattice relaxation and the smaller magnitude of tilt indicate better relaxation of the mis-matched layers. This observation is also corroborated in samples of similar design with TEM studies, where very little plastic relaxation is observed in samples with super-lattice.

The lattice tilt results obtained with a laboratory diffractometer inevitably reveals averaged values of lattice tilt due to large X-ray beam size. But this information is not adequate enough to understand the local change of tilt which is important for understanding non-planar nature of the active layers and especially the curvature of the quantum well. The local crystalline properties of individual metamorphic buffer layer are probed with the help of Scanning diffractive mapping. The qualitative analysis of local crystallinity, tilt variation and composition variation led to understanding the evolution of the defect density in each buffer layer. The diffractive maps revealed variation of tilt and local crystallinity in the form of two networks of defect lines that are either parallel or tilted with respect to [1-10] crystal direction. These defect lines in these two networks are related to regions with dislocation accumulation. The density of these lines is observed to decrease from bottom to top. In bottom layers the network of defect lines that are slightly rotated with respect to [1-10] are found to be predominant. A faint network of lines parallel to [1-10] direction is also observed. Interestingly, the top and thickest buffer layer $In_{0.05}Al_{0.95}As$ is observed to have large crystallites separated by high tilted regions and defects. Surprisingly, the composition was observed to vary along the parallel network in bottom most layers.

In addition to the structural information of metamorphic buffers, we also extracted qualitative structural information regarding the InAs layer. The variation of crystallinity, tilt and composition is observed to be predominant along the parallel network contrary to the observed pattern in individual layer of buffer, where the modulation is mostly along the inclined network. Also the periodicity of defect lines observed in this layer is about $\approx 1 - 1.2\ \mu\mathrm{m}$ and is similar to the periodicity observed in the surface cross-hatches.

So we conclude that both the inclined and parallel network appear very early during the growth of the metamorphic buffers. But the inclined network becomes predominant close to $In_{0.35}Al_{0.65}As$ and again become less prominent in the last layer of the buffer ($In_{0.75}Al_{0.25}As$). Whereas, the parallel network becomes less prominent as the indium composition increases. But the parallel network was observed to be most predominant feature in the InAs layer.

The surface cross-hatches appear to be a result of parallel network as they both are observed to have same periodicity. The most striking observation is that the inclined network, which is predominantly noticeable in most of the layers does not influence the surface cross-hatch features. Another relevant result is that the crystallite size that represents homogeneous areas in $In_{0.75}Al_{0.25}As$ layer without plastic deformations is found to be around $20\,\mu\mathrm{m}$in size. These crystallites are observed to be separated by major defect line regions which are a result of high density dislocation accumulation. We believe that a fabricated spin-valve device might not function if the developed electrodes lie on major defect lines as these areas have low structural integrity. This might account for the fact that a large number of non-working devices were found even though they have been fabricated from the same sample. So diffractive imaging can serve as a preliminary step before fabrication of devices to identify the best regions in the wafer to fabricate the spin-valve devices.

The magneto-transport measurements are performed on the same sample studied by diffractive mapping which revealed anisotropy in the mobilities in both <110> directions. This mobility is correlated to different roughness observed in both crystal directions of the heterostructure. Spin-valve devices are fabricated to study spin injection from Fe layer in InGaAs/InAs quantum well using non-local setup. The spin injection is observed to depend on the separation between the electrodes and non-local jumps are observed only when the separation is semi-ballistic. The calculated spin injection efficiency η reached a large value of 77% when spin-injection is modeled by diffusive approach which is very large when compared to literature values. The spin-injection efficiencyη is calculated also by using a recently proposed ballistic approach in which spin-dephasing length is introduced as key parameter. But the resultant spin-injection efficiency calculated by using experimental values of the spin-dephasing length yield unphysical values between 29% and much above 100%. Therefore, we assume that the new ballistic approach does not model properly the crystallographic anisotropy of the spin-orbit coupling in our device. A more involved model is needed accounting for the anisotropy of the Spin-Orbit coupling.

6 Experimental Results: Fe/MgO/GaAs interface

6.1 Introduction

As mentioned in previous chapters, Ferromagnet/Semiconductor heterostructures are extensively studied as potential spin based electronic devices.[13,76,192] In particular, thin Fe layers on GaAs substrates are widely studied as a test system for spin-injection experiments[11,85] due to small lattice mismatch and ease of preparation. But, the nature of the interface between ferromagnet and semiconductor is reported to influence the contact resistance and subsequent spin injection efficiency[15,32,85,89] as is also observed and reported in this thesis. moreover, some structural studies performed on metal alloys deposited on GaAs surfaces revealed a considerable intermixing at the heterojunction,[21,87,193] which in some cases may even lead to formation of different magnetic phases at the interface.[194] To prevent this inter-diffusion, deposition of an MgO interlayer is proposed as one of the viable approaches.[195,196] However, Kim *et al* observed formation of amorphous and crystalline MgO as two separate layers[197] at an MgO/GaAs interface, while other reports have observed intermixing at the interface as a function of MgO growth temperature.[198,199] Recently, intermixing has only been observed in samples, where the MgO layer is below a critical thickness of 2.5 nm.[33] This discrepancy of observations might be related to the differences in the MgO barrier and metal layer preparation, and a comprehensive structural study of such heterostructures is necessary to clearly understand the reasons of intermixing.

The information about the quality of the interface at thin thicknesses of MgO films is crucial as most of the working spin devices use only 2-4 nm thick MgO films.[192,199,200] The transport mechanisms such as the ratio between the tunneling current and thermionic Schottky emission is also observed to change around 2-4 nm range of MgO thickness[201] at room-temperature. However, the intermixing and crystallinity at the interface of very thin MgO layers (1-4 nm) are not well addressed so far as most of the structural studies are done on thick MgO layers.[34,202–204] In addition, crystalline layers of insulating MgO are also proposed to act as a spin filtering layer through symmetry matching of Bloch states to the ferromagnetic electrodes.[192,205] Furthermore understanding the epitaxial orientation of the Fe layers is also important as coherent transport is influenced by the orientation of the underlying MgO layers.[204,206] Hence, a comprehensive structural investigation of the GaAs/MgO and MgO/Fe interfaces at these thicknesses is essential for structure-property correlation. So the morphology and crystallinity

of Fe/MgO on GaAs (001) interfaces are comprehensively characterized in this thesis to shed light on the structural state of Fe/MgO/GaAs heterostructures.

6.2 Structural investigation of Fe/MgO/GaAs heterojunctions

In his thesis, two sample designs (Fig 6.1.(a) and (b) are studied for structural investigation of Fe/MgO/GaAs heterojunctions. Previously, Boris Landgraf performed structural investigations on samples with design similar to the one shown Fig 6.1.(a). However, he used much thicker MgO (6 nm) and Fe layers (20 nm).[119] The sample layout presented in Fig 6.1.(a) is used for both structural and magnetic investigations performed in this thesis and will be discussed later in this chapter. In addition, a different the sample layout shown in Fig 6.1.(b) is also grown and used for MgO growth calibration studies which will be discussed in next subsection 6.2.1.

The 2-point electrical measurements performed by Boris Landgraf[119] on the Fe/MgO/GaAs heterostructures revealed that the post-growth annealing influences the electrical properties leading to an increase in the Zero Bias Resistance (ZBR). This observation is in contrast to the expected rearrangement at interface due to annealing which should lead to a lowering of the potential barrier height.[207] The observed behavior of the ZBR as a function of temperature and post-growth annealing suggests presence of interfacial compounds like GaO_x and Mg_xAs_x[208] at the interface. These compounds might have formed due to a cumulative effect of growth parameters and configuration of the MgO chamber. Therefore, our MgO chamber has been refurbished at the start of this thesis work, and all the growth parameters are calibrated again with the aim of obtaining crystalline MgO layers. Obtaining thin (1-4 nm) and single crystalline MgO layers is a prerequisite for the final aim of the project is to apply MgO layers as spin-filtering layers in spin-injection experiments.[51] Therefore, structural characterization is performed on MgO layers to understand the structural quality of deposited MgO films.

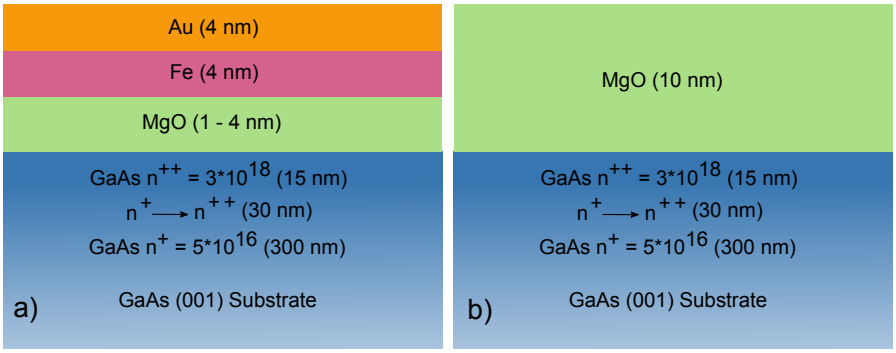

Figure 6.1: Sample layout of the Fe/MgO/GaAs heterostructure and the corresponding nominal thickness of individual layers a) layout used for TEM and magnetic studies b) Layout used for growth optimization studies.

6.2.1 Effect of MgO growth conditions on the layer crystallinity

Recent studies of Fe/MgO heterostructures on GaAs which reported highly crystalline MgO films have consistently deposited MgO layers above room temperatures and in the absence of additional oxygen background pressure.[33, 199, 202, 204, 209] The MgO layers previously studied in our group have always been deposited at room temperatures and in the presence of additional oxygen background pressures. We believe that the observed polycrystalline nature of the MgO films[119] is due to presence of excess oxygen, which leads to formation of interfacial compounds. The observed polycrystalline nature could also be due to low surface diffusion of Mg and O atoms because of room temperature deposition. Therefore, we have installed a new substrate heater in our MgO chamber to fabricate samples at different growth temperatures. We also performed an additional investigation to study the effect of oxygen background pressure on the crystallinity of MgO layers.

The entire Fe/MgO/GaAs heterostructures are prepared in a Molecular Beam Epitaxy (MBE) cluster without any exposure to ambient conditions to avoid contamination of samples. The entire growth sequence is conducted in three separate (UHV)Ultra-High Vacuum chambers connected by a UHV transfer module. The processes of oxygen desorption and growth of a GaAs conducting channel are performed in a C21 semiconductor growth chamber. Growth conditions are same as the ones described in Sec 3.2 ending with As- terminated GaAs heterostructures. Afterwards, the wafers are transferred into a dedicated MgO chamber where MgO layers are deposited using electron beam evaporation from a MgO pellet at a rate of 0.08 Å/Sec. Some of the samples are deposited in presence of an oxygen background pressure of 5×10^{-6} mbar. The growth rate is monitored by using a quartz crystal microbalance. For this particular study of growth optimization, 10 nm thick MgO layers are deposited on GaAs but the samples are not terminated with Fe and Au layers as shown in Fig 6.1.(b). These metal layers are intentionally not deposited to avoid overlapping of Bragg peaks of MgO and Au layers, which coincidentally occur in the same angular range.

Two sets of three samples with layout shown in Fig 6.1.(b) are grown in which MgO is deposited at 60°C, 100°C and 200°C. One set is deposited in the presence of additional background oxygen while the other set deposited in the absence of oxygen. Both sets are studied with both XRR and HRXRD techniques the effect of growth parameters on the MgO crystallinity of MgO layers. The X-ray based measurements mentioned in this entire chapter are performed by using a XPert-PRO (Panalytical, The Netherlands) four-circle diffractometer equipped with a Ge (220) 3-bounce analyzer and a homemade incident collimator.

The Fig 6.2(a) shows the symmetrical $\omega - 2\theta$ scan obtained along the crystal truncation rod of GaAs (004) for samples grown at 60°C with and without oxygen and an other sample deposited at 100°C in absence of oxygen. These HRXRD measurements revealed that the samples grown without additional oxygen pressure feature an intense MgO(002) peak. In contrast, the samples grown with additional oxygen pressure resulted in broad and low intensity MgO peak irrespective of growth tem-

perature. In addition, samples were also grown at 80°C, 150°C and 200°C but these samples are not discussed here as they did not show any diffraction peaks from MgO (002). In contrast, the samples grown without additional oxygen at both 60°C and 100°C showed intense MgO(002) peaks. The sharp and relatively intensive Bragg peaks suggest that better crystallinity of MgO layers is achieved when deposition is carried out in the absence of background oxygen.

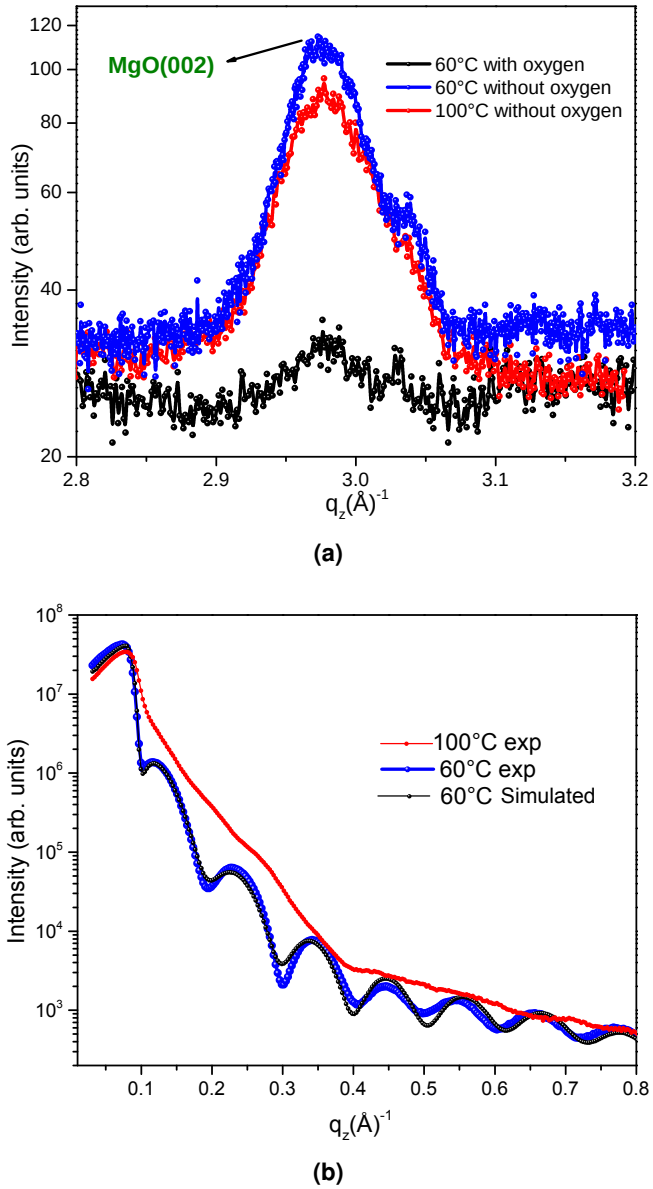

Figure 6.2: (a) XRD scan obtained along the crystal truncation rod of GaAs (004) for 60°C sample(with and without oxygen) and 100°C(without oxygen) samples showing the (002) MgO reflex. (b) XRR profiles obtained on 60°C and 100°C sample deposited in absence of additional oxygen pressure.

To establish the ideal deposition temperature of MgO films, we performed XRR measurements for studying the sharpness of the interfaces. The XRR profiles obtained on samples deposited at 60°C and

100°C without background oxygen are shown in Fig 6.2(b). These two samples are selected for compared because they both showed well pronounced MgO Bragg peaks in HRXRD measurements. The typical Kiessig fringes observed in reflectivity profiles are a signature of sharp interfaces and indicate the formation of uniform layers in the sample. As seen from Fig 6.2(b), 60°C samples reveal well pronounced Kiessig fringes while reflectivity intensity drops rapidly in 100°C sample indicating the formation of a rough interface. The reflectivity profiles are fitted using RCRefSimW program and the simulated profile (black line) of 60°C is also shown in Fig 6.2(b) which indicates good agreement with the experimental profile (blue line). Simulation is also performed on 100°C sample but it is not shown here to prevent overlapping of XRR profiles. The following roughness of individual layers are obtained from simulation of 100°C sample: $r_{MgO} = 0.45 \pm 0.02$ nm, $r_{substrate} = 0.52 \pm 0.05$ nm. The represented substrate roughness($r_{substrate}$) is the roughness at the interface of GaAs substrate and MgO layer. Considerable roughness values are obtained during simulation, if interface has additional compounds that are not considered in the simulation model. So we infer that at deposition temperature of 100°C, interfacial compounds can be formed leading to rough interfaces. Even if the assumed scenario of interface compound formation does not take place, the resultant rough interfaces of MgO/GaAs is not ideal for fabricating devices for electrical measurements. On the other hand, the sample deposited at 60°C shows relatively small roughness at the interfaces($r_{MgO} = 0.25 \pm 0.01$ nm, $r_{substrate} = 0.08 \pm 0.02$ nm). So we conclude that 60°C deposition temperature is the optimum growth condition for MgO layers.

In conclusion, we are able to identify the growth temperature and the effect of background oxygen on the crystallinity of the MgO layers. By combined study of HRXRD and XRR we determined the best quality of MgO layers are obtained when the growth is performed at 60°C and in absence of additional background oxygen.

6.2.2 Effect of MgO layer thickness on interface intermixing

As mentioned earlier, the crystallinity of Fe/MgO/GaAs interface with thin MgO films is important as most of the working spin devices use small MgO thicknesses.[192,199,200] Also, as recently reported, the structural properties of MgO layers are found to be influenced by the MgO thickness, where intermixing is observed only in samples with MgO layer thickness below 2.5 nm.[33] To study the dependence of the MgO layer on its thickness, we employed a combination of X-Ray Reflectivity (XRR) and Scanning High Resolution Transmission Electron Microscopy (HRTEM).

The sample layout of the used for this study is shown in Fig 6.1.(a). By using 60°C substrate temperature and no oxygen for MgO deposition as discussed in subsection 6.2.1, four samples with different MgO layers thicknesses are prepared. The nominal thicknesses of the MgO layers in these samples are 1-4 nm and are referred as : 1 nm for sample (I), 2 nm for sample (II), 3 nm for sample (III), and 4 nm for sample (IV). After the MgO deposition, the wafers are transferred into a metal-MBE chamber where a 4 nm Fe layer was deposited at a growth rate of 0.4 nm/min. Then the heterostructures are finally capped by a

4 nm thick Au film at a rate of 0.4 nm/min to prevent oxidation of the underlying layers. Both metal layers are deposited at room temperature. Before deposition of metal layers, the MgO surface is studied by using the RHEED setup available in the metal chamber. Both MgO and metal layers are deposited using a mask, so that only a part of the wafer is covered with both layers. In addition to the four samples mentioned above, an extra sample with 15 nm nominal MgO thickness is also prepared to study the thickness dependent surface diffraction.

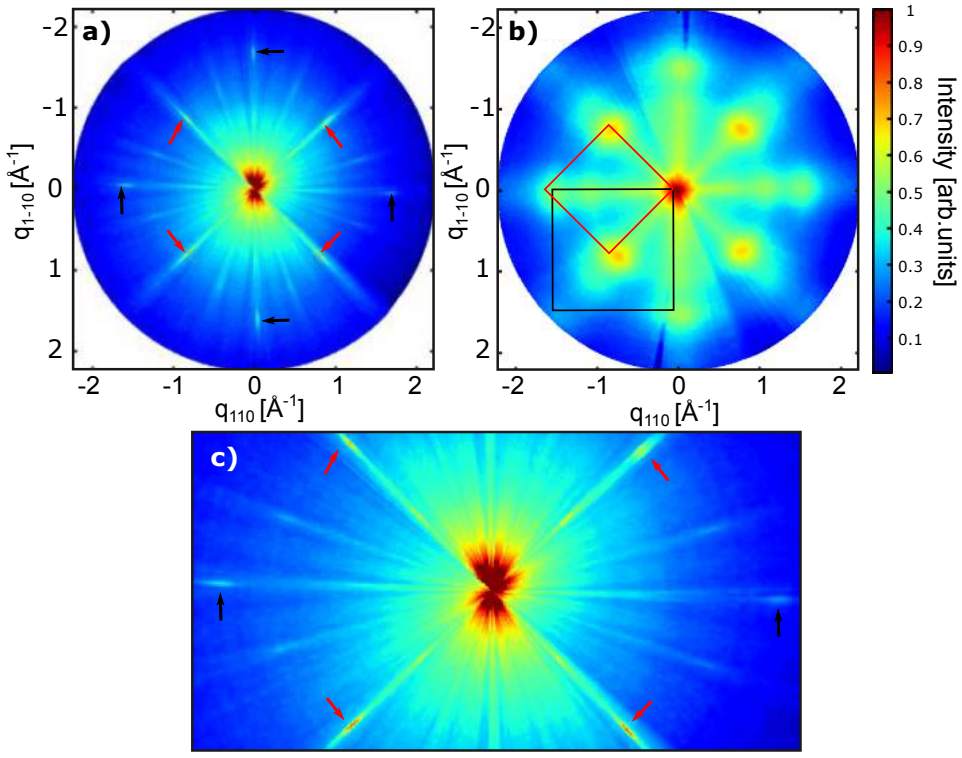

Figure 6.3: Angular dependence of the RHEED intensity for a) 1 nm and b) 15 nm MgO layers deposited on GaAs. The red arrows highlight the GaAs RHEED spots while the black arrows indicate the MgO spots. The black and red squares represent the unit cell of MgO and GaAs respectively. c) magnified image of the central part in (a).

The crystalline quality of the MgO layers is studied in-situ with RHEED at an electron acceleration energy of 15 keV. To observe reflexes of the MgO layer along different azimuthal angles, the sample is rotated while simultaneously collecting RHEED frames. The intensity from each frame is integrated in the direction towards the shadow edge of the frame. The obtained line profiles from all the frames in one rotation are used to construct a complete plain of reciprocal space called the RHEED polar plot which is described in detail in sec 2.3.2. An example of a RHEED polar plot obtained on different thicknesses of freshly deposited MgO layers is shown in Fig.6.3. The color scale in the polar plot reflects the intensity of RHEED spots is normalized to the intensity of specular beam. The polar plot obtained on 1 nm MgO sample (Fig.6.3.(a) resembles the polar plot obtained on bare As terminated GaAs substrate[67,68] which

is shown in sec 2.3.2. The polar plot of 1 nm sample also reveals additional sharp peaks belonging MgO reflexes. The GaAs spots noticed in both polar plots might be due to small glancing angle of RHEED gun, at which the foot-print of the electron beam also probes uncovered parts of the wafer. Due to small incidence angles of the electron beam used in the RHEED measurements the signal represents integral characteristics of the deposited MgO surface. The RHEED frames obtained on the thick MgO layer (15 nm) are also studied for comparative analysis and the measured polar plot is shown in Fig 6.3.(b). The RHEED spots in the polar plot obtained on the thicker sample shows broadening indicating disorder of the surface orientations.

Both polar plots display four-fold symmetry as expected for MgO layers.[210] The positions of the RHEED maxima[210] are close to those expected for a relaxed MgO crystal with the lattice constant of 0.421 nm.[211] The unit cell orientation of MgO and GaAs is marked on polar plots by placing the red ($Å^{-1}$) and black squares which represent the bulk unit cell of GaAs, $\bar{q}$=1.11 $Å^{-1}$ and MgO, $\bar{q}$=1.49 $Å^{-1}$ respectively in reciprocal space coordinates. Slight mismatch in both magnitude and orientation of these squares (unit-cells) with the observed RHEED spots is due to unsteady rotation of the substrate holder. Sharp diffraction spots observed in Fig 6.3.(a) indicate a good crystalline quality of the epitaxial films. The MgO layers are rotated by 45° with respect to the in-plane crystallographic axis of the substrate. So we conclude from polar plots that, as the thickness of MgO layers is increased from 1 nm to 15 nm, the crystalline quality of MgO layers is retained but lateral disorder in surface orientations is introduced.

Another integral technique is the XRR which is applied for *ex-situ* characterization of the interface quality on the finished structure. The measurement setup and XRR analysis is similar to the one explained in sections 2.3.6 and 3.2. The Fig 6.4.(a) shows the experimental and simulated XRR profiles of sample-II indicating good agreement. The fit yields a MgO thickness of 2.23 ± 0.11 nm and a roughness of 0.34 ± 0.06 nm. The calculated roughness of any layer is the upper interface (surface) roughness. The thickness of Fe layer is measured to be 4.40 ± 0.07 nm with interface roughness of 0.13 ± 0.03 nm. The parameters obtained from XRR represent an average over a large probed area as compared to the very small probing area of transmission microscopy which is used in further investigations discussed below.

The XRR data are also processed using a different approach to obtain depth-profiling of dielectric constant using a theoretical method developed by Kozhevnikov *et al.*[212,213] The resultant depth profile obtained from this method is compared with the results of TEM and EDS data of sample(II) and is shown in Fig 6.4.(b) The horizontal lines in Fig 6.4.(b) correspond to the bulk values of the real part of the dielectric constants in the layers. Our simulation indicates good agreement to the nominal design of the structure. Moreover, the real part of the electrical permittivity depth profile (Fig 6.4.(b) represents the behavior of the density averaged over the surface. So, the layer morphology leading to the subsequent morphology can be determined from the dielectric constant depth profile. The top Au layer in the heterostructure shows a lower value of density than the bulk, and this observation is in agreement with the density obtained with the Parratt formulation.[71] The reason for lower density can be explained with Volmer-Weber growth mode of the Au layer as observed in HRTEM images. The film density of the Fe

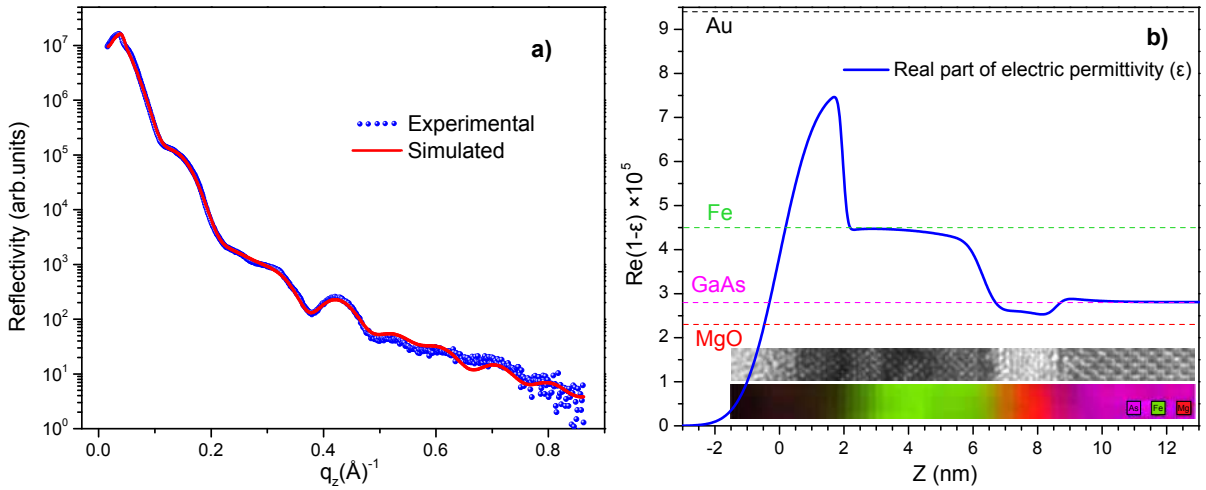

Figure 6.4: X-ray reflectometry of the sample.II: (a) fit between experimental and simulated XRR profiles, (b) reconstructed profile of the real part of the dielectric constant as a function of sample depth compared to HRTEM and EDS results. The dashed horizontal lines indicate the bulk values of the real part of dielectric constant of individual layers.

layer is observed to be constant. The MgO layer is so thin that the reconstruction of its density seems to be a bit distorted. We should emphasize that the thickness of individual layers determined by XRR technique are comparable to HRTEM results within the accuracy of the technique. The obtained fit of XRR data shows that the calculated relative densities of Fe and Au layers are close to the values of physical density. In addition, the calculated interface roughness between Au and Fe layers indicates sharp demarcation between the two layers. This sharpness of interface is also observed in EDS measurements but is not reflected in HRTEM images of all four samples.

HRTEM measurements are performed to observe the intermixing and epitaxial orientation between MgO and Fe layers. These measurements are performed in collaboration with Prof V.E. Asadchikov group at Shubnikov Institute of Crystallography, Russia. The specimens for the scanning/TEM were prepared by two methods. The first one was a standard method using cutting, gluing pieces "face-to-face" followed by mechanical thinning and Ar^+ ion milling and polishing in PIPS (Gatan, Pleasanton, CA, US) ion beam thinning machine at 5 keV at the beginning and 1 keV after the perforation of the sample. The second method consists of a Ga^+ Focus Ion Beam (FIB) milling procedure performed in a Helios (FEI, Oregon, US) scanning electron microscope (SEM)/FIB dual beam system equipped with C and Pt gas injectors and a micro-manipulator (Omniprobe, TX, US). The TEM sample preparation used for this study is described in detail elsewhere.[214,215]

All four samples are studied in a transmission/scanning electron microscope (TEM/STEM) Titan 80-300 (FEI, Oregon, US) equipped with a spherical aberration corrector (Cs), electron probe corrector (Cc), a high angle annular dark field (HAADF) detector, an atmospheric thin-window energy dispersive X-ray

(EDS) spectrometer (Phoenix System, EDAX, Mahwah, NJ, USA) and post-column Gatan energy filter (GIF), (Gatan, Pleasanton, CA, US). The TEM was operated at 300 kV. Digital Micrograph (Gatan, Pleasanton, CA, US) and TIA (FEI, Oregon, US) software was used for image analysis. Additionally, the Osiris (FEI, Oregon, US) TEM/STEM equipped with Bruker SuperX silicon drift detectors (SDD) were used for the EDS microanalysis including elemental mapping. Bruker (Bruker, US) software was used for the evaluation of EDS spectra and elemental maps.

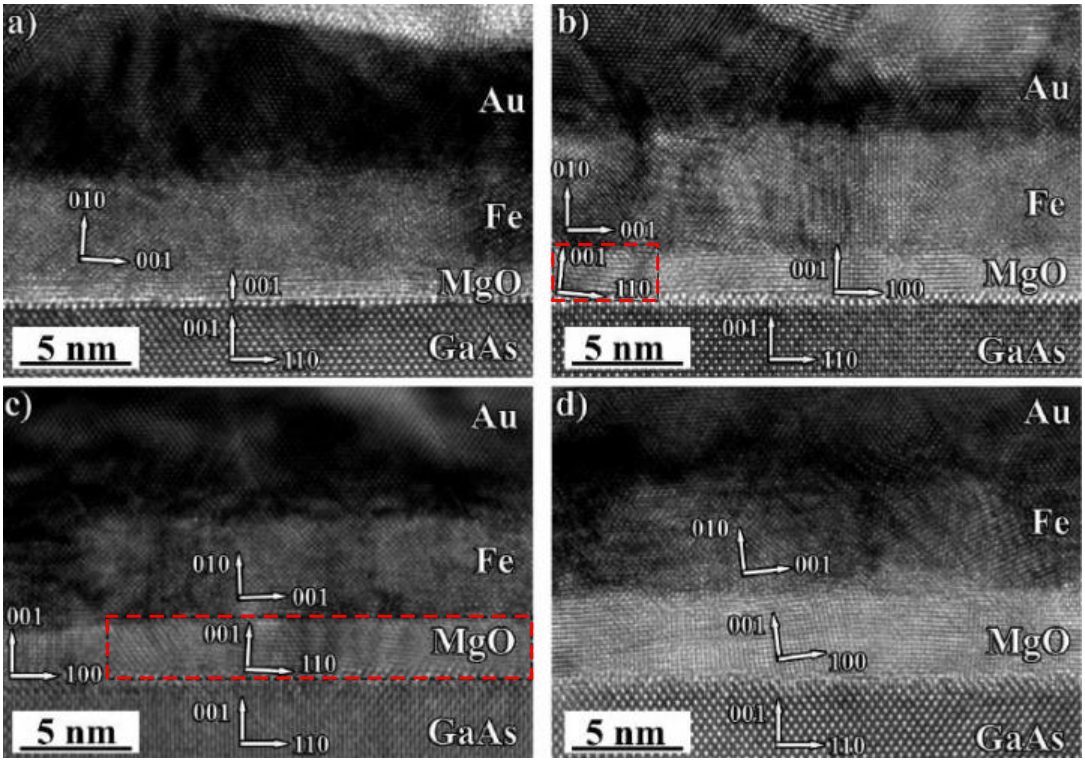

Figure 6.5: Bright field HRTEM cross-sectional images of the samples I–IV(a–d), respectively.The red dashed box highlights the regions with orientation relationship **B** between GaAs and MgO. The crystallographic directions of individual layers are marked by white arrows in corresponding layers.

The cross-sectional bright field (BF) HRTEM images of all four samples (I-IV) are shown in Fig 6.5.(a-d). The thickness of MgO layers measured from the HRTEM images are : (I) 0.75 ± 0.25 nm, (II) 1.8 ± 0.3 nm, (III) 2.45 ± 0.25 nm and (IV) 3.55 ± 0.25 nm. The MgO layers exhibit textured polycrystalline microstructure with the lateral grain sizes of 3-5 nm. For an comparative analysis between the samples, first the structure with largest MgO thickness (sample IV) is described in detail and the rest of the samples are then compared to it. The interface between GaAs and MgO is found to be atomically flat while the Fe/MgO interface is observed to be uneven with hillocks up to 0.5 nm in height. The (001) MgO crystal planes are mostly parallel to the GaAs surface and we observe the following two orientation relationships between the MgO and GaAs.

A. $(001)_{GaAs} \| (001)_{MgO}$ with the misorientation of MgO within 10°, $(1\bar{1}0)_{GaAs} \| (010)_{MgO}$

B. $(001)_{GaAs} \| (001)_{MgO}$ with the misorientation of MgO within 10°, $(1\bar{1}0)_{GaAs} \| (1\bar{1}0)_{MgO}$

The orientation relationship "**B**" is observed in only few regions of the sample and is highlighted by dashed red box in Fig 6.5. Larger field-view of TEM images that are not shown here confirm that the orientation relationship "**B**" coexists with "**A**" orientation but occur less often. The larger region with orientation relation "**B**" shown in Fig 6.5.(c) has about the maximum length of the regions with orientation relation "**B**". The coexistence of different orientation is a well known phenomenon in MgO/Si heterostructures as an effective strain relaxation mechanism[203] and we believe that this coexistence plays a similar role in the MgO/GaAs system.

The described orientation relationships are confirmed by Fast Fourier Transforms (FFT) on the obtained HRTEM images. The FFT patterns obtained from few regions having the "**A**" and "**B**" relationship orientations are shown in Fig 6.6.(a) and (b) respectively. The HRTEM of all samples have revealed that both the GaAs and MgO exhibit a cubic crystal structure with the unit cell constants a_{GaAs} = 0.5653 nm, Space Group (S.G.) $F4\bar{3}m$[216] and for MgO a_{MgO} = 0.4214 nm, S.G. $Fm\bar{3}m$.[217] As mentioned before in the orientation relationships, (001) direction of MgO layer has 10° misorientation with respect to (001) crystal direction of GaAs and this misorientation is measured by analyzing the reflexes in FFT patterns. This misorientation is evident in Fig 6.6.(a) where the reflexes from (002) planes of MgO (green circle) and (002) planes of GaAs (blue circle) are not aligned in the same plane.

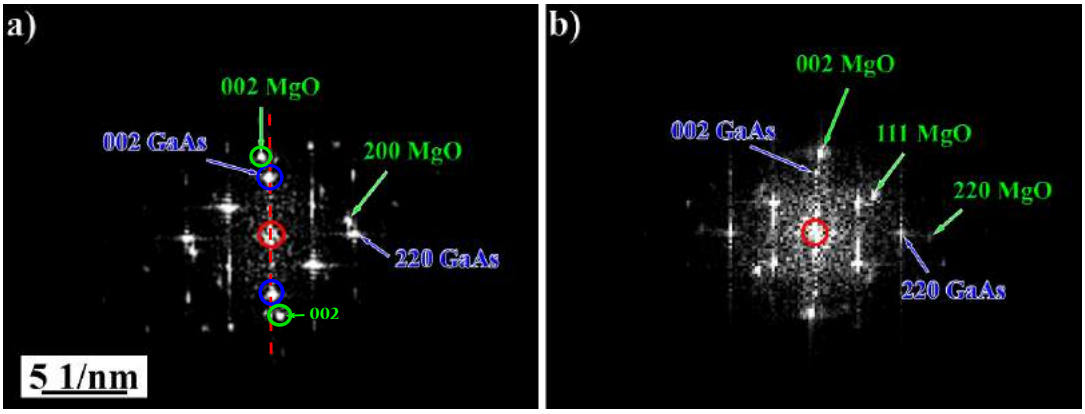

Figure 6.6: (a) & (b): FFT patterns obtained in regions with orientations "A" and "B", respectively. The (002) reflexes of GaAs and MgO are marked with blue and green circles, respectively.

For the analysis, the regions containing "**A**" and "**B**" orientations will be referred as grain-A and grain-B respectively. As seen in Fig 6.6, there is a visible difference between the FFT patterns of grains A&B due to different orientations and could also be due to light misorientation of MgO grains relative to the e^--beam. To confirm that the observed spots in the FFT patterns are correctly indexed and to prove that MgO grains orientations are chosen correctly we performed the HRTEM image simulations.

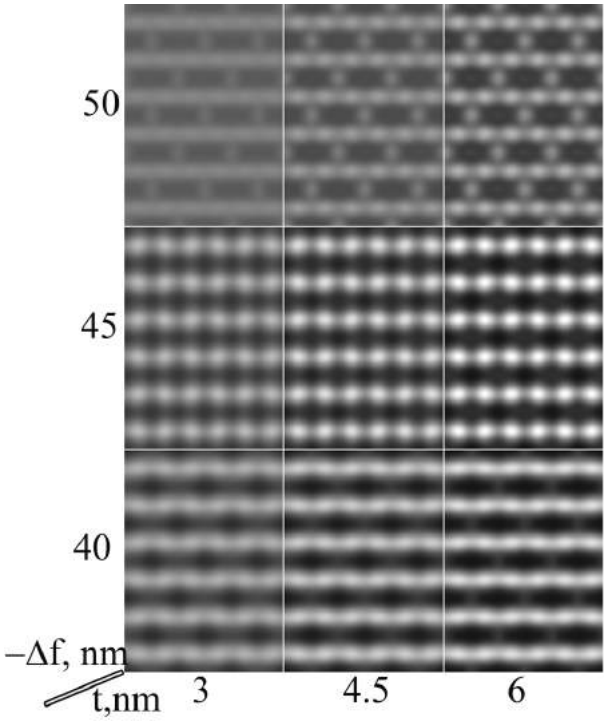

Figure 6.7: Simulation of MgO compound HRTEM data, showing the effect of thickness and objective lens defocus on contrast in HRTEM images obtained at the [110] zone axis.

A series of simulated HRTEM images of MgO compound observed in [110] zone axis at different values of MgO thicknesses (t) and objective lens defocus (Δf) values are presented in Fig 6.7. These simulations of the HRTEM images are produced using Stadelmann's EMS software package.[218] The lattice parameters used for the simulations were taken from literature.[217] The best fit between the experimental image of grain "A" of sample-IV and simulated image is obtained at thickness of 3-6 nm and Δf of 40 to 50 nm. This confirms that the assigned orientations are correctly indexed.

After confirming the relative orientations of the MgO and GaAs layers, we calculated the lattice mismatch in both "**A**" and "**B**" orientations. In the orientation "A", the MgO unit cell is rotated by 45° with respect to GaAs unit cell leading to a cube on cube-diagonal orientation. In this configuration four unit cells of MgO are almost perfectly aligned to three unit cells of GaAs and the atomic arrangement in this configuration is shown in Fig 6.8.(a) where the blue and black square represents the GaAs and MgO unit-cells respectively. In this representation, four unit cells of MgO rotated by 45° are placed on three unit cells of GaAs. It is clearly evident from the Fig 6.8.(a) that Mg and O atoms in 4 MgO unit-cells are placed almost perfectly on atoms of 3 GaAs unit-cells leading to only a small 5% mismatch. This mismatch is observed to be released mostly through the formation of misfit dislocations with projection of Burgers vector b=1/2$a_{GaAs}[\bar{1}10]$. The formation of misfit dislocations are directly observed in the filtered cross-section images of MgO/GaAs interface obtained from HRTEM images. The half-planes at the center of misfit dislocations are marked by arrows in Fig 6.8.(c). Theoretically, the cores of dis-

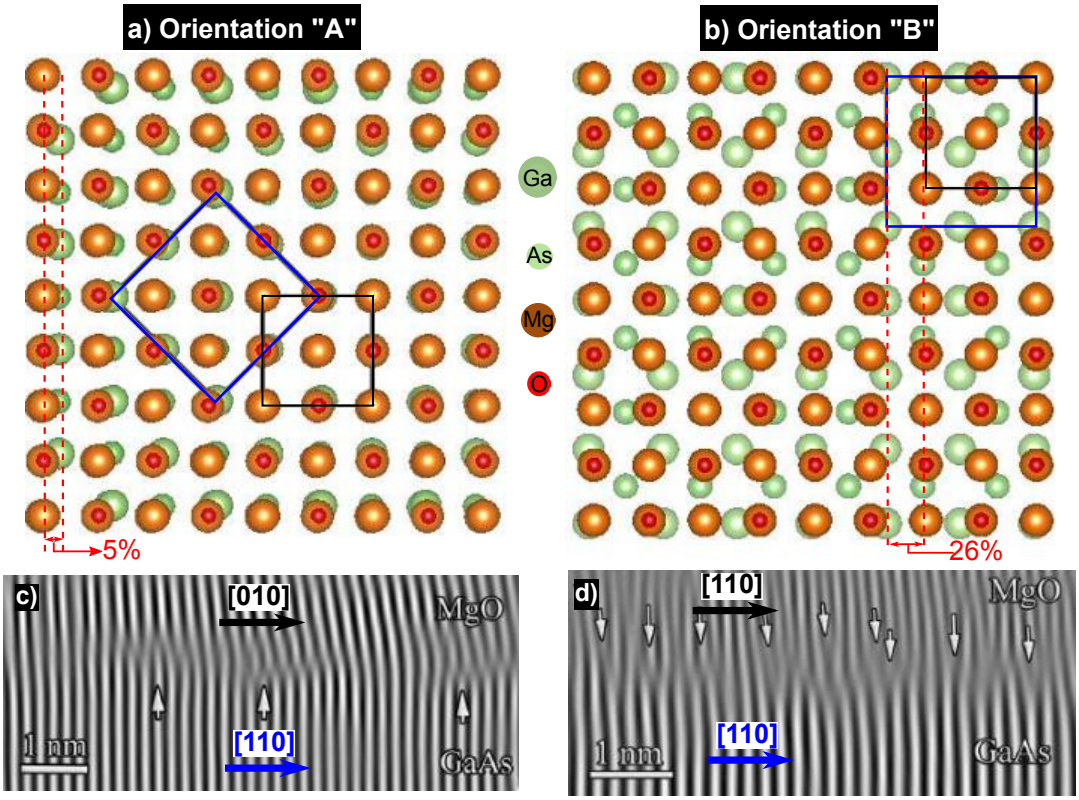

Figure 6.8: (a) & (b): Lattice images representing orientations "A" and "B" respectively. The blue and black square represent the GaAs and MgO unit cells respectively. The red dashed lines highlight the mismatch in corresponding orientation. (c) and (d): Inverted FFT filtered image at interface between $(220)_{GaAs}$ and $(200)_{MgO}$ and between $(220)_{GaAs}$ and $(220)_{MgO}$, respectively.

locations should occur at every third GaAs unit cell of the cross-section through the interface GaAs but the distance between the dislocation cores are smaller than expected and that can be associated with 10° inclinations of MgO crystals relative to [001] of GaAs.

In the "B" orientation, the mismatch between the GaAs and the MgO layers is larger than in the previous case. The cube on the cube relationship: $d(220)_{GaAs} = 0.1998$ nm and $d(220)_{MgO} = 0.1489$ nm, leads to the very large mismatch of 26%. This mismatch is depicted in the corresponding atomic arrangement of orientation "B" shown in Fig 6.8.(b), where the atoms in MgO unit cell and underneath atoms in GaAs unit-cell do not align with each other. The filtered image obtained from the orientation "B" is shown in Fig 6.8.(d) which shows much higher density of dislocation cores when compared to orientation "A". We believe that the large mismatch is the reason for very high density of misfit dislocations in Fig 6.8.(d). Our observation of two different types of MgO orientations coincides with previous reports where multiple orientations of MgO layers is observed as a effective strain relaxation mechanisms.[203]

As mentioned earlier, the discussed orientations and structural details of the MgO layer are observed in sample IV. The other three samples also exhibited similar microstructure, where the MgO layer showed

polycrystalline structure with the similar lateral grain sizes and orientation relationships. In these three samples (I-III) the MgO layer looked like continuous layer without any voids and extra amorphous seed layer as observed in some reports.[197]

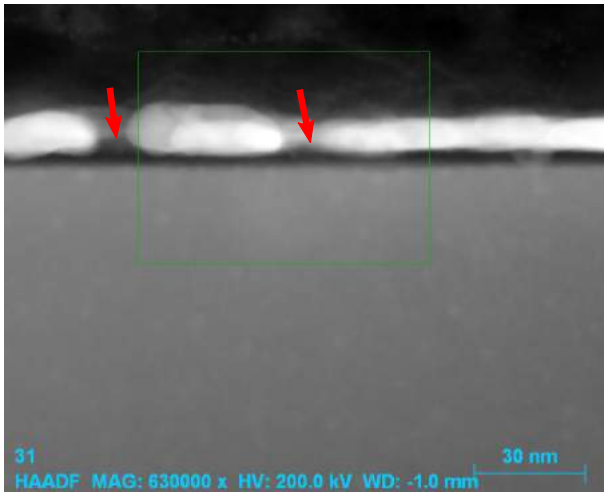

Figure 6.9: HAADF image obtained on sample-I (1 nm MgO) highlighting the gaps observed in the Fe layer.

The Fe layer is observed to grow topotaxially on MgO with highly textured polycrystalline microstructure in all four samples. The HRTEM images reveal that the Fe layer consists of particles slightly mis-oriented relative to each other with a lateral size of 2-6 nm. Close inspection of HRTEM images including FFT patterns indicate that the Fe grains have a bcc crystal structure (S.G. $Im\bar{3}m$). In addition, the Fe layer also showed high density of defects like small-angle grain boundaries (SABG's) and these defects lead to the emergence of Moiré fringes and peculiar lattice images. The following orientation relationship between GaAs and Fe layer is observed: (001)GaAs||(010)Fe, (110)GaAs||(001)Fe with a small share of (001)GaAs||(010)Fe, (110)GaAs||(101)Fe.

Irrespective of orientation, the Fe layer in samples II-IV is observed to be a uniform film as expected from homogeneous 2D growth. But the sample-I shows discontinuous Fe layers with voids in Fe layer appearing at typical distances of $\approx$ 30 nm and above. The observed gaps are highlighted in the large-field TEM image which is shown in Fig 6.9. The Au top layer of all samples is observed to be uneven which is very typical because it grows in Volmer-Weber growth mode as mentioned before when discussing XRR results. The hillocks on the Au film surface reach heights up to of 10 nm.

The intermixing at the interface is also analyzed by using EDS enabled elemental mapping performed on all four samples (I-IV). The individual elemental maps obtained across all four layers of sample-IV are shown in Fig 6.10.(a-g). Later, these individual maps are merged to form the combined elemental maps of the entire heterojunction for all four samples presented in Fig 6.11.(a-d) with separate color coding (GaAs : pink; MgO : red; Fe : green and Au : blue.). The EDS maps proves that the MgO layers exhibit relatively flat interfaces and their thickness determined from this method is in good agreement

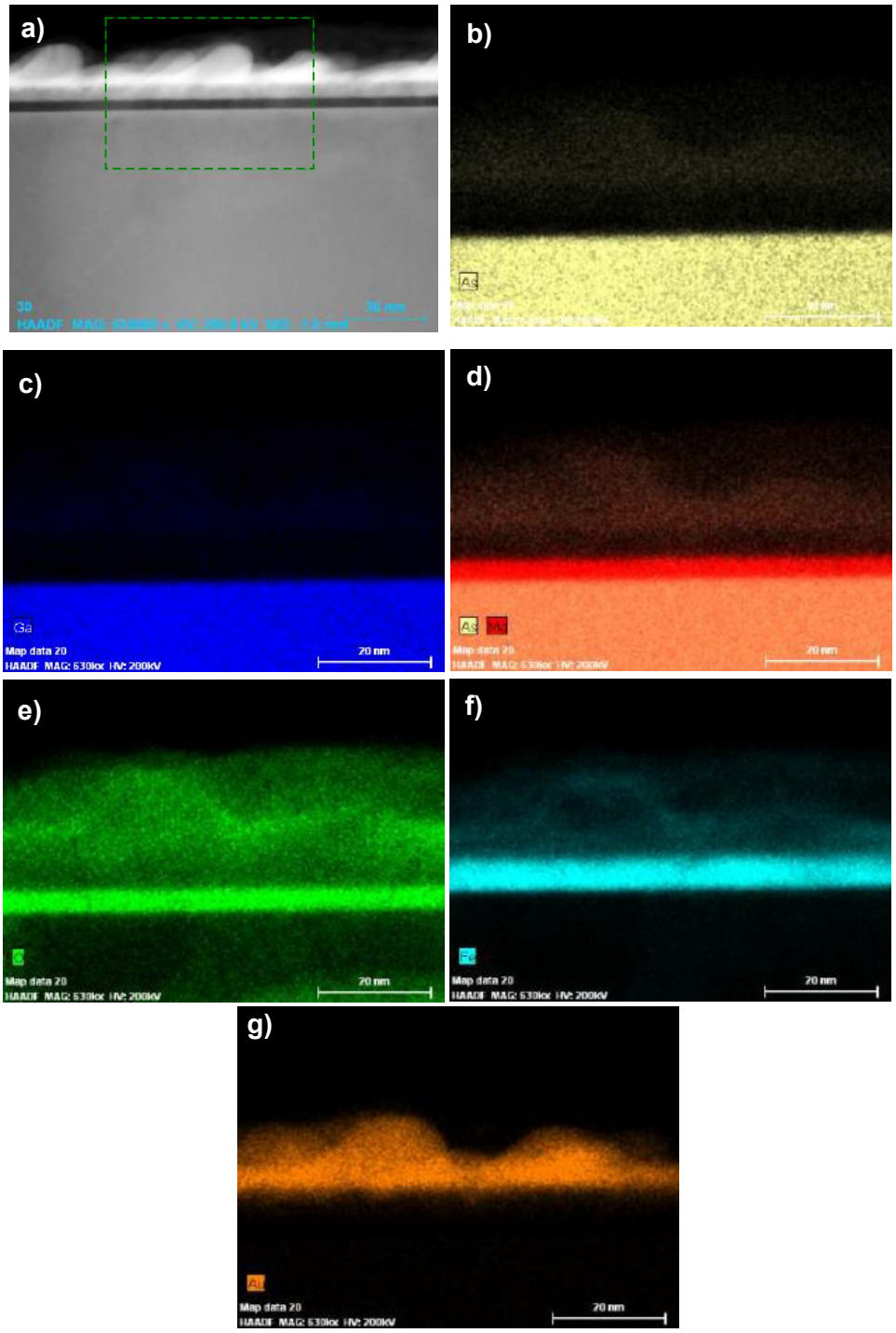

Figure 6.10: a) HAADF image obtained on sample-IV. The green doted box highlights the region selected for obtaining EDS elemental maps. (b-g) Individual EDS elemental maps of As, Ga, Mg, O, Fe and Au respectively.

with HRTEM study. The EDS elemental maps do not reveal any interface mixing at the Fe/Au interface, while the mixed Fe-Au contrast in the maps appear only due to the wavy interface. HRTEM images

together with results of EDS elemental mapping, shown in Fig 6.11.(a-d) unambiguously demonstrate the presence of four distinct layers. The Fe elemental mapping confirms that the Fe layer is almost flat which is not obvious from HRTEM images.

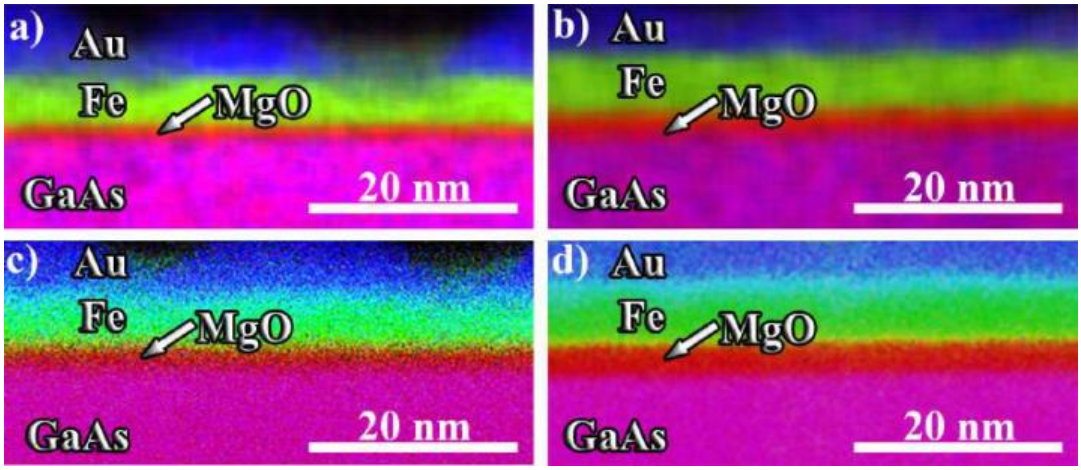

Figure 6.11: The EDS elemental maps of cross-sectional samples (a-d). Each layer is associated with a different color. GaAs represented by pink; MgO by red; Fe by green and Au by blue. The MgO layer in all samples is highlighted by a white arrow.

The separate "oxygen" EDS map acquired on sample-IV is shown in Fig.6.10.e). This map clearly demonstrates the absence of oxygen in the Fe layer. Within the experimental resolution, Oxygen was detected only within MgO layer and on the top of Au grains which were covered by epoxy resin or by Pt/C composite, which could contain small amounts of oxygen. HRTEM and EDS methods give the information about local area of the sample while, XRR technique provides depth distribution of dielectric constant averaged across the plane of about 1×1 cm^2 size. Good agreement between HRTEM and EDS images and XRR results indicates that the microstructure of the samples is homogeneous all over the sample surface.

In summary, the morphology and intermixing of MgO and Fe layers with varying MgO thickness are studied with both *in-situ* and *ex-situ* methods. We also employed techniques with different degrees of probing resolution to determine the homogeneity of the deposited layers. We observed crystalline MgO layers with atomically flat interface irrespective of the barrier thickness employed. The MgO and Fe films exhibit highly texturized polycrystalline structure without any noticeable dependence on the thickness of the MgO layer. Intermixing of Fe and O is not observed in any of the investigated structures. RHEED, S/TEM and XRR results have consistently demonstrated excellent agreement at the micro and macro levels. This comprehensive structural study helps to identify the morphology of the ferromagnetic layers and MgO barriers with respect to barriers thickness. The information of morphology is important during the fabrication of spin-devices as it influences properties like magnetic anisotropy.

6.3 Magnetic Investigations on the Fe/MgO/GaAs heterojunctions

Magnetic anisotropy is an important parameter in designing the Ferromagnetic/Semiconductor (FM/SC) based lateral spin-valves for spin injection studies as discussed in Sec 3.3&5.3. The magnetic anisotropy in Fe/GaAs and Fe/MgO/GaAs systems is found to be strongly influenced by the interface. For example, the magnetic anisotropy in FM originates from the spin-orbit coupling which usually respects the lattice symmetry of the magnetic material.[79] Therefore, a metal with fourfold lattice symmetry like Fe should show cubic magnetic anisotropy but thin Fe films deposited on GaAs show uniaxial magnetic anisotropy. This surprising result is widely debated but the general consensus regarding the origin of this result is attributed to the contribution from interface anisotropy observed at the Fe/GaAs heterojunction.[108,219–221] On the other hand, introduction of few monolayers of MgO interlayer at the Fe/GaAs interface leads to reduction of uniaxial anisotropy contribution and enhancement of cubic anisotropy in Fe films.[211]

The magnetic anisotropy in ferromagnetic layers is also observed to depend on the growth conditions like: method of deposition,[222] growth parameters[209] and also on type of capping layers.[223] In addition, the strength of uniaxial and four-fold cubic anisotropy in Fe/MgO/GaAs heterojunction is found to vary with the thickness of Fe and MgO layers.[211,224] So the resultant magnetic anisotropy in thin films of Fe is very sensitive to the structural state of the interface. Therefore, it is important to study the magnetic characteristics of Fe/MgO/GaAs samples as the information regarding the easy axis of magnetization is essential for fabrication of spin-valve devices. Also, the aspect of structure-magnetism correlation is a topic of interest as it allows us to control the magnetic anisotropy of thin Fe films which in turn is useful in design of spintronic devices.

The magnetic properties of Fe/MgO/GaAs samples are studied using the room-temperature MOKE technique and the setup is described in detail in Sec 2.3.8. In all the measurements that are described in the following subsections, the external in-plane magnetic field is swept between -60 and 60 mT with a step size of 0.1 Oe. The measurements are performed with external field oriented at different angles (Φ) with respect to sample in steps of 5°. The spot of the laser is positioned to the center of rotation of the sample stage to ensure that the same area of the film is probed during measurements. As a convention, the angle ($\Phi = 0$) is assigned to the [1-10] crystal direction of GaAs.

The MOKE measurements and data analysis is primarily focused to understand the magnetization reversal and type of magnetic anisotropy present in the sample. The polar plots are constructed which show the reversal process of the in-plane magnetization vector $\vec{M}_N(\Phi)$ during the sweeping of the external field. These polar plots are constructed by plotting normalized longitudinal signal ($M_{L,N}/|\vec{M}_N(\Phi)|$) = cos($\Phi$) versus Transversal longitudinal signal ($M_{T,N}/|\vec{M}_N(\Phi)|$) = sin($\Phi$) with the in-plane rotation angle Φ of the sample. The terms $M_{T,N}$, $M_{L,N}$ and $\vec{M}_N$ are already introduced in Sec 2.3.8. The polar plot reveals important information as it shows the rotation of magnetization vector $\vec{M}_N(\Phi)$ and hence reveals the magnetic easy and hard axes of the Fe films. The detailed description of polar plots in

discussed in sec 2.2.

Three sets of Fe/MgO/GaAs samples have been prepared for the purpose of magnetic investigations differing in their respective growth parameters. First magnetic investigation are performed on the samples that are studied by HRTEM and discussed in the previous section 6.2.2. Additional two sets of samples have the sample design as described in Sec 6.2.2 but the MgO and Fe layers are deposited at different growth conditions. The growth parameters are varied to achieve different morphologies of the Fe and MgO layers and to study their resulting magnetic properties. These 3-sets of samples will be discussed in following 3 subsections.

6.3.1 Magnetic anisotropy as function of MgO thickness in Fe/MgO/GaAs heterostructures

The same samples that have been used for characterizing interface structure with TEM and X-ray techniques as described in previous subsection 6.2.2 have also been studied with MOKE. The distinctive characteristic of these samples is that the MgO layers are deposited at substrate temperature of 60° without additional oxygen background pressure. In addition, the MgO layers are not subjected to annealing, and the subsequent Fe layers are deposited at room-temperature. In total, 4 sample with varying MgO thickness (1-4 nm) have been prepared and their detailed sample preparation is described in subsection 6.2.2. The four samples with MgO layer thickness t= 1, 2, 3, &4 nm will be referred as sample-I, II, III, and IV, respectively. This notation is same as the one used in subsection 6.2.2. The magnetic characteristics of sample-IV which has largest MgO thickness will be discussed first and the other three sample will be compared with respect to sample-IV.

Fig 6.12.a shows the longitudinal Kerr signal observed in sample-IV with the external magnetic field oriented in [1-10] and [110] crystal directions of GaAs. When the magnetic field is applied along [110] direction, the normalized longitudinal Kerr signal shows squared hysteresis loop with abrupt switching of magnetization to its saturation value at coercive field of 0.9 mT and -0.3 mT. The corresponding normalized transversal Kerr signal in Fig 6.12.(b) reveal a small hysteresis loop close to zero field. In principle, the transversal signal should be close to zero if the external field is parallel to the easy axis. However, the observed hysteresis feature is very small and could arise if the external field is not perfectly aligned to the easy axis. The notation “up” &“down” used in Fig 6.12 represents the forward and backward direction of external magnetic field respectively which are also marked by arrows representing the field directions.

In contrast, when the field is parallel to[1-10], jumps are observed in hysteresis loop of normalized longitudinal Kerr signal. These jumps are reported before on Fe/MgO system and are attributed to nucleation and propagation of 90° domain walls.[225,226] This conclusion is corroborated by the presence of peaks in the normalized transversal Kerr signal in the same field range where the longitudinal signal shows the horizontal plateau. So we can tentatively conclude that [110] crystal direction is the magnetic

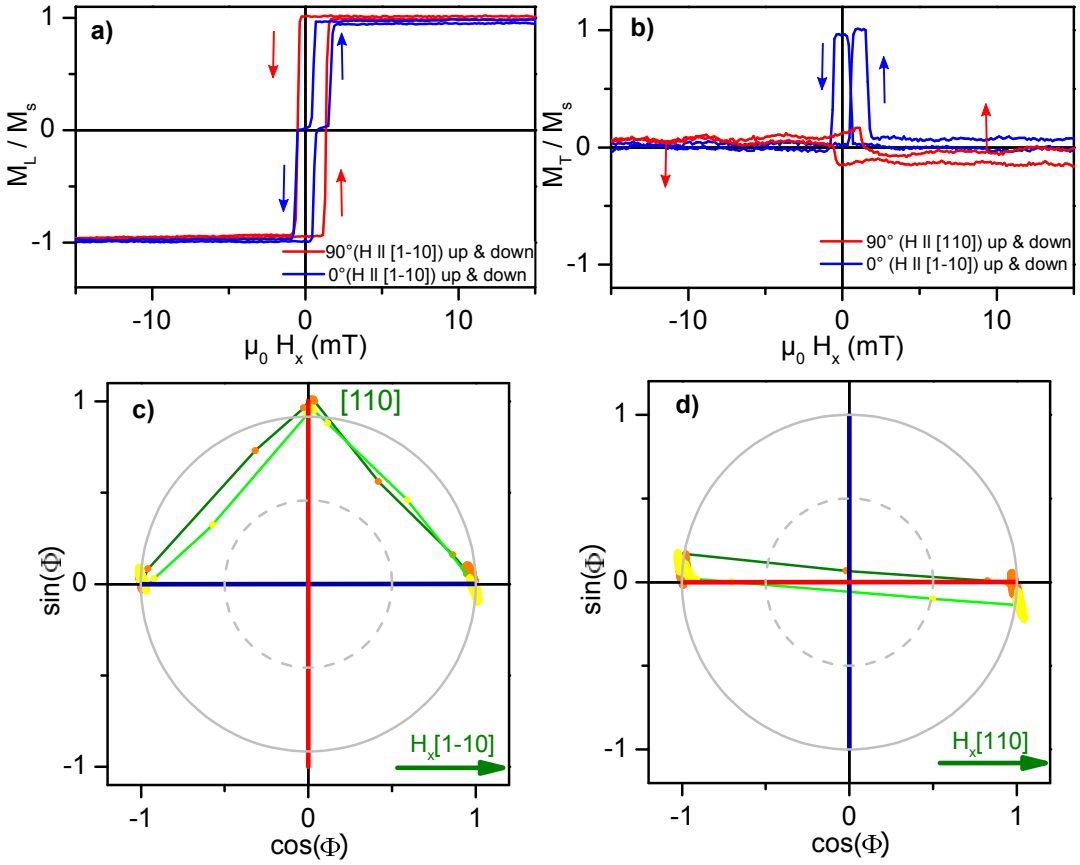

Figure 6.12: a) Longitudinal Kerr signal observed on sample-IV with external magnetic field oriented in [1-10] and [110] crystal directions. b) Transversal Kerr signal observed on sample-IV with external magnetic field oriented in [1-10] and [110] crystal directions. (c& d) reversal of normalized magnetization vector $\vec{M}_N(\Phi)$ deduced from normalized longitudinal and transversal Kerr signals obtained at [1-10] in [110] crystal directions, respectively. The blue and red arrows indicate the direction of magnetic field sweep.

easy axis of the Fe layers in this sample.

The polar plots shown in Fig 6.12.(c) and (d) show the reversal of the normalized magnetization vector $\vec{M}_N(\Phi)$ deduced from normalized longitudinal and transversal Kerr signals when the external magnetic field oriented in [1-10] in [110] crystal directions respectively. It can be seen in Fig 6.12.(c) that by sweeping the magnetic field along [1-10], the magnetization vector rotates from the [1-10] into the opposite [-110] crystal direction by crossing the magnetic easy axis of the film. While the vector changes its direction in a straight line along [110] crystal direction when the magnetic field is swept along [110]. This is an additional confirmation that the easy axis of magnetization lies in [110] crystal direction in sample-IV. It should be noted that polar-plots are a way of combined representation of both longitudinal and transversal signals.

The combined analysis of data in all four sub-figures in Fig 6.12 can only give information regarding

the magnetic easy axis of the Fe layers. Further information about the anisotropy of the Fe layers is obtained by studying the coercivity values (H_C) of the Fe layers as a function of direction of applied field with respect to the sample crystal directions. The value of H_C at every sample azimuth is obtained by averaging H_C values in forward and backward direction of the hysteresis curves.

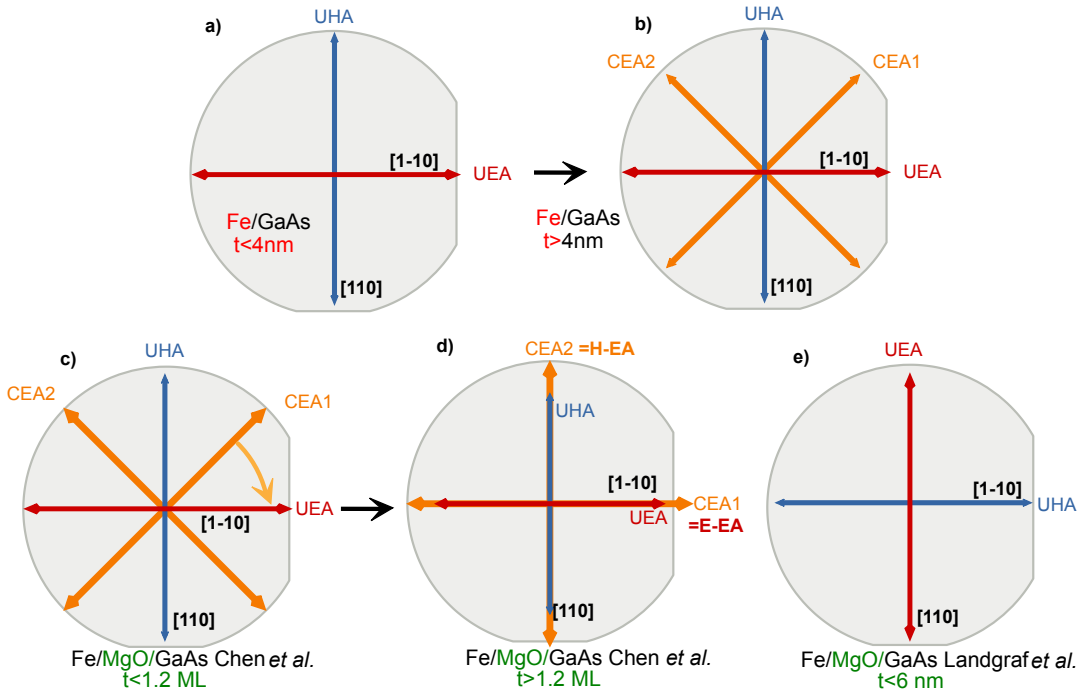

Figure 6.13: Reported magnetic anisotropy configurations at different thicknesses of Fe and MgO layers. (a) Schematic of uniaxial magnetic anisotropy in Fe films (thickness<4 nm) observed by Chen *et al*[211] on Fe/GaAs system. (b) Scheme showing coexistence of uniaxial and cubic anisotropy in Fe films at thicknesses>4-8 nm in Fe/GaAs system. (c) Reported coexistence of uniaxial and cubic anisotropy observed in Fe/MgO/GaAs system at MgO coverage less than 1.2 monolayers.[211] (d) Reported rotation of cubic anisotropy easy axes in Fe/MgO/GaAs system when MgO layers thickness is more than 2.3 monolayers.[211] (e) Uniaxial anisotropy configuration observed by Landgraf *et al.*[119] on Fe/MgO/GaAs system

Before discussing the observed anisotropy in polar plot of coercivity, an overview on the reported anisotropy in Fe/MgO/GaAs system should be given first for better understanding of our findings. The in-plane uniaxial magnetic anisotropy observed by Chen *et al*[211] on Fe/GaAs system with aid of the MOKE technique is schematically shown in Fig 6.13.(a). The red and blue lines represent easy (UEA) and hard axis (UHA) respectively. At low thicknesses of Fe t=≈4 nm, uniaxial anisotropy is predominant and a two-fold easy and hard axis of magnetization are generally observed. This uniaxial anisotropy is reported to stem from the interface anisotropy at the Fe/GaAs interface.[108,227] As the thickness of Fe layers is increased, the magneto-crystalline anisotropy contribution of Fe dominates leading to cubic

magnetic anisotropy with two easy axis of magnetizations(CEA1 & CEA2) along [010] &[100] crystal directions. These two easy axes are represented by orange lines in Fig 6.13.(b). At the Fe thickness in range of 4-8 nm both uniaxial and cubic anisotropy exists together as depicted in Fig 6.13.(b) but the cubic anisotropy dominates at thicknesses beyond t=8 nm which is also observed in the work of Boris Landgraf.[119] This anisotropy dependence as a function of thickness has also been observed by other groups.[79,219]

The magnetic anisotropy in Fe/MgO/GaAs at different thicknesses of Fe and MgO is comprehensively studied by Chen *et al.*[211] They observed coexistence of cubic and uniaxial anisotropy at low MgO coverages and the observed crystal direction of easy and hard axis is shown in Fig 6.13.(c). They also observed that the magnetic anisotropy of Fe depends on the thickness of the MgO interlayer and a predominant uniaxial anisotropy is observed in samples with up to 1.2 monolayers (ML) of MgO .This uniaxial anisotropy contribution is observed to decrease after 1.2 ML and is suppressed when MgO thickness is increased to 2.3 ML leading to predominant cubic anisotropy. In addition, Chen also observed switching of easy axis of four fold anisotropy from GaAs <100> direction to the GaAs<110> direction in the presence of 1.2 ML of MgO interlayer and this switching is shown in Fig 6.13.(d). This switch of easy axis is related to 45° in-plane rotation of the Fe unit-cell due to 45° rotation of underlying MgO unit-cell with respect to GaAs. We have directly observed this rotation of the MgO unit cell in our HRTEM investigations as discussed in subsection 6.2.2. It is worth reminding that we also observed few regions (“**B**” grains) at the interface where this rotation is not observed due to a cube-on-cube growth of MgO on GaAs.

It should be noted that the schematics in Fig 6.13.(c-d) show the scenarios where both uniaxial and cubic magnetic anisotropies are coexisting leading to different preferred axis of magnetization depending on the MgO and Fe thicknesses. These scenarios can be identified by considering both the structural orientations observed from the HRTEM studies and the observed anisotropy in coercivity polar plots. The schematics of anisotropies in Fig 6.13.(a-d)given by Chen *et al.*[211] are measured in samples with few monolayers of MgO. However, these scenarios were also observed to be valid in our samples where MgO layers are few nanometers in thickness. The scenario represented in Fig 6.13.(d) where the two easy axes of cubic anisotropy overlaps with easy and hard axis of uniaxial magnetic anisotropy leads to a new notation. The direction, in which the UEA, CEA1 and CEA2, UHA axes coincide is now called E-EA and H-EA axes, respectively.

However, results from the magnetic investigation performed by Boris Landgraf[119] on Fe/MgO/GaAs heterojunctions are different from the results of Chen *et al.*[211] The first difference that is observed from the results of Boris work is the interchange of hard and easy magnetic axis when compared to Fe/GaAs and Fe/MgO/GaAs reports.[79,211,219] The mechanism responsible for this interchange of easy and hard axes in not understood. In addition, Boris observed predominantly uniaxial anisotropy in Fe(20 nm)/MgO(6 nm)/GaAs structures with easy axis along [110] crystal direction whereas, Chen observed the uniaxial anisotropy is completely suppressed when 2.3 ML of MgO is deposited. The

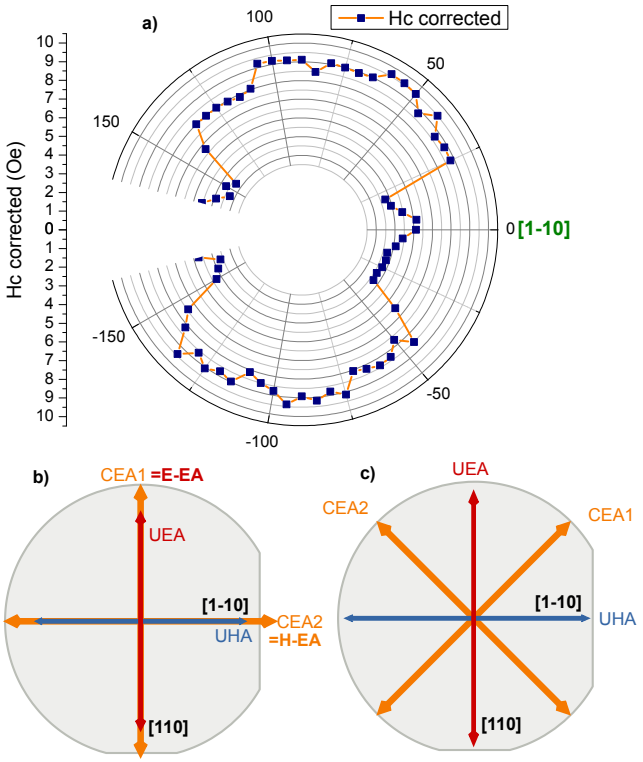

Figure 6.14: (a) Coercivity polar plot as function of sample azimuth obtained on sample-IV with 4 nm of MgO and 4 nm of Fe. (b & c) Assumed anisotropy scenarios showing overlap and coexistence of cubic and uniaxial axis of magnetization that in combination are responsible for observed coercivity anisotropy.

reason for uniaxial anisotropy at larger MgO thickness in samples of Boris might be due to non-uniform growth of MgO layers resulting in strong coupling of Fe to GaAs at certain regions of interface. The anisotropy and the respective easy and hard magnetic axes reported by Boris is shown in Fig 6.13.(e).
By considering the discussed literature, the obtained results on our samples can be explained. In principle, the magnetic easy axis is characterized by a large coercivity. The polar plot of coercivity values in sample-IV is shown in Fig 6.14.(a). which indicates that the [110] crystal axis is the easy axis of magnetization. The shape of the plot also indicates superimposed uniaxial and cubic anisotropy as a broad lobe is present across the sample angles of 45, 90, and 135°. But the direction of the easy axis is rotated by 90° (along [110]) when compared to the reported easy axis along [1-10][211] but the magnetic axes observed in this samples coincides with work of Boris.[119]
We believe that the coexistence of uniaxial and cubic anisotropy is a result of two overlapping anisotropy configurations shown in Fig 6.14.(b and c) which result from two structural orientations. The configuration shown in Fig 6.14.(b) is due to observed epitaxial orientation of Fe and MgO unit-cells which are 45° in-plane rotated with respect to GaAs leading to merging of cubic and uniaxial magnetic axes. However the structural reason for 90° rotation of uniaxial easy and hard axis is unknown. The second

configuration shown in Fig 6.14.(c) arises due to high mismatch cube-on-cube growth of MgO and Fe on GaAs leading to coexistence of cubic and uniaxial magnetic axes. The orientation of Fe and MgO responsible for second configuration in Fig 6.14.(c) is observed during HRTEM investigations in few regions across the heterostructure. The two structural orientations called A & B are responsible for the two anisotropy configurations which are well discussed in subsection 6.2.2. The HRTEM analysis reveals that the orientation "A" is prevalent in the samples and Fe layers existing in each orientation behave differently to external magnetic field. Therefore we believe that the observed anisotropy of sample is resultant of superimposed behavior of these two configurations. The small lobe observed at 0° is due to assumed overlap of hard axis (UHA) and easy axis (CEA2) leading to formation of less energetically favorable easy magnetic axis. But this lobe is not prominent as other lobes due to presence of high-energy landscape contribution from hard axis of uniaxial anisotropy. The presence of this small lobe confirms the right assignment of assumed hard and easy axes in Fig 6.14.(b & c).

It should be noted that in HRTEM investigations, Fe layers are observed to exist in the form of crystallites showing different orientations with respect to GaAs. Therefore we should not observe magnetic anisotropy in our samples. But the observed anisotropy in the samples indicates that Fe layers have preferred orientations across the heterostructure even though many orientations were observed in small scale HRTEM images.

Moreover, the samples III & II (3 and 2 nm MgO) also showed similar magnetic behavior with few exceptions. The magnetic hysteresis characteristics of both sample III & II are observed to be same. Therefore, only the date of sample-II is shown in Fig 6.15.(a). It shows the longitudinal Kerr signal observed in sample-II with external magnetic field oriented in [1-10] and [110] crystal directions. When H is parallel to [1-10] direction, the normalized longitudinal Kerr signal showed squared hysteresis loop with abrupt switching of magnetization to its saturation value at cohesive field of 2.1 mT and -1.1 mT. While the corresponding normalized transversal Kerr signal in Fig 6.15.(b) does not show any features indicating that the easy axis points parallel to the [1-10] crystal direction. It should be noted that the hysteresis curves in this sample show larger coercivity than sample-IV.

Few jumps are observed in normalized longitudinal Kerr signal when H is parallel to [110]. As mentioned earlier, these jumps are attributed to nucleation and propagation of 90° domain walls.[225,226] So we can tentatively conclude that [1-10] crystal direction is the magnetic easy axis of the Fe layers in this sample.

The polar plots shown in Fig 6.15.(c) and (d) show the reversal of normalized magnetization vector $\vec{M}_N(\Phi)$ deduced from normalized longitudinal and transversal Kerr signals when the external magnetic field oriented in [1-10] and [110] crystal directions respectively. It can be seen in Fig 6.15.(c) that by sweeping the magnetic field along [1-10], the magnetization vector changes its direction in a straight line along [1-10] crystal direction. In contrast the vector rotates from the [110] into the opposite [-1-10] crystal direction by crossing the magnetic easy axis when the magnetic field is swept along [110]. This validates our observation that [1-10] is the easy axis of magnetization in sample.

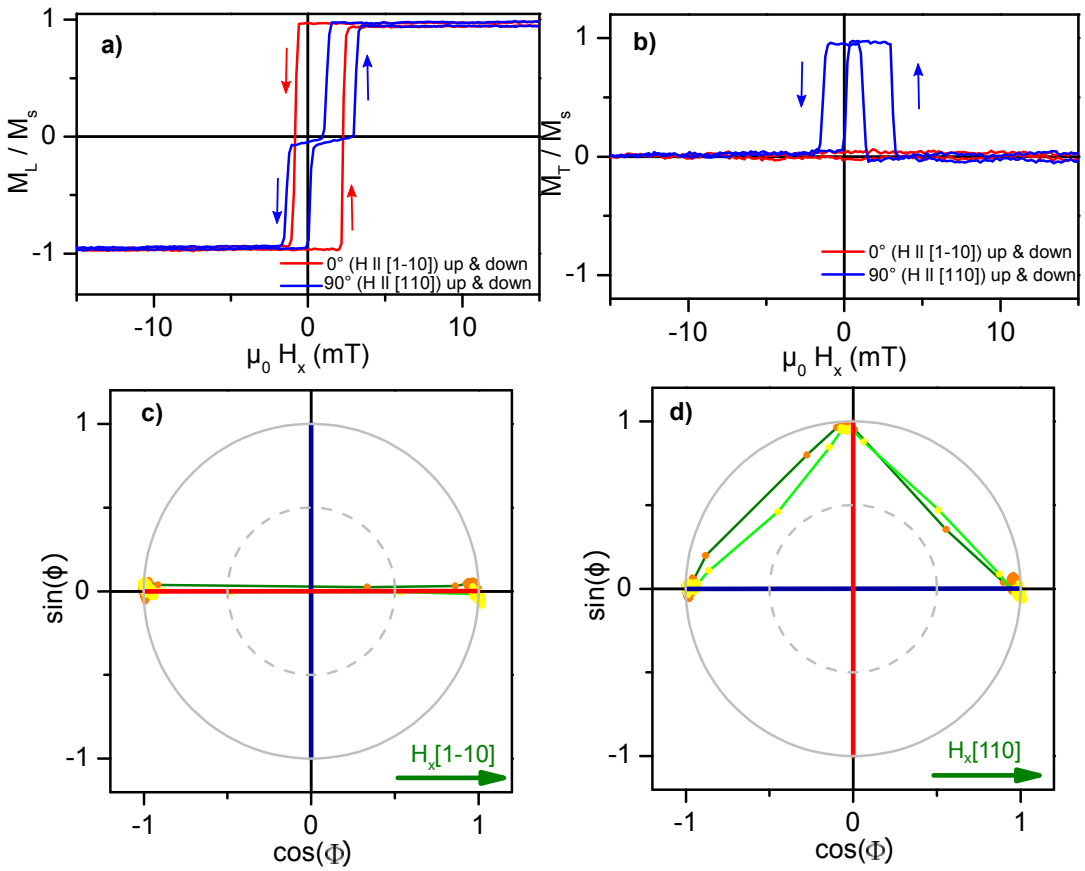

Figure 6.15: (a) Longitudinal Kerr signal observed on sample-II with external magnetic field oriented in [1-10] and [110] crystal directions. (b) Transversal Kerr signal observed on sample-II with external magnetic field oriented in [1-10] and [110] crystal directions. (c& d) reversal of normalized magnetization vector $\vec{M}_N(\Phi)$ deduced from normalized longitudinal and transversal Kerr signals when the magnetic fields are swept along [1-10] and [110] crystal directions. The blue and red arrows indicate the direction of magnetic field sweep.

The polar plot of coercivity values of sample-III and II as a function of sample rotation are shown in Fig 6.16.(a and b). Both polar plots of coercivity confirm that the [1-10] crystal direction is the magnetic easy axis for these two samples. The shape of both plots also indicates superimposed uniaxial and cubic anisotropy as a broad lobe is present across the sample angles of 45, 90, and 135° with respect to [1-10] direction. As discussed before, the observed coexisting uniaxial and cubic anisotropy is a result of two overlapping anisotropy configurations shown in Fig 6.16.(c and d) which in turn result from the two structural orientations. However, the direction of uniaxial easy axis (UEA) is along [1-10] direction and agrees with reported work of Chen *et al.*[211] The small difference in the shape of the polar plots of both samples is due to different step-sizes used for sample rotation.

The sample I(1 nm MgO) is also studied with MOKE technique but this sample did not show any change in hysteresis as a function of sample rotation. Also we could not reach magnetic saturation (M_S) state

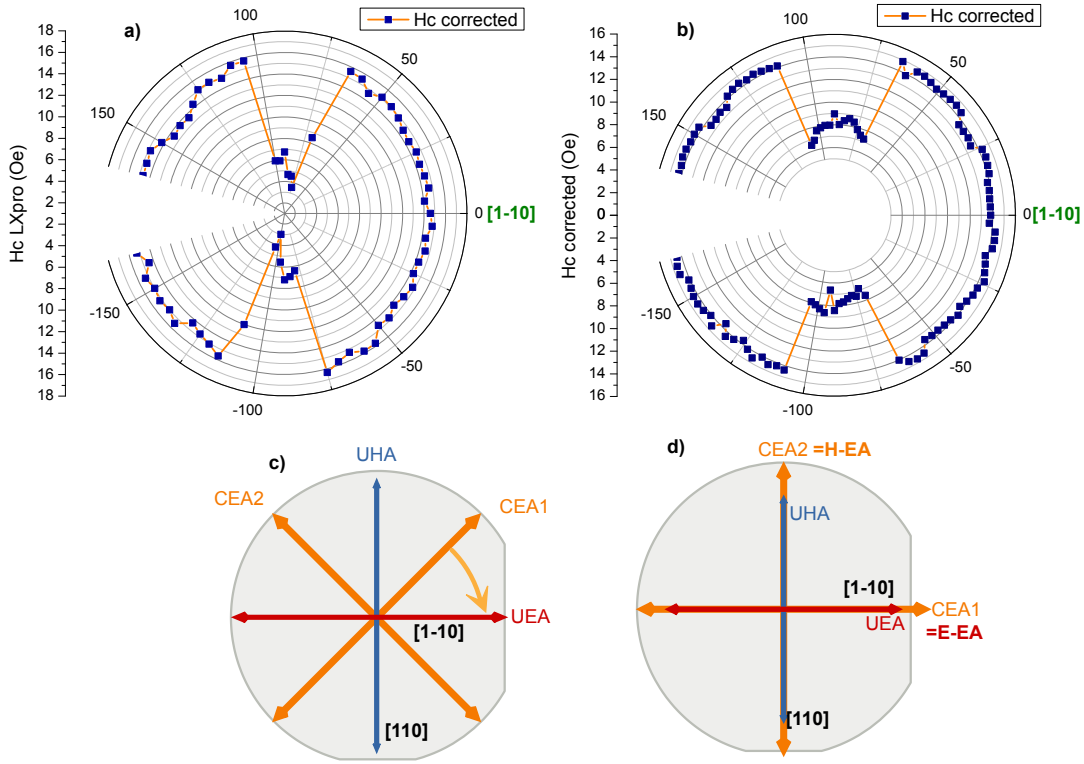

Figure 6.16: (a & b) Coercivity polar plots as function of sample azimuth obtained on sample-III and Sample-II respectively. (c & d) Assumed anisotropy scenarios showing overlap and coexistence of cubic and uniaxial axis of magnetization that in combination are responsible for observed coercivity anisotropy in sample-III and II.

with the adopted MOKE setup. This behavior suggests the presence of Fe islands instead of 2D layer of Fe.[228] This magnetic behavior correlates with our observation of discontinuous Fe layer in sample I (see Fig 6.9). The Fe islands have large saturation fields and a broad reversal of magnetization due to distribution of island sizes which requires large magnetic field to attain saturation. Therefore no data are not collected on sample-I.

6.3.2 Magnetic anisotropy as function of MgO annealing temperature in Fe/MgO/GaAs heterostructures

As mentioned in Sec 6.2 the Fe/MgO/GaAs are not annealed before deposition of metal layers as formation of interfacial compounds like GaO_x and Mg_xAs_x due to annealing was reported.[208] The work of Boris Landgraf also indicated the presence of these compounds, since annealing resulted in unusual zero-bias resistance values.[119] However, the MgO samples prepared previously in our group are deposited at room-temperature and in presence of additional oxygen background pressure. In contrast, the sample used for this thesis work are deposited without additional oxygen background pressure. So

we decided to study the effect of annealing on the magnetic properties also on the new Fe/MgO/GaAs heterostructures.

Samples with MgO layer thickness of 1 and 2 nm are prepared using the same growth procedure that is described in Sec 6.2.2 but with one exception. These two samples differ from the four samples discussed in previous subsection (6.3.1) by just one additional step of *in-situ* annealing at 250°C for one hour before the depsoition of metal layers. However, the thickness and growth conditions used for metal layer deposition are same as the one mentioned in Sec 6.2.

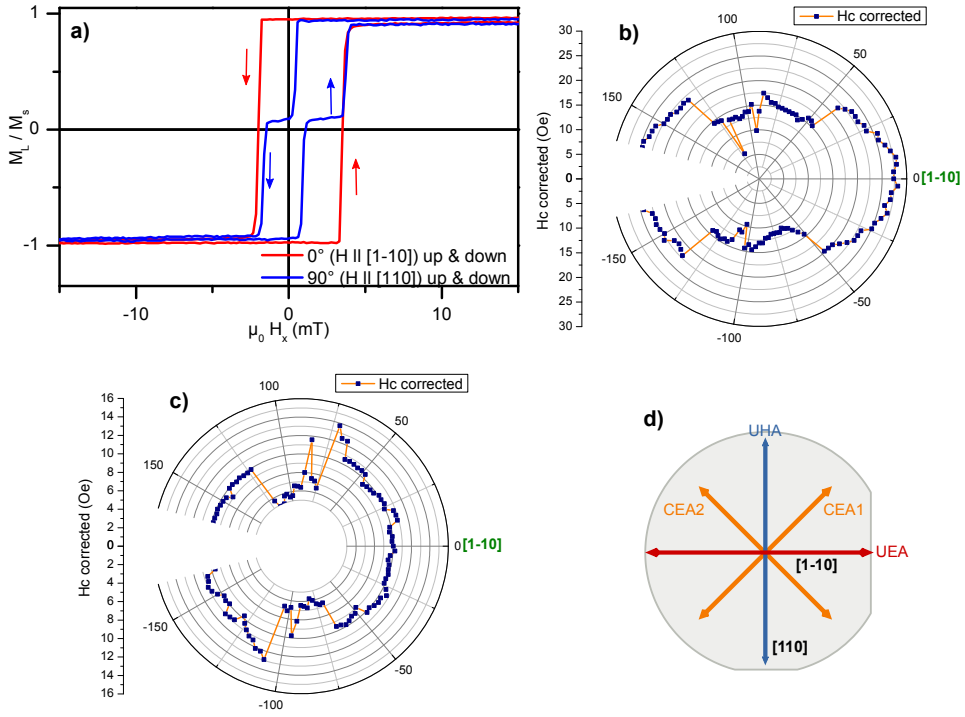

Figure 6.17: (a) Longitudinal Kerr signal observed on 1 nm sample with external magnetic field oriented in [1-10] and [110] crystal directions. (b & c) Coercivity polar plots as function of sample azimuth obtained on 1 nm and 2 nm samples respectively. Assumed anisotropy scenario showing coexistence of predominant uniaxial anisotropy and less dominant cubic anisotropy responsible for observed anisotropy in 1 nm and 2 nm samples. The blue and red arrows indicate the direction of magnetic field sweep.

Both of these samples showed similar magnetic characteristics, so hysteresis curves of 1 nm sample are discussed in detail and 2 nm sample is compared against the former. The Fig 6.17.(a) shows the longitudinal Kerr signal observed in 1nm sample with external magnetic field oriented [1-10] and [110] crystal directions. When the magnetic field is parallel to [1-10] direction, the normalized longitudinal Kerr signal showed a squared hysteresis loop with abrupt switching of magnetization to its saturation value at coercive fields of 3.4 mT and -1.7 mT. On the other hand, when the magnetic field is parallel to [110] direction, jumps are observed in hysteresis loop of normalized longitudinal Kerr signal indicating

that the [1-10] crystal direction is the easy axis of magnetization in these two samples. The polar plot showing reversal of normalized magnetization vector $\vec{M}_N(\Phi)$ are not shown here as they resemble the plots obtained on sample II & III discussed in previous subsection 6.3.1 which indicate that [1-10] is the easy axis of magnetization.

It should be noted that this sample shows higher coercivity values than the samples discussed in subsection 6.3.1. The coercivity polar plots of 1 and 2 nm samples are shown in Fig 6.17.(b) and (c) respectively and they indicate that the annealed MgO samples show pronounced uniaxial anisotropy. The observed coercivity lobes in these two samples are less broad when compared to sample discussed in subsection 6.3.1 and these lobes are prominently aligned along [1-10] direction. In addition, small lobes are observed along the cubic axis directions (<010>) but they are less pronounced when compared to samples discussed in previous subsection. The shape of both coercivity plots also indicates superimposed uniaxial and cubic anisotropy with dominant uniaxial contribution. However the general shape of the coercivity polar plot of two samples differ slightly with relatively broad uniaxial lobe in 2 nm sample and sharp lobe in 1 nm sample. We believe that this difference is due to better decoupling of GaAs and Fe layers in 2 nm sample leading to reduced uniaxial contribution which actually stems from the structural anisotropy GaAs interface.[108]

Unfortunately, the structural reason for dominant uniaxial behavior is unknown as the HRTEM characterization of these samples is still underway. But we tentatively conclude that, annealing leads to reduction of regions in MgO layers with orientation "B"(cube-on-cube growth) leading to reduction of cubic anisotropy contribution. The scenario of the assumed anisotropy axes responsible for observed magnetic behavior is shown in Fig 6.17.(d). The dominant uniaxial is represented by blue (UHA) and red (UEA) arrows, whereas, the reduced cubic contribution is represented by the smaller arrows of orange.

In conclusion, the *in-situ* MgO annealing has affected the resultant magnetic anisotropy of the Fe layer resulting in a more dominant uniaxial behavior compared to samples deposited without annealing. In addition, the coercivity is found to be stronger than in un-annealed samples and is also found to depend on the MgO thickness. For example, the higher MgO thickness (2 nm) sample yielded an average coercivity value of 9.32 Oe while, the 1 nm sample yielded a value of 18.46 Oe.

6.3.3 Magnetic anisotropy as function of Fe deposition temperature in Fe/MgO/GaAs heterostructures

As evident form the previous subsection 6.3.2, magnetic properties are observed to be influenced by the deposition conditions. The growth parameters are further modified with the aim of studying the magnetic anisotropy as a function of structural state of the Fe and MgO layers. Therefore, we prepared new set of Fe/MgO/GaAs samples that are subjected to 250°C of annealing before metal deposition and Fe layers are deposited at substrate temperature of 200°C. So this sample set is unique in the sense that

Fe layers are deposited at elevated temperatures which is not done for any other samples discussed in last two sections. However the Au capping layers are deposited at room temperature once the substrate is cooled from 200°C. The mentioned 2 samples are grown at these deposition conditions with 1 and 2 nm of MgO. The value of Fe thickness is kept constant at 4 nm which is same as the Fe thickness used in last two subsections 6.3.1&6.3.2.

Surprisingly, both samples revealed very different magnetic characteristics. Fig 6.18.(a) shows the longitudinal Kerr signal observed in 1 nm sample with external magnetic field oriented in [1-10] and [110] crystal directions. When H is parallel to [1-10], the normalized longitudinal Kerr signal shows squared hysteresis loop with abrupt switching of magnetization to its saturation value at of 20.7 mT and -18.4 mT. The hysteresis curves observed in this sample is found to have the highest average coercivity fields when compared to rest of the samples studied in all three subsections(6.3.1, 6.3.2& 6.3.3).

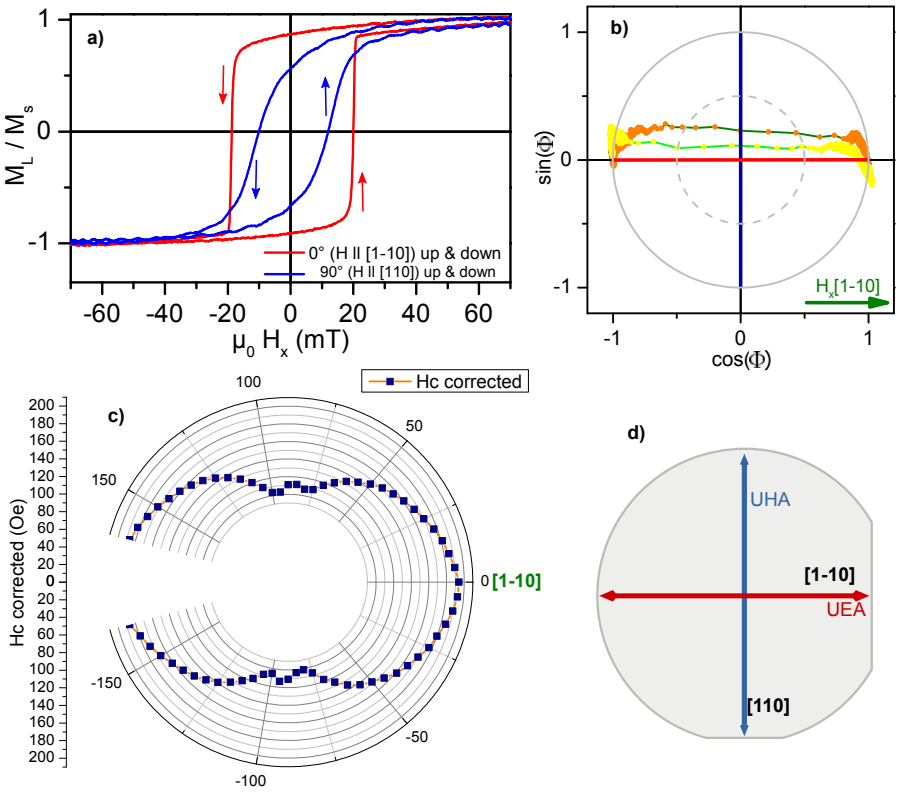

Figure 6.18: (a) Longitudinal Kerr signal observed on 1 nm sample with external magnetic field oriented in [1-10] and [110] crystal directions. (b) Reversal of normalized magnetization vector $\vec{M}_N(\Phi)$ deduced from normalized longitudinal and transversal Kerr signals when H ll [1-10]. (c) Coercivity polar plots as function of sample azimuth obtained on 1 nm. (d) Assumed anisotropy scenario showing dominant uniaxial anisotropy in the form of easy and hard axis of magnetization. The blue and red arrows indicate the direction of magnetic field sweep.

In contrast, normalized longitudinal Kerr signal obtained when magnetic field is parallel to [110] re-

vealed rounded hysteresis curves. Interestingly the hysteresis curves did not show any horizontal plateaus but instead results in reduction of area in the hysteresis curve. This behavior is a typical signature indicating that the applied field is along the hard axis of uniaxial anisotropy. The polar plots shown in Fig 6.18.(b) show the reversal of normalized magnetization vector $\vec{M}_N(\Phi)$ deduced from normalized longitudinal and transversal Kerr signals obtained when magnetic field is parallel to [1-10]. It can be seen in Fig 6.15.(c) that by sweeping the magnetic field along [1-10], the magnetization vector rotates in a straight line along [1-10] crystal direction with a slight rotation at the beginning which we believe arises from mis-orientation of external field to easy axis.

The polar plot of coercivity of 1 nm MgO sample is shown in Fig 6.18.(c). The polar plots reveals very sharp lobes along [1-10] crystal direction which confirms that this is the magnetic easy axis for this samples. The shape of this plot also indicates very dominant uniaxial anisotropy as lobes are absent across the sample angles of 45, 90, and 135°. Unfortunately, the structural reason for exclusive uniaxial behavior is unknown as the HRTEM characterization of these samples is still underway. But we tentatively conclude that in-situ annealing and elevated temperature deposition of Fe leads to reduction of Fe grains causing the cubic anisotropy contribution. So we assume that B grains discussed in sec 6.2.2 are reduced due to applied growth conditions. The scenario of the assumed anisotropy axes responsible for observed magnetic behavior is shown in Fig 6.18.(d). The dominant uniaxial anisotropy is represented by blue (UHA) and red (UEA) arrows.

The 2 nm MgO is also studied with MOKE technique but this sample did not show any change in hysteresis as a function of sample rotation as shown in Fig 6.19.(a). Also we could not achieve magnetic saturation (M_S) with the adopted low-field setup. This behavior suggests presence of Fe material as islands instead of 2D layer of Fe.[228] So there is a significant change in the observed magnetic properties with a difference of 1 nm and we note that the only difference between the two samples is the accumulated strain due to different thickness of MgO layer. So probably, the accumulated strain defines the morphology of subsequent Fe layers leading to varied magnetic anisotropies. This drastic change has not been observed in the previous section where anisotropy of annealed MgO layers are studied as function of MgO thickness. So we see that in addition to the MgO annealing, the deposition temperature of Fe also plays an important role in observed anisotropy by probably influencing the Fe layer morphology in Fe/MgO/GaAs heterostructures.

The hysteresis curves obtained at various angles are observed to be same, but the polar plot of coercivity revealed lobes resembling weak cubic anisotropy. But it should be noted that the magnitude of change in coercivity values is very small and the scale of the polar plot is magnified to show these small features. Also the hysteresis curves could not be saturated indicating a presence of out-of-plane magnetization. So the observed anisotropy in coercivity polar plots is inconclusive.

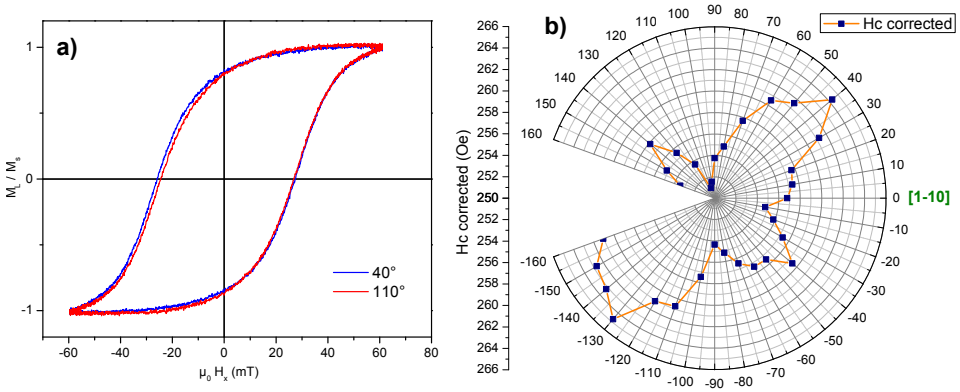

Figure 6.19: a) Longitudinal Kerr signal observed on 2 nm sample with external magnetic field oriented at 40° and 110° with respect to [1-10] crystal direction. b) Coercivity polar plots as function of sample azimuth obtained on 2 nm indicating small hint of cubic anisotropy.

6.4 Chapter Summary

Comprehensive structural characterization are performed on Fe/MgO/GaAs heterojunctions to study the crystallinity and morphology of MgO layers. The structural investigations are also performed with aim achieving single crystalline MgO layers as this is not observed in previous works performed in our group.[119] The reason for polycrystalline nature of MgO layers observed in previous works is due room-temperature growth and probable presence of interfacial compounds at the interface of GaAs and MgO. Therefore, the MgO chamber has been modified as a part of this thesis work and a substrate heater is added. In addition, growth parameters like deposition temperature and the influence of additional background oxygen pressure are calibrated extensively in order to identify the ideal conditions to obtain single crystalline MgO layers.

With a combination of XRR and XRD techniques, we observed that crystalline MgO layers with sharp interfaces are obtained when MgO is deposited at 60°C and in absence of additional background pressure. In addition, the morphology of MgO layers and their influence on the crystallinity of the Fe layers is studied as function of MgO layer thickness. This investigation of MgO layers is conducted with XRR and HRTEM in combination with EDS elemental mapping. The HRTEM investigations reveal that the MgO layer in thickness range of 1-4 nm crystallizes as flat layer in two epitaxial orientations ("**A**" and "**B**") with respect to the GaAs substrate. The orientation "**A**" is more prevalent and results in lattice mismatch of ≈5%. The orientation "**B**" which leads to lattice mismatch of ≈26% is less often seen. The coexistence of these orientations might be a strain relieve mechanism as similar coexistence of different epitaxial orientations has previously been observed in MgO/Si system.[203] In our samples, the strain at the MgO/GaAs interface is observed to be relived by formation of misfit dislocations.

The Fe layers in all samples showed high density of defects like small-angle grain boundaries (SABG's) and these defects led to the emergence of Moiré fringes in HRTEM images. The EDS elemental map-

ping revealed that there is no considerable intermixing at any of the interfaces of heterostructure. Also the EDS maps revealed that oxygen is not present in layers other than MgO indicating contaminant free growth of heterostructures.

The XRR data are modeled by two different methods. Both revealed sharp interface and a thickness close to the values obtained by HRTEM analysis. XRR results also indicated Volmer-Weber mode of the Au layer growth, and this observation is corroborated by the elemental mapping which showed island like growth of Au layers. But these islands occurs on top of thin homogeneous layer of Au which still protects the underlying Fe layer from oxidation.

In addition, MOKE investigation are performed on samples studied by HRTEM to study the effect of MgO thickness on the magnetic characteristic of the Fe layers. Moreover, additional samples are prepared with the aim of modifying the MgO and Fe layer morphology and to study the resulting magnetic anisotropies. All the samples studied by MOKE revealed that Fe/MgO/GaAs heterostructures show a combination of uniaxial and cubic in-plane magnetic anisotropy with one showing a dominant influence. However this anisotropy is observed to be strongly influenced by growth conditions like *in-situ* annealing and Fe deposition temperature. The resulting magnetic characteristics due to thickness of MgO and deposition conditions are tabulated in Table 6.1. The change in magnetic anisotropy due to growth conditions allows us to control and tune the in-plane easy axes of magnetization which in-turn enables controlled engineering of spin-device geometries.

MgO thickness	MgO annealing	Fe Temperature°C	Observed anisotropy	in-plane Easy axis	Average coercivity Oe
4 nm	no annealing	60°C	UMA+CMA (Dominant CMA)	[110]	7.5
3 nm	no annealing	60°C	UMA+CMA (Dominant CMA)	[1-10]	12.6
3 nm	no annealing	60°C	UMA+CMA (Dominant CMA)	[1-10]	15.3
1 nm	no annealing	60°C	no visible anisotropy	-	-
1 nm	250°C	60°C	UMA+CMA (Dominant UMA)	[1-10]	18.46
2 nm	250°C	60°C	UMA+CMA (Dominant UMA)	[1-10]	9.32
1 nm	250°C	200°C	UMA (Dominant UMA)	[1-10]	257.7
2 nm	250°C	200°C	no anisotropy (Weak CMA)	[010]	146.8

Table 6.1: Summary of growth parameters and magnetic characteristics measured on Fe/MgO/GaAs samples as a part of magnetic investigations by MOKE.

7 Summary and Outlook

The following three Ferromagnet-Semiconductor (FM-SC) heterojunctions: Fe on modulation doped GaAs (Fe/GaAs), Fe on InGaAs/InAs quantum wells (Fe/InAlAs) and Fe on modulation doped GaAs with MgO as tunneling barrier (Fe/MgO/GaAs) were structurally characterized with the help of high-resolution X-ray diffraction techniques. All three hybrid structures were grown in a ultra-high vacuum molecular beam epitaxy cluster to achieve highly crystalline and contamination free interfaces. In addition to the structural characterization, spin injection across the Fe/GaAs and Fe/InAlAs interfaces is also successfully demonstrated by using all-electrical non-local spin valve setup.

The crystallinity and intrinsic strain of Fe/GaAs interface as a function of Fe film thickness and deposition temperature are investigated. Fe films are observed to be highly crystalline and compressively strained when the Fe films were deposited at room-temperature. Previous investigations performed on Fe/GaAs interfaces reported a tensile strain in the Fe films which contradicts our observation of compressive strained Fe films. This contradiction might be due to very thin Fe layers deposited in our sample design, where the intrinsic strain is dominant. In addition, the compressive strain of Fe films is observed to increase with post growth annealing at 200°C, leading to reduction of lattice mismatch between the GaAs and Fe unit-cells from 0.5% to 0.12%. Further X-ray investigations using GID technique revealed the presence of Fe_3GaAs islands at the interface of Fe/GaAs. Previous investigations reported existence of tertiary phases of Fe_3GaAs at the interface by using electron microscopy.[89,92] But in our studies, we did not only observe the existence of tertiary phases at the interface but we were also able to observe the change in strain of these phases as function of post-growth annealing.

The spin-injection from Fe in to GaAs is also observed to be influenced by two subsequent post-growth annealing steps at 200°C for 10 minutes. Before annealing spin-injection was not observed. After the first cycle of annealing, the characteristic jumps in the non-local voltage (ΔU_{nl}) were observed and a spin-injection efficiency of 5.5% was calculated in diffusive limit. The second cycle of annealing decreased the calculated spin-injection efficiency to 2.6%. At both annealing steps, the spin-injection efficiency showed a bias dependent asymmetry and an unexpected positive orientation of spin-valve signal (ΔU_{nl}).

The I-V curves of the injector electrode recorded at subsequent annealing steps showed that the contact resistance is dependent on the applied bias and annealing steps, where the zero-bias contact resistance increased with each step of annealing. In contrast, the non-local resistance signal ΔR_{nl} is not observed without annealing and is maximal after first annealing step and decreases by factor of five after the

second step of annealing. Therefore, the dependence of non-local resistance ΔR_{nl} due to annealing could not be attributed to the corresponding change in contact resistance.

To explain our observations, we invoke the predicted spin-polarized interface states in the vicinity of the Fermi level. The energetic position of these interface states which are close to Fermi level significantly influences the spin detection in non-local geometry due to the unbiased detector electrode. Therefore, any small changes in energetic position of interface states will have a strong impact on the spin detection process which we believe is reflected in our data. However, we were unable to identify the mechanisms that directly lead to assumed change in energetic positions of interface states. But we did observe increase in compressive strain of Fe layer after first cycle of annealing and we believe that changes in spin-injection efficiency and strain state of Fe/GaAs interface are correlated. To completely study the changes in strain state of Fe layers and Fe_3GaAs islands at the interface, additional GID measurements are performed with varying incidence angles. The analysis of these experiments is still underway and might shed additional information regarding the size of the Fe_3GaAs islands and their structural changes as a function of both annealing cycles. In addition we also propose that theses Fe_3GaAs islands should be considered while modeling spin-injection from Fe into GaAs.

Successful spin-injection from Fe into InGaAs/InAs quantum wells was demonstrated in the intermediate limit of ballistic and diffusive transport. However, quantifying the spin-injection efficiency in this material system has led to new questions regarding the appropriate theory needed for approximation. By applying the diffusive theory to calculate the spin-injection efficiencies, we obtained values up to 77% that are much larger than the reported values in diffusive limit. The origin of larger values could be due to application of diffusive theory to a ballistic system, as proposed by Oltscher *et al*.[14] Recently Chen *et.al* proposed a new model to calculate spin-injection efficiency to account for the ballistic contributions and the spin-orbit interactions of the system by introducing the ballistic spin-dephasing length as a major parameter.[25]

The ballistic spin-dephasing length is inversely proportional to the spin-obit coupling parameter. Therefore, a strong SOI necessarily yields a short-scale spin-dephasing length. Taking into account the experimentally determined spin-orbit coupling parameter in the quantum wells, the estimated spin-injection efficiencies from the observed non-local resistance ΔR_{nl} yield values above 100%. But spin-injection efficiencies reached reasonable values below 100% when longer spin-dephasing lengths are used for calculations. Therefore, we believe that the spin-orbit interaction is not appropriately modeled in the ballistic limit and the crystallographic orientation of electron momentum and spin-polarization must be taken into account.

So our experimental observations suggest that the spin-relaxation length in our configuration is larger than expected, due to the spin-orbit coupling. Therefore, further investigations on spin injection in the ballistic limit in the presence of spin-obit coupling are required. The ballistic contributions can be enhanced by increasing the mean-free-paths in quantum wells which in turn can be controlled by increasing the carrier concentration in the quantum wells. This enhancement can be achieved by fine

tuning the design of the heterostructure to achieve better carrier concentration and mobilities. The ballistic contributions can also be enhanced by fabricating spin-valve devices with reduced dimensions to realize spin-injection in purely ballistic regime.

The InGaAs/InAs quantum well heterostructures are deposited on GaAs (001) substrates by using $In_xAl_{1-x}As$ buffer layers with increasing indium composition. The buffer layers lead to surface cross-hatched due to misfit-relaxation and the resulting roughness from cross-hatches leads to non-planar nature of the active layers. These morphological variation in individual buffer layers are studied with the help of Scanning diffractive mapping available at ID01, ESRF facility. The diffractive maps revealed regions of low crystallinity and high tilt variation in the form of two superimposed network of lines that are parallel and slightly rotated with respect to [1-10] direction. These lines are related to regions with dislocation accumulation and are called defect lines and the composition variation is observed to occur along these lines.

The density of defect lines are observed to decrease with increasing indium content. In bottom buffer layers the network of slightly rotated defect lines are found to be more predominant features in both intensity and tilt maps. Whereas, the change in local composition in bottom most layers is observed to occur as network of parallel lines along [1-10] direction.

We also extracted qualitative structural information regarding the InAs layer. The variation of crystallinity, tilt and composition in this layer is observed to be predominant along the parallel network contrary to the observed pattern in $In_xAl_{1-x}As$ buffer layers, where the modulation is mostly along the inclined network. The periodicity of defect lines observed in InAs layer is about $\approx 1 - 1.2\ \mu\mathrm{m}$ which is similar to the surface cross-hatches periodicity observed by AFM.

It should be noted that the results obtained in our diffractive imaging experiments are only a qualitative representation and does not give any information regarding the magnitude of tilt and composition variation. We were unable to obtain the quantitative results, because the sample is not rocked at spatial point during the scan. This renders the obtained data to be four dimensional dataset instead of five dimensional data which is usually obtained in standard diffractive imaging experiments. This extra dimension in reciprocal space is required to measure quantitative change of local tilt and composition. Therefore, these measurements should be performed once again in future to measure all three dimensions in reciprocal space. The quantitative information is important to understand the influence of structural inhomogeneity of buffer layers on the transport properties of active layers. For example, the size of crystallites representing homogeneous areas in $In_{0.75}Al_{0.25}As$ layer without plastic deformations is measured to be $20\,\mu\mathrm{m}$. These crystallites are separated by major defect lines which are regions with higher density of dislocation accumulation. This quantitative information is important because the fabricated spin-valve devices might not work if the developed electrodes lie on major defect lines as these areas have low structural integrity. Likewise, the quantitative information of local tilt and composition variation is also needed for understanding their effect of non-planar nature of the quantum wells deposited above them.

Fe/MgO/GaAs system constitutes the third and last FM-SC heterostructure that is structurally investi-

gated as part of this thesis. The growth condition like deposition temperature of MgO and the additional background oxygen pressure are calibrated extensively in order to identify the ideal conditions to obtain single crystalline MgO layers. In addition, the morphology of MgO layers and their influence on the crystallinity of Fe layers as function of MgO layer thickness is also studied. The HRTEM investigations revealed that the MgO layer in thickness range of 1-4 nm crystallizes as flat layer in two epitaxial orientations ("**A**" and "**B**") with respect to GaAs substrate. The orientation "**A**" is a cube on cube-diagonal epitaxial relation between GaAs and MgO with lattice mismatch of 5%. The orientation "**B**" is a cube on cube epitaxial relation between GaAs and MgO with lattice mismatch of 26%. The coexistence of these orientation is assumed to be an effective strain relieve mechanism similar to coexistence of different oriented crystallites observed in MgO/Si system as an effective lattice strain relief mechanism.[203]

3-point transport measurements were also performed on Fe/MgO/GaAs heterostructures with MgO thickness varying from 1-4 nm to characterize the contact characteristics arising from different tunneling barrier thicknesses. However, we were unable to obtain consistent I-V data from these samples and we assume this might be due to electrically active pin-holes like excessive Mg which might be present in MgO layers. But we did not observe any physical pin-holes or voids in HRTEM images obtained on Fe/MgO/GaAs. Moreover, I-V curves of samples with 1 and 2 nm MgO were fitted with Simmons model[229] to obtain the barrier height and widths of MgO tunneling barrier. However these fittings did not yield expected values of barriers heights corresponding to the MgO thickness used in the sample. We observed that even atomically flat and structurally intact MgO layers still show inconsistent electrical data. Therefore, further structural investigations are needed to establish a perfect stoichiometry and avoid excess magnesium and oxygen regions in the MgO layers.

MOKE investigation performed on Fe/MgO/GaAs heterostructures deposited with different MgO thicknesses and growth conditions. Most of these heterostructures showed a coexisting uniaxial and cubic in-plane magnetic anisotropy with one contribution showing a prominent influence. The magnetic anisotropy is observed to be influenced by growth conditions like *in-situ* annealing and Fe deposition temperature. For example, the sample with 1 nm MgO and subjected to *in-situ* annealing with Fe deposited at 200°C showed a predominant in-plane uniaxial characteristic. However 1 nm sample that is subjected to *in-situ* annealing with Fe deposited at room-temperature showed coexistence of uniaxial and cubic in-plane anisotropy. Likewise the contributions of different anisotropies were observed to change depending on the deposition conditions. The structural orientation of Fe and MgO layers with respect to GaAs substrate is directly observed by HRTEM in only set of samples where Fe is deposited at room-temperature. New TEM data has been obtained on other set of samples where the Fe deposition temperature is varied and their analysis is ongoing. This understanding of correlation between structural orientations and observed anisotropy will be of major importance while designing spintronic devices with MgO tunneling barriers.

An *in-situ* beamline technique is also developed as part of this thesis to study the effect of external stress on the strain state of Fe layers in Fe/GaAs system. For this purpose, a portable AFM is integrated

onto two different micro-beam synchrotron end-stations. This integration study is motivated to enable simultaneous access to the real and reciprocal space information of spintronic microstructures.
First, the integration and stability of the AFM on beamline conditions is tested at P10, PETRA-III facility. This integration study is used to identify the geometrical restrictions regarding combining the grazing incidence diffraction (GID) geometry and scanning probe microscope. After few modification to our AFM setup, we were able to use this *in-situ* technique for both alignment and imaging of individual microstructures. For example, Fe/MgO/GaAs rings of $4\,\mu\mathrm{m}$ in diameter are individually probed by measuring GID RSM's around GaAs(220) Bragg peak. In addition, the strain fields induced by MgO and Fe layers on GaAs substrate in the individual microstructure is observed by the presence of diffuse cloud around Bragg peak of GaAs.
The developed *in-situ* technique is then integrated on ID13, ESRF facility to study the external stress on the strain state of Fe/GaAs microstructures. This technique is also used to study the intrinsic strain in $2\,\mu\mathrm{m}$Fe/GaAs microstructures. GID geometry is used to study the evolution in-plane lattice plane spacing of Fe layer in microstructure due to nano-indentation. The Fe layer is found to be compressively strained in the direction normal to surface and this strain is further increased due to indentation.
One of the purpose of the developed technique is also to study the change in electrical properties of spintronic heterostructures under strain. But this aspect of the project is not realized due to large photocurrent signal masking the local conductivity measured using CAFM mode. These photoelectrons are generated due to interaction ionizing X-ray beam with sample are detected in the CAFM mode and this signal is used as alignment tool. However, this interaction of X-ray beam with samples resulted in formation of local deposition with composition of carbon and oxygen. These deposits are observed to be formed by cumulative effect of force inducing tip and ionizing X-ray beam.
The observed change in the strain in Fe layers due to external pressure is observed to be very small. Therefore, the microstructure dimensions have to be reduced with respect to the tip dimensions to induce considerable strain. The sample fabrication could be varied in future experiments to achieve this. We also observed few changes in the intensity distribution of reciprocal maps while applying pressure. In further studies this change in intensity distribution around Bragg peaks in RSM should be accounted by simulating the RSM at different applied strains.

8 Appendix

8.1 Additional material of GID measurements during indentation

GID maps obtained are shown in Fi 8.1. The sub-figure (a) is obtained with no external load. The sub-figure (b) is obtained when tip is displaced by 100 nm inducing force equivalent to $\approx$ 269 nN. The load is increased in steps up to final load of 1.08 μN (sub-figure(i)) for the final displacement of 400 nm.

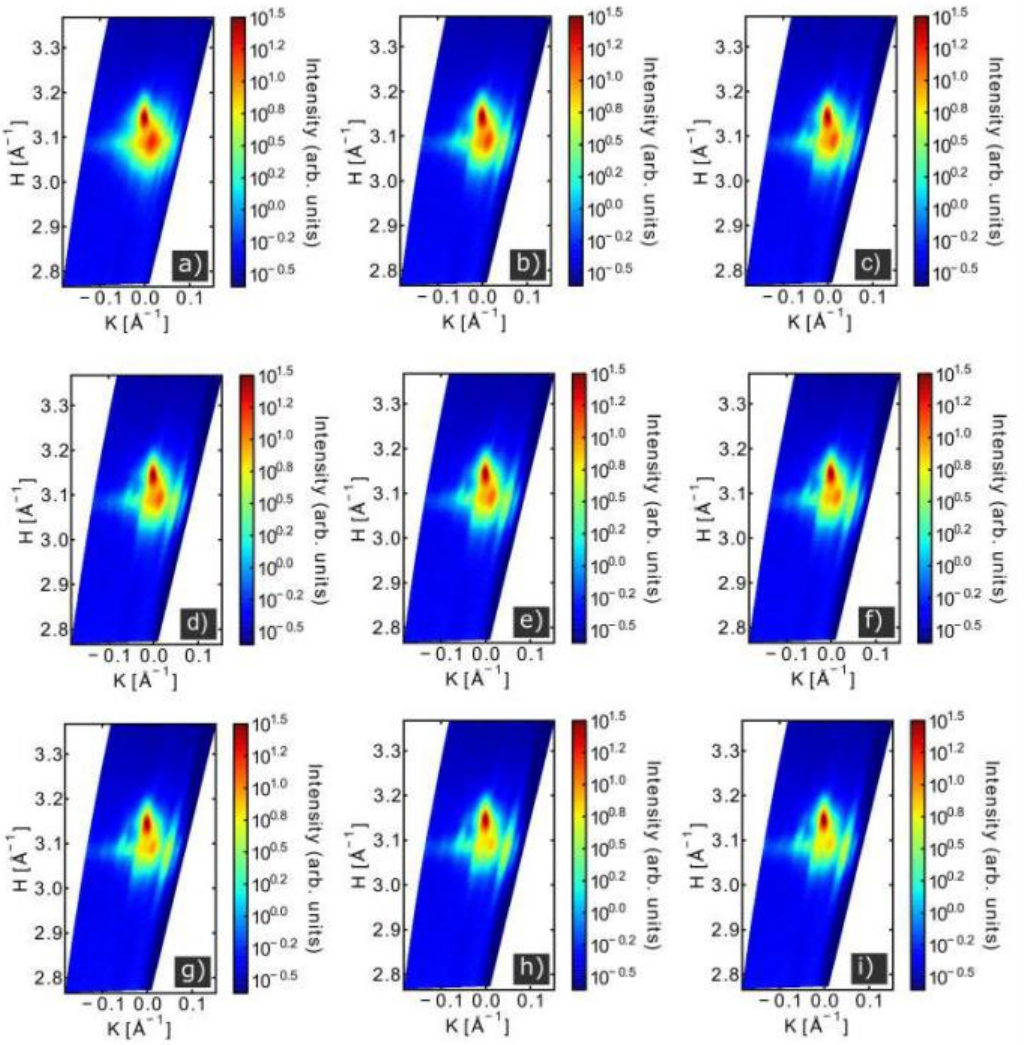

Figure 8.1: (a-i) RSM around GaAs (220) obtained at subsequent loading steps.

Bibliography

[1] X. Cartoixà, D. Z.-Y. Ting, and Y.-C. Chang. A resonant spin lifetime transistor. *Appl. Phys. Lett.*, 83(7):1462–1464, aug 2003.

[2] Kimberley C. Hall and Michael E. Flatté. Performance of a spin-based insulated gate field effect transistor. *Appl. Phys. Lett.*, 88(16):162503, apr 2006.

[3] Supriyo Datta and Biswajit Das. Electronic analog of the electro-optic modulator. *Appl. Phys. Lett.*, 56(7):665–667, feb 1990.

[4] S. A. Wolf. Spintronics: A Spin-Based Electronics Vision for the Future. *Science (80-.).*, 294(5546):1488–1495, nov 2001.

[5] S. Bandyopadhyay and M. Cahay. *Introduction to spintronics*. CRC Press, 2008.

[6] P.P Freitas, F Silva, N.J Oliveira, L.V Melo, L Costa, and N Almeida. Spin valve sensors. *Sensors Actuators A Phys.*, 81(1-3):2–8, apr 2000.

[7] Jianguo Wang, Hao Meng, and Jian-Ping Wang. Programmable spintronics logic device based on a magnetic tunnel junction element. *J. Appl. Phys.*, 97(10):10D509, may 2005.

[8] M Holub and P Bhattacharya. Spin-polarized light-emitting diodes and lasers. *J. Phys. D. Appl. Phys.*, 40(11):R179–R203, jun 2007.

[9] A. Boudine, L. Kalla, K. Benhizia, M. Zaabat, and A. Benaboud. Two-Dimensional Spin-FET Transistor. pages 337–343. Springer, Cham, 2015.

[10] S Bandyopadhyay, B Das, and A E Miller. Supercomputing with spin-polarized single electrons in a quantum coupled architecture. *Nanotechnology*, 5(2):113–133, apr 1994.

[11] S A Crooker, M Furis, X Lou, C Adelmann, D L Smith, C J Palmstrøm, and P a Crowell. Imaging spin transport in lateral ferromagnet/semiconductor structures. *Science*, 309(5744):2191–2195, sep 2005.

[12] S A Crooker, E S Garlid, A N Chantis, D L Smith, K S M Reddy, Q O Hu, T Kondo, C J Palmstrøm, and P A Crowell. Bias-controlled sensitivity of ferromagnet/semiconductor electrical spin detectors. *Phys. Rev. B*, 80(4):041305, jul 2009.

[13] Xiaohua Lou, Christoph Adelmann, Scott a. Crooker, Eric S. Garlid, Jianjie Zhang, K. S. Madhukar Reddy, Soren D. Flexner, Chris J. Palmstrøm, and Paul a. Crowell. Electrical detection of spin transport in lateral ferromagnet-semiconductor devices. *Nat. Phys.*, 3(3):197–202, mar 2007.

[14] M. Oltscher, M. Ciorga, M. Utz, D. Schuh, D. Bougeard, and D. Weiss. Electrical Spin Injection into High Mobility 2D Systems. *Phys. Rev. Lett.*, 113(23):236602, dec 2014.

[15] Thomas J. Zega, Aubrey T. Hanbicki, Steven C. Erwin, Igor Žutić, George Kioseoglou, Connie H. Li, Berend T. Jonker, and Rhonda M. Stroud. Determination of Interface Atomic Structure and Its Impact on Spin Transport Using Z-Contrast Microscopy and Density-Functional Theory. *Phys. Rev. Lett.*, 96(19):196101, may 2006.

[16] Luke Roger Fleet, H. Kobayashi, Y. Ohno, J.-Y. Kim, C. H. W. Barnes, and Atsufumi Hirohata. Interfacial structure and transport properties of Fe/GaAs(001). *J. Appl. Phys.*, 109(7):07C504, 2011.

[17] L. R. Fleet, K. Yoshida, H. Kobayashi, Y. Kaneko, S. Matsuzaka, Y. Ohno, H. Ohno, S. Honda, J. Inoue, and A. Hirohata. Correlating the interface structure to spin injection in abrupt Fe/-GaAs(001) films. *Phys. Rev. B - Condens. Matter Mater. Phys.*, 87(2):1–5, 2013.

[18] X Lou, C Adelmann, M Furis, S A Crooker, C J Palmstrøm, and P A Crowell. Electrical Detection of Spin Accumulation at a Ferromagnet-Semiconductor Interface. *Phys. Rev. Lett.*, 96(17):176603, may 2006.

[19] G. Salis, a. Fuhrer, R. R. Schlittler, L. Gross, and S. F. Alvarado. Temperature dependence of the nonlocal voltage in an Fe/GaAs electrical spin-injection device. *Phys. Rev. B - Condens. Matter Mater. Phys.*, 81(May):23–27, 2010.

[20] Q. O. Hu, E. S. Garlid, P. A. Crowell, and C. J. Palmstrøm. Spin accumulation near Fe/GaAs (001) interfaces: The role of semiconductor band structure. *Phys. Rev. B*, 84(8):085306, aug 2011.

[21] L R Fleet, K Yoshida, H Kobayashi, Y Ohno, H Kurebayashi, J.-Y. Kim, C H W Barnes, and a Hirohata. Schottky Barrier Height in Fe / GaAs Films. *IEEE Trans. Magn.*, 46(6):1737–1740, 2010.

[22] A. Richter, M. Koch, T. Matsuyama, Ch. Heyn, and U. Merkt. Transport properties of modulation-doped InAs-inserted-channel In[sub 0.75]Al[sub 0.25]As/In[sub 0.75]Ga[sub 0.25]As structures grown on GaAs substrates. *Appl. Phys. Lett.*, 77(20):3227, 2000.

[23] Hyun Cheol Koo, Jae Hyun Kwon, Jonghwa Eom, Joonyeon Chang, Suk Hee Han, and Mark Johnson. Control of spin precession in a spin-injected field effect transistor. *Science*, 325(5947):1515–8, sep 2009.

[24] M. Zwierzycki, K. Xia, P. J. Kelly, G. E W Bauer, and I. Turek. Spin-injection through an Fe/InAs interface. *Phys. status solidi*, 196(1):25–28, mar 2003.

[25] Kai Chen and Shufeng Zhang. Enhancement of spin accumulation in ballistic transport regime. *Phys. Rev. B - Condens. Matter Mater. Phys.*, 92(21), 2015.

[26] Junsaku Nitta, Tatsushi Akazaki, Hideaki Takayanagi, and Takatomo Enoki. Gate control of spin-orbit interaction in an InAs-inserted $In_{0.53}Ga_{0.47}As/In_{0.52}Al_{0.48}As$ heterostructure. *Phys. E Low-dimensional Syst. Nanostructures*, 2(1-4):527–531, jul 1998.

[27] S Löhr, Ch Heyn, and W Hansen. Nonplanar two-dimensional electron gases in InAs heterostructures on GaAs. *Appl. Phys. Lett.*, 84(4):550–552, jan 2004.

[28] A. W. Cummings, R. Akis, D. K. Ferry, J. Jacob, T. Matsuyama, U. Merkt, and G. Meier. Cascade of Y-shaped spin filters in InGaAs/InAs/InGaAs quantum wells. *J. Appl. Phys.*, 104(6):066106, sep 2008.

[29] Srijit Goswami, K. A. Slinker, Mark Friesen, L. M. McGuire, J. L. Truitt, Charles Tahan, L. J. Klein, J. O. Chu, P. M. Mooney, D. W. van der Weide, Robert Joynt, S. N. Coppersmith, and Mark A. Eriksson. Controllable valley splitting in silicon quantum devices. *Nat. Phys.*, 3(1):41–45, jan 2007.

[30] Mark Friesen, M. A. Eriksson, and S. N. Coppersmith. Magnetic field dependence of valley splitting in realistic Si-SiGe quantum wells. *Appl. Phys. Lett.*, 89(20):202106, nov 2006.

[31] G. Schmidt, D. Ferrand, L. W. Molenkamp, a. T. Filip, and B. J. van Wees. Fundamental obstacle for electrical spin injection from a ferromagnetic metal into a diffusive semiconductor. *Phys. Rev. B*, 62(8):R4790–R4793, aug 2000.

[32] C. Adelmann, J. Q. Xie, C. J. PalmstroÌ¸m, J. Strand, X. Lou, J. Wang, and P. a. Crowell. Effects of doping profile and post-growth annealing on spin injection from Fe into (Al,Ga)As heterostructures. *J. Vac. Sci. Technol. B Microelectron. Nanom. Struct.*, 23:1747, 2005.

[33] Anirban Sarkar, Shibo Wang, Wolfgang Grafeneder, Martin Arndt, and Reinhold Koch. Ultrathin MgO diffusion barriers for ferromagnetic electrodes on GaAs(001). *Nanotechnology*, 26(16):165203, 2015.

[34] C. Martinez Boubeta, E. Navarro, A. Cebollada, F. Briones, F. Peiró, and A. Cornet. Epitaxial Fe/MgO heterostructures on GaAs(001). *J. Cryst. Growth*, 226(2-3):223–230, jun 2001.

[35] J. M. Teixeira, J. Ventura, J. P. Araujo, J. B. Sousa, P. Wisniowski, and P. P. Freitas. Tunneling processes in thin MgO magnetic junctions. *Appl. Phys. Lett.*, 96(26):262506, jun 2010.

[36] B. J. Jonsson, R Escudero, C Leighton, S Kim, Ivan K Schuller, and D A Rabson. Reliability of normal-state current-voltage characteristics as an indicator of tunnel-junction barrier quality. *Appl. Phys. Lett.*, 77(12):1870, 2000.

[37] G. X. Miao, Y. J. Park, J. S. Moodera, M. Seibt, G. Eilers, and M. Münzenberg. Disturbance of Tunneling Coherence by Oxygen Vacancy in Epitaxial Fe/MgO/Fe Magnetic Tunnel Junctions. *Phys. Rev. Lett.*, 100(24):246803, jun 2008.

[38] W. Heisenberg. Zur Theorie des Ferromagnetismus. *Zeitschrift für Phys.*, 49(9-10):619–636, sep 1928.

[39] B. D. Cullity and C. D. Graham. *Introduction to Magnetic Materials*. Wiley-IEEE Press, 2 edition, 2008.

[40] Solid State Physics. Von N. W. Ashcroft und N. D. Mermin; Holt, Rinehart and Winston, New York 1976, XXII. *Phys. unserer Zeit*, 9(1):33–33, 1978.

[41] Jagadeesh S. Moodera and George Mathon. Spin polarized tunneling in ferromagnetic junctions. *J. Magn. Magn. Mater.*, 200(1-3):248–273, oct 1999.

[42] N. F. Mott. The Resistance and Thermoelectric Properties of the Transition Metals. *Proc. R. Soc. London A Math. Phys. Eng. Sci.*, 156(888), 1936.

[43] I. A. Campbell, A. Fert, and R. Pomeroy. Evidence for two current conduction iron. *Philos. Mag.*, 15(137):977–983, may 1967.

[44] A. Fert and I. A. Campbell. Two-Current Conduction in Nickel. *Phys. Rev. Lett.*, 21(16):1190–1192, oct 1968.

[45] M. N. Baibich, J. M. Broto, A. Fert, F. Nguyen Van Dau, F. Petroff, P. Etienne, G. Creuzet, A. Friederich, and J. Chazelas. Giant Magnetoresistance of (001)Fe/(001)Cr Magnetic Superlattices. *Phys. Rev. Lett.*, 61(21):2472–2475, nov 1988.

[46] G. Binasch, P. Grünberg, F. Saurenbach, and W. Zinn. Enhanced magnetoresistance in layered magnetic structures with antiferromagnetic interlayer exchange. *Phys. Rev. B*, 39(7):4828–4830, mar 1989.

[47] T Valet and A Fert. Theory of the perpendicular magnetoresistance in magnetic multilayers. *Phys. Rev. B*, 48(10):7099–7113, sep 1993.

[48] G. Schmidt, L. W. Molenkamp, a. T. Filip, and B. J. van Wees. Basic obstacle for electrical spin-injection from a ferromagnetic metal into a diffusive semiconductor. 62(8):4, 1999.

[49] E. I. Rashba. Theory of electrical spin injection: Tunnel contacts as a solution of the conductivity mismatch problem. *Phys. Rev. B - Condens. Matter Mater. Phys.*, 62(24):267–270, 2000.

[50] A. Fert and H. Jaffrès. Conditions for efficient spin injection from a ferromagnetic metal into a semiconductor. *Phys. Rev. B*, 64(18):184420, oct 2001.

[51] William H Butler. Tunneling magnetoresistance from a symmetry filtering effect. *Sci. Technol. Adv. Mater.*, 9(1):014106, apr 2008.

[52] Mark Johnson and R. H. Silsbee. Interfacial charge-spin coupling: Injection and detection of spin magnetization in metals. *Phys. Rev. Lett.*, 55(17):1790–1793, oct 1985.

[53] F J Jedema, a T Filip, and B J van Wees. Electrical spin injection and accumulation at room temperature in an all-metal mesoscopic spin valve. *Nature*, 410(6826):345–348, 2001.

[54] F J Jedema, H B Heersche, a T Filip, J J a Baselmans, and B J van Wees. Electrical detection of spin precession in a metallic mesoscopic spin valve. *Nature*, 416(6882):713–716, 2002.

[55] X. Lou, C. Adelmann, S. a. Crooker, E. S. Garlid, J. Zhang, S. M. Reddy, S. D. Flexner, C. J. Palmstrom, and P. a. Crowell. Electrical Detection of Spin Transport in Lateral Ferromagnet-Semiconductor Devices. pages 197–202, 2006.

[56] Mark Johnson. Spin accumulation in gold films. *Phys. Rev. Lett.*, 70(14):2142–2145, apr 1993.

[57] S Takahashi and S Maekawa. Spin injection and detection in magnetic nanostructures. *Phys. Rev. B*, 67(5):052409, feb 2003.

[58] P. C. van Son, H. van Kempen, and P. Wyder. New method to study the proximity effect at the normal-metal-superconductor interface. *Phys. Rev. Lett.*, 59(19):2226–2228, nov 1987.

[59] L. Liefeith. *Spin injection through metal-semiconductor contacts*. PhD thesis, University of Hamburg, 2016.

[60] Joachim Stöhr and Hans Christoph Siegmann. *Magnetism*. Springer Berlin Heidelberg, Berlin, Heidelberg, 2006.

[61] Charles. Kittel. *Introduction to solid state physics*. Wiley, 2005.

[62] M T Johnson, P J H Bloemen, F J A den Broeder, and J J de Vries. Magnetic anisotropy in metallic multilayers. *Reports Prog. Phys.*, 59(11):1409–1458, nov 1996.

[63] E.C. Stoner and E.P. Wohlfarth. A mechanism of magnetic hysteresis in heterogeneous alloys. *Phil. Trans. Roy.Soc.*, A-240(826):599–642, 1948.

[64] E M Kneedler, B T Jonker, P M Thibado, R J Wagner, B V Shanabrook, and L J Whitman. Influence of substrate surface reconstruction on the growth and magnetic properties of Fe on GaAs(001). *Phys. Rev. B*, 56(13):8163–8168, oct 1997.

[65] N. Tournerie, P. Schieffer, B. Lépine, C. Lallaizon, P. Turban, and G. Jézéquel. In-plane magnetic anisotropies in epitaxial Fe(001) thin films. *Phys. Rev. B*, 78(13):134401, oct 2008.

[66] Wolfgang Braun. *Applied RHEED : reflection high-energy electron diffraction during crystal growth*. Springer, 1999.

[67] W. Braun. Reflection high-energy electron diffraction during substrate rotation: A new dimension for in situ characterization. *J. Vac. Sci. Technol. B Microelectron. Nanom. Struct.*, 16(3):1507, may 1998.

[68] Dillip K. Satapathy, Bernd Jenichen, Klaus H. Ploog, and Wolfgang Braun. Azimuthal reflection high-energy electron diffraction study of MnAs growth on GaAs(001) by molecular beam epitaxy. *J. Appl. Phys.*, 110(2):1–8, 2011.

[69] Mario. Birkholz, Paul F. Fewster, and Christoph. Genzel. *Thin film analysis by X-ray scattering*. Wiley-VCH, 2006.

[70] Carlo. Lamberti, Giovanni Agostini, Giuseppe Portale, and Alessandro Longo. *Characterization of Semiconductor Heterostructures and Nanostructures*. Elsevier, 2013.

[71] L. G. Parratt. Surface Studies of Solids by Total Reflection of X-Rays. *Phys. Rev.*, 95(2):359–369, jul 1954.

[72] David B. Williams and C. Barry Carter. *Transmission Electron Microscopy*. Springer US, Boston, MA, 2009.

[73] David B. Williams and C. Barry Carter. *The Transmission Electron Microscope*, pages 3–17. Springer US, Boston, MA, 1996.

[74] John Kerr. XLIII. On rotation of the plane of polarization by reflection from the pole of a magnet. *Philos. Mag. Ser. 5*, 3(19):321–343, may 1877.

[75] M. Faraday. Experimental Researches in Electricity. *Philos. Trans. R. Soc. London*, 122(January):125–162, jan 1832.

[76] H. J. Zhu, M. Ramsteiner, H. Kostial, M. Wassermeier, H.-P. Schönherr, and K. H. Ploog. Room-Temperature Spin Injection from Fe into GaAs. *Phys. Rev. Lett.*, 87(1):016601, jun 2001.

[77] X Lou. Electrical detection of spin transport in ferromagnet-semiconductor heterostructures. *arXiv Prepr. cond-mat/0701021*, 2007.

[78] J. R. Waldrop and R. W. Grant. Interface chemistry of metal-GaAs Schottky-barrier contacts. *Appl. Phys. Lett.*, 34(10):630–632, 1979.

[79] G. Wastlbauer and J. A. C. Bland *. Structural and magnetic properties of ultrathin epitaxial Fe films on GaAs(001) and related semiconductor substrates. *Adv. Phys.*, 54(2):137–219, mar 2005.

[80] O. Wunnicke, Ph. Mavropoulos, R. Zeller, P. H. Dederichs, and D. Grundler. Ballistic spin injection from Fe(001) into ZnSe and GaAs. *Phys. Rev. B*, 65(24):241306, may 2002.

[81] G. Salis, A. Fuhrer, R. R. Schlittler, L. Gross, and S. F. Alvarado. Temperature dependence of the nonlocal voltage in an Fe/GaAs electrical spin-injection device. *Phys. Rev. B*, 81(20):205323, may 2010.

[82] M. Ciorga, A. Einwanger, U. Wurstbauer, D. Schuh, W. Wegscheider, and D. Weiss. Electrical spin injection and detection in lateral all-semiconductor devices. *Phys. Rev. B*, 79(16):165321, apr 2009.

[83] A. T. Hanbicki, O. M. J. van 't Erve, R. Magno, G. Kioseoglou, C. H. Li, B. T. Jonker, G. Itskos, R. Mallory, M. Yasar, and A. Petrou. Analysis of the transport process providing spin injection through an Fe/AlGaAs Schottky barrier. *Appl. Phys. Lett.*, 82(23):4092–4094, jun 2003.

[84] M. Ciorga, M. Utz, D. Schuh, D. Bougeard, and D. Weiss. Effect of contact geometry on spin-transport signals in nonlocal (Ga,Mn)As/GaAs devices. *Phys. Rev. B*, 88(15):155308, oct 2013.

[85] Lennart-Knud Liefeith, Rajkiran Tholapi, Max Hänze, Robert Hartmann, Taras Slobodskyy, and Wolfgang Hansen. Influence of thermal annealing on the spin injection and spin detection through Fe/GaAs interfaces. *Appl. Phys. Lett.*, 108(21):212404, 2016.

[86] L. R. Fleet, K. Yoshida, H. Kobayashi, Y. Kaneko, S. Matsuzaka, Y. Ohno, H. Ohno, S. Honda, J. Inoue, and A. Hirohata. Correlating the interface structure to spin injection in abrupt Fe/-GaAs(001) films. *Phys. Rev. B*, 87(2):024401, jan 2013.

[87] B. D. Schultz, N. Marom, D. Naveh, X. Lou, C. Adelmann, J. Strand, P. a. Crowell, L. Kronik, and C. J. Palmstrøm. Spin injection across the Fe/GaAs interface: Role of interfacial ordering. *Phys. Rev. B - Condens. Matter Mater. Phys.*, 80:1–4, 2009.

[88] James M. LeBeau, Qi O. Hu, Christopher J. PalmstroÌ¸m, Susanne Stemmer, Christopher J. Palmstrøm, Susanne Stemmer, Christopher J. PalmstroÌ¸m, and Susanne Stemmer. Atomic structure of postgrowth annealed epitaxial Fe/(001)GaAs interfaces. *Appl. Phys. Lett.*, 93(12):121909, 2008.

[89] L R Fleet, K Yoshida, H Kobayashi, Y Ohno, H Kurebayashi, J.-Y. Kim, C H W Barnes, and a Hirohata. Schottky Barrier Height in Fe / GaAs Films. *IEEE Trans. Magn.*, 46(6):1737–1740, jun 2010.

[90] Luke Roger Fleet, H. Kobayashi, Y. Ohno, J.-Y. Kim, C. H. W. Barnes, and Atsufumi Hirohata. Interfacial structure and transport properties of Fe/GaAs(001). *J. Appl. Phys.*, 109(7):07C504, 2011.

[91] George Kirczenow. Ideal spin filters: A theoretical study of electron transmission through ordered and disordered interfaces between ferromagnetic metals and semiconductors. *Phys. Rev. B*, 63(5):054422, jan 2001.

[92] A. Filipe, A. Schuhl, and P. Galtier. Structure and magnetism of the Fe/GaAs interface. *Appl. Phys. Lett.*, 70(1):129, 1997.

[93] G. Wastlbauer and J. a. C. Bland *. Structural and magnetic properties of ultrathin epitaxial Fe films on GaAs(001) and related semiconductor substrates. *Adv. Phys.*, 54(2):137–219, 2005.

[94] J. Freeland, I. Coulthard, W. Antel, and a. Stampfl. Interface bonding for Fe thin films on GaAs surfaces of differing morphology. *Phys. Rev. B*, 63(19):1–4, 2001.

[95] P. Zaumseil. High Resolution Determination of the Ge Depth Profile in SiGe Heterobipolar Transistor Structures by X-Ray Diffractometry. *Phys. status solidi*, 165(1):195–204, jan 1998.

[96] B. Lépine, S Ababou, A. Guivarch, G. Jeézéquel, S. Députier, R. Guérin, A Filipe, A Schuhl, F Abel, C Cohen, A Rocher, and J Crestou. Solid state interdiffusions in epitaxial Fe/GaAs(001) heterostructures during ultrahigh vacuum annealings up to 450 Â°C. *J. Appl. Phys.*, 83(6):3077, 1998.

[97] B. D. Schultz, C. Adelmann, X. Y. Dong, S. McKernan, and C. J. Palmstrom. Phase formation in the thin film Fe-GaAs system. *Appl. Phys. Lett.*, 92(9):091914, 2008.

[98] Justin M. Shaw and Charles M. Falco. Structure, spin dynamics, and magnetic properties of annealed nanoscale Fe layers on GaAs. *J. Appl. Phys.*, 101(3):033905, 2007.

[99] O. Thomas, Q. Shen, P. Schieffer, N. Tournerie, and B. Lépine. Interplay between Anisotropic Strain Relaxation and Uniaxial Interface Magnetic Anisotropy in Epitaxial Fe Films on (001) GaAs. *Phys. Rev. Lett.*, 90(1):017205, jan 2003.

[100] G Wedler, J Walz, A Greuer, and R Koch. Stress dependence of the magnetoelastic coupling constants B1 and B2 of epitaxial Fe(001), 1999.

[101] T Ashraf, C Gusenbauer, J Stangl, G Hesser, M Wegscheider, and R Koch. Stress and interdiffusion during molecular beam epitaxy of Fe on As-rich GaAs(001). *J. Phys. Condens. Matter*, 23(4):042001, 2011.

[102] Hc Su and Chih-hao Lee. A Comparison Between X-ray Reflectivity and Atomic Force Microscopy on the Characterization of a Surface Roughness. *Chinese J. . . .* , 50(2):291–300, 2012.

[103] P. Schieffer, A. Guivarch, C. Lallaizon, B. Lépine, D. Sébilleau, P. Turban, and G. Jézéquel. Formation of a body-centered-cubic Fe-based alloy at the Fe-GaAs(001) interface. *Appl. Phys. Lett.*, 89(16):161923, 2006.

[104] T Ashraf, C Gusenbauer, J Stangl, G Hesser, and R Koch. Growth, structure and morphology of epitaxial Fe(001) films on GaAs(001)c(4 $\times$ 4). *J. Phys. Condens. Matter*, 27(3):036001, 2015.

[105] S. Mirbt, B. Sanyal, C. Isheden, and B. Johansson. First Principles Calculations of Fe on GaAs (100). *Phys. Rev. B*, 67(15):155421, 2003.

[106] R. Gordon, E. Crozier, D.-T. Jiang, T. Monchesky, and B. Heinrich. Distorted iron films on GaAs(001)-(4$\times$6). *Phys. Rev. B*, 62(001):2151–2157, 2000.

[107] Y. B. Xu, D. J. Freeland, M. Tselepi, and J. A. C. Bland. Anisotropic lattice relaxation and uniaxial magnetic anisotropy in InAs(100)-4$\times$ 2. *Phys. Rev. B*, 62(2):1167–1170, jul 2000.

[108] K Tivakornsasithorn, X Liu, X Li, M Dobrowolska, and J K Furdyna. Magnetic anisotropy in ultrathin Fe films on GaAs, ZnSe, and Ge (001) substrates. *J. Appl. Phys.*, 116(4):043915, jul 2014.

[109] Seul-Ki Bac, Hakjoon Lee, Sangyoep Lee, Seonghoon Choi, Taehee Yoo, Sanghoon Lee, X Liu, and J K Furdyna. Observation of uniaxial anisotropy along the [100] direction in crystalline Fe film. *Sci. Rep.*, 5:17761, dec 2015.

[110] V Crisan, P Entel, and G Rollmann. Electronic properties of the Fe / GaAs(001) interface. 240:417–419, 2002.

[111] D. O. Demchenko and Amy Y. Liu. Influence of interface structure on electronic properties and Schottky barriers in Fe/GaAs magnetic junctions. page 9, 2006.

[112] S. Honda, H. Itoh, J. Inoue, H. Kurebayashi, T. Trypiniotis, C. H. W. Barnes, A. Hirohata, and J. A. C. Bland. Spin polarization control through resonant states in an Fe/GaAs Schottky barrier. *Phys. Rev. B*, 78(24):245316, dec 2008.

[113] B. Lepine, C. Lallaizon, P. Schieffer, A. Guivarch, G. Jezequel, A. Rocher, F. Abel, C. Cohen, S. Dputier, and F. Nguyen Van Dau. Fe_3GaAs/GaAs(001): a stable and magnetic metal-semiconductor heterostructure. *Thin Solid Films*, 446(1):6–11, jan 2004.

[114] Athanasios N. Chantis, Kirill D. Belashchenko, Darryl L. Smith, Evgeny Y. Tsymbal, Mark van Schilfgaarde, and Robert C. Albers. Reversal of Spin Polarization in Fe/GaAs (001) Driven by Resonant Surface States: First-Principles Calculations. *Phys. Rev. Lett.*, 99(19):196603, nov 2007.

[115] H Dery and L J Sham. Spin Extraction Theory and Its Relevance to Spintronics. *Phys. Rev. Lett.*, 98(4):046602, jan 2007.

[116] R I Dzhioev, K V Kavokin, V L Korenev, M V Lazarev, B Ya Meltser, M N Stepanova, B P Zakharchenya, D Gammon, and D S Katzer. Low-temperature spin relaxation in n -type GaAs. *Phys. Rev. B*, 66(24):245204, dec 2002.

[117] I-H. Tan, G. L. Snider, L. D. Chang, and E. L. Hu. A self-consistent solution of Schrödinger-Poisson equations using a nonuniform mesh. *J. Appl. Phys.*, 68(8):4071–4076, oct 1990.

[118] J. R. Waldrop. Schottky-barrier height of ideal metal contacts to GaAs. *Appl. Phys. Lett.*, 44(10):1002–1004, may 1984.

[119] Boris Landgraf. Structural , magnetic and electrical investigation of iron-based iii / v-semiconductor hybrid structures.

[120] Kh. Zakeri, Th. Kebe, J. Lindner, M. Farle, and M Spasova. Magnetic anisotropy of Fe/-GaAs(001) ultrathin films investigated by in situ ferromagnetic resonance. *J. Magn. Magn. Mater.*, 299(1):8791–8802, 2006.

[121] X Lou. Electrical detection of spin transport in ferromagnet-semiconductor heterostructures. *arXiv Prepr. cond-mat/0701021*, 2007.

[122] Mark Johnson and R. H. Silsbee. Interfacial charge-spin coupling: Injection and detection of spin magnetization in metals. *Phys. Rev. Lett.*, 55(17):1790–1793, 1985.

[123] H Kurebayashi, S J Steinmuller, J B Laloë, T Trypiniotis, S Easton, A Ionescu, J R Yates, and J A C Bland. Initial final state selection of the spin polarization in electron tunneling across an epitaxial Fe-GaAs(001) interface. *Appl. Phys. Lett.*, 91(10):102114, sep 2007.

[124] C. Adelmann, X. Lou, J. Strand, C. J. Palmstrøm, and P. A. Crowell. Spin injection and relaxation in ferromagnet-semiconductor heterostructures. *Phys. Rev. B*, 71(12):121301, mar 2005.

[125] Series in Material Science and Engineering. Taylor & Francis, Jan 2007. 0.

[126] T. Mizuno, S. Takagi, N. Sugiyama, H. Satake, A. Kurobe, and A. Toriumi. Electron and hole mobility enhancement in strained-Si MOSFET's on SiGe-on-insulator substrates fabricated by SIMOX technology. *IEEE Electron Device Lett.*, 21(5):230–232, 2000.

[127] Els Parton and Peter Verheyen. Strained silicon - the key to sub-45 nm CMOS. *III-Vs Rev.*, 19(3):28–31, 2006.

[128] C. Mocuta, J. Stangl, K. Mundboth, T. H. Metzger, G. Bauer, I. A. Vartanyants, M. Schmidbauer, and T. Boeck. Beyond the ensemble average: X-ray microdiffraction analysis of single SiGe islands. *Phys. Rev. B - Condens. Matter Mater. Phys.*, 77(24):2–7, 2008.

[129] M. Hanke, M. Dubslaff, M. Schmidbauer, T. Boeck, S. Schöder, M. Burghammer, C. Riekel, J. Patommel, and C. G. Schroer. Scanning x-ray diffraction with 200 nm spatial resolution. *Appl. Phys. Lett.*, 92(19):10–13, 2008.

[130] M. Hanke, M. Schmidbauer, and R. Köhler. Lateral correlation of SiGe Stranski-Krastanow islands on silicon as probed by high resolution x-ray diffraction. *J. Appl. Phys.*, 96(4):1959–1962, 2004.

[131] M. S. Rodrigues, M. Hrouzek, O. Dhez, J. Chevrier, F. Comin, R. Garrett, I. Gentle, K. Nugent, and S. Wilkins. Integration of an Atomic Force Microscope in a Beamline Sample Environment. Number 1234, pages 609–612, 2010.

[132] Nicolas Pilet, Joerg Raabe, Stephanie E Stevenson, Sara Romer, Laetitia Bernard, Christopher R McNeill, Rainer H Fink, Hans J Hug, and Christoph Quitmann. Nanostructure characterization by a combined x-ray absorption/scanning force microscopy system. *Nanotechnology*, 23(47):475708, nov 2012.

[133] Carole Fauquet, Mael Dehlinger, Franck Jandard, Sylvain Ferrero, Daniel Pailharey, Sylvia Larcheri, Roberto Graziola, Juris Purans, Aniouar Bjeoumikhov, Alexei Erko, Ivo Zizak, Brahim Dahmani, and Didier Tonneau. Combining scanning probe microscopy and x-ray spectroscopy. *Nanoscale Research Letters*, 6(1):308, 2011.

[134] Cedric Leclere, Thomas W. Cornelius, Zhe Ren, Anton Davydok, Jean Sabastien Micha, Odile Robach, Gunther Richter, Laurent Belliard, and Olivier Thomas. In situ bending of an Au nanowire monitored by micro Laue diffraction. *J. Appl. Crystallogr.*, 48(1):291–296, 2015.

[135] C. Leclere, T. W. Cornelius, Z. Ren, O. Robach, J.-S. Micha, A. Davydok, O. Ulrich, G. Richter, and O. Thomas. KB scanning of X-ray beam for Laue microdiffraction on accelero-phobic samples: application to in-situ mechanically loaded nanowires. *J. Synchrotron Radiat.*, 23(6):1–6, 2016.

[136] M. S. Rodrigues, T. W. Cornelius, T. Scheler, C. Mocuta, A. Malachias, R. Magalhães-Paniago, O. Dhez, F. Comin, T. H. Metzger, and J. Chevrier. In situ observation of the elastic deformation of a single epitaxial SiGe crystal by combining atomic force microscopy and micro x-ray diffraction. *J. Appl. Phys.*, 106(10), 2009.

[137] P. Schroth, T. Slobodskyy, D. Grigoriev, A. Minkevich, M. Riotte, S. Lazarev, E. Fohtung, D.Z. Hu, D.M. Schaadt, and T. Baumbach. Investigation of buried quantum dots using grazing incidence X-ray diffraction. *Mater. Sci. Eng. B*, 177(10):721–724, jun 2012.

[138] M S Rodrigues, O Dhez, S Le Denmat, J Chevrier, R Felici, F Comin, and S Le Denmat. Local detection of X-ray spectroscopies with an in-situ Atomic Force Microscope. *J. Instrum.*, 3(12):P12004–P12004, 2008.

[139] T. Slobodskyy, a. V. Zozulya, R. Tholapi, L. Liefeith, M. Fester, M. Sprung, and W. Hansen. Versatile atomic force microscopy setup combined with micro-focused X-ray beam. *Rev. Sci. Instrum.*, 86(6):065104, 2015.

[140] R Tholapi, L Liefeith, G Ekindorf, K Perumal, T Slobodskyy, and W Hansen. Effect of low-temperature post-growth annealing on anisotropic strain in epitaxial Fe layers deposited on GaAs (001). 245304(001):0–5, 2016.

[141] Ian N. Sneddon. The relation between load and penetration in the axisymmetric boussinesq problem for a punch of arbitrary profile. *Int. J. Eng. Sci.*, 3(1):47–57, may 1965.

[142] E. M. joint author Lifshits and Landau Davidovich, Lev. *Theory of elasticity*. Pergamon Press, 1959.

[143] B. V. Yakshinskiy, R. Wasielewski, E. Loginova, and Theodore E. Madey. Carbon accumulation and mitigation processes, and secondary electron yields of ruthenium surfaces. *Proc. SPIE*, 6517:65172Z–65172Z–11, 2007.

[144] M. V. Vitorino, Y. Fuchs, T. Dane, M. S. Rodrigues, M. Rosenthal, A. Panzarella, P. Bernard, O. Hignette, L. Dupuy, M. Burghammer, and L. Costa. An in situ atomic force microscope for normal-incidence nanofocus X-ray experiments. *J. Synchrotron Radiat.*, 23(5), 2016.

[145] Mark Johnson, Hyun Cheol Koo, Suk Hee Han, and Joonyeon Chang. Spin injection in indium arsenide. *Front. Phys.*, 3, aug 2015.

[146] A Manchon, H C Koo, J Nitta, S M Frolov, and R A Duine. New perspectives for Rashba spin-orbit coupling. *Nat. Mater.*, 14(9):871–882, aug 2015.

[147] Tomotsugu Ishikura, Lenanrt-Knud Liefeith, Zhixin Cui, Keita Konishi, Kanji Yoh, and Tetsuya Uemura. Electrical spin injection from ferromagnet into an InAs quantum well through a MgO tunnel barrier. *Appl. Phys. Express*, 7(7):073001, jul 2014.

[148] Hyun Cheol Koo, Hyunjung Yi, Jae Beom Ko, Joonyeon Chang, Suk Hee Han, Donghwa Jung, Seon Gu Huh, and Jonghwa Eom. Electrical spin injection and detection in an InAs quantum well. *Appl. Phys. Lett.*, 90(2):022101, jan 2007.

[149] J. M. Chauveau, Y. Androussi, A. Lefebvre, J. Di Persio, and Y. Cordier. Indium content measurements in metamorphic high electron mobility transistor structures by combination of x-ray reciprocal space mapping and transmission electron microscopy. *J. Appl. Phys.*, 93(7):4219–4225, 2003.

[150] X Z Shang, S D Wu, C Liu, W X Wang, L W Guo, Q Huang, and J M Zhou. Low temperature step-graded InAlAs/GaAs metamorphic buffer layers grown by molecular beam epitaxy. *J. Phys. D. Appl. Phys.*, 39(9):1800–1804, 2006.

[151] Wan Khai Loke, Kian Hua Tan, Satrio Wicaksono, Soon Fatt Yoon, Man Hon Samuel Owen, and Yee-Chia Yeo. Effect of growth temperature on the epitaxy strain relaxation and the tilt of $In_xGa_{1-x}As$ graded layer grown by solid source molecular beam epitaxy. *J. Phys. D. Appl. Phys.*, 45(50):505106, 2012.

[152] Yvon Cordier, Sylvain Bollaert, Mohammed Zaknoune, Jean Dipersio, and Denise Ferre. InAlAs/InGaAs metamorphic high electron mobility transistors on GaAs substrate: Influence of indium content on material properties and device performance. *Japanese J. Appl. Physics, Part 1 Regul. Pap. Short Notes Rev. Pap.*, 38(2 B):1164–1168, 1999.

[153] Y. Cordier, D. Ferre, J. M. Chauveau, and J. Dipersio. Surface morphology and strain relaxation of InAlAs buffer layers grown lattice mismatched on GaAs with inverse steps. *Appl. Surf. Sci.*, 166(1):442–445, 2000.

[154] Ian Mathews, Donagh O'Mahony, Agnieszka Gocalinska, Marina Manganaro, Emanuele Pelucchi, Michael Schmidt, Alan P. Morrison, and Brian Corbett. InAlAs solar cell on a GaAs substrate employing a graded $In_xGa_{1-x}As$-InP metamorphic buffer layer. *Appl. Phys. Lett.*, 102(3):033906, jan 2013.

[155] R Winkler. Spin orientation and spin precession in inversion-asymmetric quasi-two-dimensional electron systems. *Phys. Rev. B*, 69(4):045317, jan 2004.

[156] Sergey D. Ganichev and Leonid E. Golub. Interplay of Rashba/Dresselhaus spin splittings probed by photogalvanic spectroscopy -A review. *Phys. status solidi*, 251(9):1801–1823, sep 2014.

[157] S. Mendach, C. M. Hu, Ch Heyn, S. Schnüll, H. P. Oepen, R. Anton, and W. Hansen. Strain relaxation in high-mobility InAs inserted-channel heterostructures with metamorphic buffer. *Phys. E Low-Dimensional Syst. Nanostructures*, 13(2-4):1204–1207, 2002.

[158] D. Araújo, D. González, R. García, A. Sacedón, and E. Calleja. Dislocation behavior in InGaAs step- and alternating step-graded structures: Design rules for buffer fabrication. *Appl. Phys. Lett.*, 67(1995):3632, 1995.

[159] Kevin H. Chang, Pallab K. Bhattacharya, and Ronald Gibala. Characteristics of dislocations at strained heteroepitaxial InGaAs/GaAs interfaces. *J. Appl. Phys.*, 66(7):2993, 1989.

[160] Ch Heyn, D. Endler, K. Zhang, and W. Hansen. Formation and dissolution of InAs quantum dots on GaAs. *J. Cryst. Growth*, 210(4):421–428, 2000.

[161] Hao Lee, Roger Lowe-Webb, Weidong Yang, and Peter C. Sercel. Determination of the shape of self-organized InAs/GaAs quantum dots by reflection high energy electron diffraction. *Appl. Phys. Lett.*, 72(7):812, 1998.

[162] Y. Cordier, P. Lorenzini, J. M. Chauveau, D. Ferré, Y. Androussi, J. DiPersio, D. Vignaud, and J. L. Codron. Influence of MBE growth conditions on the quality of InAlAs/InGaAs metamorphic HEMTs on GaAs. *J. Cryst. Growth*, 251(1-4):822–826, 2003.

[163] Y. Yoneda. Anomalous Surface Reflection of X Rays. *Phys. Rev.*, 131(5):2010–2013, sep 1963.

[164] A. Zhylik, A. Benediktovich, A. Ulyanenkov, H. Guerault, M. Myronov, A. Dobbie, D. R. Leadley, and T. Ulyanenkova. High-resolution x-ray diffraction investigation of relaxation and dislocations in SiGe layers grown on (001), (011), and (111) Si substrates. *J. Appl. Phys.*, 109(12):0–12, 2011.

[165] D. Lee, M. S. Park, Z. Tang, H. Luo, R. Beresford, and C. R. Wie. Characterization of metamorphic $In_xAl_{1-x}As/GaAs$ buffer layers using reciprocal space mapping. *J. Appl. Phys.*, 101(6):063523, 2007.

[166] B. Landgraf, T. Slobodskyy, Ch Heyn, and W. Hansen. Strain relaxation in metamorphic InAlAs buffers. *Mater. Sci. Eng. B Solid-State Mater. Adv. Technol.*, 177(10):762–767, 2012.

[167] Gilbert André Chahine, Marie Ingrid Richard, Roberto Arturo Homs-Regojo, Thu Nhi Tran-Caliste, Dina Carbone, Vincent Louis Robert Jaques, Raphael Grifone, Peter Boesecke, Jens Katzer, Ioan Costina, Hamid Djazouli, Thomas Schroeder, and Tobias Urs Schülli. Imaging of strain and lattice orientation by quick scanning X-ray microscopy combined with three-dimensional reciprocal space mapping. *J. Appl. Crystallogr.*, 47(2):762–769, 2014.

[168] Marie-ingrid Richard, Marvin H Zoellner, Gilbert A Chahine, Peter Zaumseil, Giovanni Capellini, Maik Háberlen, Peter Storck, Tobias Schúlli, and Thomas Schroeder. Structural Mapping of Functional Ge Layers Grown on Graded SiGe Buffers for sub-10 nm CMOS Applications Using Advanced X-ray Nanodiffraction. *ACS Appl. Mater. Interfaces*, 7(48):26696–26700, dec 2015.

[169] Marvin H. Zoellner, Marie Ingrid Richard, Gilbert A. Chahine, Peter Zaumseil, Christian Reich, Giovanni Capellini, Francesco Montalenti, Anna Marzegalli, Ya Hong Xie, Tobias U. Schülli,

Maik Häberlen, Peter Storck, and Thomas Schroeder. Imaging structure and composition homogeneity of 300 mm SiGe virtual substrates for advanced CMOS applications by scanning X-ray diffraction microscopy. *ACS Appl. Mater. Interfaces*, 7(17):9031–9037, 2015.

[170] C Ponchut, J M Rigal, J Clément, E Papillon, A Homs, and S Petitdemange. MAXIPIX, a fast readout photon-counting X-ray area detector for synchrotron applications. *J. Instrum.*, 6(01):C01069–C01069, jan 2011.

[171] R. S. Goldman, K. L. Kavanagh, H. H. Wieder, S. N. Ehrlich, and R. M. Feenstra. Effects of GaAs substrate misorientation on strain relaxation in $In_xGa_{1-x}As$ films and multilayers. *J. Appl. Phys.*, 83(10):5137–5149, may 1998.

[172] A. E. Romanov, W. Pompe, S. Mathis, G. E. Beltz, and J. S. Speck. Threading dislocation reduction in strained layers. *J. Appl. Phys.*, 85(1):182–192, jan 1999.

[173] J S Speck, M A Brewer, G Beltz, A. E. Romanov, and W Pompe. Scaling laws for the reduction of threading dislocation densities in homogeneous buffer layers. *J. Appl. Phys.*, 80(7):3808–3816, oct 1996.

[174] F. K. LeGoues, B. S. Meyerson, J. F. Morar, and P. D. Kirchner. Mechanism and conditions for anomalous strain relaxation in graded thin films and superlattices. *J. Appl. Phys.*, 71(9):4230–4243, may 1992.

[175] Srikanth B Samavedam and E. a. Fitzgerald. Novel dislocation structure and surface morphology effects in relaxed Ge/Si-Ge(graded)/Si structures. *J. Appl. Phys.*, 81(1997):3108, 1997.

[176] Yu B. Bolkhovityanov, A. S. Deryabin, A. K. Gutakovskii, M. A. Revenko, and L. V. Sokolov. Dominating nucleation of misfit dislocations from the surface in GeSi/Si(0 0 1) films with a stepwise composition grown by means of molecular-beam epitaxy. *J. Cryst. Growth*, 293(2):247–252, 2006.

[177] L. B. Freund. A criterion for arrest of a threading dislocation in a strained epitaxial layer due to an interface misfit dislocation in its path. *J. Appl. Phys.*, 68(5):2073–2080, sep 1990.

[178] P. M. Mooney. Strain relaxation and dislocations in SiGe/Si structures. *Mater. Sci. Eng. R Reports*, 17(3):105–146, 1996.

[179] Yu B Bolkhovityanov and L V Sokolov. Ge-on-Si films obtained by epitaxial growing: edge dislocations and their participation in plastic relaxation. *Semicond. Sci. Technol.*, 27(4):043001, apr 2012.

[180] Sergey Yu Shiryaev, Flemming Jensen, and Jon Wulff Petersen. On the nature of crosshatch patterns on compositionally graded $Si_{1-x}Ge_x$ alloy layers. *Appl. Phys. Lett.*, 64(24):3305–3307, jun 1994.

[181] P M Mooney, J L Jordan-Sweet, I C Noyan, S K Kaldor, and P C Wang. Observation of local tilted regions in strain-relaxed SiGe/Si buffer layers using x-ray microdiffraction. *Appl. Phys. Lett.*, 74(5):726–728, 1999.

[182] C. Ferrari, P. Franzosi, L. Lazzarini, G. Salviati, M. Berti, A.V. Drigo, M. Mazzer, F. Romanato, M.R. Bruni, and M.G. Simeone. Mechanisms of strain release in molecular beam epitaxy grown InGaAs/GaAs buffer heterostructures. *Mater. Sci. Eng. B*, 28(1-3):510–514, dec 1994.

[183] Valeria Mondiali, Monica Bollani, Stefano Cecchi, Marie Ingrid Richard, Tobias Schülli, Gilbert Chahine, and Daniel Chrastina. Dislocation engineering in SiGe on periodic and aperiodic Si(001) templates studied by fast scanning X-ray nanodiffraction. *Appl. Phys. Lett.*, 104(2), 2014.

[184] G. Dresselhaus. Spin-Orbit Coupling Effects in Zinc Blende Structures. *Phys. Rev.*, 100(2):580–586, oct 1955.

[185] S. Löhr, S. Mendach, T. Vonau, Ch. Heyn, and W. Hansen. Highly anisotropic electron transport in shallow InGaAs heterostructures. *Phys. Rev. B*, 67(4):1–4, 2003.

[186] nextnano GmbH. nextnano - semiconductor software solutions.

[187] E. H. Hall. On a New Action of the Magnet on Electric Currents. *Am. J. Math.*, 2(3):287, sep 1879.

[188] K. v. Klitzing, G. Dorda, and M. Pepper. New Method for High-Accuracy Determination of the Fine-Structure Constant Based on Quantized Hall Resistance. *Phys. Rev. Lett.*, 45(6):494–497, aug 1980.

[189] L Schubnikow and W.J De Haas. A New Phenomenon in the Change of Resistance in a Magnetic Field of Single Crystals of Bismuth : Abstract : Nature. *Nature*, 126:500–500, 1930.

[190] Supriyo Datta. *Electronic transport in mesoscopic systems*. Cambridge University Press, 1995.

[191] N. Tournerie, P. Schieffer, B. Lepine, C. Lallaizon, and G. Jezequel. Structural and magnetic anisotropy properties in epitaxial Fe films on $Al_{0.48}In_{0.52}As$(001). *IEEE Trans. Magn.*, 41(10):3322–3324, 2005.

[192] Y J Park, M C Hickey, M J Van Veenhuizen, J Chang, D Heiman, C H Perry, and J S Moodera. Efficient spin transfer phenomena in Fe/MgO/GaAs structure. *J. Phys. Condens. Matter*, 23(11):116002, 2011.

[193] C. Gusenbauer, T. Ashraf, J. Stangl, G. Hesser, T. Plach, A. Meingast, G. Kothleitner, and R. Koch. Interdiffusion in Heusler film epitaxy on GaAs(001). *Phys. Rev. B - Condens. Matter Mater. Phys.*, 83(3):1–8, 2011.

[194] K Tivakornsasithorn, A M Alsmadi, X Liu, J C Leiner, Y Choi, and D J Keavney. Exchange bias and asymmetric magnetization reversal in ultrathin Fe films grown on GaAs (001) substrates. *J. Appl. Phys.*, 113(13):133908, 2013.

[195] W. H. Lee, H. L. Cho, B. S. Cho, J. Y. Kim, W. J. Nam, Y-S. Kim, W. G. Jung, H. Kwon, J. H. Lee, J. G. Lee, P. J. Reucroft, C. M. Lee, and E. G. Lee. Diffusion barrier and electrical characteristics of a self-aligned MgO layer obtained from a Cu(Mg) alloy film. *Appl. Phys. Lett.*, 77(14):2192, 2000.

[196] Shu-Huei Hsieh, Wen Chen, and Chu-Mo Chien. Structural Stability of Diffusion Barriers in Cu/Ru/MgO/Ta/Si. *Nanomaterials*, 5(4):1840–1852, nov 2015.

[197] Kyung-Ho Ho Kim, Hyung-jun Jun Kim, Jae-Pyung Pyung Ahn, Seung-Cheol Cheol Lee, Sung Ok Won, Jun Woo Choi, and Joonyeon Chang. Epitaxial growth of Fe and MgO layers on GaAs (001): Microstructure and magnetic property. *J. Appl. Phys.*, 110(11):114910, 2011.

[198] Shibo Wang, Anirban Sarkar, Markus Gruber, and Reinhold Koch. Epitaxy and stress of MgO/-GaAs(001) heterostructures. *J. Appl. Phys.*, 114(15):154511, 2013.

[199] Takashi Manago, Asawin Sinsarp, and Hiro Akinaga. Growth condition dependence of spin-polarized electroluminescence in Fe / MgO/light-emitting diodes. *J. Appl. Phys.*, 102(8), 2007.

[200] Kun Rok Jeon, Byoung Chul Min, Hun Sung Lee, Jae Shin, Chang Yup Park, and Sung Chul Shin. Single crystalline CoFe/MgO tunnel contact on nondegenerate Ge with a proper resistance-area product for efficient spin injection and detection. *Appl. Phys. Lett.*, 97(2):15–18, 2010.

[201] Y. J. Park, M. C. Hickey, M. J. Van Veenhuizen, J. Chang, D. Heiman, and J. S. Moodera. Analysis of current-voltage characteristics of Fe/MgO/GaAs junctions using self-consistent field modeling. *Phys. Rev. B - Condens. Matter Mater. Phys.*, 80:1–7, 2009.

[202] Shibo Wang, Anirban Sarkar, Markus Gruber, and Reinhold Koch. Epitaxy and stress of MgO/-GaAs(001) heterostructures. *J. Appl. Phys.*, 114(15):154511, 2013.

[203] Hak Ki Yu and Jong-Lam Lee. Growth Mechanism of MgO Film on Si (100), Domain Matching Epitaxy, Strain Relaxation, Preferred Orientation Formation. *Cryst. Growth Des.*, 10(12):5200–5204, dec 2010.

[204] G. X. Miao, J. Y. Chang, M. J. Van Veenhuizen, K. Thiel, M. Seibt, G. Eilers, M. Münzenberg, and J. S. Moodera. Epitaxial growth of MgO and Fe/MgO/Fe magnetic tunnel junctions on (100)-Si by molecular beam epitaxy. *Appl. Phys. Lett.*, 93(14):1–4, 2008.

[205] William H Butler. Tunneling magnetoresistance from a symmetry filtering effect. *Sci. Technol. Adv. Mater.*, 9(1):014106, apr 2008.

[206] W H Butler, X.-G. Zhang, X Wang, J van Ek, and J M MacLaren. Electronic structure of FM|semiconductor|FM spin tunneling structures. *J. Appl. Phys.*, 81(8):5518–5520, 1997.

[207] H. Saito, Y. Mineno, S. Yuasa, and K. Ando. Reducing Schottky barrier height for Fe/ n -GaAs junction by inserting thin GaO x layer. *J. Appl. Phys.*, 109(7):07C701, apr 2011.

[208] Faqiang Xu, Haibin Pan, Wenhua Zhang, Guodong Wang, Zongmu Li, and Pengshou Xu. Electronic structure of the interface of GaAs(100) with MgO overlayer grown by thermal evaporation of Mg in O_2under UHV. *J. Electron Spectros. Relat. Phenomena*, 144-147:385–388, jun 2005.

[209] Jun Woo, Hyung-jun Kim, Kyung-ho Kim, Andreas Scholl, and Joonyeon Chang. Uniaxial magnetic anisotropy in epitaxial Fe / MgO films on GaAs (001). *Cryst. Growth Des.*, 360:109–112, 2014.

[210] X H Wei, Y R Li, J Zhu, Y Zhang, Z Liang, and W Huang. In situ analysis of lattice relaxation by reflection high-energy electron diffraction. *J. Phys. D. Appl. Phys.*, 38(23):4222–4226, dec 2005.

[211] G. Chen, J. X. Li, J. Zhu, J. H. Liang, and Y. Z. Wu. In-plane magnetic anisotropy in Fe/MgO/-GaAs(001) system. *J. Appl. Phys.*, 109(7):07C108, 2011.

[212] Igor V. Kozhevnikov, Luca Peverini, and Eric Ziegler. Development of a self-consistent free-form approach for studying the three-dimensional morphology of a thin film. *Phys. Rev. B - Condens. Matter Mater. Phys.*, 85(12):1–15, 2012.

[213] Igor V. Kozhevnikov. Physical analysis of the inverse problem of X-ray reflectometry. *Nucl. Instruments Methods Phys. Res. Sect. A Accel. Spectrometers, Detect. Assoc. Equip.*, 508(3):519–541, 2003.

[214] V. V. Roddatis, U. Hubner, B. I. Ivanov, E. Ilichev, H.-G. Meyer, M. V. Kovalchuk, and A. L. Vasiliev. The morphology of Al-based submicron Josephson junction. *J. Appl. Phys.*, 110(12):123903, dec 2011.

[215] Vladimir V. Roddatis, Sergey N. Yakunin, Alexander L. Vasiliev, Mikhail V. Kovalchuk, Alexej Yu Seregin, Timur M. Burbaev, and Michail N. Gordeev. The microstructural and op-

tical properties of Ge/Si heterostructures grown by low-temperature molecular beam epitaxy. *J. Mater. Res.*, 28(11):1432–1441, jun 2013.

[216] E.A. Owen and E.L. Yates. XLI. Precision measurements of crystal parameters. *London, Edinburgh, Dublin Philos. Mag. J. Sci.*, 15(98):472–488, feb 1933.

[217] V. G. Tsirelson, A. S. Avilov, Yu. A. Abramov, E. L. Belokoneva, R. Kitaneh, D. Feil, and IUCr. X-ray and Electron Diffraction Study of MgO. *Acta Crystallogr. Sect. B Struct. Sci.*, 54(1):8–17, feb 1998.

[218] P.A. Stadelmann. EMS - a software package for electron diffraction analysis and HREM image simulation in materials science. *Ultramicroscopy*, 21(2):131–145, jan 1987.

[219] M. Brockmann, M. Zölfl, S. Miethaner, and G. Bayreuther. In-plane volume and interface magnetic anisotropies in epitaxial Fe films on GaAs(001). *J. Magn. Magn. Mater.*, 198-199:384–386, jun 1999.

[220] R. Moosbuhler, F Bensch, M Dumm, and G Bayreuther. Epitaxial Fe films on GaAs(001): Does the substrate surface reconstruction affect the uniaxial magnetic anisotropy. *J. Appl. Phys.*, 91(10):8757, 2002.

[221] M Madami, S Tacchi, G Carlotti, G Gubbiotti, and R L Stamps. In situ Brillouin scattering study of the thickness dependence of magnetic anisotropy in uncovered and Cu-covered Fe/GaAs(100) ultrathin films. *Phys. Rev. B*, 69(14):144408, apr 2004.

[222] Bartek Kardasz, Oleksandr Mosendz, Bret Heinrich, Marek Przybylski, and Jiirgen Kirschner. Magnetic anisotropies in GaAs/Fe(001) structures. *J. Phys. Conf. Ser.*, 200(7):072046, jan 2010.

[223] P.K.J. Wong, Y. Fu, W. Zhang, Y. Zhai, Y.B. Xu, Z.C. Huang, Y.X. Xu, and H.R. Zhai. Influence of Capping Layers on Magnetic Anisotropy in Fe/MgO/GaAs(100) Ultrathin Films. *IEEE Trans. Magn.*, 44(11):2907–2910, nov 2008.

[224] S. Sakshath, S. V. Bhat, P. S. Anil Kumar, D. Sander, and J. Kirschner. Enhancement of uniaxial magnetic anisotropy in Fe thin films grown on GaAs(001) with an MgO underlayer. *J. Appl. Phys.*, 109(7):07C114, 2011.

[225] Qing-feng Zhan, Stijn Vandezande, Kristiaan Temst, and Chris Van Haesendonck. Magnetic anisotropy and reversal in epitaxial Fe-MgO(001) films. *Phys. Rev. B*, 80(9):094416, sep 2009.

[226] Qing-feng Zhan, Stijn Vandezande, Chris Van Haesendonck, and Kristiaan Temst. Manipulation of in-plane uniaxial anisotropy in Fe-MgO(001) films by ion sputtering. *Appl. Phys. Lett.*, 91(12):122510, sep 2007.

[227] O Thomas, Q Shen, P Schieffer, N Tournerie, and B Lépine. Interplay between anisotropic strain relaxation and uniaxial interface magnetic anisotropy in epitaxial Fe films on (001) GaAs. *Phys. Rev. Lett.*, 90(January):017205, 2003.

[228] C. Martínez Boubeta, C. Clavero, J. M. García-Martín, G. Armelles, A. Cebollada, Ll Balcells, J. L. Menéndez, F. Peiró, A. Cornet, and Michael F. Toney. Coverage effects on the magnetism of Fe/MgO (001) ultrathin films. *Phys. Rev. B*, 71(1):014407, jan 2005.

[229] John G. Simmons. Electric Tunnel Effect between Dissimilar Electrodes Separated by a Thin Insulating Film. *J. Appl. Phys.*, 34(9):2581, 1963.

Journal Publications

- R. Tholapi, I. A. Karateev, B. S. Roshchin, V. E. Asadchikov, T. Slobodskyy, W. Hansen, and A. L. Vasiliev, “Interface matching and intermixing of thin MgO barriers and ferromagnetic layers deposited on GaAs (001)," J. Appl. Phys., vol. 121, no. 20, p. 205308, May 2017.

- L.-K. Liefeith, R. Tholapi, T. Ishikura, M. Hänze, R. Hartmann, T. Slobodskyy, and W. Hansen, “Spin injection beyond the diffusive limit in the presence of spin-orbit coupling” *Phys. Rev. B* 95, 81303(R), Feb.2017.

- R. Tholapi, L. Liefeith, G. Ekindorf, K. Perumal, T. Slobodskyy, and W. Hansen, “Effect of low-temperature post-growth annealing on anisotropic strain in epitaxial Fe layers deposited on GaAs(001)," *J. Appl. Phys.*, vol. 119, no. 24, p. 245304, Jun. 2016.

- L.-K. Liefeith, R. Tholapi, M. Hänze, R. Hartmann, T. Slobodskyy, and W. Hansen, “Influence of thermal annealing on the spin injection and spin detection through Fe/GaAs interfaces," *Appl. Phys. Lett.*, vol. 108, no. 21, p. 212404, May 2016.

- T. Slobodskyy, A. V. Zozulya, R. Tholapi, L. Liefeith, M. Fester, M. Sprung, and W. Hansen, “Versatile atomic force microscopy setup combined with micro-focused X-ray beam," *Rev. Sci. Instrum.*, vol. 86, no. 6, p. 65104, Jun. 2015.

Conference Contributions

- Rajkiran Tholapi, Taras Slobodskyy, Lennart-Knud Liefeith, Alexey Zozulya, Michael Sprung, Martin Sztucki, Wolfgang Hansen, Effect of indentation induced strain on epitaxial Fe layers, XTOP-2106, Brno, Czech Republic, September 4-8, 2016.

- Rajkiran Tholapi, Taras Slobodskyy, Lennart-Knud Liefeith, Alexey Zozulya, Michael Sprung, Martin Sztucki, Wolfgang Hansen, Diffraction mapping of strain fields induced by AFM tip in epitaxial spintronic structures using micro focus beam European XFEL/ HASYLAB User’s Meeting, Hamburg, January 28-29, 2016.

- Rajkiran Tholapi, Taras Slobodskyy, Alexey Zozulya, Lennart-Knud Liefeith, Michael Sprung and Wolfgang Hansen, Structural investigations of Fe/GaAs (001) heterojunctions containing MgO tunneling barriers, European XFEL/ HASYLAB User’s Meeting, Hamburg, January 28-30, 2015.

- Lennart-Knud Liefeith, Rajkiran Tholapi, Ann-Kathrin Michel, Taras Slobodskyy and Wolfgang Hansen, Spin-injection through Fe/GaAs Schottky contacts 21st International Conference on Electronic Properties of Two-Dimensional Systems/ 17th International Conference on Modulated Semiconductor Structures Sendai, Japan, July 26-31, 2015.

- Lennart-Knud Liefeith, Rajkiran Tholapi, Ann-Kathrin Michel, Taras Slobodskyy and Wolfgang Hansen, Spin-injection through meal-semiconductor contacts, DPG Tagung , Berlin, March 15 - 20, 2015.

- Taras Slobodskyy, Gerda Ekindorf, Rajkiran Tholapi, Lennart-Knud Liefeith and Wolfgang Hansen, CAFM on metal/semiconductor interfaces, European XFEL/ HASYLAB User's Meeting, Hamburg, January 28-30, 2015.

- Rajkiran Tholapi, Lennart-Knud Liefeith, Michael Wachtel,Gerda Ekindorf, Taras Slobodskyy, and Wolfgang Hansen, Crystallinity of the Fe/GaAs interface for Spintronics, DPG Tagung, Berlin, March 15-20, 2015.

Acknowledgments

First, I would like to express my sincere gratitude to Prof. Wolfgang Hansen who has given me the opportunity to work in his group. Dear Wolfgang, thank you very much for your patience and effort to help me understand many aspects of this thesis.

I would like to thank my co-supervisor, Dr. Taras Slobodskyy for teaching me every technique that I have done during this work. Without his motivation and persistent help this thesis would have never taken shape and for that, I am eternally grateful to him. I would also like to thank Dr. Michael Sprung for agreeing to be the second reviewer of my thesis and also for his support during my application for Joachim Hertz Stiftung scholarship.

I owe a huge thanks to my collaborator Dr. Alexey Zozulya for his companionship and support during many beamtimes at PETRA III and ESRF. I would also like to acknowledge Stephan Martens for his help performing MOKE measurements and data analysis.

I would also like to thank other members of "spintronics" project; Boris Landgraf for introducing me to the MBE-cluster and teaching me regarding Epitaxial growth. Lennart Liefeith for his collaboration in performing spin-injection experiments. I am especially thankful to him for being a friendly office-mate and for always finding time to a grab a cup of coffee with me. And Robert Hartmann for helping me run the electrical measurements on close-cycle cryostat.

I am thankful to Dr. Christian Heyn for always helping me with MBE related issues and for explaining me the basics of epitaxial growth. I would like to thank Michael Zocher for helping me with clean-room processes and also for his company during many late hours in the lab. I would also like to extend my gratitude to other group members, Achim Küster, Nils Gayer, Katrin Groth, Olga Weber and Sandra Schnüll for their support in lab and help in administrative work.

During these last three, I had a huge privilege of sharing my work with Gerda Ekindorf as part of her both bachelor and master's thesis. I thank her for the effort and companionship. I would also like to thank Michael Wachter for his work on X-ray diffractometer as part of his bachelor thesis.

I would like to acknowledge the Joachim Hertz Stiftung for granting me a scholarship to pursue my Ph.D. I would also like to thank Eva Ackermann at JHS for indulging me with my funding requests. I also like to thank Stefanie Tepass and PIER team for helping me to participate in many graduate school events. I also like to acknowledge the efforts of International office at DESY for their immense help with any administrative need I have had over the years.

Furthermore I would like to sincerely thank Karthick, Moon, Rashmi and Uday for making me feel at home. You have accepted me for who I am and made my time in Hamburg ever so memorable. I am grateful to all my family and friends back home for their encouragement and support. Finally I thank my parents Pramela and Appalachari for allowing me choose my own path and for always being there for me.

Declaration on oath

I hereby declare, on oath, that I have written the present dissertation by my own and have not used other than the acknowledged resources and aids.

Hamburg,
September 06, 2017,
(date & place)

Rajkiran Tholapi